

AD \_\_\_\_\_

Award Number: DAMD17-03-C-0086

TITLE: The Thermal Stabilization of Vaccines Against Agents of Bioterrorism

PRINCIPAL INVESTIGATOR: C. R. Middaugh, Ph.D.

CONTRACTING ORGANIZATION: The University of Kansas Center for Research, Inc.  
Lawrence, KS 66045-7563

REPORT DATE: September 2005

TYPE OF REPORT: Final

20060215 140

PREPARED FOR: U.S. Army Medical Research and Materiel Command  
Fort Detrick, Maryland 21702-5012

DISTRIBUTION STATEMENT: Approved for Public Release;  
Distribution Unlimited

The views, opinions and/or findings contained in this report are those of the author(s) and should not be construed as an official Department of the Army position, policy or decision unless so designated by other documentation.

# REPORT DOCUMENTATION PAGE

*Form Approved  
OMB No. 0704-0188*

Public reporting burden for this collection of information is estimated to average 1 hour per response, including the time for reviewing instructions, searching existing data sources, gathering and maintaining the data needed, and completing and reviewing this collection of information. Send comments regarding this burden estimate or any other aspect of this collection of information, including suggestions for reducing this burden to Department of Defense, Washington Headquarters Services, Directorate for Information Operations and Reports (0704-0188), 1215 Jefferson Davis Highway, Suite 1204, Arlington, VA 22202-4302. Respondents should be aware that notwithstanding any other provision of law, no person shall be subject to any penalty for failing to comply with a collection of information if it does not display a currently valid OMB control number. PLEASE DO NOT RETURN YOUR FORM TO THE ABOVE ADDRESS.

<b>1. REPORT DATE (DD-MM-YYYY)</b> 01-09-2005			<b>2. REPORT TYPE</b> Final		<b>3. DATES COVERED (From - To)</b> 4 Aug 2003 – 3 Aug 2005	
<b>4. TITLE AND SUBTITLE</b> The Thermal Stabilization of Vaccines Against Agents of Bioterrorism			<b>5a. CONTRACT NUMBER</b>			
			<b>5b. GRANT NUMBER</b> DAMD17-03-C-0086			
			<b>5c. PROGRAM ELEMENT NUMBER</b>			
<b>6. AUTHOR(S)</b> C. R. Middaugh, Ph.D.  E-mail: middaugh@ku.edu			<b>5d. PROJECT NUMBER</b>			
			<b>5e. TASK NUMBER</b>			
			<b>5f. WORK UNIT NUMBER</b>			
<b>7. PERFORMING ORGANIZATION NAME(S) AND ADDRESS(ES)</b> The University of Kansas Center for Research, Inc. Lawrence, KS 66045-7563			<b>8. PERFORMING ORGANIZATION REPORT NUMBER</b>			
			<b>10. SPONSOR/MONITOR'S ACRONYM(S)</b>			
<b>9. SPONSORING / MONITORING AGENCY NAME(S) AND ADDRESS(ES)</b> U.S. Army Medical Research and Materiel Command Fort Detrick, Maryland 21702-5012			<b>11. SPONSOR/MONITOR'S REPORT NUMBER(S)</b>			
			<b>12. DISTRIBUTION / AVAILABILITY STATEMENT</b> Approved for Public Release; Distribution Unlimited			
<b>13. SUPPLEMENTARY NOTES</b>						
<b>14. ABSTRACT</b> No abstract provided.						
<b>15. SUBJECT TERMS</b> Adenovirus, valley fever, excipients, stability, formulation						
<b>16. SECURITY CLASSIFICATION OF:</b>			<b>17. LIMITATION OF ABSTRACT</b> UU	<b>18. NUMBER OF PAGES</b> 292	<b>19a. NAME OF RESPONSIBLE PERSON</b> USAMRMC <b>19b. TELEPHONE NUMBER (include area code)</b>	
<b>a. REPORT</b> U	<b>b. ABSTRACT</b> U	<b>c. THIS PAGE</b> U				

## **Table of Contents**

<b>Cover.....</b>	<b>1</b>
<b>SF 298.....</b>	<b>2</b>
<b>Table of Contents.....</b>	<b>3</b>
<b>Introduction.....</b>	<b>4</b>
<b>Body.....</b>	<b>5</b>
<b>Key Research Accomplishments.....</b>	<b>181</b>
<b>Reportable Outcomes.....</b>	<b>181</b>
<b>Conclusions.....</b>	<b>181</b>
<b>References.....</b>	<b>182</b>
<b>Appendices.....</b>	<b>184</b>

## **Introduction:**

Vaccines are without doubt the most powerful approach currently available for the prevention of the deleterious effects of toxins and infectious agents that might be used in a bioterrorism against civilians or military personnel. Recent disclosures have indicated that numerous countries/or terrorists organizations may possess biological weapons that could indeed be used for this purpose. Likely, agents include anthrax, botulinum toxin, smallpox, tularemia, plague, and Venezuelan equine encephalitis. With the exception of plague, vaccines exist for all these agents. Unfortunately, at least in the case of anthrax, the vaccine is very unstable and is inactivated at 37°C, limiting the ability to deliver the vaccine under battlefield conditions. It is probable the other vaccines will display similar instability. It is believed that this stability issue needs to be addressed by a systematic, molecular approach.

The work in this grant investigated a systematic approach to the stabilization of vaccines utilized for the protection of civilians and military personnel against potential bioterrorism agents. Adenovirus was used as a model organism to study degradative pathways in viruses that could be responsible for thermal instability. Recombinant protein vaccine candidates against anthrax and valley fever were studied as the initial candidates for stabilization. This approach utilized a variety of physical methods (2<sup>nd</sup> derivative UV absorption spectroscopy, intrinsic and extrinsic fluorescence, circular dichroism, dynamic light scattering, differential scanning calorimetry etc.) to identify the molecular event(s) responsible for degradation of the vaccine components. This information was used to generate empirical phase diagrams that define different stability states for each vaccine. Once regions of stability were identified, high-throughput screening assays were developed based on phase boundaries and used to screen libraries of excipients to identify potential stabilizers. The combination and concentration of excipients were optimized to provide both conformational stability to the protein/virus particles/protein complex and protect against aggregation.

**Body:** Three vaccine candidates were selected to investigate our systematic approach to vaccine stabilization. Studies performed with each of these are discussed in detail below.

### **Anthrax Protective Antigen (rPA)**

The following studies were carried out with the recombinant Anthrax Protective Antigen. The anthrax protective antigen was obtained in collaboration with BD Technologies. A manuscript entitled, “Anthrax vaccine powder formulations for nasal mucosal delivery” is accepted by Journal of Pharmaceutical Sciences (see appendices).

#### **UV Absorption Spectroscopy:**

Temperature perturbation studies were conducted at a protein concentration of 2.4  $\mu$ M with an Agilent 8453 UV-Visible spectrophotometer. Spectra were collected over a temperature range of 10 to 90°C at 2.5°C intervals. An integration time of 25 seconds was used to obtain spectra with a high degree of precision. A 5-min equilibration was included before collection of each spectrum, sufficient for equilibrium to be reached. The optical density at 360 nm was also monitored under the same temperature conditions to detect protein aggregation. Duplicate samples were run at each pH (3 to 8) to ensure measurement repeatability. Spectral analysis was performed using Chemstation™ software from Agilent. Second derivative spectra were obtained by using a nine point filter and the Savitsky-Golay method to fit data to a third order polynomial. The spectra were smoothed using 99 interpolated points between each raw data point, permitting 0.01 nm resolution. Peak positions were determined from the interpolated spectra using Microcal Origin™ 6.0 software.

Protein second derivative UV absorbance spectra typically displays six distinctive negative peaks for aromatic amino acids (not illustrated), all of which were monitored as a function of temperature at various pH values (PH 3-8). At 10°C, the negative peaks of rPA occurred at approximately 253 nm (peak 1: Phe), 259 nm (peak 2: Phe), 268.5 nm (peak3: Phe), 276 nm (peak 4: Tyr), 284 nm (peak 5: Tyr/Trp) and 291.6 nm (peak 6: Trp). Structural changes in the protein as a function of temperature and pH can be characterized by alterations in the positions of these peaks. The responses of the positions of the peaks to changes in temperature are shown in Figures 1-6. The peaks exhibited no significant changes in wavelength with changes in pH at 10°C. At

pH 3.0, significant deviations in peak position response to temperature are observed at temperatures above 20°C especially for peaks 1, 2 and 4. At higher pH values, transitions were observed at higher temperatures (40-60°C) and varied in their shape and the temperature range over which they occurred. The transitions were both pH and temperature dependent and often gave evidence of multiple events. This is best summarized in the form of a phase diagram as described below.

The effect of temperature on rPA aggregation/oligomerization was followed by monitoring the turbidity at 360 nm (Figure 7, Table 1). At pH 3, aggregation of rPA was only detected at temperatures above 80°C. Extensive aggregation of rPA was observed at pH 4, 5 and 6 beginning at 30.4, 36.4 and 43.7°C, respectively. The extent of rPA temperature-induced aggregation was decreased at pH 7 and 8. The aggregation onset values at pH 7 and 8 were 46.8 and 47.9°C, respectively. At pH values of 4 to 8, large increase in turbidity were observed, followed by a maximum in the intensities of scattering and then sharp decreases in magnitude, indicative of extensive protein precipitation. The turbidity data suggests that rPA is thermally more stable at pH 7 and 8.

### **Circular Dichroism Studies**

CD studies were performed with a Jasco-810 spectropolarimeter equipped with a Peltier temperature controller to measure changes in the secondary structure of rPA as a function of temperature. Briefly, the CD signal of rPA (0.2mg/ml) at 222 nm was monitored every 0.5°C as a function of pH and temperature from 10 to 90°C with a scanning rate of 15°C/hr using a 0.1 cm path length cuvette sealed with a Teflon stopper. A scanning speed of 20nm/min and a resolution of 1 nm were used. The CD signals were converted to molar ellipticity using Spectra Manager software (Jasco), and the melting temperatures ( $T_m$ ) were determined using Microcal Origin software.

The CD spectra of rPA displayed a single minima at about 206-208 nm with a marked shoulder at 216-217 nm at all pH values (Figure 8). The data suggests that rPA primarily consists of a mixture (e.g. alpha helix and beta sheet) of secondary structure types. It has

been earlier reported that anthrax protective antigen contains approximately 28% helix, 17% sheet, 22% turns with the remaining portion random coil. (C. Radha et. al., Journal of Biotechnology, p-235-242, 1996). The secondary structure of rPA undergoes significant pH and temperature-dependent transition, primarily suggestive of a loss of secondary structure (Figure 9, Table 1). These changes occur at significantly lower temperatures at acidic pH values (pH 3-4) suggesting that rPA is structurally more labile at pH 3 and 4. At pH 7 and 8, the CD signal did not show any measurable change with an increase in temperature suggesting that rPA is thermally more stable at these pH values. At pH 3, an increase in the negative ellipticity of protein was observed with an increase in temperature suggesting that rPA acquires a completely different secondary structure at this pH compared to that seen at higher pH values.

### **Intrinsic Fluorescence Studies**

Fluorescence studies were performed to measure alterations in the tertiary structure of rPA as a function of temperature and pH. Fluorescence emission spectra of rPA (1.2  $\mu$ M) were recorded as a function of temperature (10-85°C) and pH (3-8) using a PTI Quanta Master Spectrophotometer equipped with a turreted four-cell thermostatically controlled holder. The intrinsic fluorescence spectrum of tryptophan was monitored using an excitation wavelength of 295 nm (> 95% Trp emission). Emission spectra were collected over a range of 305 to 440 nm. Excitation and emission slits were set at 4 nm and a 1 cm path length quartz cuvette was used in all experiments. The spectra were collected at 2.5°C intervals with a 5 min equilibration time at each temperature. Buffer baselines were subtracted from each spectrum prior to data analysis. Data analysis was performed using Felix™ (PTI) software. Emission peak positions were determined by a “center of spectral mass” method. Thus, the reported values do not correspond to actual peak positions, but accurately reflect changes in peak position values. The actual peak position determined by derivative analysis of the native (10°C) protein at pH 7 is 330 nm, an approximately 14 nm red shift from actual values.

The change in fluorescence emission maxima (Peak position) as a function of temperature at various pH values is shown in Figure 10. A red shift in the peak positions of rPA with an increase in temperature was observed at all pH values. This corresponds to an increase in exposure of the tryptophan sidechains at elevated temperatures. The observed transitions, however, occurred at

different temperatures for each pH with an increase in transition temperature (transition start and midpoint) detected as the pH was increased (Table1). As seen during the CD studies, fluorescence analysis also finds that the most stable environment for rPA is within the pH range of 6-8. The fluorescence intensity at the maximum emission wavelength versus temperature curves for rPA (Figure 11) demonstrate a typical decrease in fluorescence intensity with temperature at all pH values with small but marked transitions occurring at different temperatures for different pH values confirming the peak shift results. At both pH 4 and 5, changes in tertiary structure commence at temperatures approximately 11°C lower than those at which changes in secondary structure are observed (Table1). This suggests that a range of temperature exists (22-33°C and 25-36°C for pH 3 and 4, respectively) in which rPA may adopt a molten globule like state. Molten globule states, with a pronounced secondary structure and compactness but without a tightly packed tertiary structure, are often induced under acidic conditions. Interestingly, the secondary and tertiary structure alterations started concurrently at pH 3. In addition, at pH 6-8, secondary structure changes were detected at approximately 5°C lower temperature than tertiary structure alterations, again suggesting the presence of molten globule-like states. Note that such states are often considered the source of a protein aggregation.

### **ANS Fluorescence**

8-Anilino-1-naphthalene sulfonate (ANS) was used as an extrinsic fluorescent probe to further study the alterations in the tertiary structure of rPA under conditions of varying pH and temperature. The binding of the apolar dye ANS to apolar (hydrophobic) sites on protein is often associated with an enhanced fluorescence and a blue shift in the wavelength of peak emission. In some cases, however, the negative charge on ANS is also thought to be involved in its interaction with proteins. ANS is also thought to have a much stronger affinity to protein “molten globule states” compared to its affinity for native and strongly structurally disrupted conformational states. The interactions of the hydrophobic fluorescent dye ANS with rPA was monitored as a function of temperature (10-85°C) and pH (3-8) using the same PTI Quanta Master Spectrophotometer described above. The concentration of protein was 1.2 µM and a molar ratio of ANS to protein of 20:1 was employed in all experiments. An excitation wavelength of 375 nm was used and spectra were collected from 400-600 nm. Excitation and emission slits were set at 4 nm and a 1 cm path

length quartz cuvette was used. The spectra were collected at 2.5°C intervals with a 5 min equilibration time at each temperature.

The change in ANS fluorescence maxima emission wavelength and intensity as a function of temperature and pH are shown in Figures 12 and 13, respectively. Sharp transitions, occurring at distinct temperatures for each pH, were apparent and closely model those seen by the previously described techniques. At pH 3.0, the protein appears to manifest significant apolar character at 10°C, typified by a large increase in ANS intensity and a large blue shift in maximum emission wavelength, suggesting that the protein is structurally altered. As the temperature is increased, the maximum emission wavelength at pH 3 exhibits a linear increase through 85°C. In contrast, at pH 4-7, a blue shift is observed with increases in temperature and the transitions were pH dependent as seen earlier with intrinsic fluorescence (Table 1). In addition, changes in the fluorescence of ANS become less pronounced with the increase in pH from 3 to 5, suggesting less binding of ANS to rPA at these pH values. The fluorescence intensity of ANS was much weaker at pH 6-8. These results are consistent with the increased molten globule character seen at lower pH by the other methods. Furthermore, the transitory appearance of such states at higher pH is also evident in the ANS studies as manifested by the small transitions seen under these conditions.

#### **Phase diagram of rPA using 2<sup>nd</sup> derivative UV spectroscopy data**

The six peak position data obtained from high-resolution 2<sup>nd</sup> derivative UV absorption spectroscopy was used to generate a phase diagram of rPA using a multidimensional vector approach. By phase diagram, we refer to an empirical determination of regions of control variables, such as pH, temperature and ionic strength, in which the structural data are substantially uniform and coherent. The phase diagrams are created by a multicomponent vector approach in which the peaks that most reflect structural changes are represented by red, blue or green colors. Thus, each final color in the diagram is representative of a different physical state of the protein. Further explanation of this approach was described earlier<sup>1,2</sup>.

The phase diagram (Figure 14) suggests that rPA exists in similar physical state at lower temperatures (10 to 30°C) over the entire pH range (3-8) studied. At temperatures greater than 45°C, a major structurally disruptive transition occurs at pH 6-8. The structural changes occur at

much lower temperatures at the lower pH values indicating that the protein is more stable in the pH range of 6.0 to 8.0. The phase diagram generated in this manner, however, did not correlate well with biophysical data obtained using the CD or fluorescence techniques. The transitions at various pH values in the phase diagram appeared to occur at much higher temperatures than those observed by the above mentioned methods. Furthermore, the transitions obtained at pH 3 by the other biophysical measurements were not clearly reflected in this phase diagram.

#### **Phase diagram of rPA using CD, intrinsic and extrinsic fluorescence data**

In an attempt to generate phase diagrams, that more comprehensively correlate with the biophysical data, phase diagrams were constructed using the CD and fluorescence (intrinsic and extrinsic) data. This approach has the potential to give more definitive phase boundaries than the UV-absorption based phase diagrams since they are developed from techniques that provide information about both secondary and tertiary structure as well as apolar binding sites of the protein. Phase diagram was constructed from the ANS fluorescence intensity data, intrinsic tryptophan fluorescence spectral center of mass data and the CD intensity data using Mathematica software.

From this phase diagram (Figure 15), it appears that rPA adopts at least five primary phases. The properties of the phases can be established by reference to other biophysical measurements. Combining the improved phase diagram with knowledge of the behavior of the protein determined thus far, it appears that the pink-colored region at the lower, right-hand corner of the diagram is the phase of maximum stability (Figure 15). This correlates well with CD, intrinsic and ANS fluorescence, and second derivative UV data. As anticipated, midpoints of transitions observed by the biophysical measurements generally correspond to the temperature borders between the phases. A second phase (blue/purple) is apparent at pH 3 at temperatures below 45°C and also seems to encompass pH 4.0 at temperatures greater than 30°C and pH 5.0 at temperatures greater than 35°C. This state appears to have significant molten globule character. As the temperature increases at pH 3.0, the protein rapidly enters another phase near 50°C. A third phase appears to be present at pH 5-8 in the higher temperature region. This depicts a phase in which the protein is severely structurally altered and tends to aggregate and may also involve molten globule behavior.

At pH 8, a completely different phase appears at very high temperatures which we assume corresponds to a more structurally disrupted form. This phase diagram was used to select conditions to develop a high throughput assay to screen potential stabilizers of rPA.

### **Excipient Screening**

An aggregation based turbidity assay was developed for rPA to produce conditions that could achieve significant aggregation by monitoring the turbidity of the solution at 360 nm using a 96-well plate reader. Aggregation was the most apparent pathway of physical degradation of this protein and therefore seemed an obvious choice on which to focus for stabilization analysis. To identify potential stabilizers for rPA, excipients from a 32 compound GRAS library were screened for their ability to inhibit the aggregation of rPA. A common buffer solution (citrate-phosphate, pH 5, containing 0.1 M NaCl) was used in all experiments. In 96 well plates, rPA (final concentration 0.25 mg/ml, 3.0  $\mu$ M), excipients (Table 2) and buffer solutions were added prior to induction of aggregation. The optical density of the solutions in the 96 well plates was measured at 360 nm for 70 minutes at 37°C in a Fluostar Galaxy microplate reader (BMG Labtechnologies, Germany). Experiments were performed both with and without excipients and the aggregation seen with protein alone was used as a control. The maximum OD observed in control samples at 70 minutes was used as the maximum extent of aggregation since aggregation was complete by this time. Inhibition by excipients was then characterized by their ability to lower the maximum OD obtained.

A number of potent inhibitors of aggregation were identified by this method (Table 2). Sorbitol, manitol, trehalose, dextrose and sodium citrate were found to be most effective inhibitors. Figure 16 shows a representative of aggregation kinetics of anthrax rPA at 37°C either alone or in the presence of excipients. Some of the other potent inhibitors include histidine, arginine, Brij 35, glutamic acid and malic acid.

### **Excipient Titration Studies**

Six potential stabilizers of rPA were identified from a 32 compound GRAS library based on their ability to inhibit the aggregation of rPA. These were arginine, histidine, sodium citrate, trehalose, manitol and Brij 35. To determine the minimal concentrations of these excipients that would

provide optimal stabilization of rPA, titration studies were performed using the turbidity assay and varying the concentrations of these excipients. The conditions for the turbidity assay were same as described above except that the time for the aggregation studies was increased from 70 min to 120 min in this series of experiments to ensure completion of the aggregation process. The maximum OD observed in control samples (no excipients) at 2 hours was used as the maximum extent of aggregation since aggregation was complete by this time. Inhibition by excipients at different concentrations was then characterized by their ability to lower the maximum OD obtained.

Table 3 shows the results of the titration studies with various excipients. Based on this data, the minimal concentrations of excipients that may provide optimal stabilization of rPA were determined to be 0.2 M for arginine, 0.1 M for histidine, 0.1 M for sodium citrate, 5% for manitol and 20% for trehalose. For Brij 35, two different concentrations (0.1 and 0.05%) were chosen for further studies as a slight discrepancy was observed in the aggregation (turbidity) data obtained from studies performed at different times.

### **Conformational Stabilization of rPA in the Presence of Excipients**

Once inhibitors of aggregation were identified and their optimal concentrations determined, the effect of these excipients on the conformational stability of the rPA was studied using intrinsic Trp fluorescence and circular dichroism. This approach applies stress to the protein by increasing the temperature while monitoring a measure of its tertiary structure. From this technique, a transition temperature ( $T_m$ : the temperature at which half the conformational change is complete) can be determined. A stabilizer is identified when an increase in the transition temperature of the protein is observed in the presence of that compound.

An empirical phase diagram of rPA (see above) indicated that the protein was most stable at pH 7.0. Therefore we chose to perform these studies at pH 7.0. The buffer used for these studies was 10 mM phosphate, pH 7.0 containing 150 mM NaCl.

Previous turbidity studies identified the following excipients as good inhibitors of rPA aggregation: Brij<sup>®</sup> 35 (0.05% and 0.1%), histidine (0.1M), arginine (0.2M), trehalose (20%), mannitol (5%) and citrate (0.1M). The effect of these excipients on the conformational stability of the protein was studied using CD (Figure 17) and intrinsic Trp fluorescence (Figures 18 and 19).

CD and fluorescence studies were performed as described above. Due to signal interference by arginine and histidine, only Brij® 35, citrate, mannitol and trehalose were studied by CD. The CD signal was converted to molar ellipticity using Spectra Manager software (Jasco), and the melting temperatures ( $T_m$ ) were determined using Microcal Origin software. The data indicate that citrate, mannitol and trehalose stabilize the secondary structure of rPA, while Brij® 35 at the two concentrations has a slight destabilizing effect (Figure 20). The fluorescence studies indicate that the same excipients that stabilize the secondary structure of rPA also stabilize the tertiary structure. Thus, citrate, mannitol and trehalose all provide stabilization of rPA's tertiary structure (Figure 21). Arginine actually destabilizes the tertiary structure of rPA, while Brij® 35 and histidine have little effect. Both CD and fluorescence studies indicate that 20% trehalose provides significantly more stabilization than citrate or mannitol alone. To determine the stabilizing effect of lower concentrations of trehalose, these experiments were repeated using 5, 10, and 15 percent trehalose. Results suggest 20% trehalose provides greater stabilization than 5, 10 or 15 percent (Figure 22).

### **Conformational Stabilization of rPA in the Presence of combination of Excipients**

Various combinations of excipients that had stabilizing effects on rPA (see above) were used to study if a particular combination would have a synergistic effect on rPA stability. Based on these studies, it was decided that only two excipients, trehalose and mannitol, would be used for further studies. The range of disaccharide ratio that we focused on was from 70%/30% mannitol/trehalose to 100% mannitol and 100% trehalose. The total excipient content in all the experiments was 20% by weight. The effect of these two excipients on the conformational stability of the rPA was studied using CD (Figure 23) and intrinsic Trp fluorescence (Figures 24 and 25).

CD studies were performed as described above and the CD signal of rPA (0.2mg/ml) at 222nm was monitored as a function of temperature from 10-90°C, collecting data every 0.5°C. The data indicate that the secondary structure of rPA is stabilized to similar extents at all compositions of disaccharides used in this study (Figure 23). At all of the different excipient compositions, the  $T_m$

of rPA was increased by about 6°C, from 48°C in the absence of excipients to about 54°C in their presence.

Fluorescence studies were performed as described above and spectra of rPA (0.1mg/ml) were collected from 300-400nm at a rate of 1nm/s. The  $T_m$  was determined by plotting spectral center of mass as a function of temperature, and fitting a sigmoidal curve using Microcal Origin software. The results from the fluorescence studies were similar to those obtained from the CD measurements in which all compositions of disaccharides stabilized rPA equally by increasing the  $T_m$  from 41°C to approximately 48°C (a 7°C increase) with the exception of trehalose alone which appeared to have a slightly lower stabilizing effect on rPA compared to mannitol alone or other combinations of mannitol and trehalose (Figures 24 and 25).

### **Isoelectric Focusing of rPA**

Isoelectric focusing (IEF) was performed on rPA (0.1mg/ml) using a Convergent Biosciences iCE<sub>280</sub> Analyzer connected to an Alcott Autosampler. ICE280 CFR software V2.0 was used to run the instrument and analyze the data. Samples were prepared by adding rPA (0.1mg/ml in 10 mM phosphate buffer, pH 7, 0.15 M NaCl) to a mixture of methyl cellulose (0.35%), pharmalytes (4%) and two pI markers (pI-3.78 and 9.71) in a total volume of 200 micro liters. The injection volume was 35 micro liter and focusing was performed initially at 500 volts for 1 minute and then at 3000 volts for 5 minutes.

The pI of the dominating peak was 5.89 (Figure 26). An additional peak of lower intensity was also observed with a pI of 5.81. This could correspond to deamidated rPA. The two other dominating peaks at the two ends of the chromatogram with pI's of 3.78 and 9.71 are the marker peaks.

### **Adsorption of rPA to Alhydrogel®**

The interaction between rPA and aluminum hydroxide adjuvant (Alhydrogel®) was studied by obtaining binding isotherms. We wanted to determine (1) whether rPA in the formulation buffer in the absence of excipients binds to Alhydrogel® and (2) the binding capacity. The aluminum content of the Alhydrogel® stock solution was 10.5 mg/ml. Prior to sample preparation, the

concentration of the rPA stock solution was determined by recording the UV/VIS spectra using an Agilent UV/VIS diode array spectrophotometer and calculating the concentration based on an extinction coefficient ( $E^{0.1\%}_{1cm}$ ) of 0.915 at 280 nm. Two different buffers (10 and 22 mM sodium phosphate, pH 7.0, containing 150mM NaCl ) were used to study the effect of phosphate on the rPA/adjuvant interaction. Binding of the adjuvant to rPA was conducted by adding adjuvant to microcentrifuge tubes containing rPA at various concentrations (final concentration 100 – 800  $\mu$ g/ml rPA). The final sample volume was 200  $\mu$ l, and the aluminum content was 0.1 mg per sample (0.5 mg aluminum/ml). The samples were mixed by gentle end-over-end rotation at 4 °C for 15 minutes and then centrifuged at 14,000 x g (again at 4 °C) for 5 minutes to pellet the adjuvant. The supernatant was assayed for rPA using the Agilent UV/VIS diode array spectrophotometer to determine the  $A_{280}$ . The amount of rPA adsorbed was calculated by subtracting the amount of rPA remaining in solution from the initial amount of rPA added to the tube.

The binding isotherms for rPA using two different buffers are shown in Figures 27 and 28. Although rPA binds to Alhydrogel® in both buffer systems; the extent of binding is much more in 10 mM sodium phosphate buffer compared to 20 mM phosphate buffer. This confirms the earlier findings by many different groups that the presence of phosphate decreases the adsorption of antigens onto the aluminum hydroxide adjuvant probably by converting it into aluminum phosphate. The binding of rPA to Alhydrogel® increases with increasing amount of rPA in solution and reaches saturation about 700 $\mu$ g/ml of rPA.

### **Conformational Stability of rPA adsorbed to the Aluminum Salt Adjuvant**

- Intrinsic Trp Fluorescence studies**

Intrinsic Trp fluorescence studies employing front-face geometry were performed to evaluate the effect of temperature on the conformational stability of rPA when adsorbed to the surface of Alhydrogel. The front face geometry was necessary due to the opaqueness of the suspension created by the insoluble aluminum salts. In addition, it was necessary for the samples to settle completely (approximately 15 hours) before performing measurements. After tumbling the samples for 5 minutes at 4°C, the samples were settled at 4°C for approximately 15 hours. An excitation wavelength of 295 nm was used and spectra were collected from 305-400 nm. Spectra

were obtained every 2.5°C from 10-87.5°C for all samples. Spectra of buffer (10mM sodium phosphate, pH 7.0, 150 mM NaCl) at each temperature were subtracted from the spectra of rPA in solution, and spectra of Alhydrogel alone at each temperature were subtracted from the spectra of rPA adsorbed to Alhydrogel. Peak positions were determined by taking the first derivative of each spectrum.

From plots of peak position vs. temperature (Figure 29, top panel), the temperature at which rPA begins to lose structure when adsorbed to Alhydrogel is lower than that of rPA in solution, suggesting destabilization of rPA upon adsorption to the adjuvant. In solution, the transition observed for rPA is quite sharp, occurring from ~40-50°C. On the surface of the adjuvant, however, the transition is much broader, starting as low as ~35°C and not reaching completeness until ~80°C. The destabilization of rPA when adsorbed to Alhydrogel may also be reflected in the plot of fluorescence intensity vs. temperature (Figure 29, bottom panel). The sharp decrease in fluorescence intensity observed near 25°C for rPA adsorbed to Alhydrogel occurs at temperatures much lower than that of rPA in solution, which occurs near 45°C; however, we prefer not to rely too heavily on this plot for our conclusions until further studies have been performed to evaluate the reproducibility of this phenomenon.

- **Differential Scanning Calorimetric Studies**

Differential scanning calorimetry was used to investigate the effect of surface adsorption on the thermal stability of rPA. A high-throughput capillary differential scanning calorimeter (MicroCal LLC, Northampton, MA) was used to determine thermal transition temperatures ( $T_m$ ) of rPA in solution and adsorbed onto Alhydrogel®. Samples containing protein completely adsorbed onto the surface of the adjuvant were prepared based on the rPA/adjuvant adsorption study described above. DSC experiments were performed using rPA at 0.4 mg/ml in 10 mM phosphate buffer containing 0.15 M NaCl (pH 7.0). For DSC studies in the presence of adjuvant, 2.5 mg Al/ml Alhydrogel® was employed. Samples and reference buffer solutions were loaded in triplicate into a 96-well plate, which was thermostated at 10 °C. An autosampler equipped with a 2.5 ml Hamilton GASTIGHT® syringe was utilized to load the DSC cells and clean the cells between experiments. Samples were mixed by loading and expelling the syringe three times to ensure that the suspensions were well dispersed. A scan rate of 90 °C/hour was used to scan from 10 °C to 90

°C. Buffer and adjuvant samples were examined separately to evaluate the independent behavior of each.

DSC data was analyzed using Origin v. 7.0 (OriginLab Corporation, Northampton, MA). The thermogram for buffer alone was subtracted from the thermograms of the rPA in solution prior to further processing. Similarly, the thermogram of adjuvant alone was subtracted from the thermograms of the adsorbed protein. rPA thermograms were analyzed using a single peak, 2-state model. For rPA adsorbed to Alhydrogel®, transition temperatures were determined by fitting the data to a 2-state model using two peaks.

Differences in  $T_m$ 's and thermograms are observed when rPA is adsorbed onto the adjuvant in comparison to rPA in solution under the same conditions (Figures 30 A and B). The  $T_m$  of rPA is decreased by 5°C (i.e., from ~49 °C to ~44 °C) when the protein is adsorbed onto the surface of Alhydrogel®, indicating that the thermal stability of rPA is significantly perturbed by adsorption to the adjuvant. Unbound rPA has a major transition centered at 49°C (Figure 30A). When the protein is adsorbed onto Alhydrogel®, there are at least two different transitions now present underlying a large, broad peak spanning from approximately 30 to 50 °C (Figure 30 B). In total, the fluorescence and DSC studies demonstrate destabilization of rPA when it is adsorbed to the aluminum salt adjuvant.

### Potential Interactions between rPA and CpG

Fluorescence thermal melts were obtained as described above with 0.1mg/mL rPA in the presence of a CpG adjuvant. A spectrum of CpG in buffer at 10°C was subtracted from all spectra in which the sample contained CpG. The  $T_m$  of rPA in the presence of CpG was essentially the same as rPA alone (Figure 31), suggesting that CpG oligonucleotides either don't bind to rPA or have no effect on its thermal stability.

Differential Scanning Calorimetry (DSC) was performed using a Microcal VP-DSC. Thermograms were obtained through a single scan from 10-90°C at a scan rate of 60°C/hr. The sample and reference solutions were degassed before filling the cells and allowed to equilibrate for 15 min. before beginning the scan. Thermograms (Figure 32) were obtained for rPA (0.73mg/mL)

alone, CpG (0.73mg/mL) alone, and CpG + rPA (0.73mg/mL each). Baselines were obtained in duplicate between sample runs by scanning buffer in both the sample and reference cells. There were no differences in melting temperature observed between rPA alone and rPA + CpG suggesting again that there is no interaction between rPA and CpG oligonucleotides or if there is an interaction, then it produces no effect on the protein's stability.

As a direct test of any interaction between the protein and oligonucleotides, isothermal titration calorimetry (ITC) was performed using a Calorimetry Sciences calorimeter maintained at 25°C by a circulating water bath. Both rPA (2.5mg/mL) and CpG (3.67mg/mL) were dialyzed in the same beaker containing 10mM sodium phosphate buffer, pH 7.0, containing 150mM NaCl using Slide-A-Lyzer Dialysis Cassettes (Pierce)—10,000 MWCO, 0.1-0.5mL sample volume for the rPA and 3500 MWCO, 0.1-0.5mL sample volume (x 2) for the CpG. The samples were degassed and titrations of rPA (2.5mg/mL) into CpG (0.53mg/mL) were performed using a program of 15 injections of 15 $\mu$ L each with a 300s equilibration time between injections. The concentrations of rPA and CpG were selected such that a 1:1 ratio (by weight) would be achieved near the end of the program. Blank titrations of buffer into CpG were performed to obtain accompanying heats of dilution. The total heats obtained in these experiments were very small (Figure 33). This again suggests that there is no interaction between rPA and CpG oligonucleotides or any interaction is very weak ( $K_d > 1\text{mM}$ ). Overall, we find no evidence for interaction between the protein and CpG adjuvant.

Figure 1. Derivative absorbance studies of rPA as a function of temperature at pH 3.

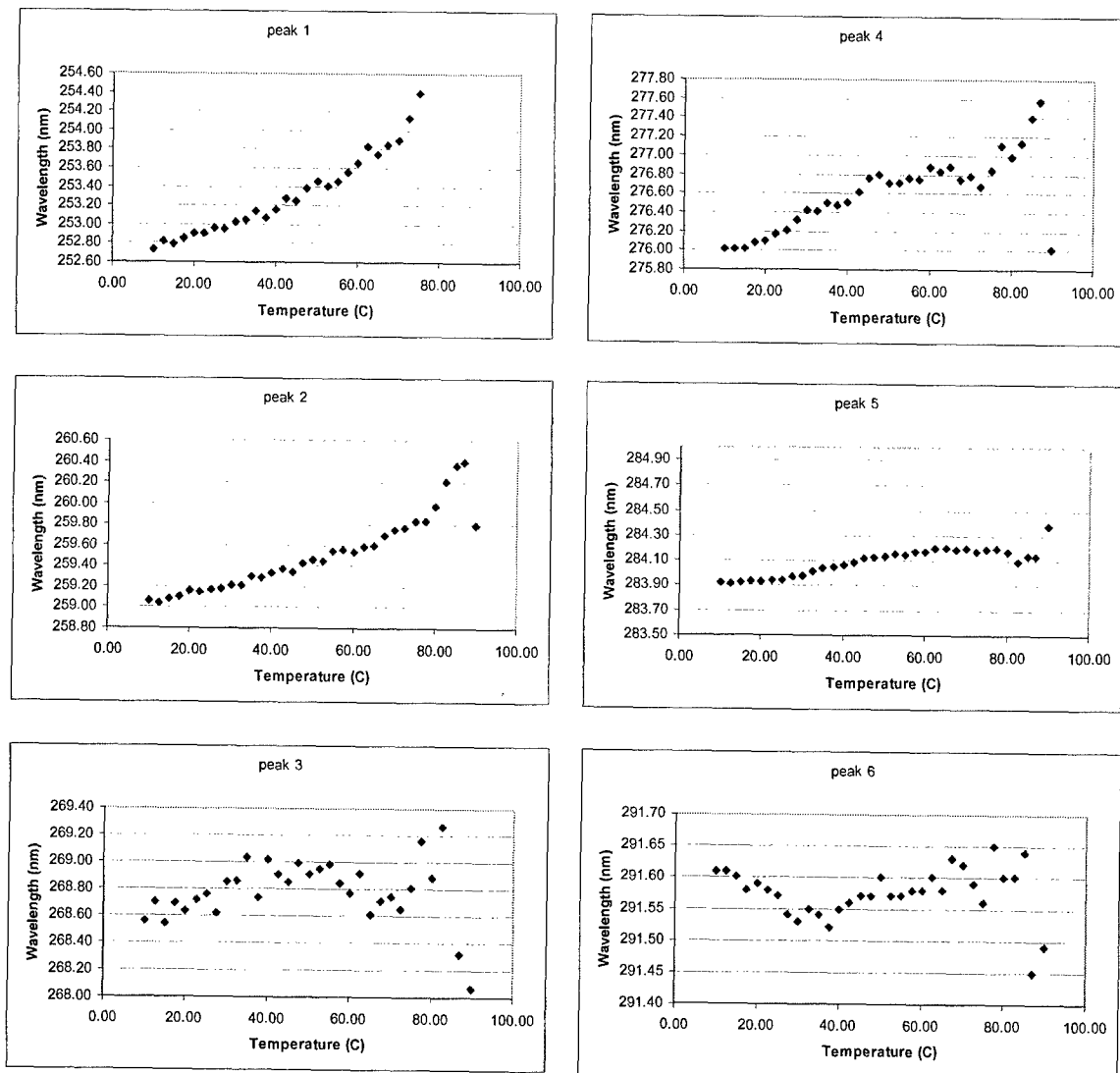


Figure 2. Derivative absorbance studies of rPA as a function of temperature at pH 4.

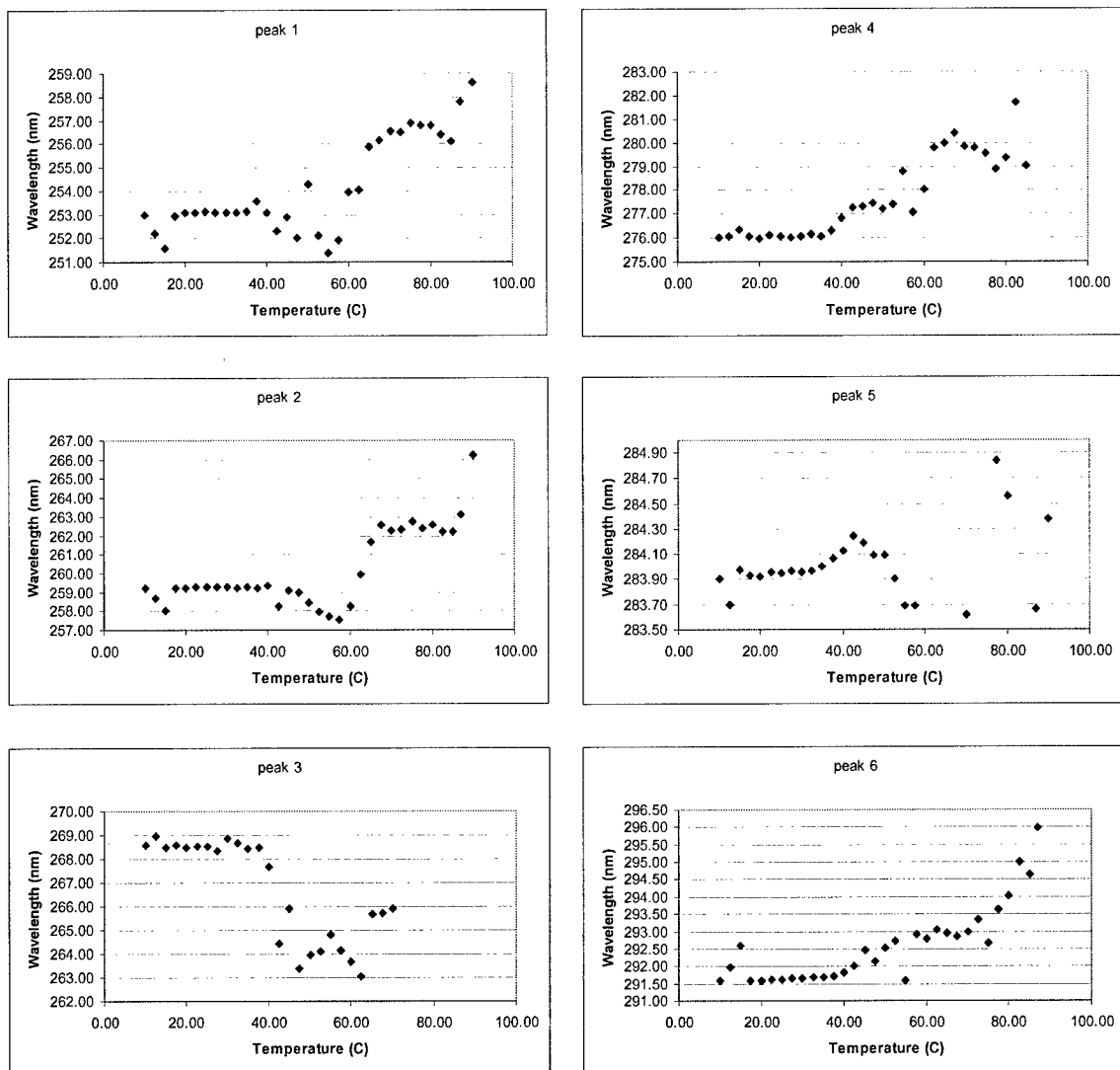


Figure 3. Derivative absorbance studies of rPA as a function of temperature at pH 5.

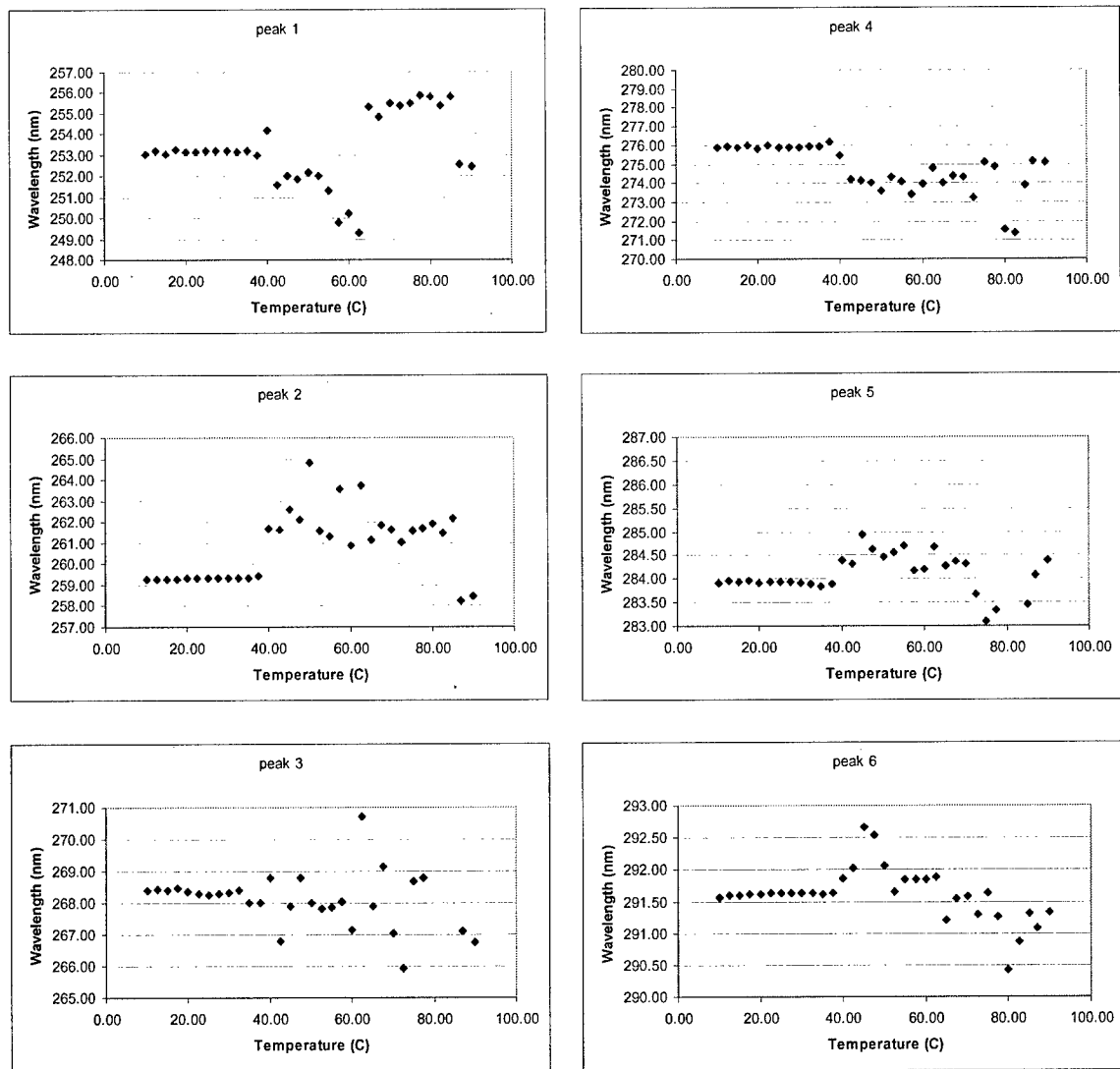


Figure 4. Derivative absorbance studies of rPA as a function of temperature at pH 6.

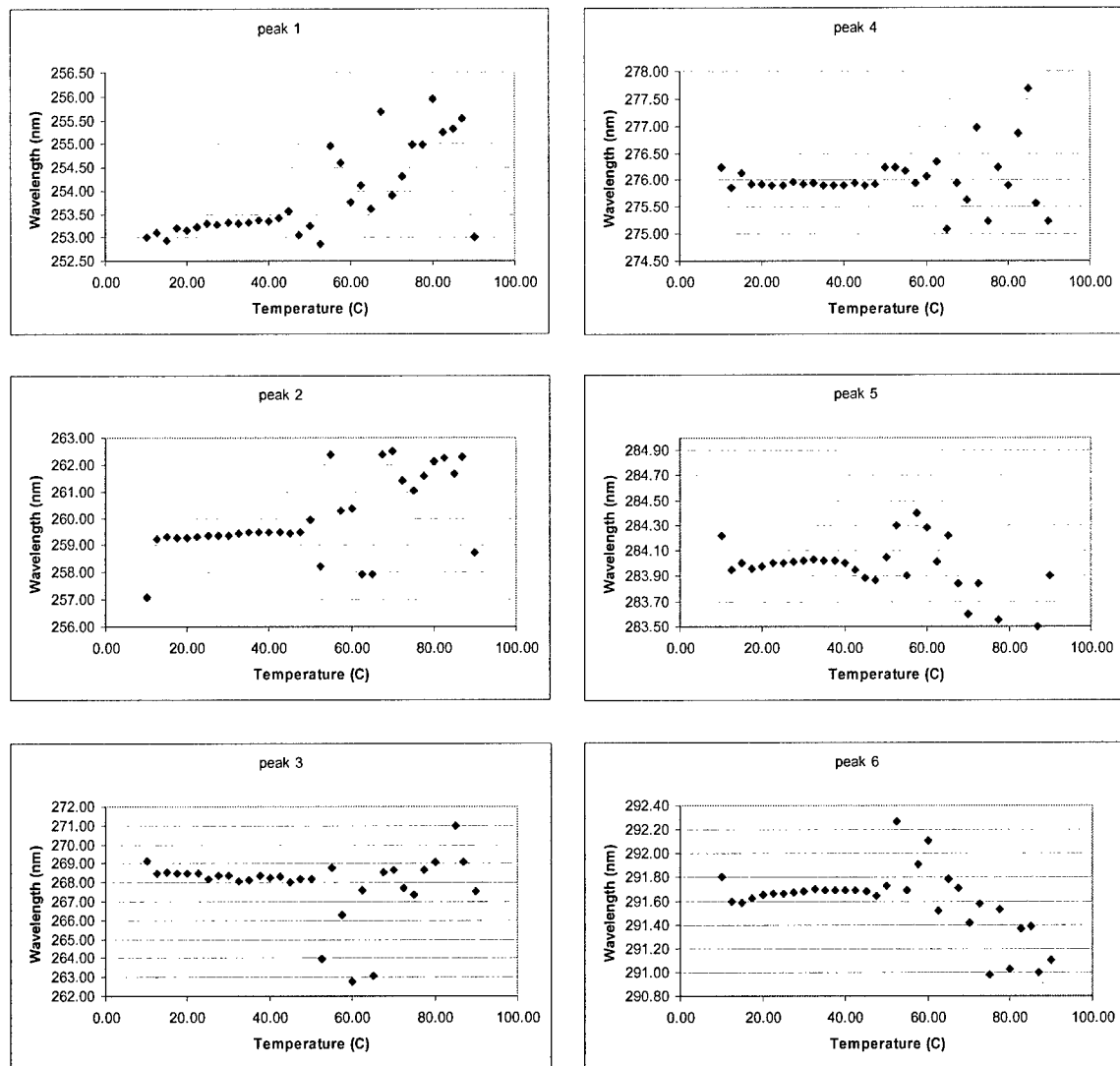


Figure 5. Derivative absorbance studies of rPA as a function of temperature at pH 7.

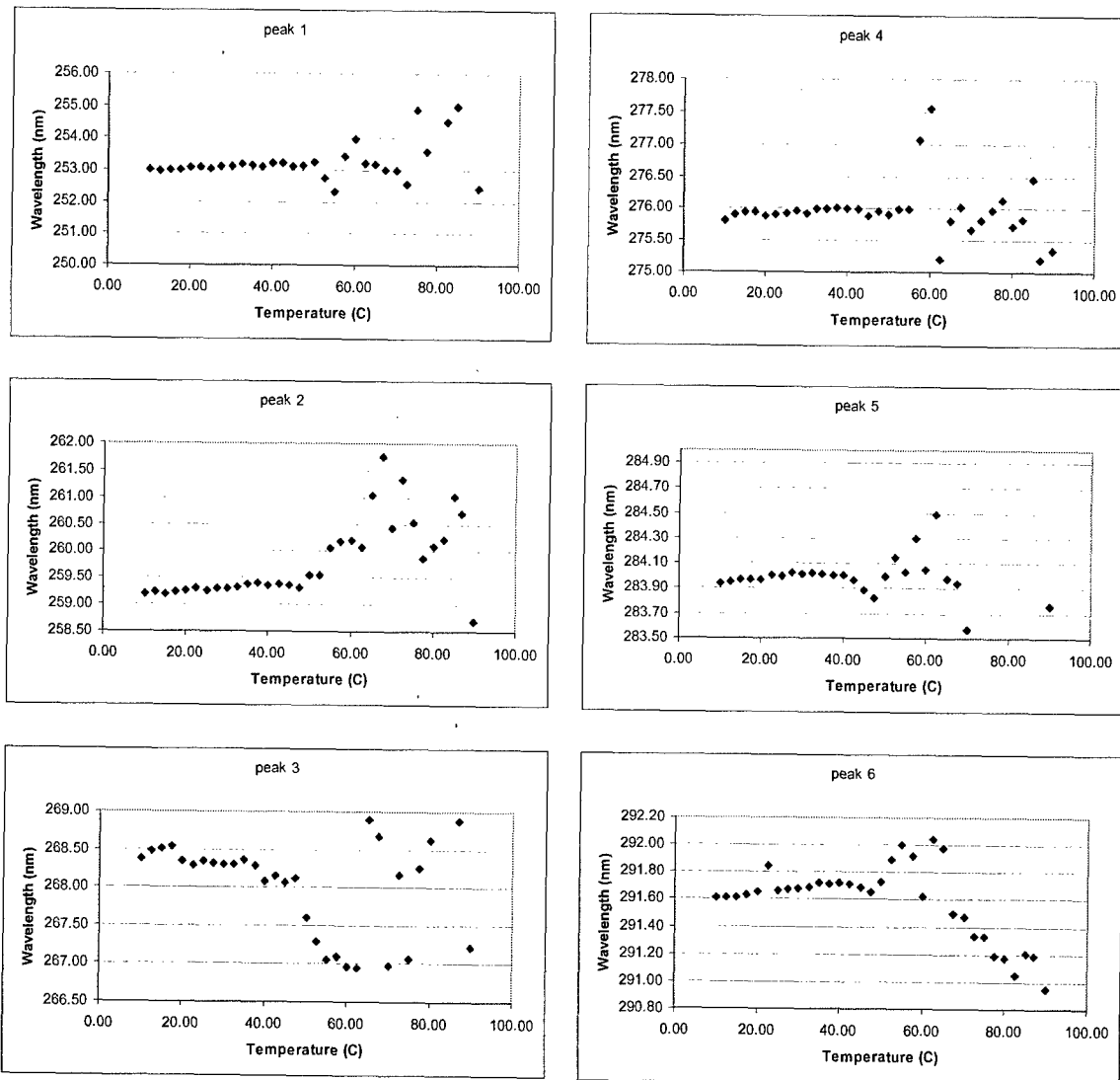
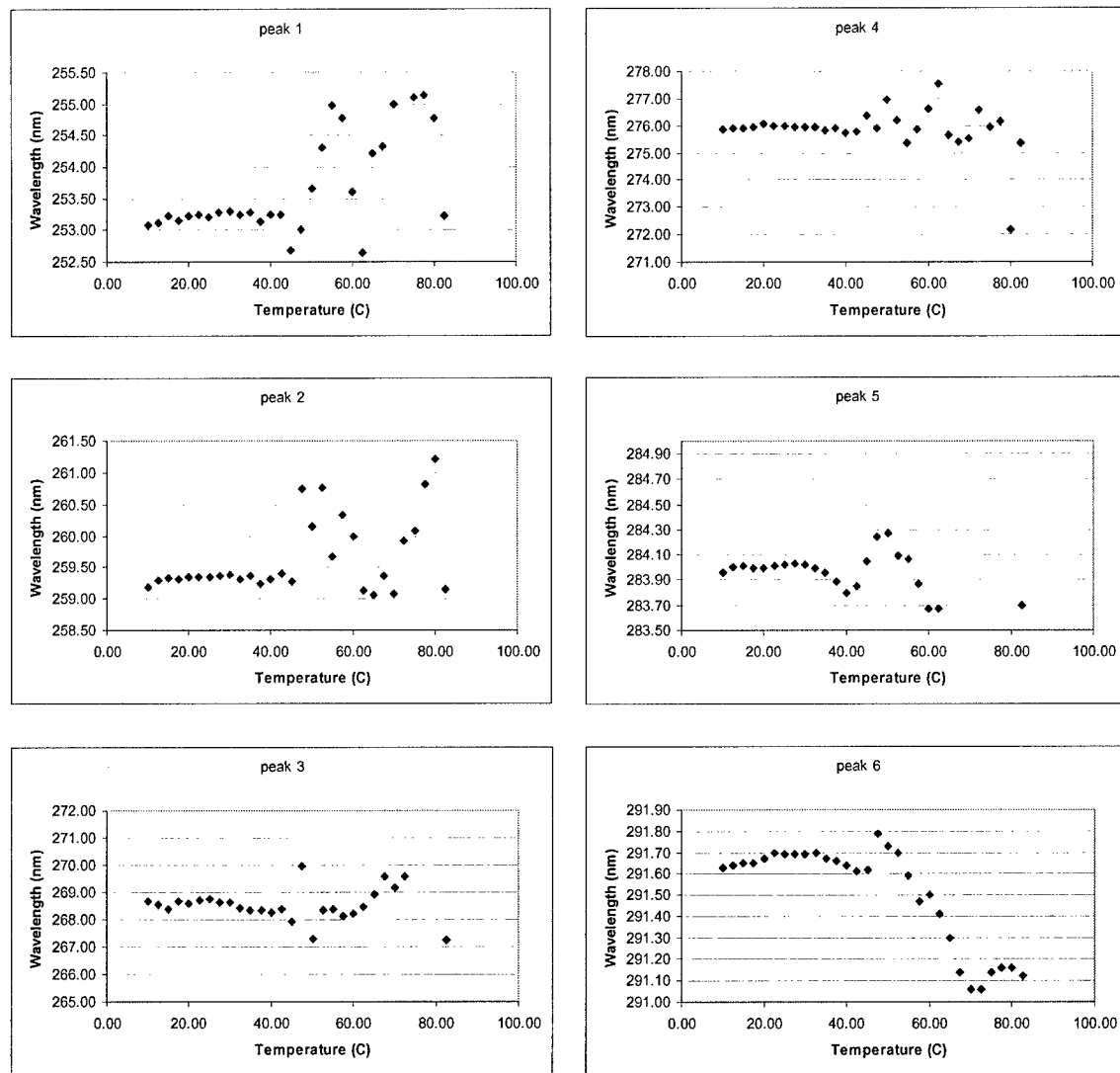
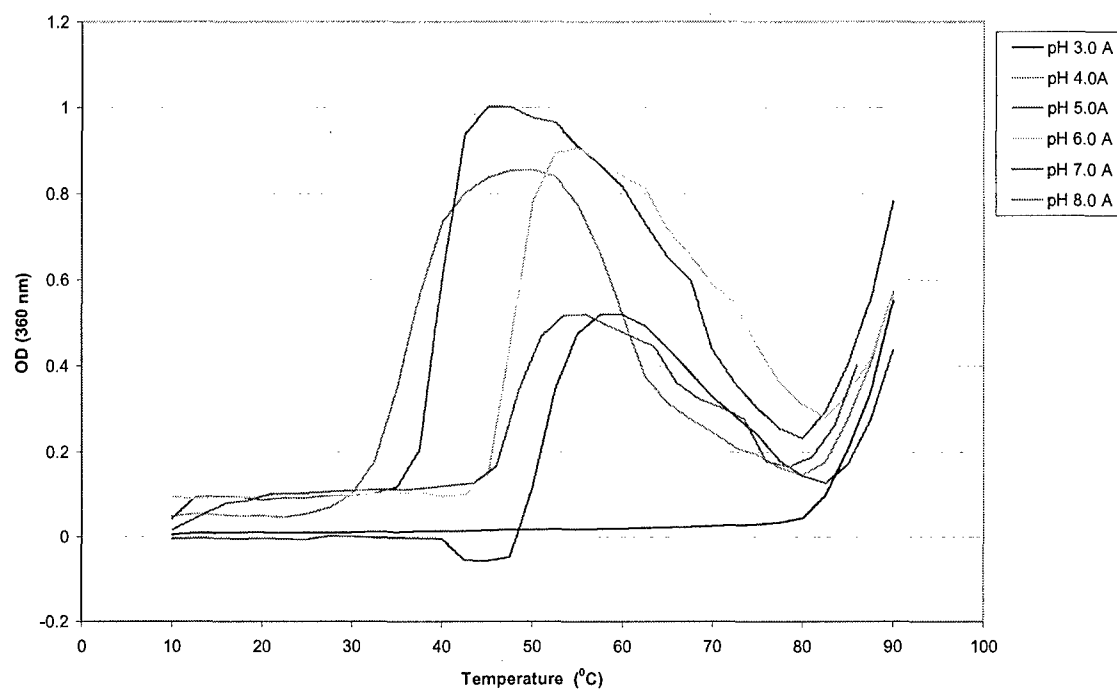


Figure 6. Derivative absorbance studies of rPA as a function of temperature at pH 8.



**Figure 7.** Temperature induced aggregation of anthrax rPA at various pHs in citrate-phosphate buffers.



**Figure 8.** CD spectra of anthrax rPA at  $10^0\text{C}$  at various pHs in citrate-phosphate buffers.

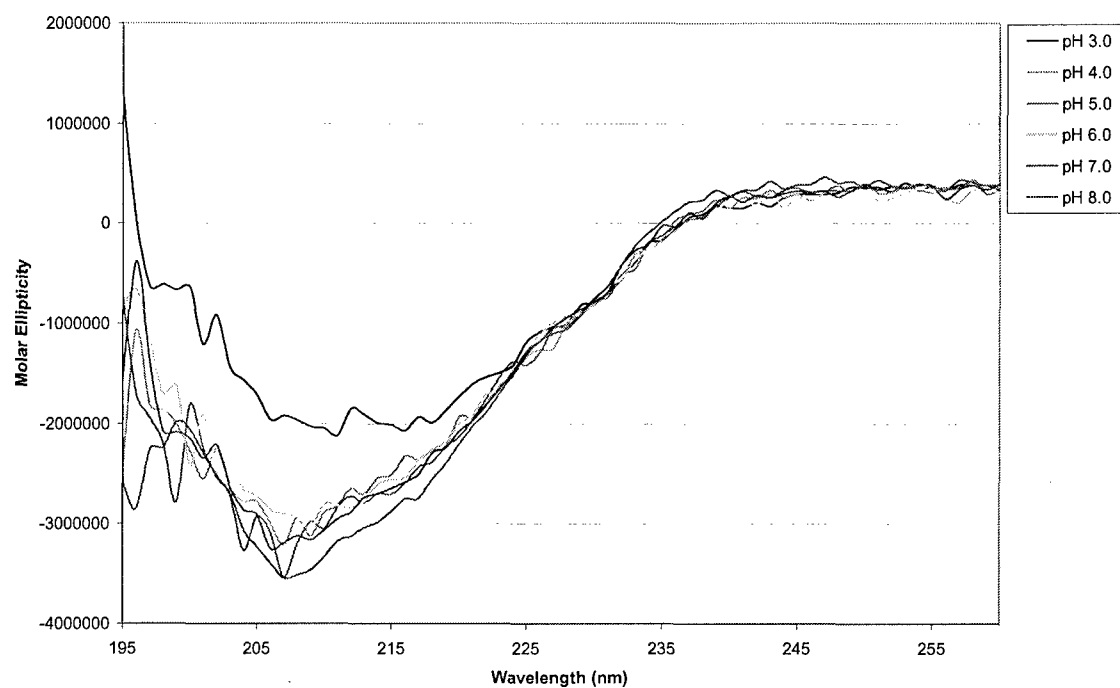


**Figure 9.** CD thermal melts of anthrax rPA at 222 nm at various pHs in citrate-phosphate buffers.

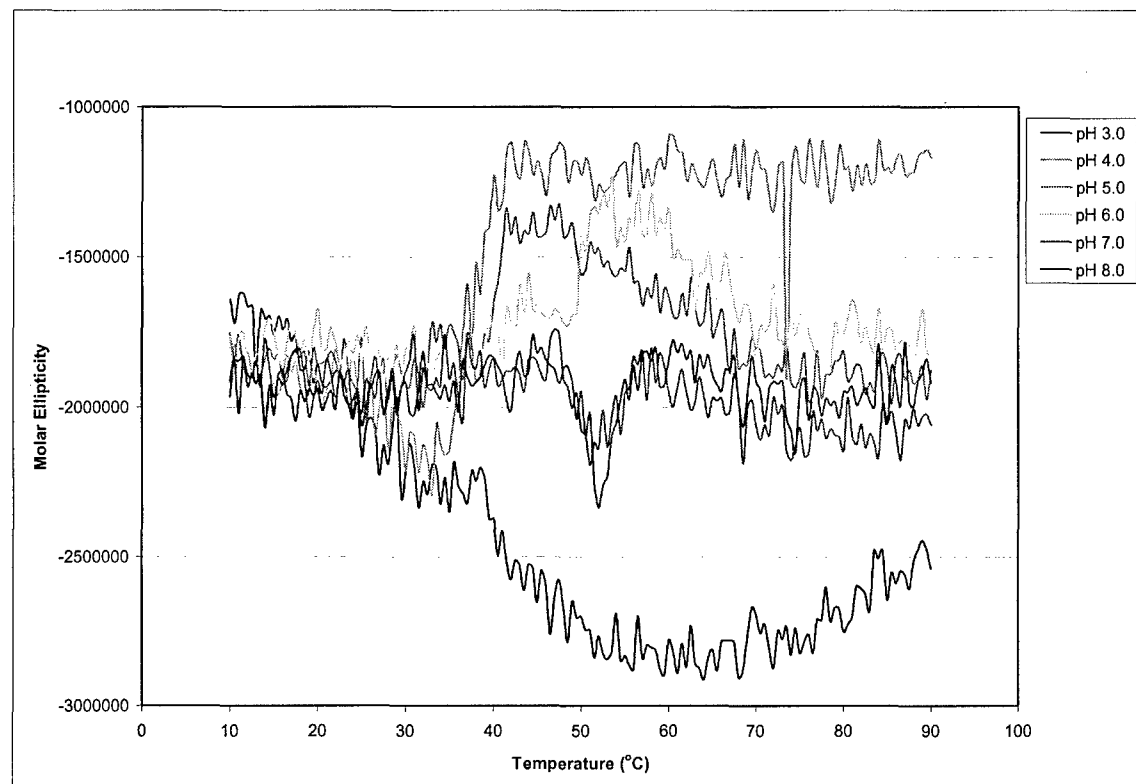


**Figure 10.** Effect of temperature and pH on the intrinsic Trp fluorescence spectral center of mass of anthrax rPA. (Results are shifted +14 nm from actual peak maxima.)

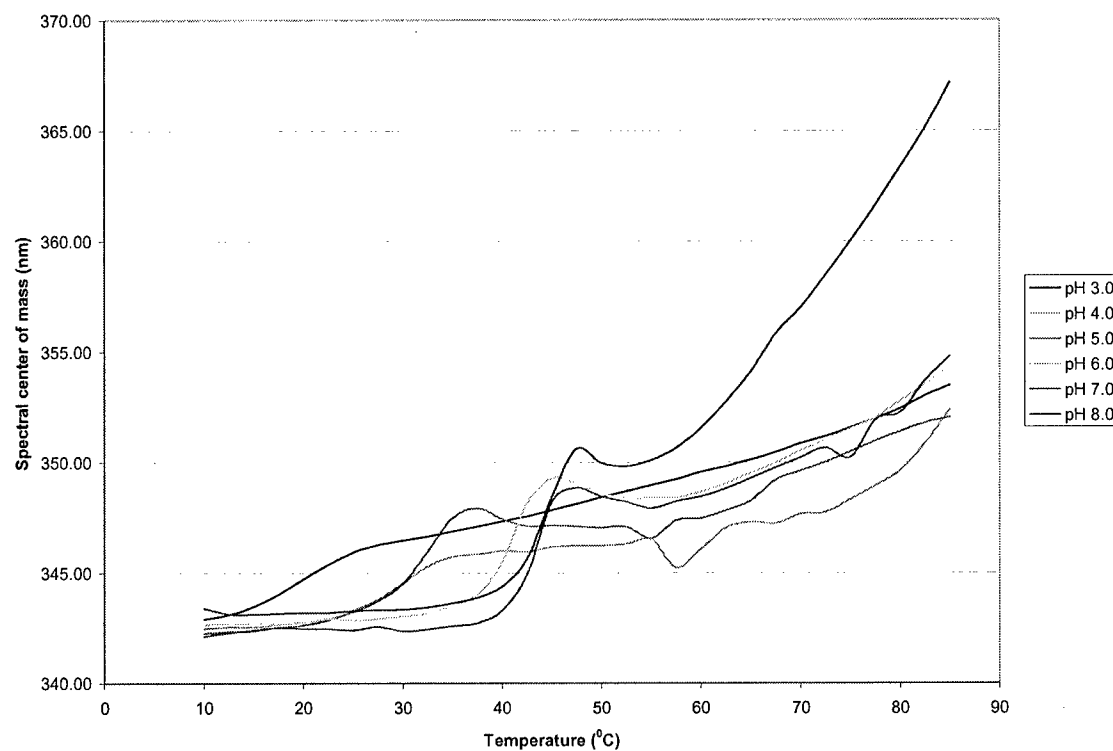


**Figure 11.** Effect of temperature and pH on the intrinsic fluorescence intensity of anthrax rPA.

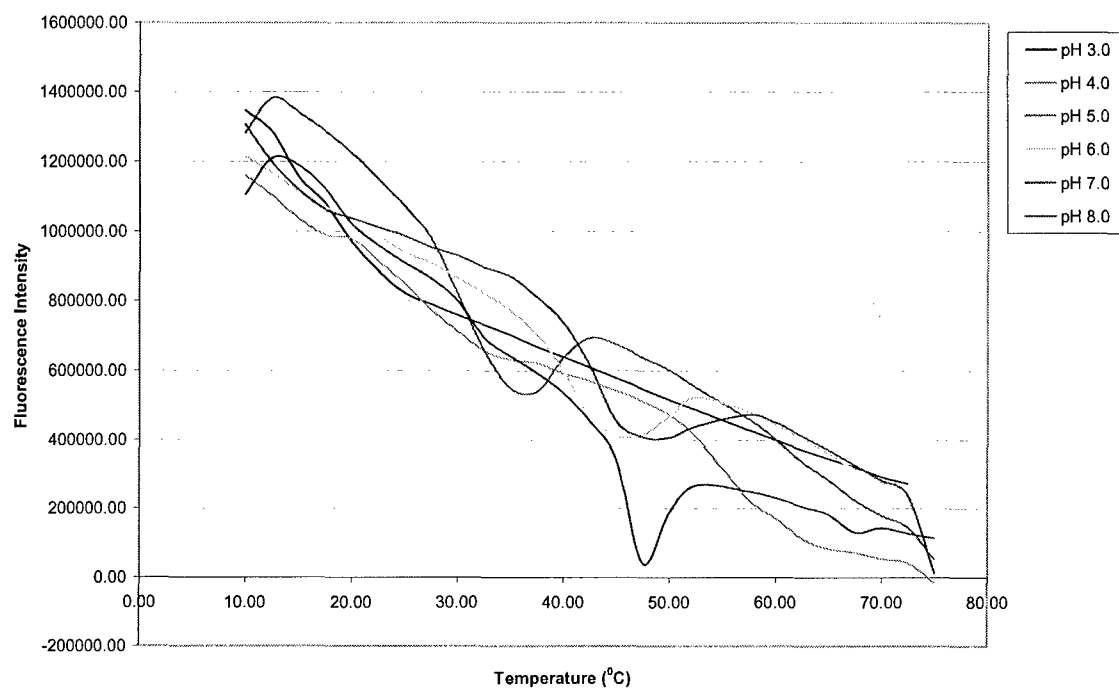


**Figure 12.** Effect of temperature and pH on the ANS-Anthrax rPA fluorescence spectral center of mass.

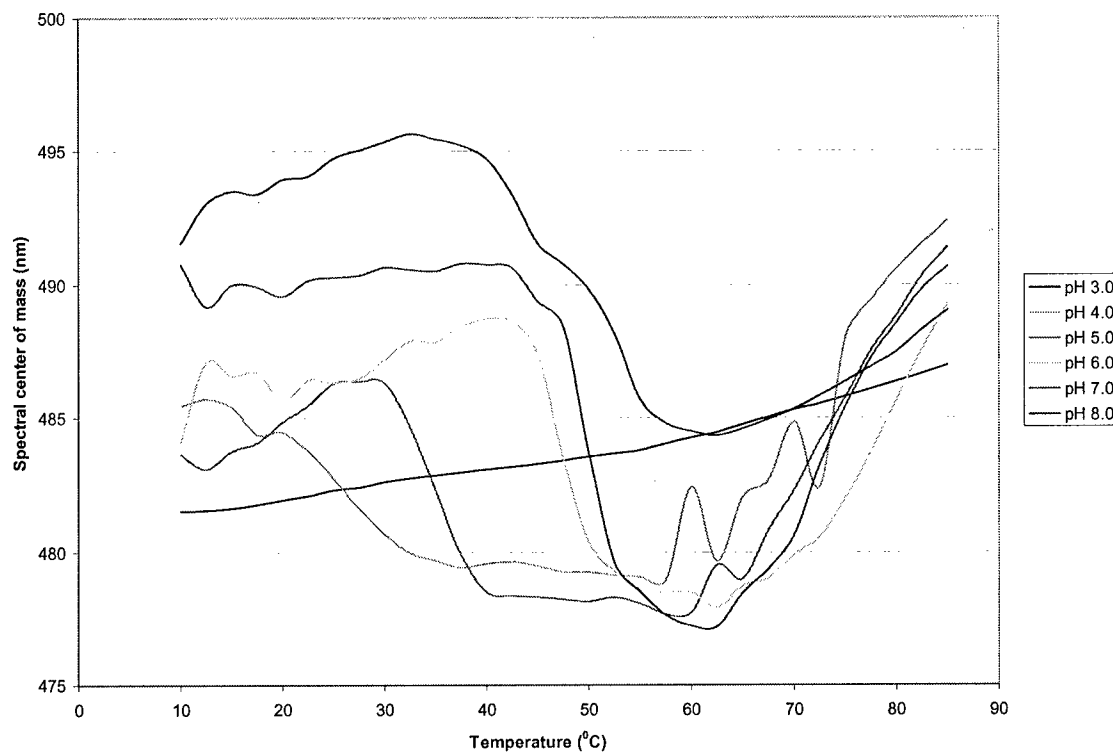


**Figure 13.** Effect of temperature and pH on the ANS-Anthrax rPA fluorescence intensity.

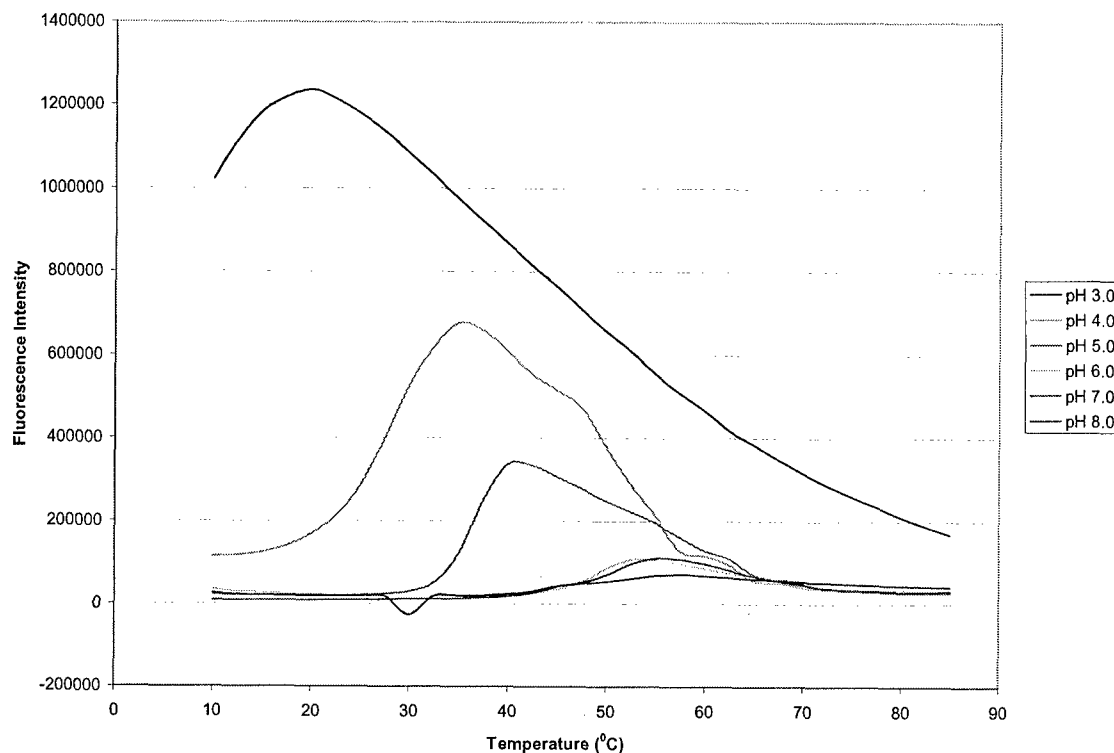


**Figure 14.** Temperature-pH phase diagram of anthrax rPA based on second-derivative absorbance data.

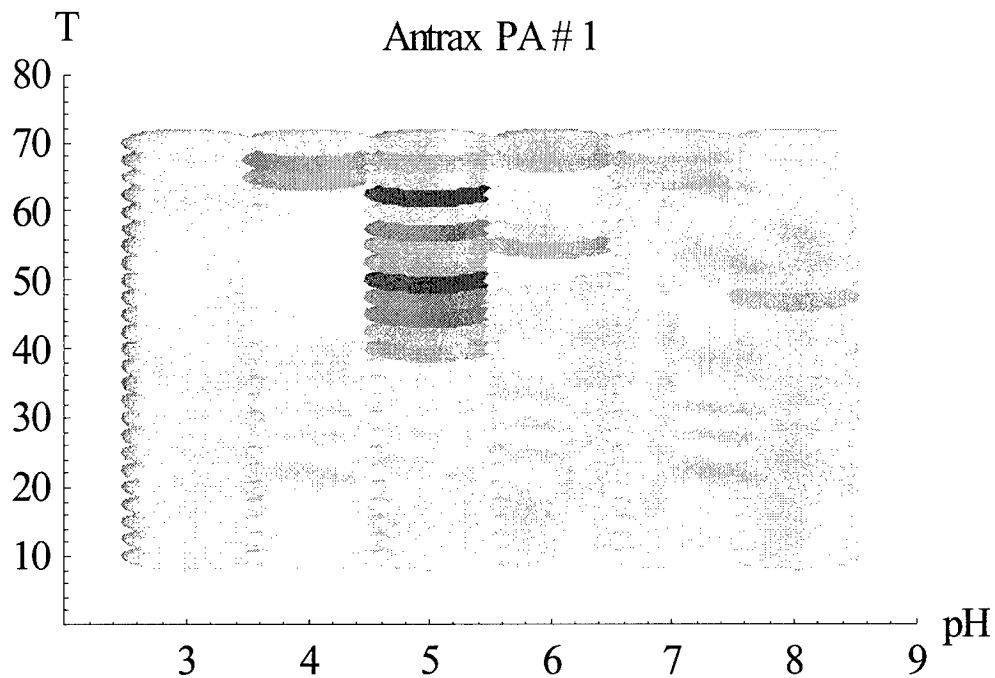


**Figure 15.** Temperature-pH phase diagram of anthrax rPA based on ANS fluorescence intensity data, intrinsic Trp fluorescence spectral center of mass data and CD intensity data.

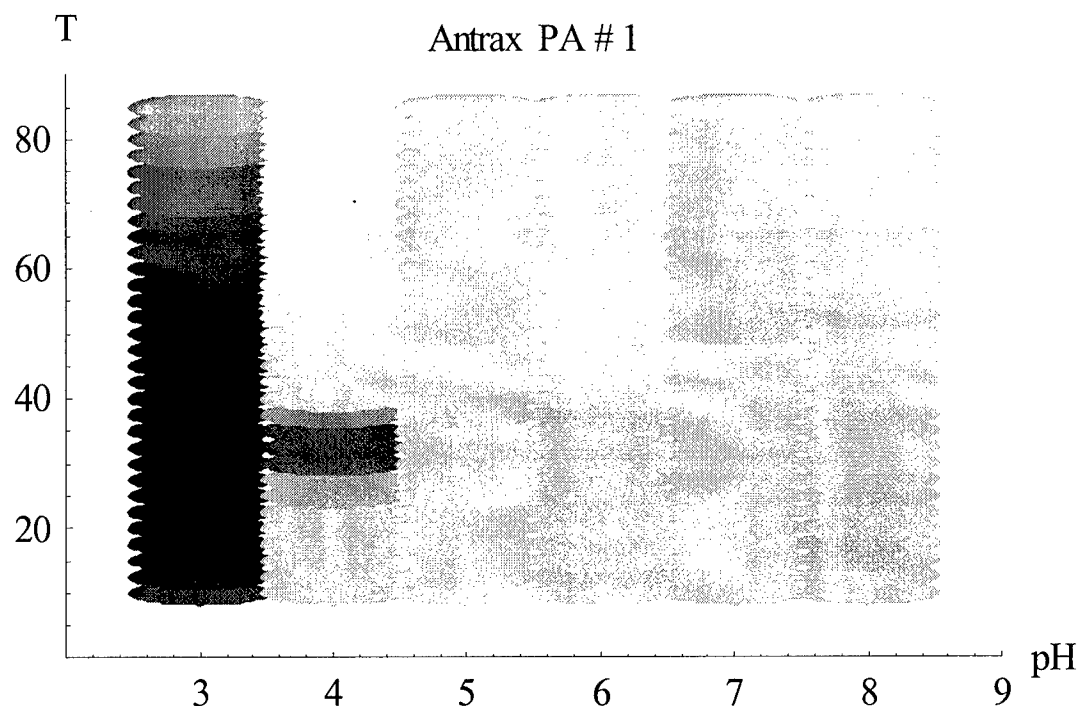


**Figure 16.** Aggregation of anthrax rPA in the presence and absence of excipients

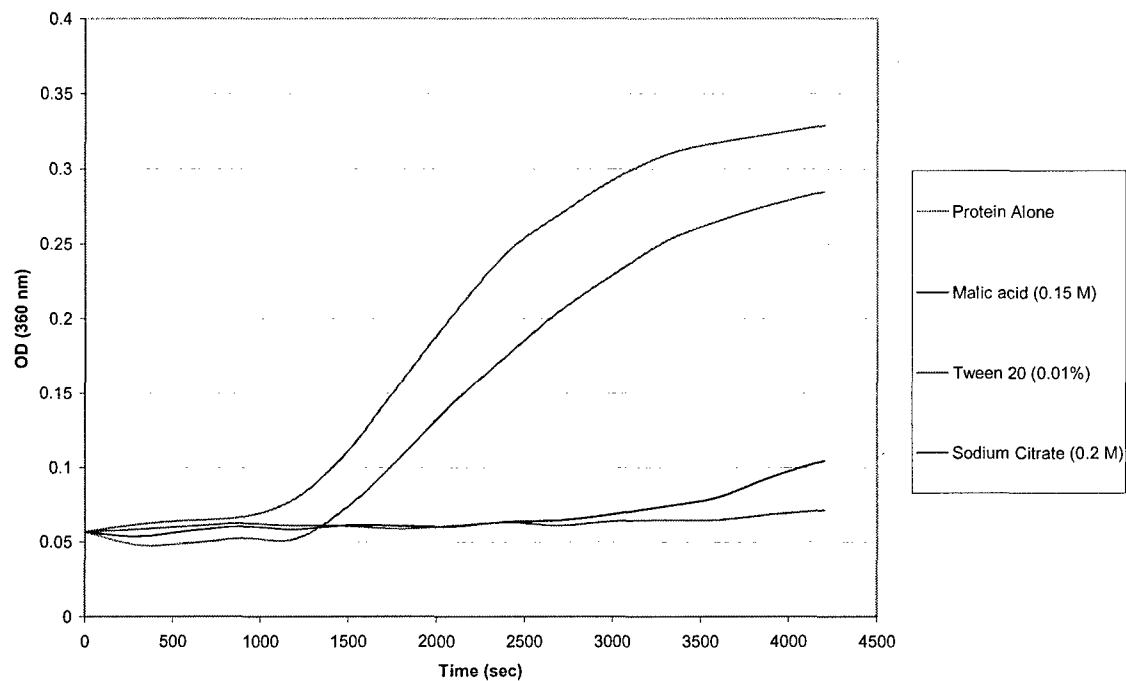


**Figure 17.** Effect of Excipients on the Secondary Structure Stability of rPA as determined by CD

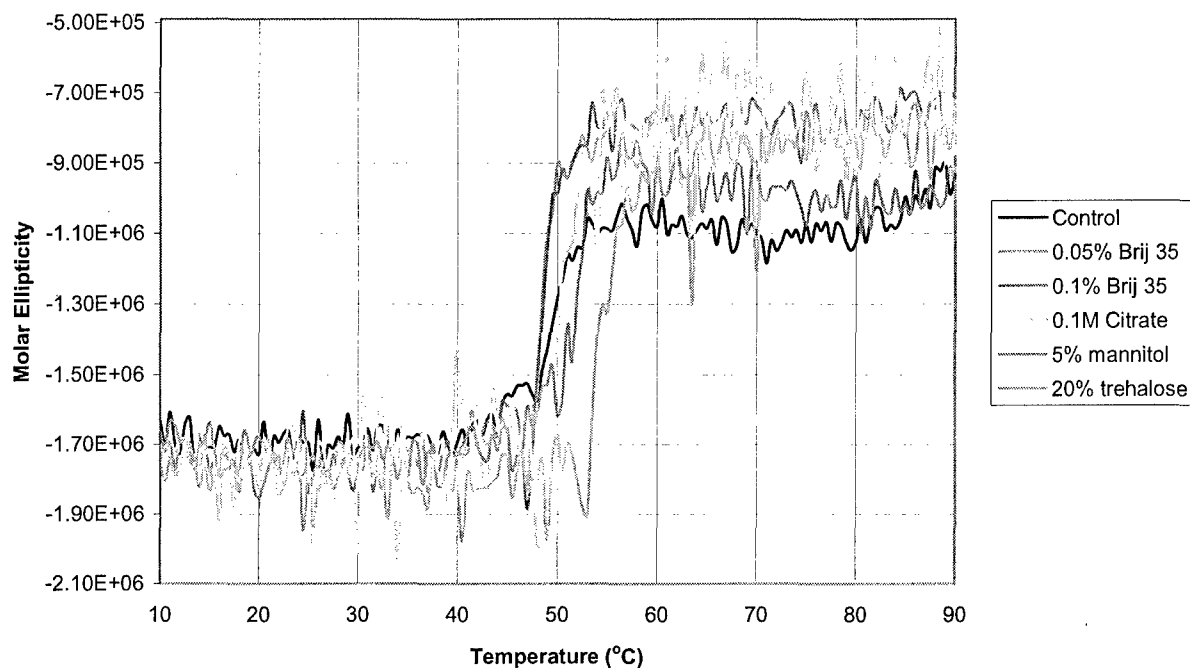


**Figure 18.** Effect of Excipients and Temperature on the Intrinsic Tryptophan Fluorescence Spectral Center of Mass of rPA.

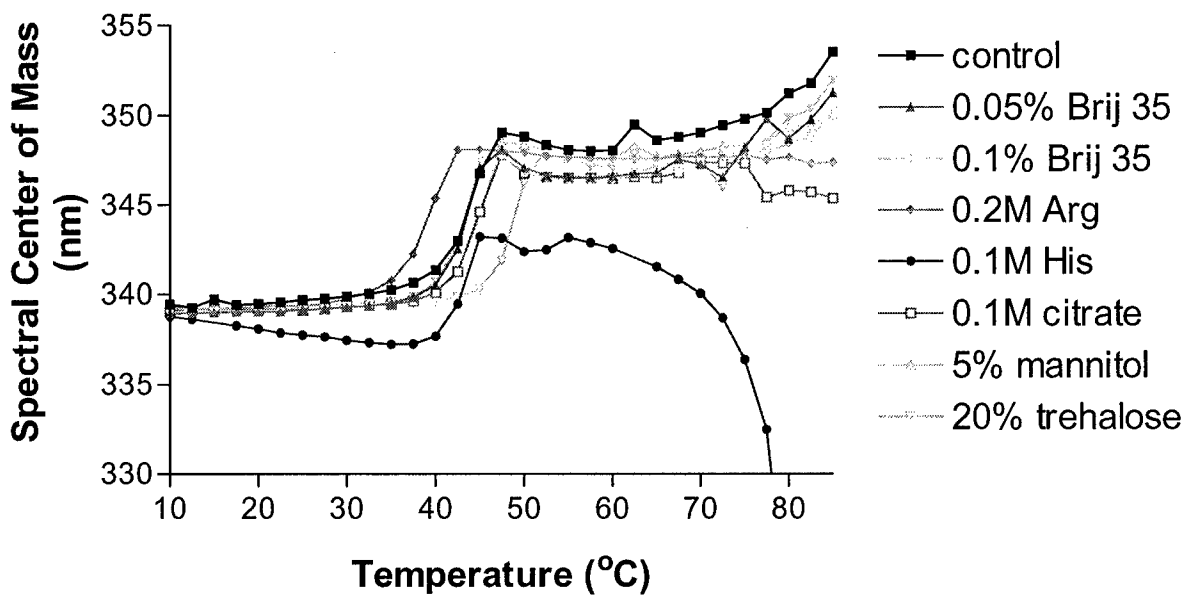


**Figure 19.** Effect of Excipients and Temperature on the Intrinsic Tryptophan Fluorescence Intensity of rPA.

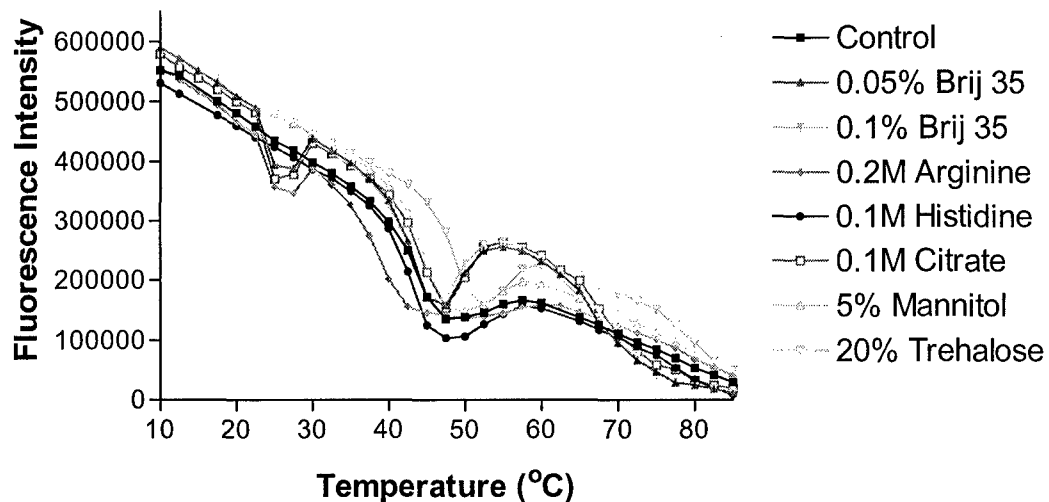


**Figure 20.** Effect of Excipients on the Secondary Structure  $T_m$  of rPA as determined by CD.

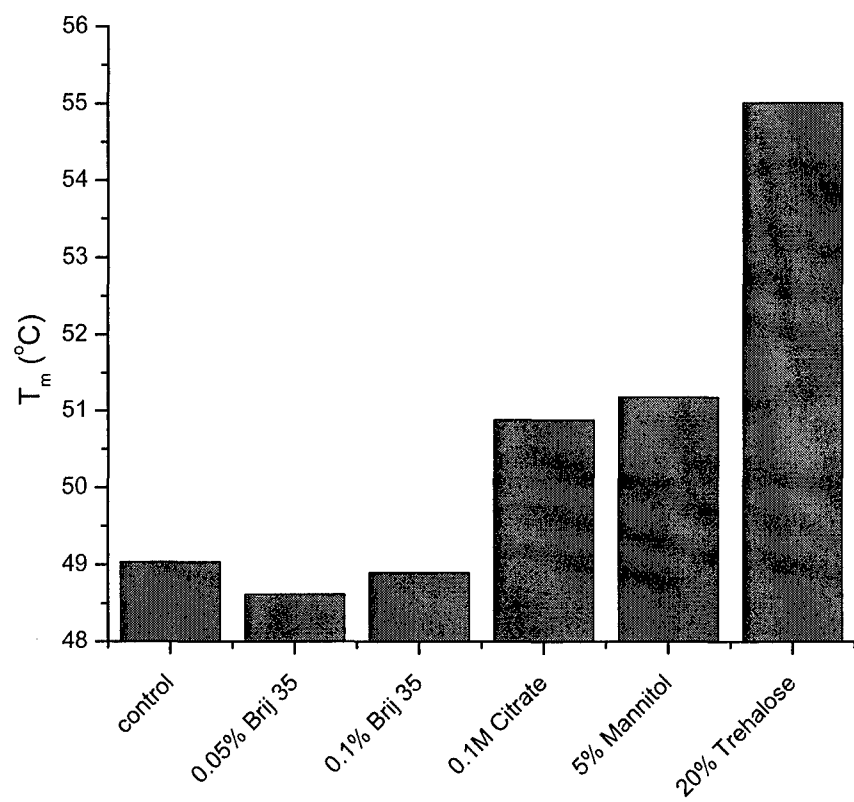
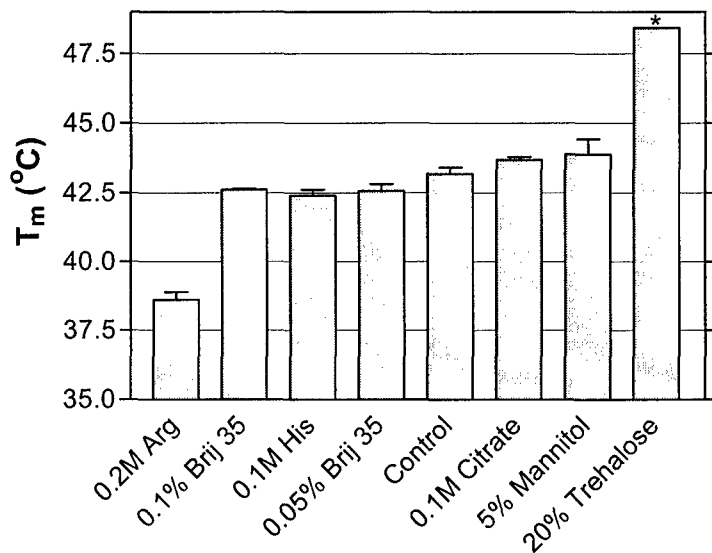


**Figure 21.** Effect of Excipients on the Tertiary Structure  $T_m$  of rPA as determined by Intrinsic Trp Fluorescence. Error bars represent standard error of the mean (N=2).



\* N=1 for 20% trehalose due to impurities in the Sigma-brand trehalose that was used in Run 1. Run 2 was performed using Ferro-Pfanstiehl-brand trehalose.

**Figure 22.** Effect of Different Concentrations of Trehalose on the Conformational Stability of rPA.

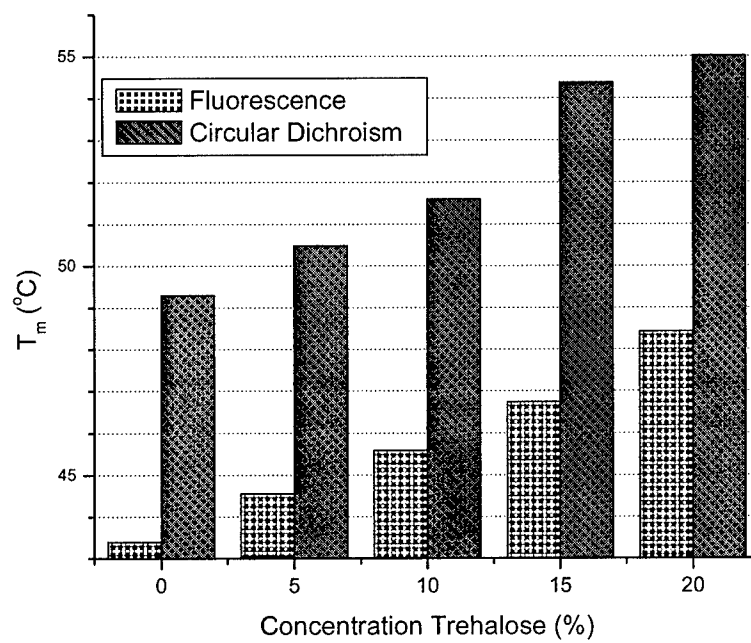


**Figure 23.** CD thermal melts of rPA in the presence and absence of excipients at pH 7 in 10 mM phosphate buffer containing 150 mM NaCl.

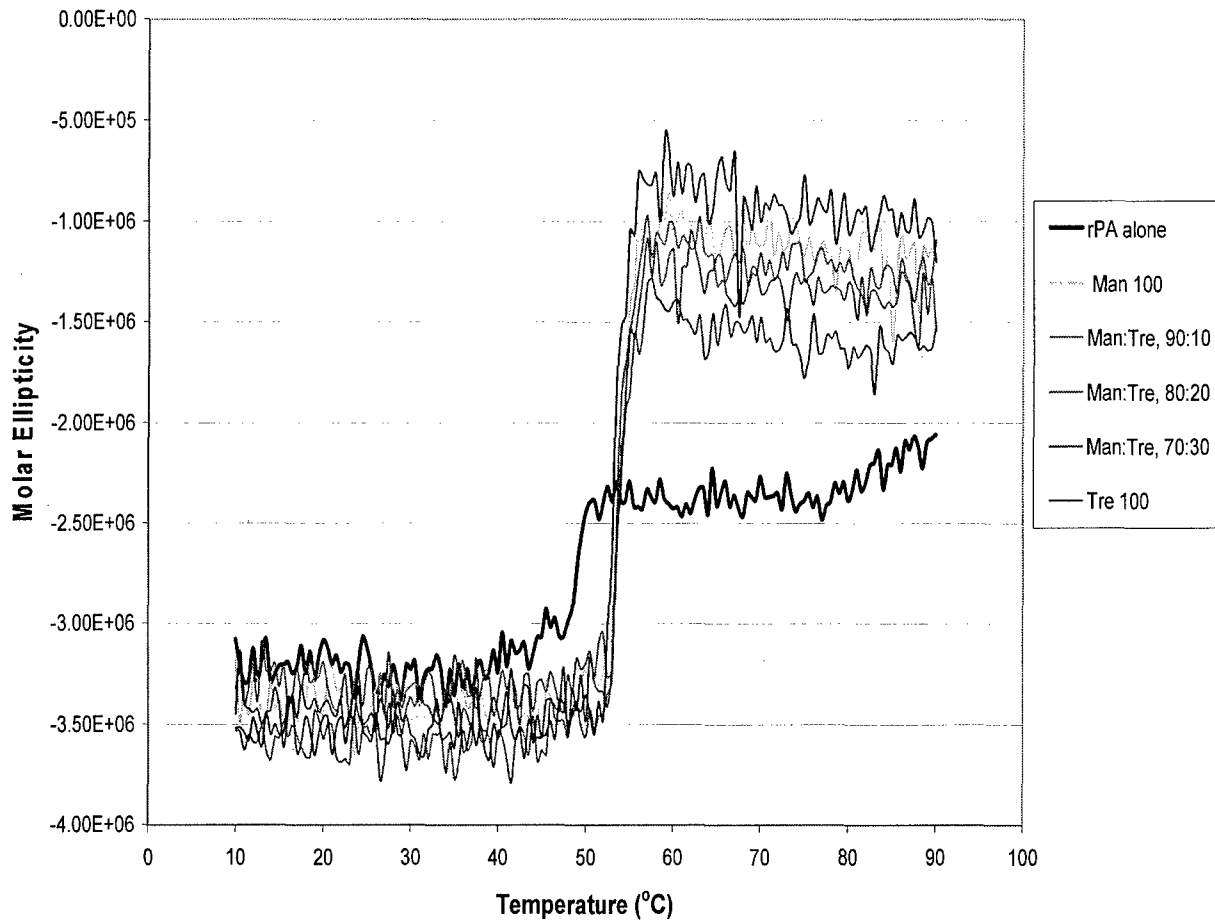


**Figure 24.** Effect of excipients (alone or combination) on the intrinsic Trp fluorescence spectral center of mass of anthrax rPA as a function of temperature. (Results are shifted +14 nm from actual peak maxima.)

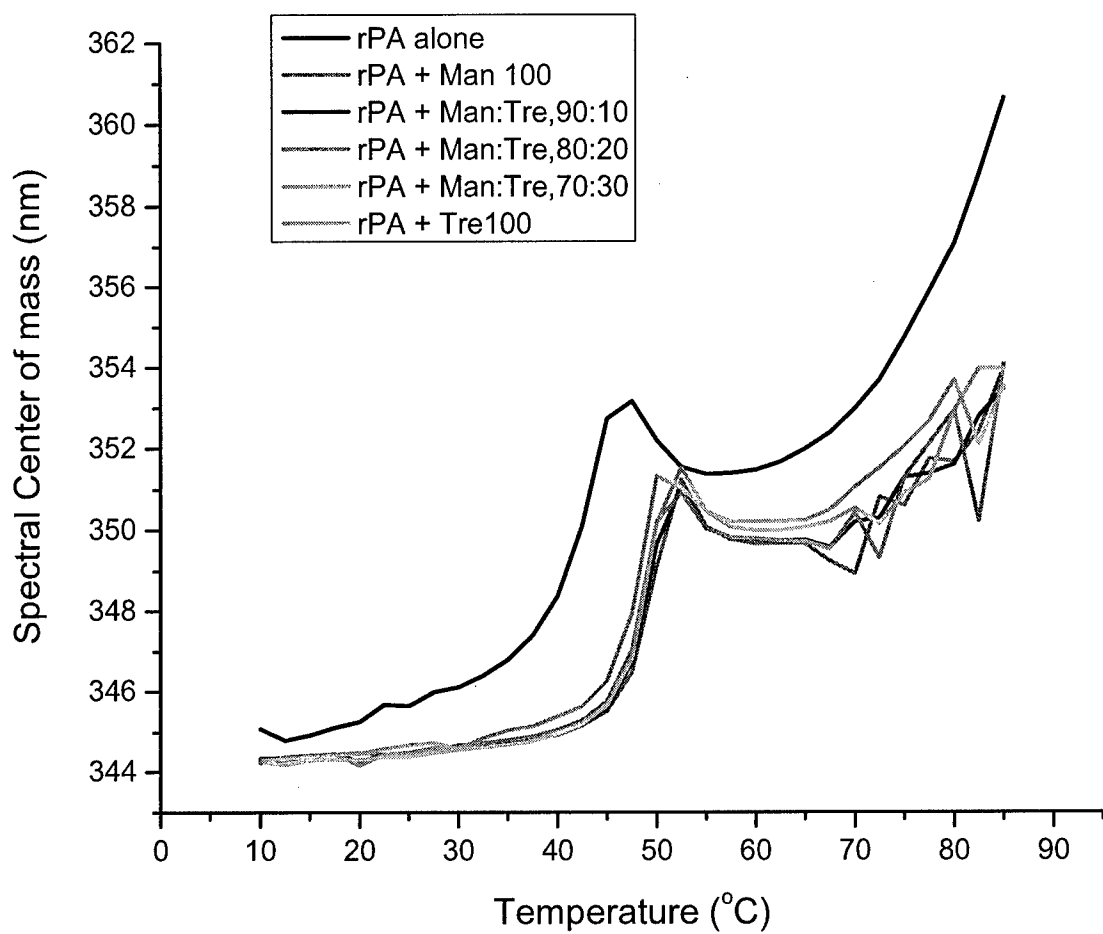


**Figure 25.** Effect of excipients on the intrinsic fluorescence intensity of anthrax rPA as a function of temperature.

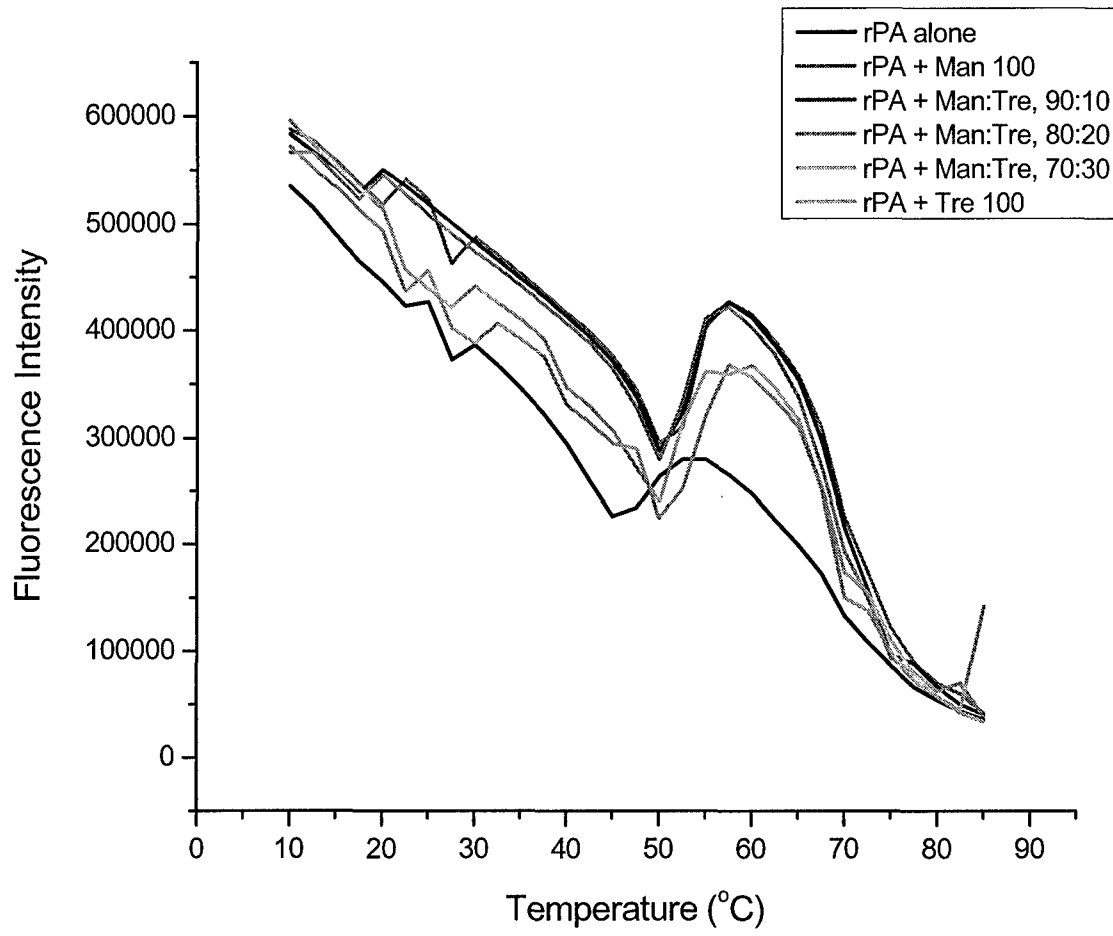


**Figure 26.** ICE chromatogram of rPA.

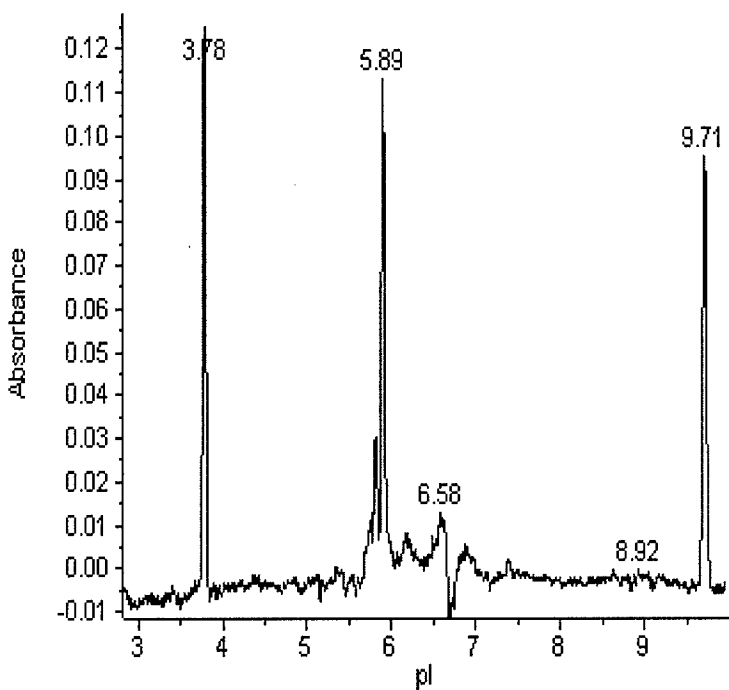


**Figure 27.** Adsorption isotherms for rPA and alhydrogel in 10 mM phosphate buffer, pH 7 containing 150 mM NaCl.

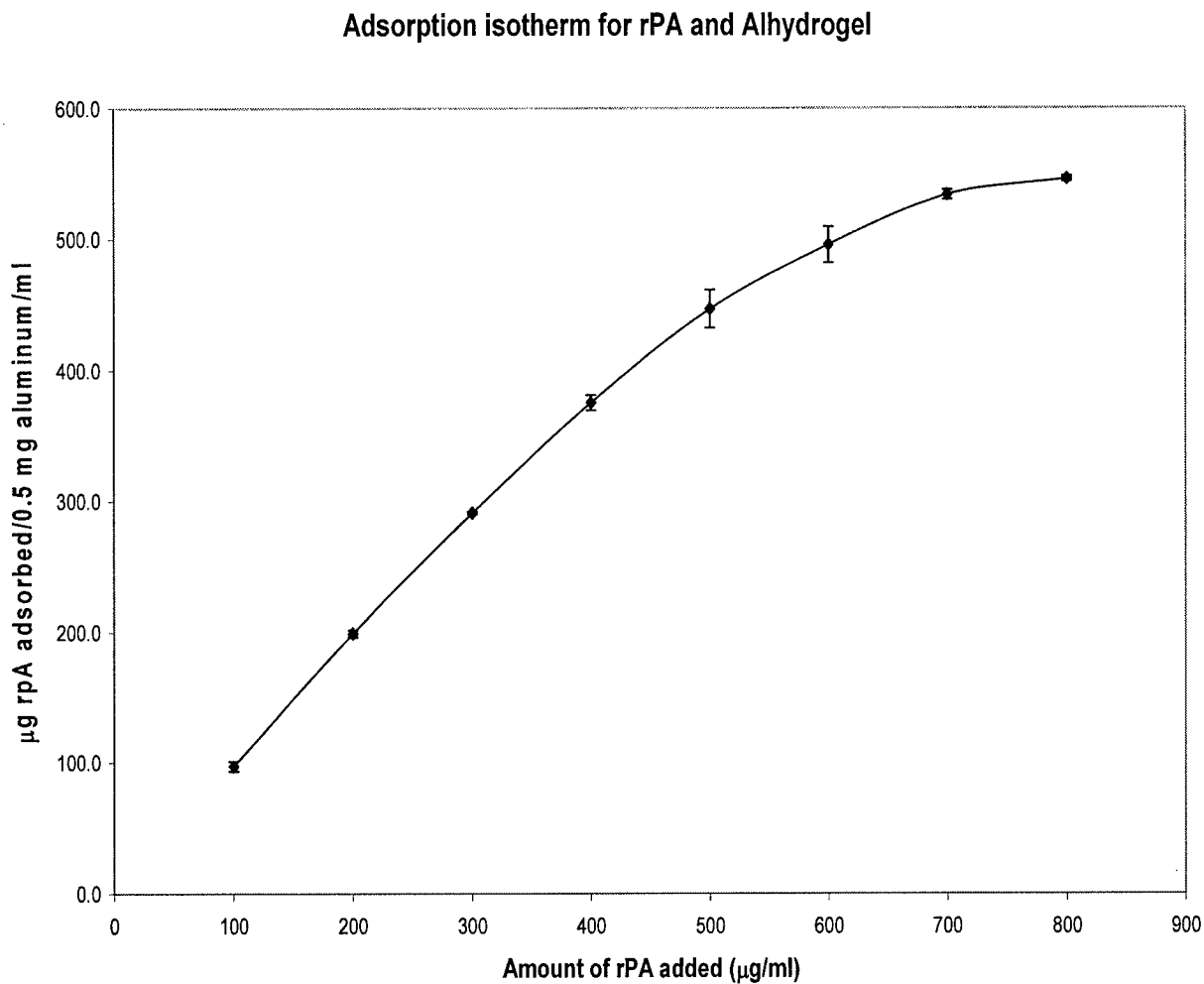


**Figure 28.** Adsorption isotherms for rPA and alhydrogel in 22 mM phosphate buffer, pH 7 containing 150 mM NaCl.

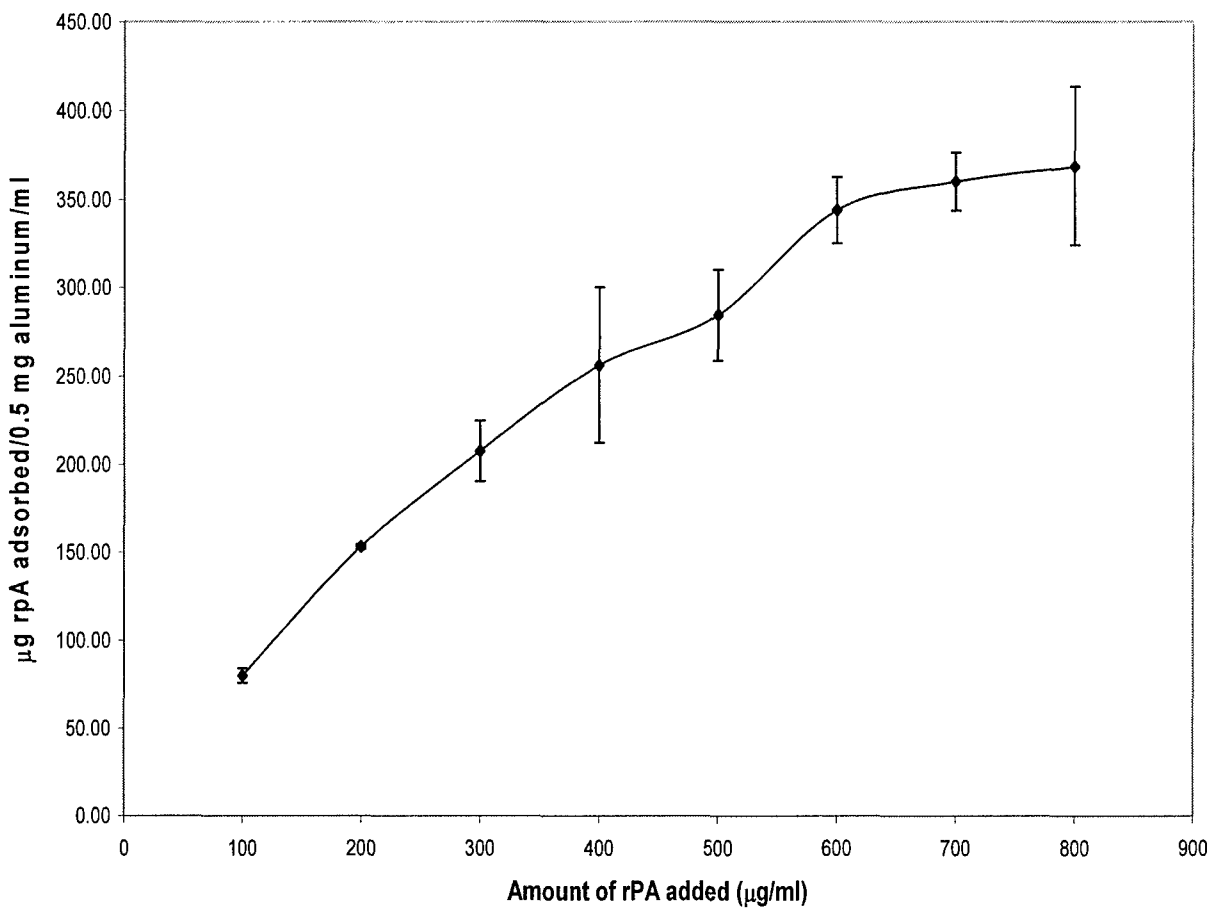


**Figure 29.** Fluorescence thermal melt plots of rPA in solution compared to rPA adsorbed to Alhydrogel—peak position vs. temperature (top) and fluorescence intensity vs. temperature (Bottom). A front face, triangular geometry was employed in these studies.

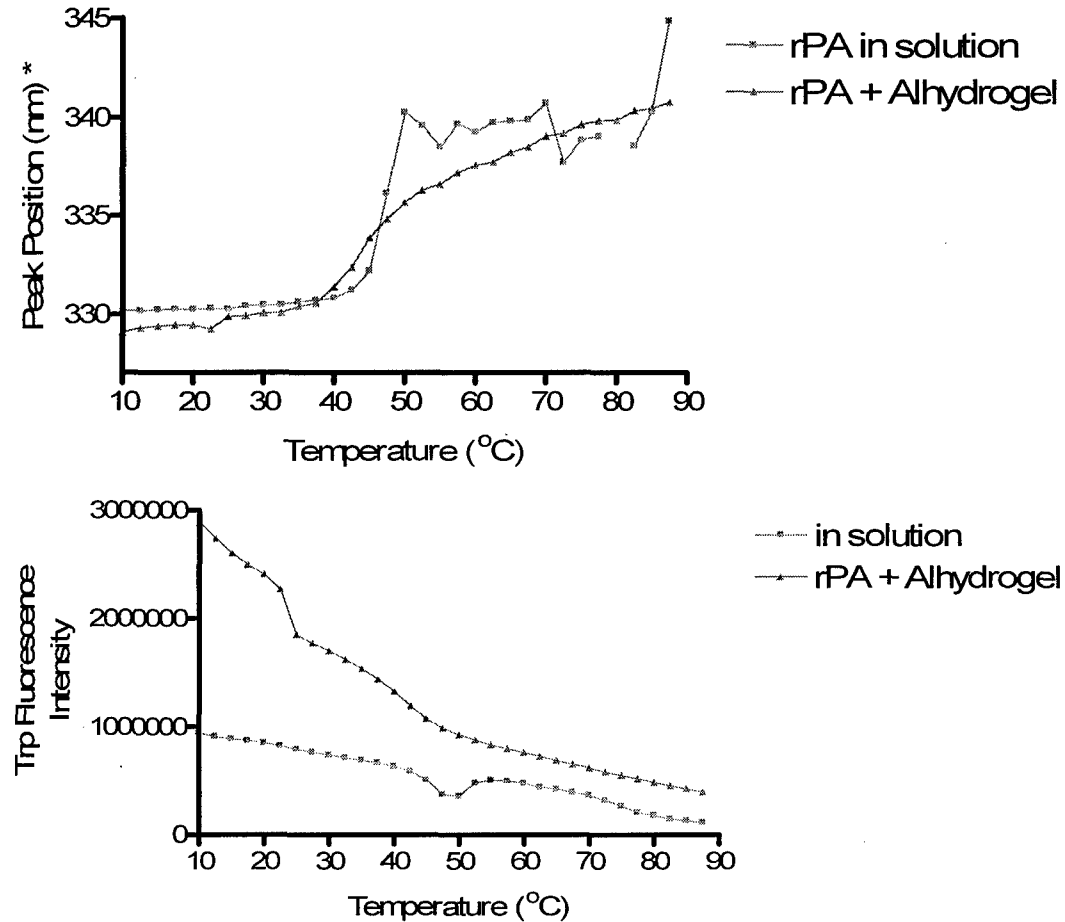
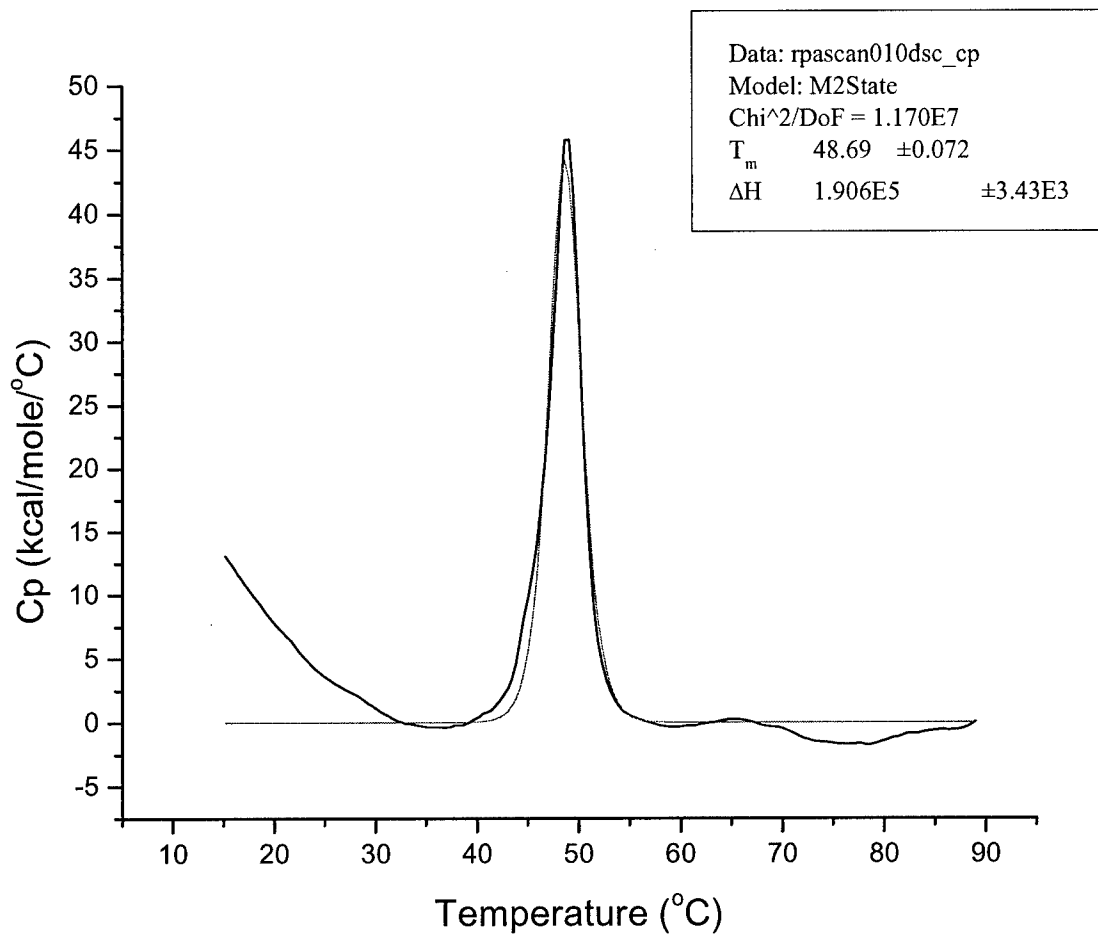


**Figure 30 A.** DSC thermograms and peak fits comparing thermal stabilities of rPA. (A) rPA in solution. (B) rPA adsorbed onto Alhydrogel®.

A.



B.

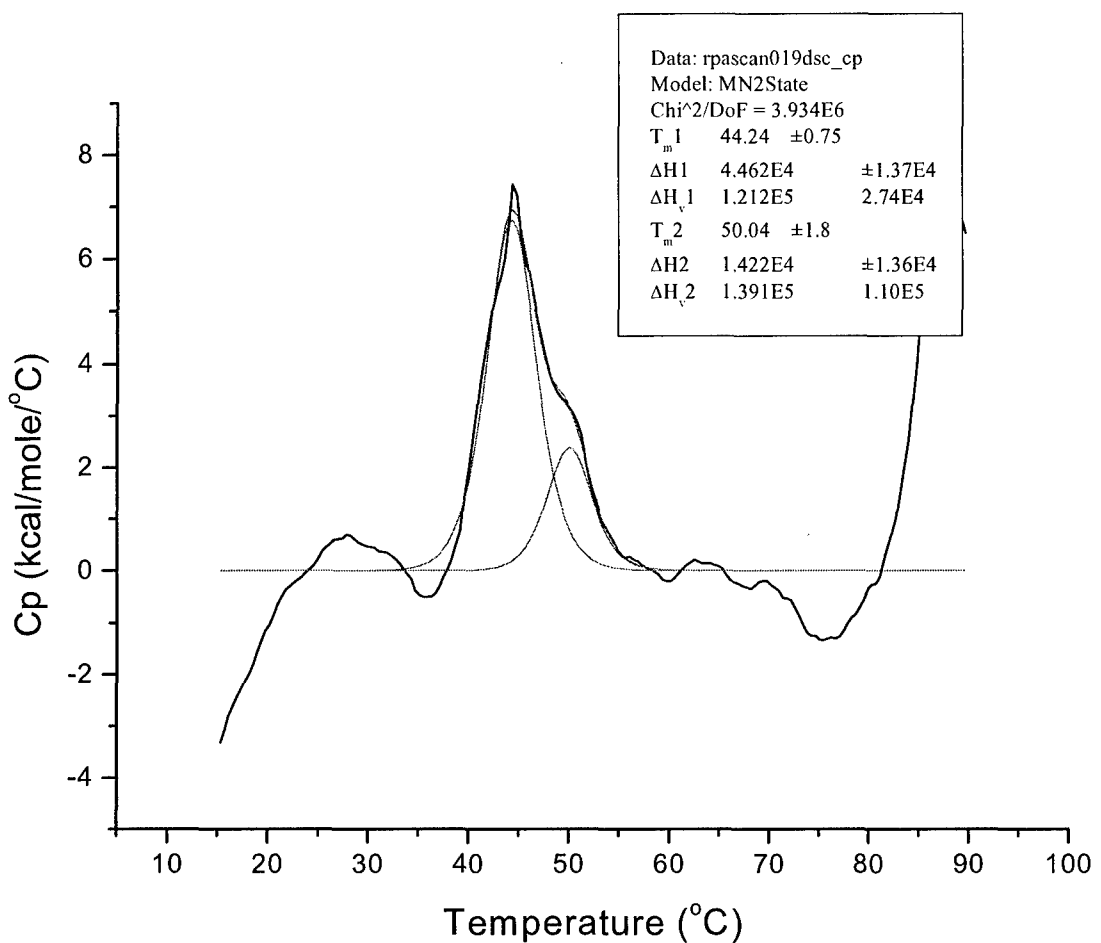


**Figure 31.** Effect of CpG oligonucleotides and temperature on the Fluorescence Spectral Center of Mass of rPA. Error bars represent standard error of the mean ( $N=2$ ). (Results are shifted approximately +13nm from actual peak maxima.)

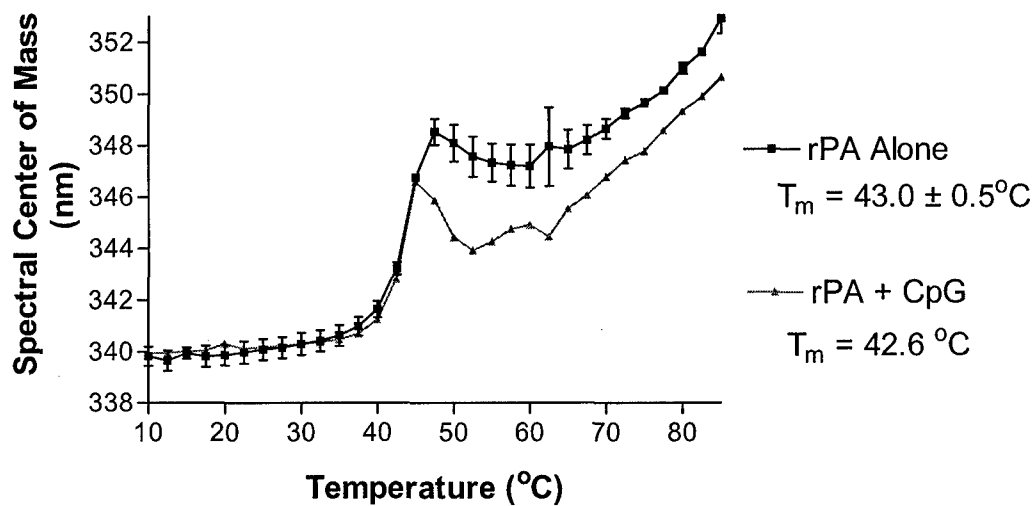


**Figure 32.** Differential Scanning Calorimetry Thermograms. Effect of CpG oligonucleotides on the melting temperature of rPA.

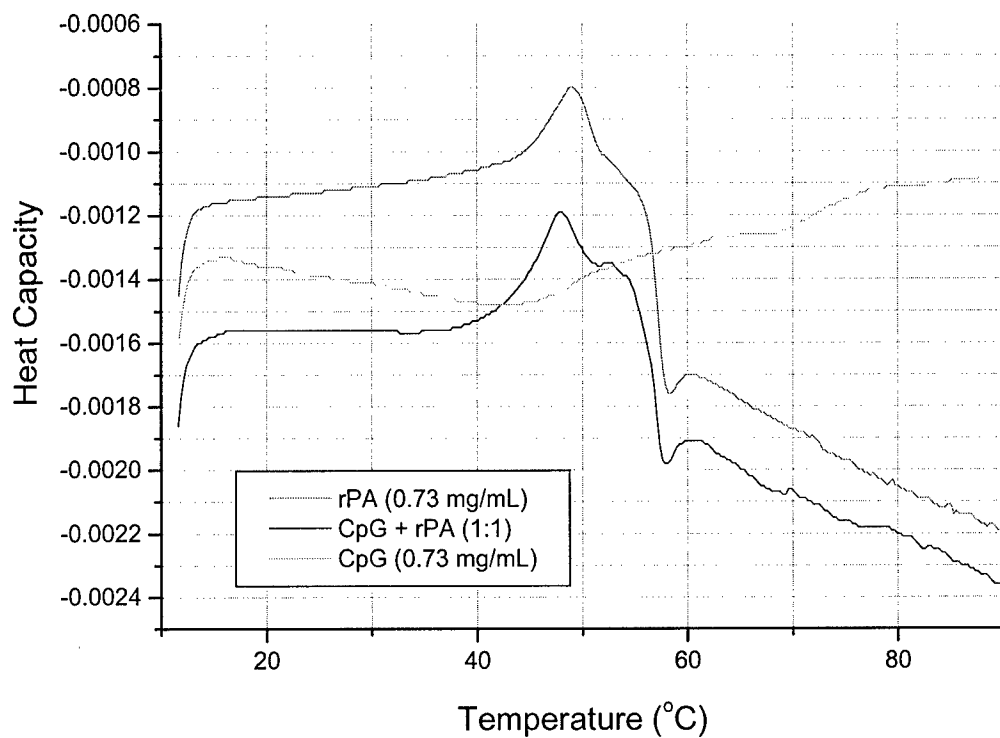


**Figure 33.** Isothermal Titration Calorimetry to study the binding of rPA to CpG oligonucleotides.

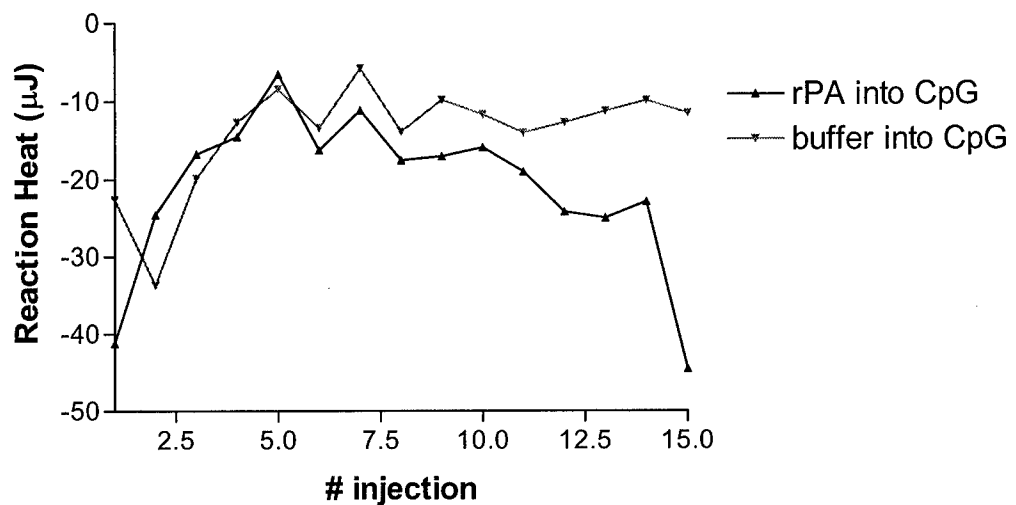


**Table 1.** Characterization of anthrax rPA by optical density, circular dichroism and fluorescence.

Method	pH	Transition Start (°C)	Transition Midpoint (°C)
OD	3	81.7	nd*
	4	30.4	37.7
	5	36.4	39.2
	6	43.7	48.2
	7	46.8	51.8
	8	47.9	52.1
CD	3	16.4	nd
	4	32.8	38.4
	5	36.5	40.3
	6	43.0	50.2
	7	48.0	nd
	8	46.3	nd
Intrinsic Trp Fluorescence	3	16.5	22.7
Peak Shift	4	22.5	30.2
	5	25.2	32.8
	6	37.5	43.0
	7	42.1	45.3
	8	40.0	45.2
ANS Fluorescence	3	10.0	nd
Peak Shift	4	21.5	28.7
	5	30.1	35.5
	6	42.3	49.4
	7	45.0	52.1
	8	40.8	52.5

**Table 2.** Inhibition of anthrax rPA aggregation by GRAS excipients.

Excipient	Molar ratio (Excipient: PA), Molarity (excipient) or wt. Percent (Excipient)	% Inhibition
Sorbitol	20.00%	106.08
Mannitol	10.00%	99.65
Sodium Citrate	0.2 M	94.77
Sodium Citrate	0.1 M	94.34
Trehalose	20.00%	93.78
Dextrose	10.00%	93.34
Histidine	0.3 M	88.25
Dextrose	20.00%	84.91
Malic Acid	0.15 M	82.57
Arginine	0.3 M	79.14
Trehalose	10.00%	78.45
Sorbitol	10.00%	73.21
Brij 35	0.05%	72.50
Dietanolamine	0.3 M	61.69
Glutamic Acid	0.15 M	61.47
Lactose	20.0%	59.07
Sucrose	20.0%	58.91
Glycerol	20.00%	55.71
Lactose	10.0%	54.43
Lysine	0.3 M	53.51
Glycerol	10.00%	48.26
Sucrose	10.00%	45.77
Tween 80	0.10%	45.73
Guanidine	0.3 M	43.05
2-OH propyl $\gamma$ -CD	10.00%	42.39
Glycine	0.3 M	41.91
Brij 35	0.01%	41.22
CaCl <sub>2</sub>	0.015 M	39.63
Aspartic Acid	0.075 M	35.54
2-OH propyl $\beta$ -CD	10.00%	32.12
Lactic Acid	0.15 M	30.94
Proline	0.3 M	30.75
Ascorbic acid	0.15 M	26.94
Tween 80	0.05%	22.53
Tween 20	0.05%	22.00
2-OH propyl $\gamma$ -CD	5.00%	19.53
Tween 80	0.01%	16.78
Tween 20	0.01%	16.24

Tween 20	0.10%	14.27
2-OH propyl β-CD	5.00%	13.50
Dextran T40	0.1	12.37
α Cyclodextrin	2.50%	5.61
Dextran T40	2.5	1.18
Dextran Sulfate	0.1	0.00
Dextran Sulfate	1	0.00
Dextran Sulfate	2.5	0.00
Brij 35	0.10%	0.00
Albumin	1.00%	0.00
Albumin	2.50%	0.00
Albumin	5.00%	0.00
Gelatin	2.50%	0.00
Gelatin	5.00%	0.00
Dextran T40	1.0	-2.85
Pluronic F-68	0.10%	-11.51
Pluronic F-68	0.05%	-14.12
Pluronic F-68	0.01%	-19.05

**Table 3.**

Excipient	Conc (M or %) *	% Inhibition
Arginine	0.3	47
Arginine	0.2	54
Arginine	0.1	21
Arginine	0.05	23
Histidine	0.3	96
Histidine	0.2	118
Histidine	0.1	101
Histidine	0.05	67
Sodium Citrate	0.2	98
Sodium Citrate	0.1	90
Sodium Citrate	0.05	79
Sodium Citrate	0.025	87
Sodium Citrate	0.01	46
Brij 35	0.10%	99
Brij 35	0.05%	45
Brij 35	0.01%	56
Brij 35	0.025%	39
Brij 35	0.005%	39
Mannitol	10.00%	75
Mannitol	7.50%	62
Mannitol	5.00%	72
Mannitol	2.50%	23
Mannitol	1.00%	11
Trehalose	20.00%	75
Trehalose	15.00%	67
Trehalose	10.00%	46
Trehalose	5.00%	46
Trehalose	2.50%	21

## **Valley Fever Antigens**

The vaccine to prevent Valley Fever has centered on three recombinant protein antigens: Ag2/PRA, GEL1, and CSA. Initially, our efforts focused on the biophysical characterization and stabilization of Ag2/PRA; however, Ag2/PRA and CSA have been covalently linked by two amino acids that act as a spacer between the two proteins. The resultant protein possesses antigenicity that is similar to that of the unlinked antigens and is referred to as fusion antigen (FA). The structural stability of FA was examined as a function of temperature in citrate/phosphate buffer at 0.1M and 1.0M NaCl over the pH range 3-8. Circular dichroism (CD), 2<sup>nd</sup> derivative UV absorption, and intrinsic fluorescence (only run at high salt concentration due to material limitations) spectroscopies were employed to assess the stability of the secondary (CD) and tertiary (UV and fluorescence) structures of the antigen. Data obtained indicate that the protein is especially unstable at the extremes of pH that were studied. The 2<sup>nd</sup> derivative UV absorption data are summarized in the form of a phase diagram in Figures 34 and 35 and the detailed data are presented in Figures 36-63. Aggregation was detected by eye prior to thermal perturbation at pH 3 and structural transitions were detected at lower temperatures for pH 3 and pH 8 compared to other pH values studied. The instability of FA in 1M NaCl at pH 3 was also confirmed by the lack of an observable fluorescence spectrum at this pH and ionic strength due to its precipitation from solution following aggregation. Additionally, losses in secondary and tertiary structure, as well as increases in optical density occur at significantly lower temperatures at pH 4 (near the pI of the protein) suggesting significant structural lability at this pH. Data suggest that the protein is more thermally stable in the presence of 1M NaCl near neutral pH values with pH 6 showing the best stability. Since a 1M salt concentration is hypertonic and not physiologically acceptable, it was recommended that the antigen be formulated at the highest ionic strength tolerable near neutral to slightly acidic pH for employment in primate studies that began in November of 2003.

The determination of concentration throughout these studies was difficult due to the presence of soluble aggregates. Numerous methods were employed to obtain protein concentration (i.e., BCA assays, UV-vis spectroscopy, and Bradford assays); however, a different concentration was obtained for each method. The presence of soluble aggregates inhibited initial attempts at

screening FA for stabilizers since our primary screening method monitors increases in turbidity with time at elevated temperatures.

A reverse construct of the fusion antigen (*Coccidioides* specific antigen + Ag2/PRA 1-106) against valley fever was synthesized and purified by scientists at the Southern Arizona Veterans Administrations Medical Center. The reverse construct (rFA) was characterized and its thermal stability was assessed by monitoring changes in intrinsic fluorescence, circular dichroism, and UV absorption spectra as a function of temperature.

### **Experimental Procedures on rFA**

Samples of rFA were received frozen on dry ice in 5mM citrate, 5mM phosphate, pH 7. Samples were thawed at room temperature and analyzed without modifying the buffer.

**UV Absorption Spectroscopy** – UV absorption spectra were obtained employing a Hewlett-Packard 8453 diode-array spectrophotometer. A baseline was obtained with 5mM citrate, 5mM phosphate, pH 7 and baseline-corrected spectra were obtained every 2.5° C from 10-85° C. Calculated second derivative spectra were fit to a spline function with 99 points of interpolation using software supplied with the instrument. Negative peak positions were determined and plotted as a function of temperature using Microcal Origin® version 7. Additionally, the optical density at 350 nm (OD) was monitored as a function of temperature concomitant with absorption spectra.

**Circular Dichroism Spectroscopy** – CD data were obtained employing a Jasco 810 spectropolarimeter equipped with a Peltier temperature control device and a 6-position sample holder. CD spectra were acquired from 10-85° C at 5° C intervals and single wavelength CD measurements at 208 nm were taken over the same temperature range. rFA samples were contained in sealed 0.1 cm path length cells at a concentration of 100 µg/mL. A resolution of 0.2 nm and a scanning speed of 20 nm/min with a 2-s response time were employed. Spectra presented are an average of three consecutive scans. CD at 200 nm was measured at 0.2° C intervals using a 15° C/h temperature ramp rate and a 2-s response time. Data was smoothed using software supplied with the instrument; plotting was performed in Microcal Origin®.

**Fluorescence Spectroscopy** – Fluorescence emission spectra were obtained in 2.5° C increments from 10-85° C using a QuantaMaster™ spectrofluorometer (Photon Technology International, Inc.) equipped with a 4-position cell holder and Peltier temperature control device. A 5-minute equilibration time was used at each temperature before data acquisition. The intrinsic fluorescence spectra were collected by exciting samples at 295 nm and emission was monitored between 305 and 450 nm using excitation and emission slit widths of 6 nm. The spectra were corrected for the Raman band of water by subtraction of the buffer spectrum at each corresponding temperature. Spectra were smoothed using the software included with the instrument; buffer subtraction and plotting were performed in Microsoft Excel®.

## Results and Discussion

Slight changes in the tertiary structure of proteins can lead to exposure of hydrophobic side chains, potentially resulting in aggregation and an increase in optical density. In addition to monitoring the optical density at 350nm (OD) to assess the aggregation state of the protein by varying the temperature, high resolution second derivative analysis of UV absorption spectra was employed as a function of temperature. Analysis by this method permits the detection of small changes in the polarity of the local environment of the aromatic amino acid side chains (tertiary structural changes) since the wavelength of absorbed light is altered as a result of those changes. The zero order UV absorption spectrum of rFA possesses a non-zero slope above 300 nm at 10° C (Figure 64) suggesting that significant aggregation occurs during or following the purification process. Figure 65 illustrates that the OD increases slightly as the temperature is increased from 10-50° C at which point a decrease in the OD occurs. This is followed by an increase in the OD above 62° C and suggests that tertiary structural changes occur that result in the aggregation of rFA. The sharp decrease in OD above 75° C suggests that structural perturbations occur which ultimately result in either precipitation or a decrease in self-association. Second derivative analysis of the UV spectra as a function of temperature reveals a temperature-dependent increase in the wavelength of absorbed light below 60° C (Figure 66). An abrupt transition near 62° C in the peak near 258 nm as well as the lack of resolution of the peak near 252 nm above 60° C is observed suggesting that a change in the tertiary structure occurs near this temperature.

As a complementary technique to second derivative UV absorption spectroscopy, intrinsic fluorescence spectroscopy was employed to detect changes in the tertiary structure of rFA. As the polarity of the local environment of tryptophan is altered, its fluorescence emission spectrum should change thereby permitting the detection of changes in tertiary structure. The intrinsic fluorescence spectrum of rFA displays a maximum emission wavelength ( $\lambda_{\text{max}}$ ) of 393 nm at 10° C suggesting either a unique, solvent-exposed environment for the tryptophan residues of rFA (Figure 67) or perhaps oxidation of the Trp residues to kynurine or its derivatives. Alternatively, dityrosine formation may be occurring. As the temperature is increased the  $\lambda_{\text{max}}$  increases in a near-linear fashion and has a value of 420 nm at 85° C (Figure 68). This is probably most consistent with chemical changes in the aromatic residues at highly elevated temperatures.

Plotting the fluorescence intensity at  $\lambda_{\text{max}}$  as a function of temperature can yield additional information about tertiary structural transitions that take place. In this case, however, the fluorescence intensity at  $\lambda_{\text{max}}$  as a function of temperature appears to continuously change suggesting only a gradual change in structure, inconsistent with the presence of highly organized structure (Figure 69).

Circular dichroism spectroscopy (CD) was employed to monitor thermal perturbations in the secondary structure of rFA. The CD spectrum at 10° C illustrates a minimum near 197 nm and suggests that rFA possesses primarily unordered secondary structure (Figure 70). The CD at 200 nm was followed as a function of temperature from 10-85° C and a gradual loss in negative ellipticity was observed (Figure 71) without a gain in other secondary structural characteristics ( $\alpha$ -helix or  $\beta$  structure).

Together, the data suggest that rFA is present in an unfolded and aggregated state. Whether this recombinant protein could be used in an effective vaccine is not known, but changes in the purification process are already underway. These changes should result in rFA possessing greater secondary and tertiary structure which could lead to greater thermal and long-term storage stability, more like the original constructs.

The chimeric valley fever protein was encapsulated into nanoparticles in an effort to improve protein protection during challenge. Two distinct nanoparticle formulations were fabricated to conduct the challenge studies. Briefly, poly(DL-lactide-co-glycolide) (PLG) particles were fabricated by modifying a reported double-emulsion/solvent extraction procedure (Panyam 2003). Approximately 360 mg of PLG (Mw ~ 60 kDa) was dissolved in 6 mL of a mixture of chloroform and acetone. 600  $\mu$ L of buffered chimeric protein (120  $\mu$ g/mL) was emulsified into the polymer solution for one minute. This emulsion was further emulsified for 10 minutes into 120 mL of 2.5% polyvinyl alcohol (PVA) in deionized water. The resultant double emulsion was stirred overnight to facilitate solvent extraction and hardening of the nanoparticles. Hardened nanoparticles were centrifuged and washed three times with deionized water to remove PVA. After the final centrifugation, nanoparticles were resuspended in ~25 mL of a 5% wt/vol sucrose solution before freeze-drying for 48 hours. The resulting solid was gently stirred to form a free-flowing powder.

Nanoparticles were also formed by ionic complexation of oppositely charged polymers using a reported procedure<sup>3</sup>. 100  $\mu$ L of the 120  $\mu$ g/mL stock solution of chimeric protein was added to 1 mL of 1% wt/vol polyethylenimine (Mw = 100 kDa) and stirred for 30 minutes. This mixture was then added to 2 mL of 1% wt/vol dextran sulfate (Mw = 500 kDa) and stirred for 30 minutes. Then, 25  $\mu$ L of 1 M zinc sulfate was added as a particle stabilizer. The resulting colloidal suspension was dialyzed (100 kDa cutoff membrane) against a 5% wt/vol mannose solution for 24 hours. Sucrose was added to the dialyzed solution to reach a concentration of 5% wt/vol. The particle solution was then freeze-dried for 48 hours.

The loading of chimeric protein (wt protein/wt particle) was estimated by measuring the concentration of unencapsulated protein. Aliquots of the nanoparticle formulations were centrifuged at 15,000 rpm to remove particles from solution. The supernatant was analyzed at 280 nm (Agilent 8453) and converted to concentration to determine the mass of unencapsulated protein to mass of particles formed. This technique serves as a rough estimate and will be verified by direct extraction and quantification of protein from the nanoparticles. This material is currently being used for immunogenicity and challenge testing at the University of Arizona.

T FA in 0.1 M NaCl, 10/08/03

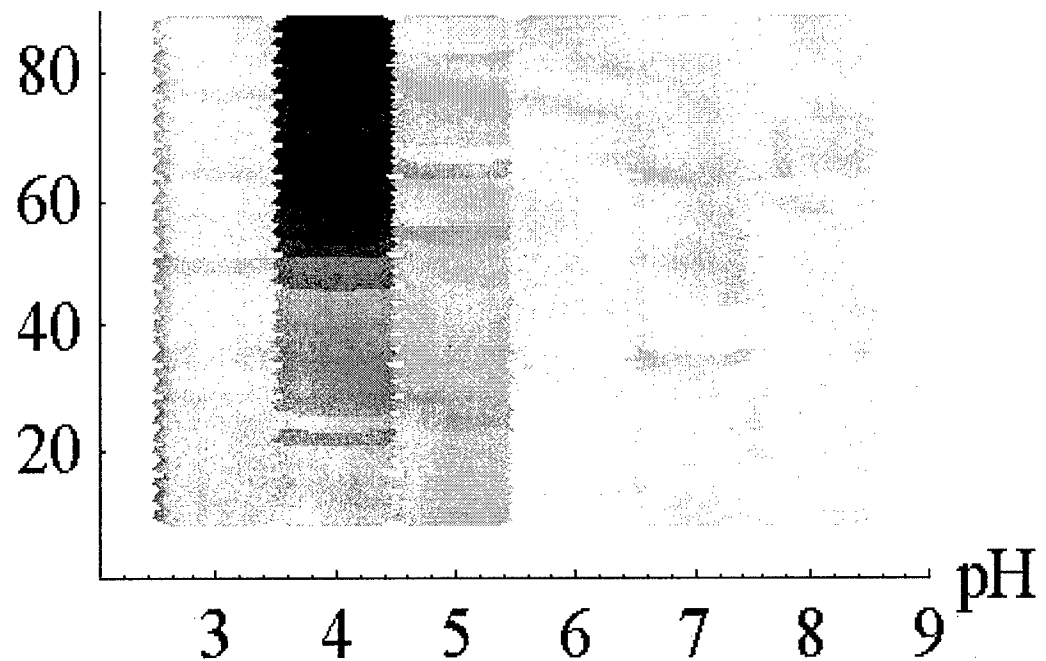


Figure 34. Phase diagram of FA in 0.1 M NaCl as a function of temperature and pH.

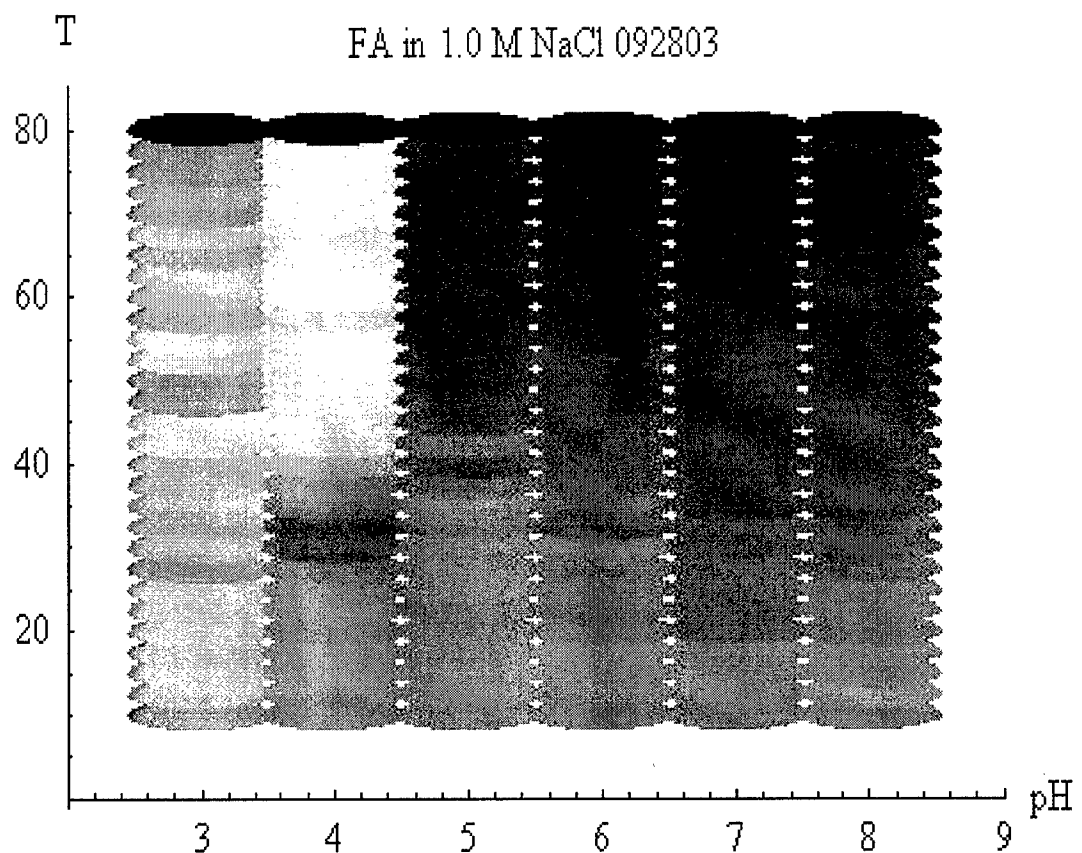


Figure 35. Phase diagram of FA in 1.0 M NaCl as a function of temperature and pH.

FA in 0.1 M NaCl  
100803

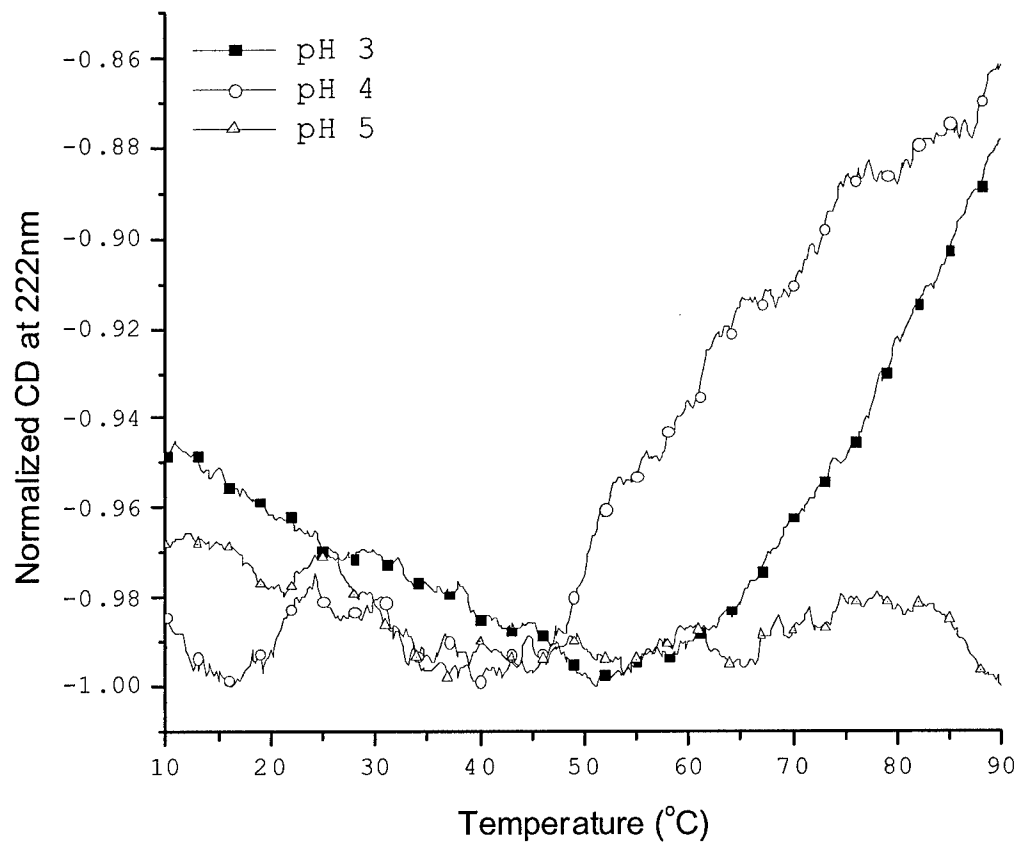


Figure 36. CD spectra of FA in 0.1M NaCl as a function of temperature.

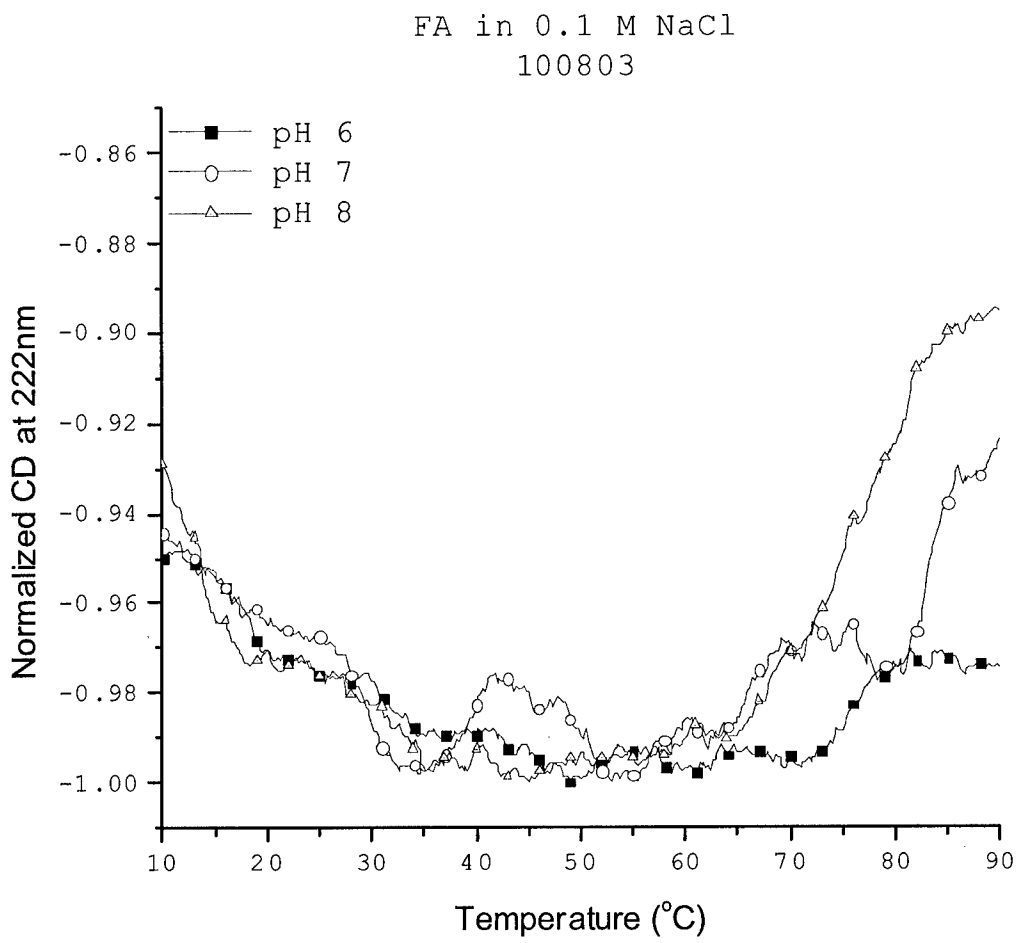


Figure 37. CD spectra of FA in 0.1M NaCl as a function of temperature.

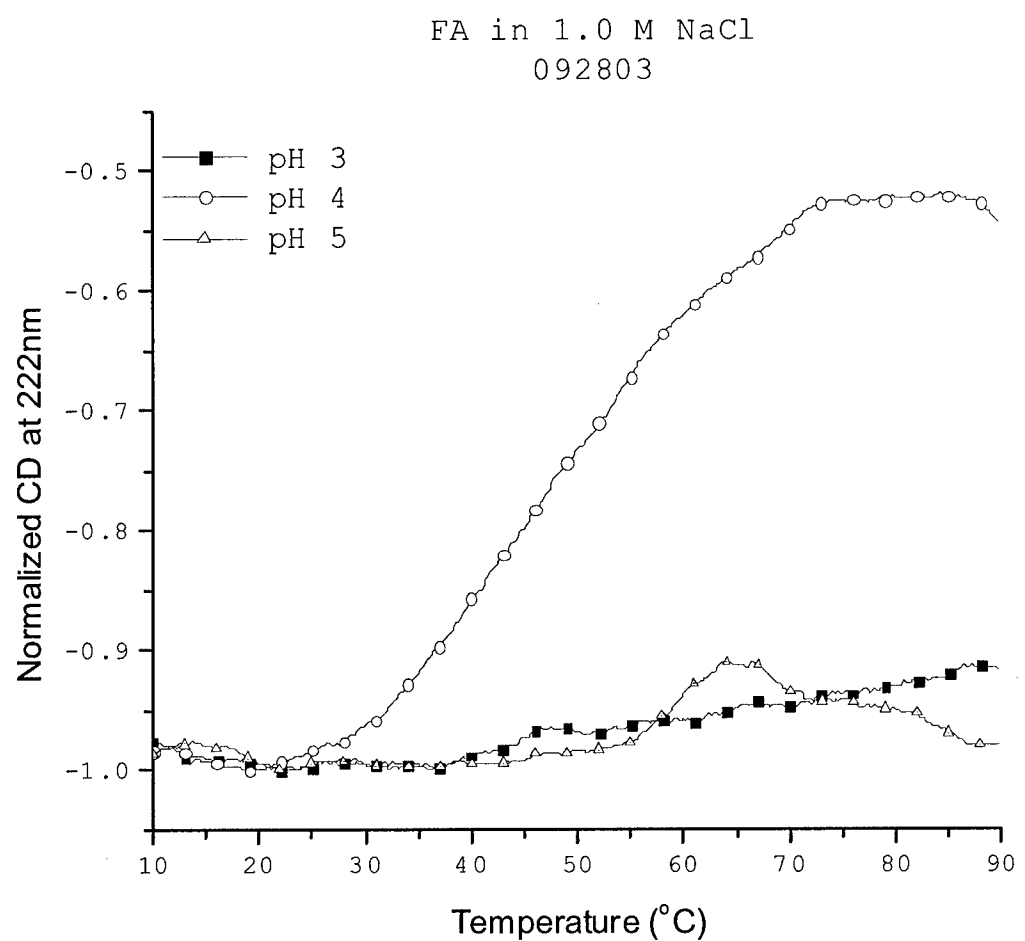


Figure 38. CD spectra of FA in 1.0M NaCl as a function of temperature.

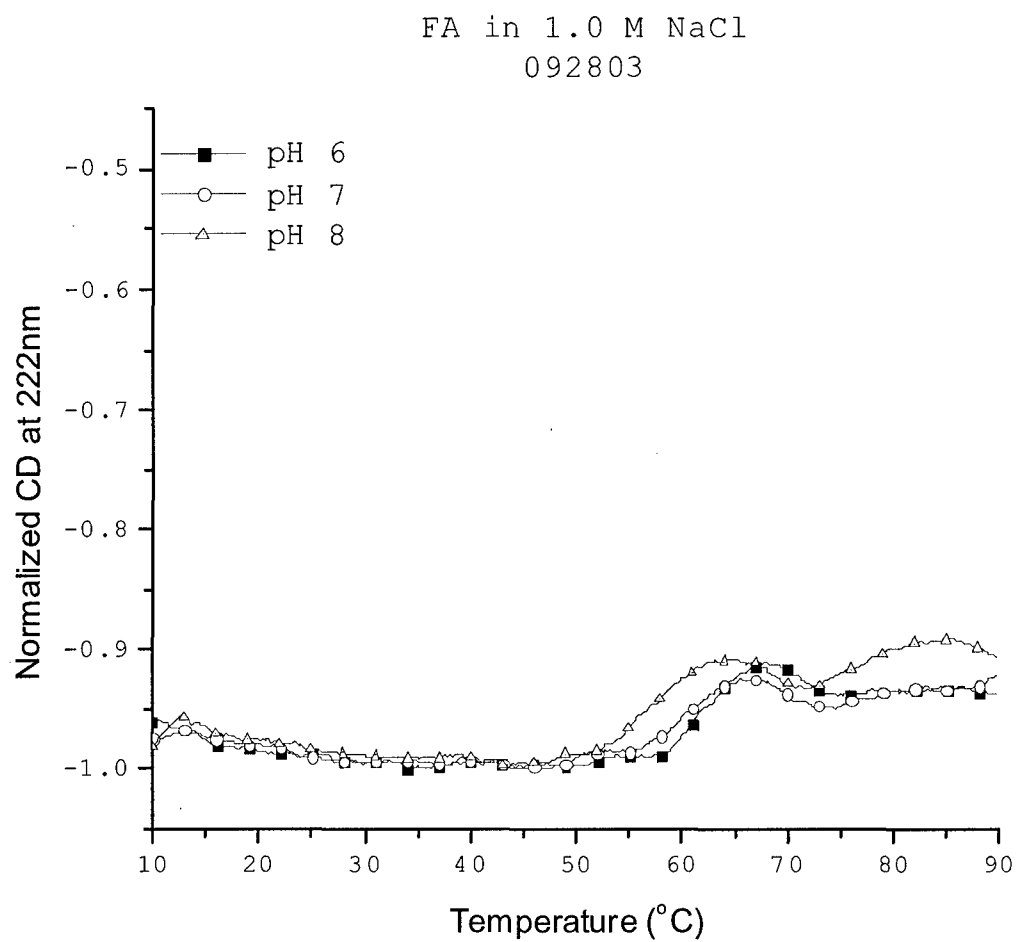


Figure 39. CD spectra of FA in 1.0M NaCl as a function of temperature.

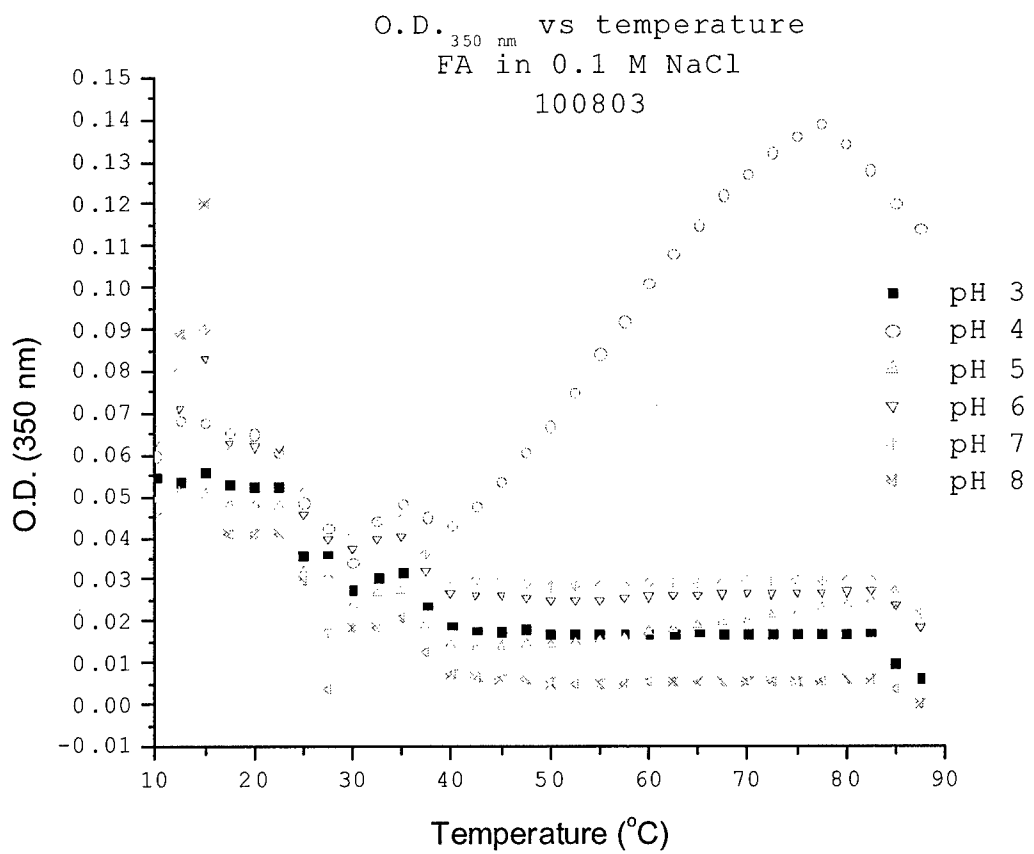


Figure 40. Optical density at 350 nm as a function of temperature for FA in 0.1M NaCl.

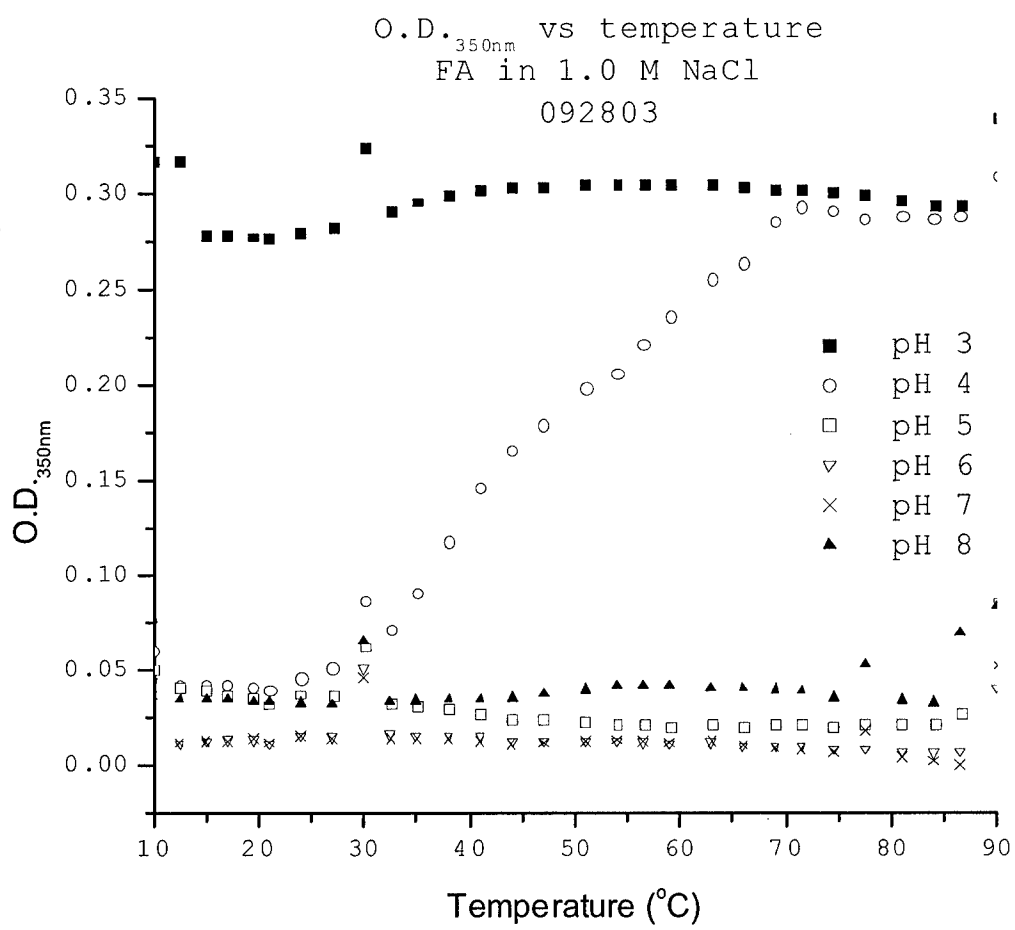


Figure 41. Optical density at 350 nm as a function of temperature for FA in 1.0M NaCl.

FA in 0.1 M NaCl  
pH 3.0, 100803

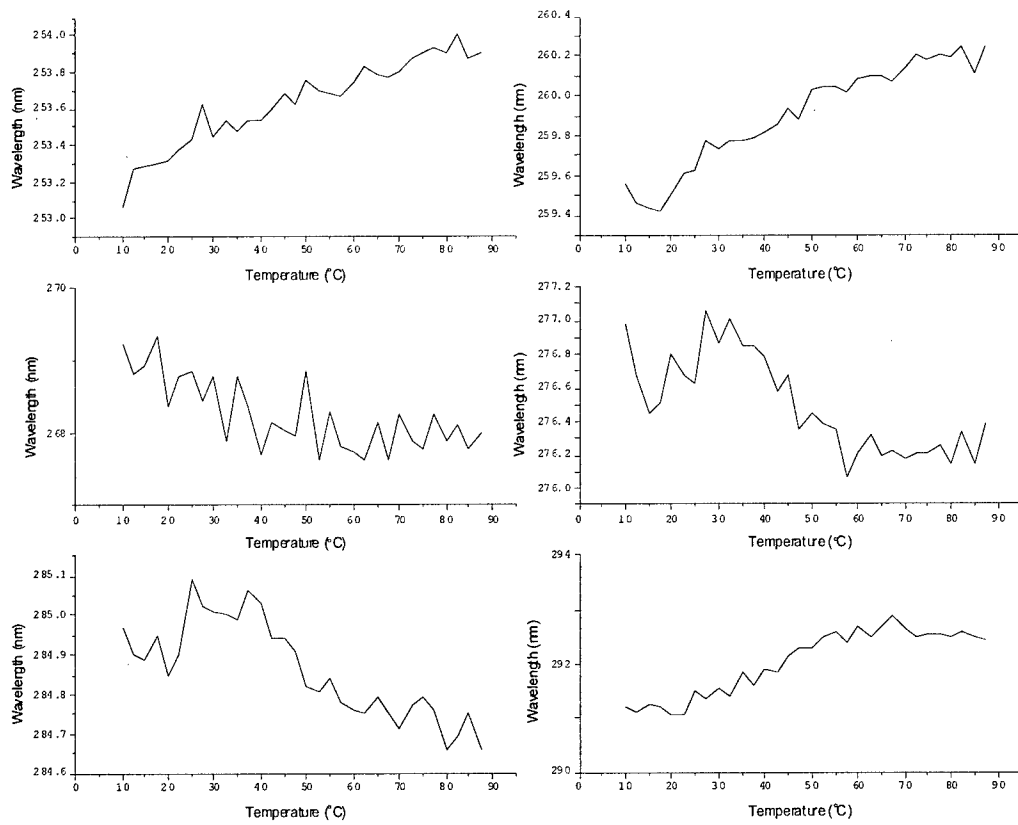


Figure 42. 2<sup>nd</sup> derivative UV peak position as a function of temperature for FA in 0.1 M NaCl at pH 3.0.

FA in 0.1M NaCl  
pH 4.0, 100803

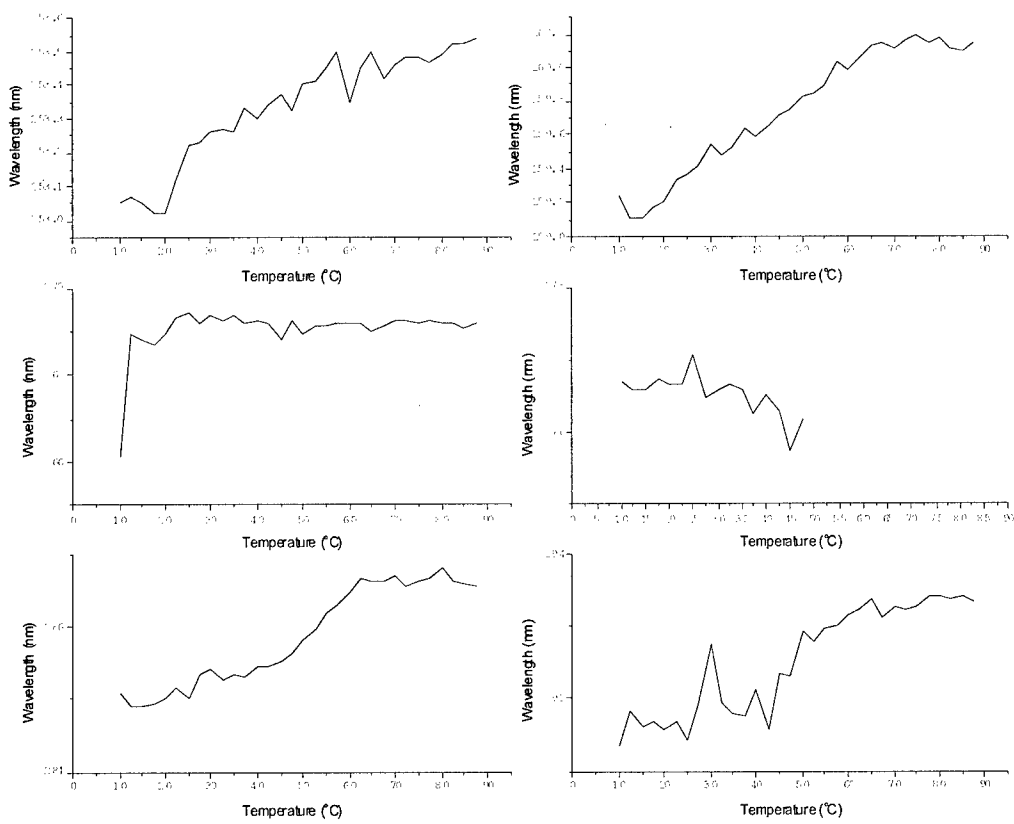


Figure 43. 2<sup>nd</sup> derivative UV peak position as a function of temperature for FA in 0.1 M NaCl at pH 4.0.

FA in 0.1 M NaCl  
pH 5.0, 100803

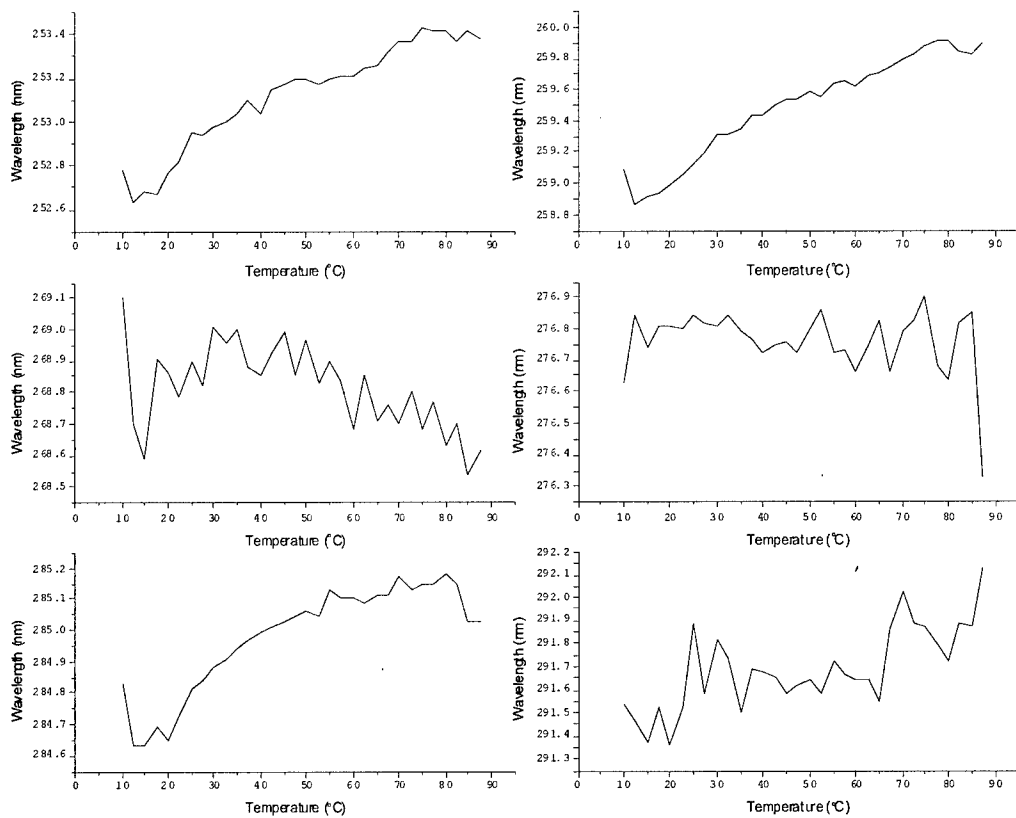


Figure 44. 2<sup>nd</sup> derivative UV peak position as a function of temperature for FA in 0.1 M NaCl at pH 5.0.

FA in 0.1 M NaCl  
pH 6, 100803

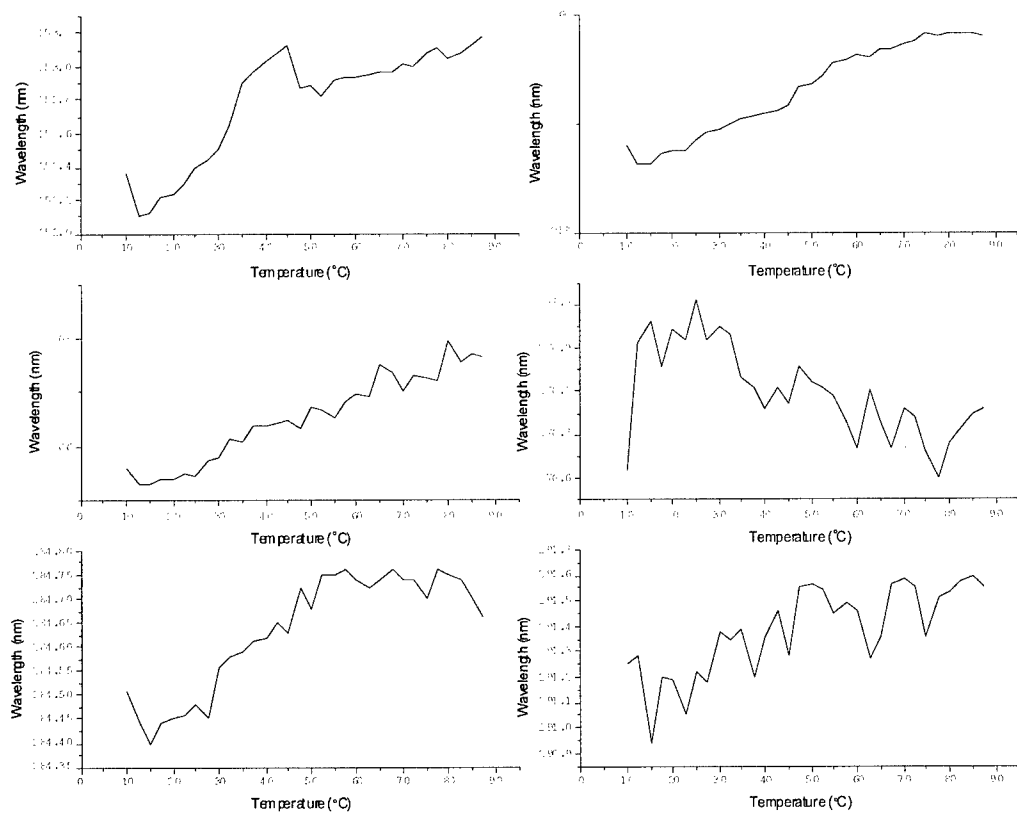


Figure 45. 2<sup>nd</sup> derivative UV peak position as a function of temperature for FA in 0.1 M NaCl at pH 6.0.

FA in 0.1 M NaCl  
pH 7.0, 100803

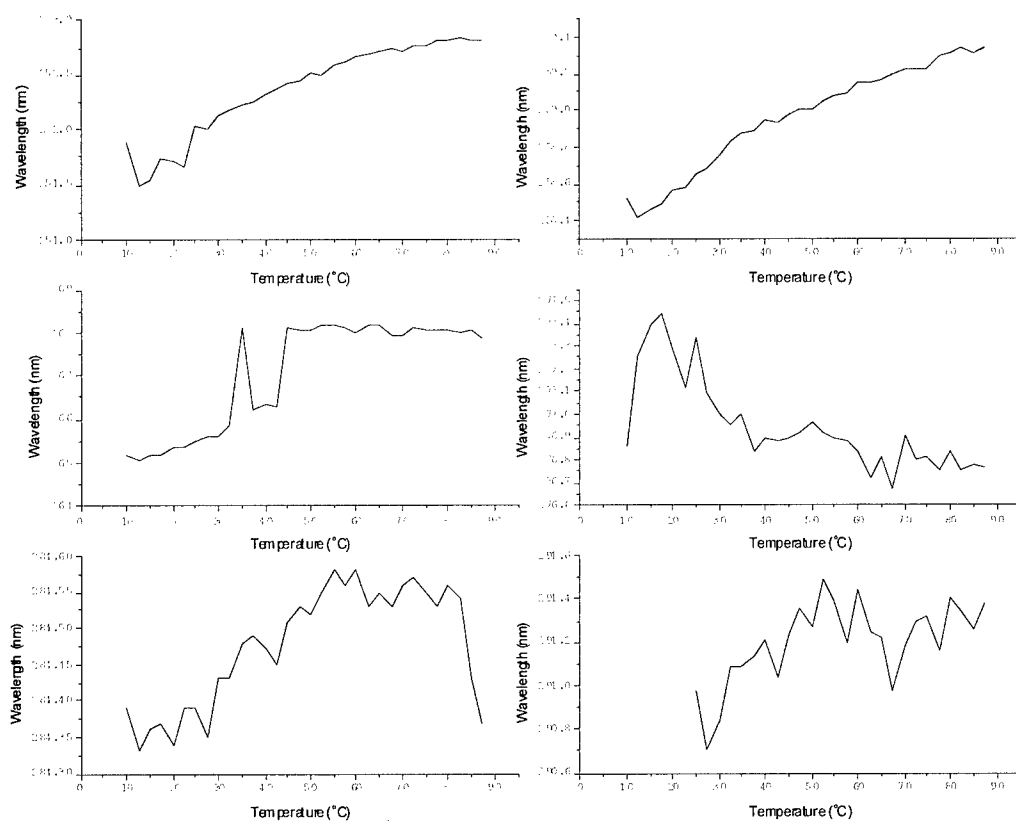


Figure 46. 2<sup>nd</sup> derivative UV peak position as a function of temperature for FA in 0.1 M NaCl at pH 7.0.

FA in 0.1 M NaCl  
pH 8.0, 100803

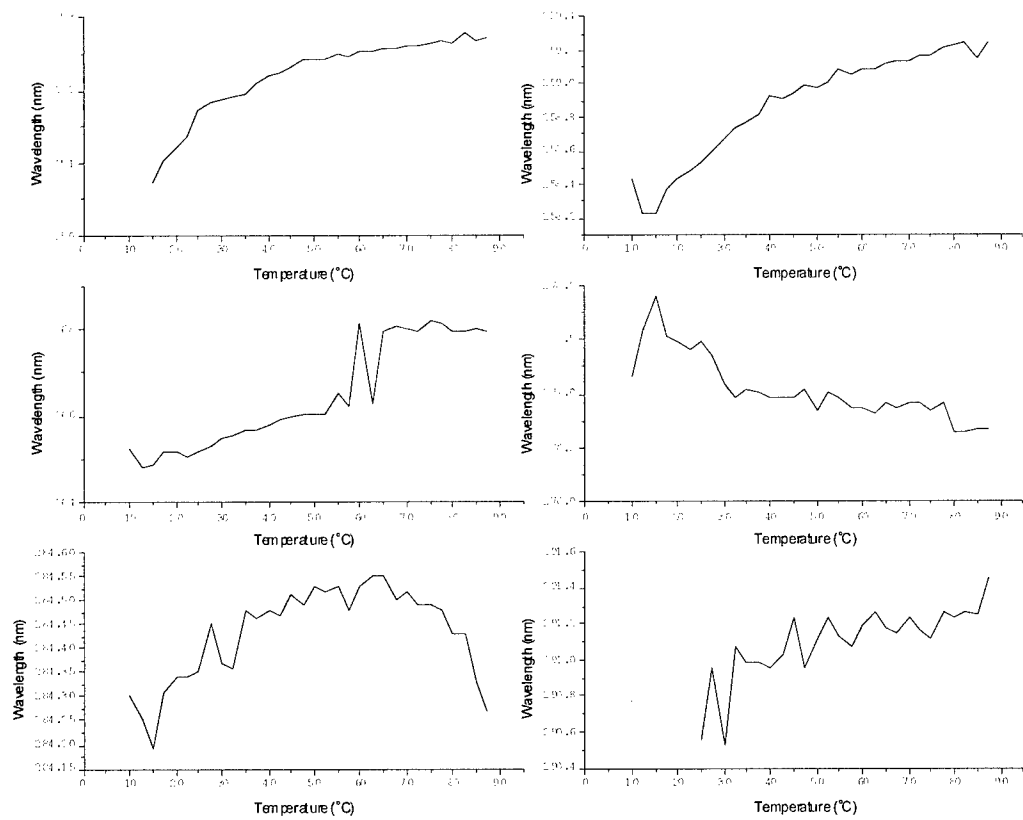


Figure 47. 2<sup>nd</sup> derivative UV peak position as a function of temperature for FA in 0.1 M NaCl at pH 8.0.

FA in 1.0 M NaCl  
pH 3.0, 092803

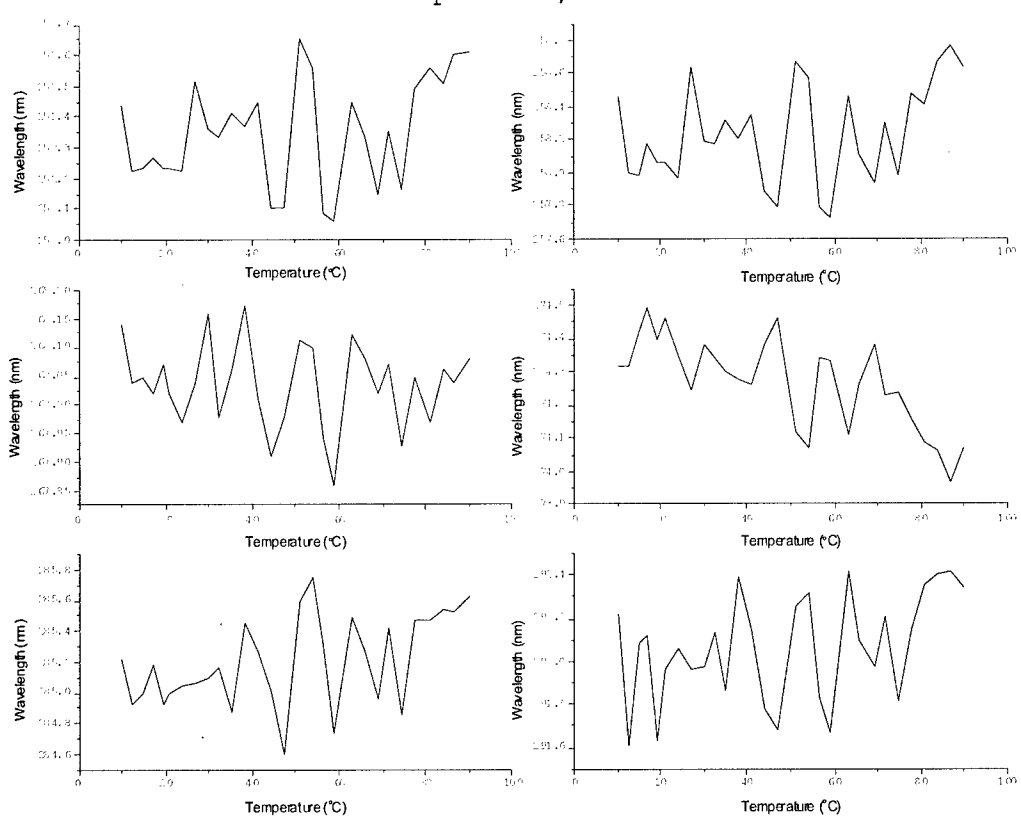


Figure 48. 2<sup>nd</sup> derivative UV peak position as a function of temperature for FA in 1.0 M NaCl at pH 3.0.

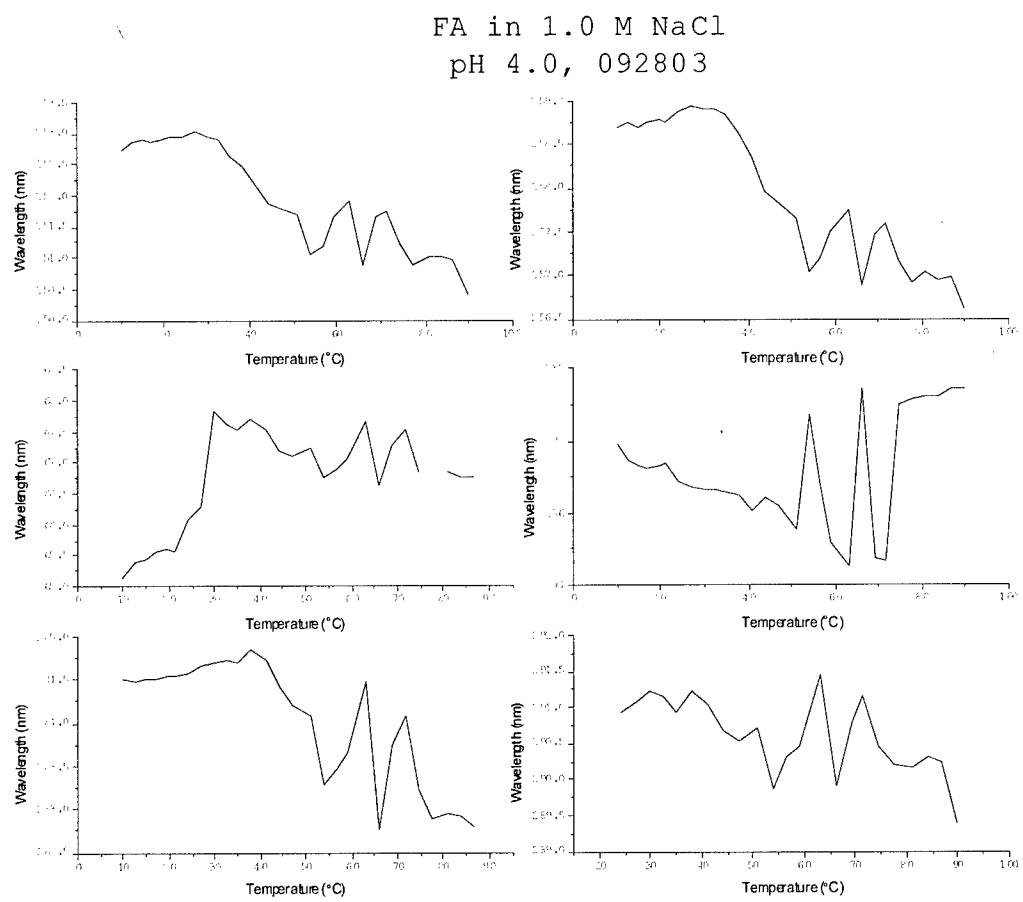


Figure 49. 2<sup>nd</sup> derivative UV peak position as a function of temperature for FA in 1.0 M NaCl at pH 4.0.

FA in 1.0 M NaCl  
pH 5.0, 092803

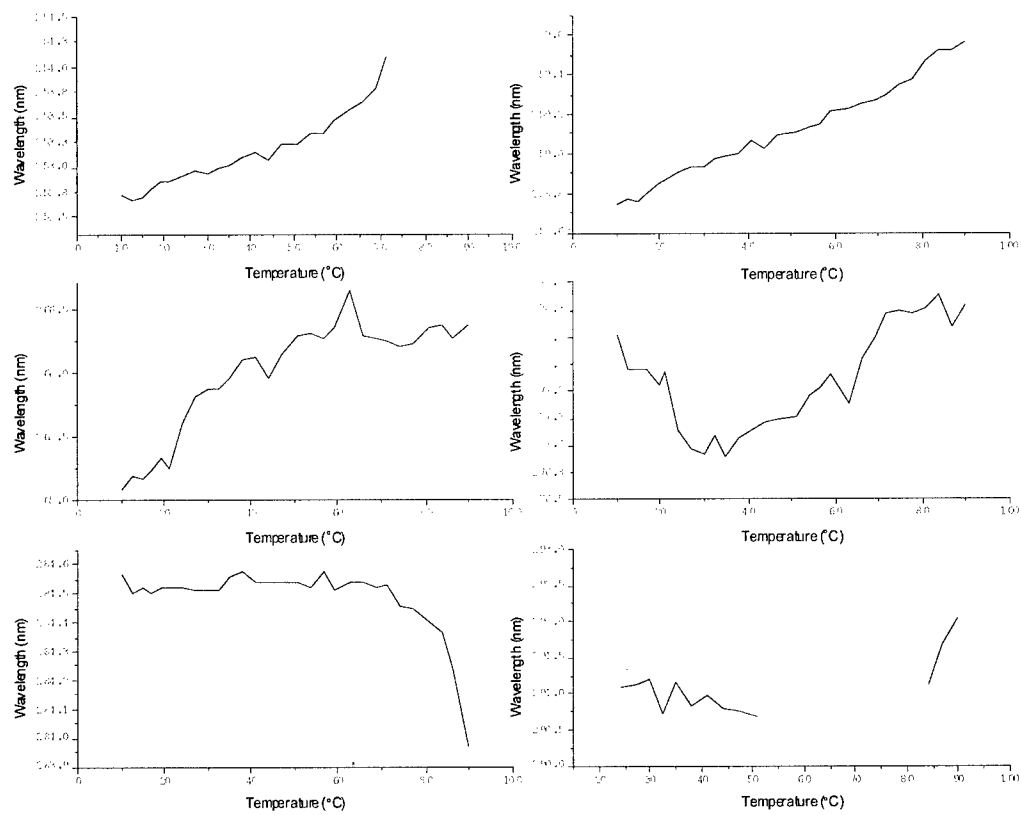


Figure 50. 2<sup>nd</sup> derivative UV peak position as a function of temperature for FA in 1.0 M NaCl at pH 5.0.

FA in 1.0 M NaCl  
pH 6.0, 092803

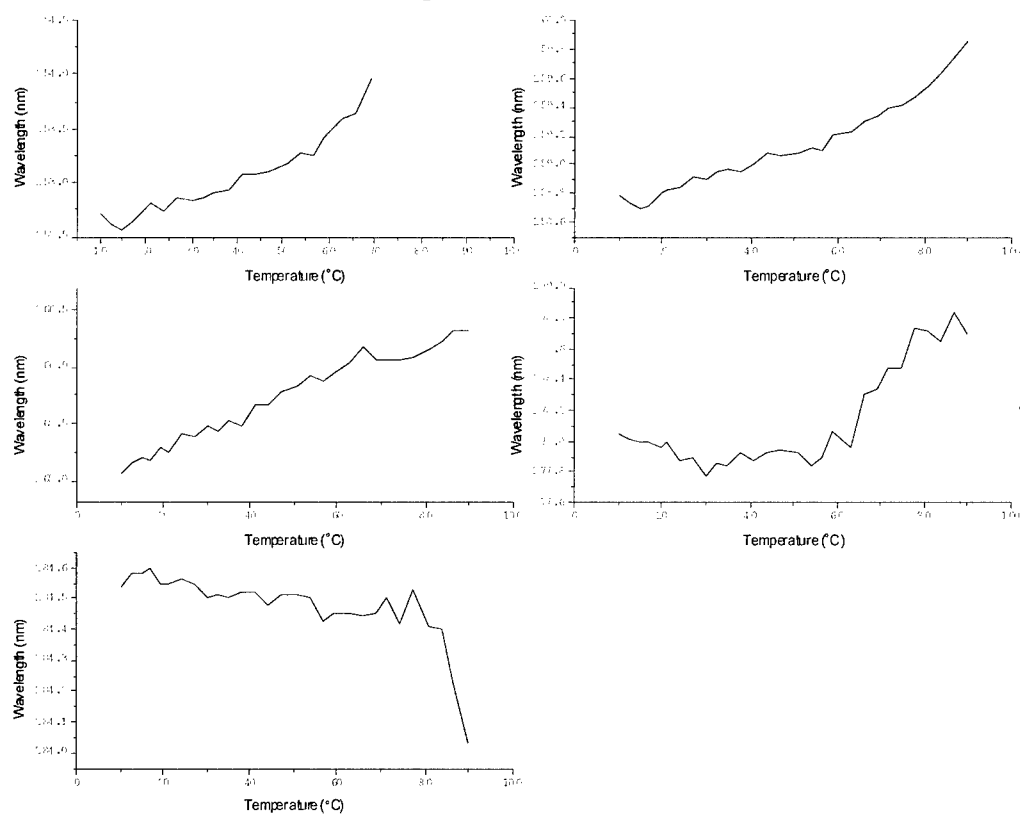


Figure 51. 2<sup>nd</sup> derivative UV peak position as a function of temperature for FA in 1.0 M NaCl at pH 6.0.

FA in 1.0 M NaCl  
pH 7.0, 092803

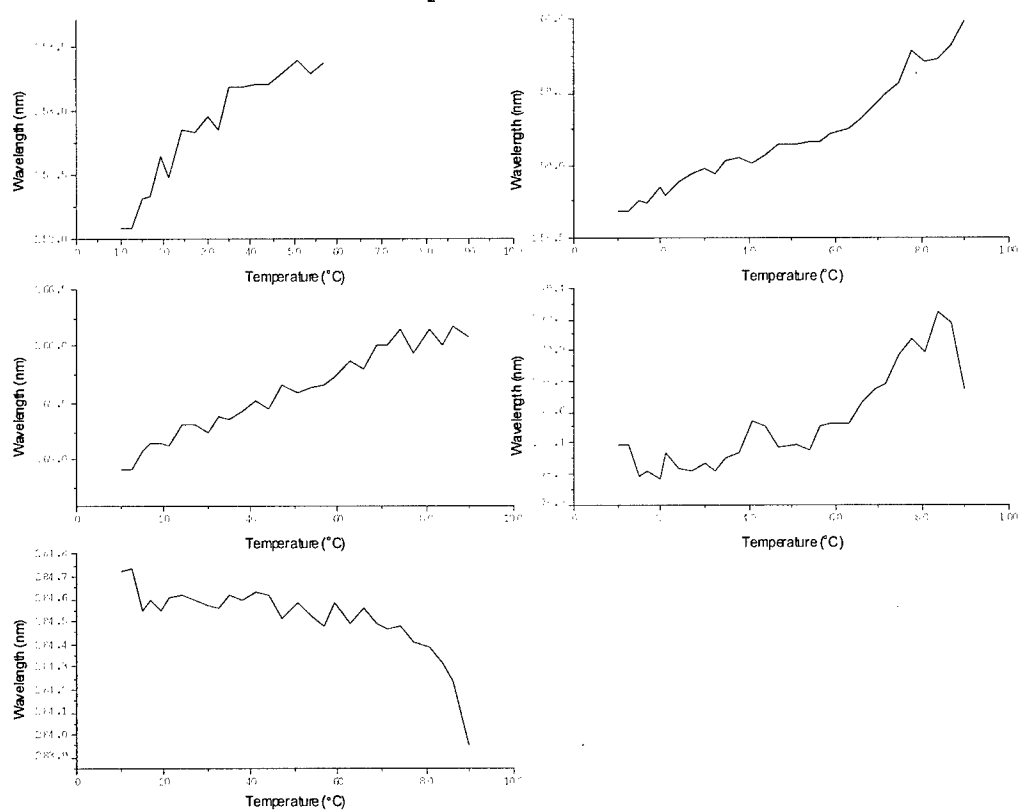


Figure 52. 2<sup>nd</sup> derivative UV peak position as a function of temperature for FA in 1.0 M NaCl at pH 7.0.

FA in 1.0 M NaCl  
pH 8.0, 092803

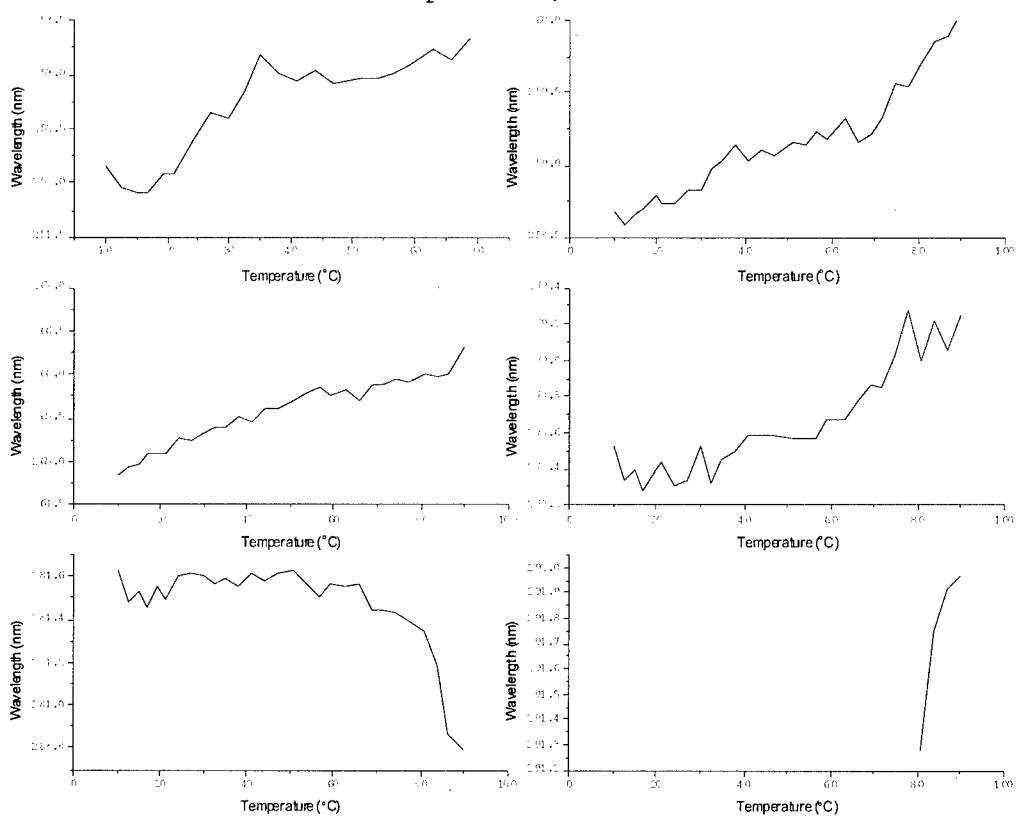


Figure 53. 2<sup>nd</sup> derivative UV peak position as a function of temperature for FA in 1.0 M NaCl at pH 8.0.

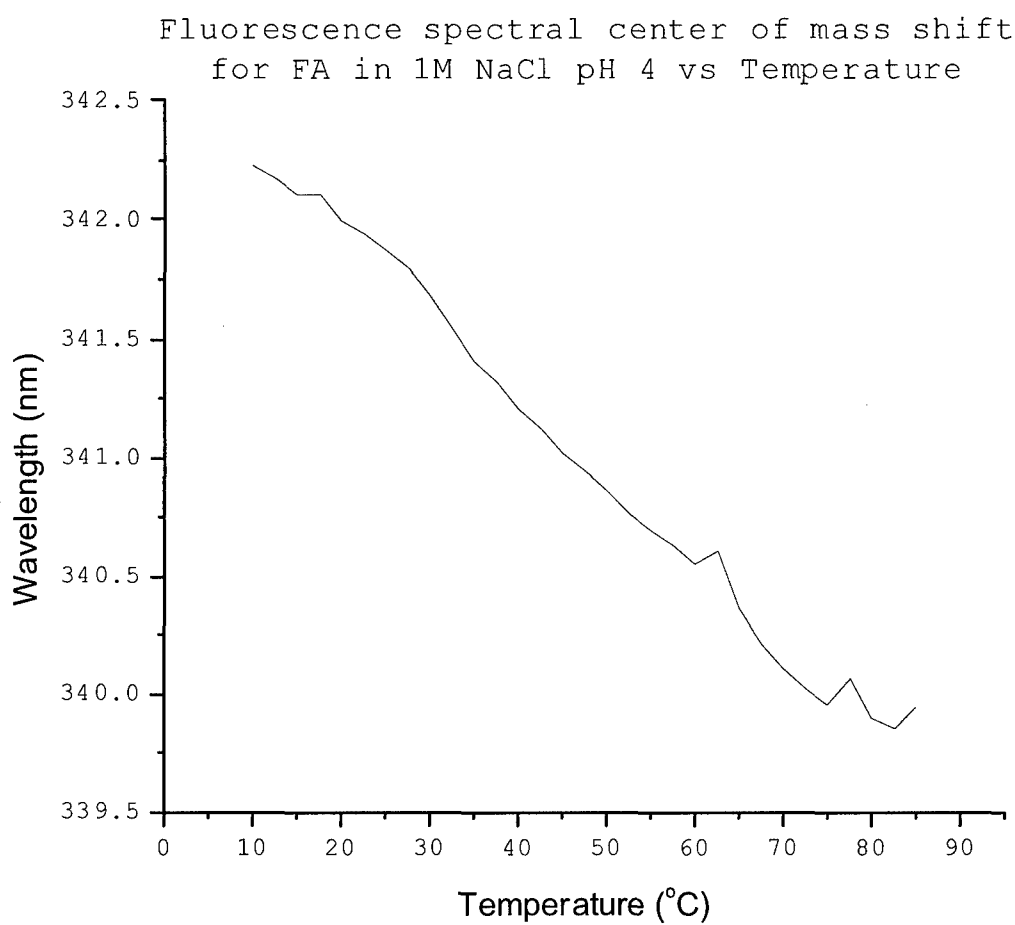


Figure 54. Fluorescence spectral center of mass as a function of temperature for FA in 1M NaCl at pH 4.

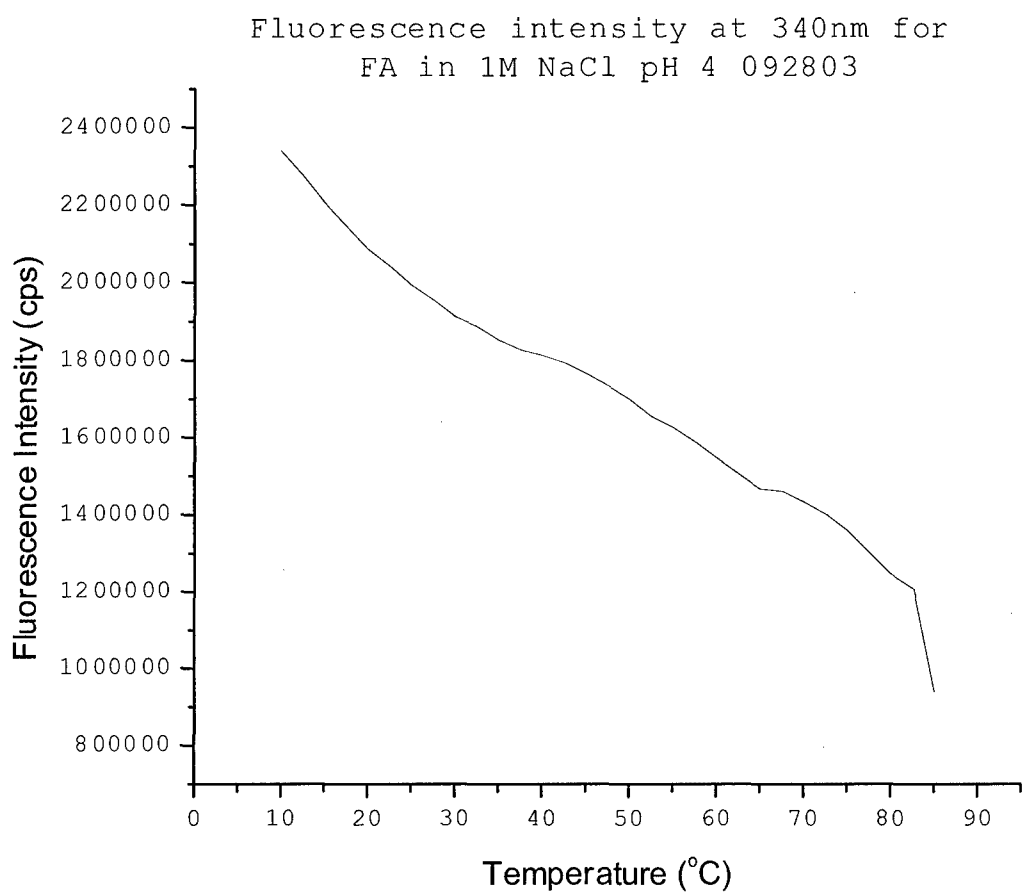


Figure 55. Fluorescence intensity at 340 nm as a function of temperature for FA in 1M NaCl at pH 4.

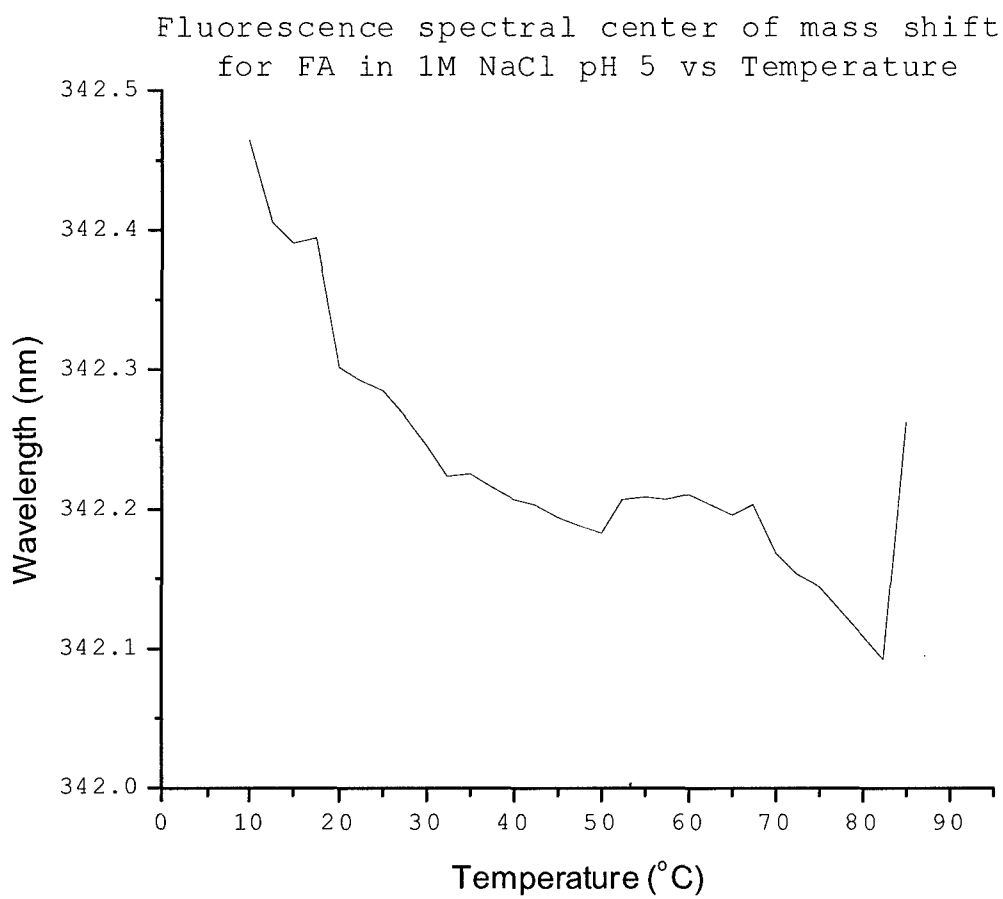


Figure 56. Fluorescence spectral center of mass as a function of temperature for FA in 1M NaCl at pH 5.

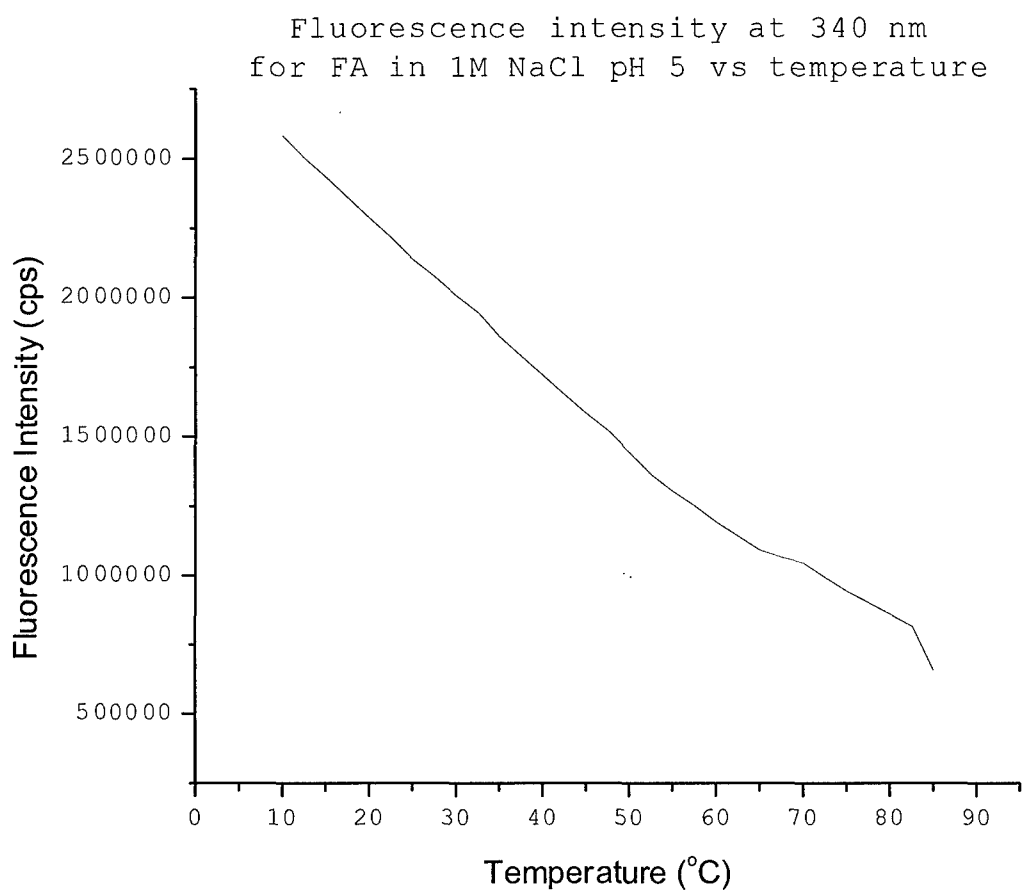


Figure 57. Fluorescence intensity at 340 nm as a function of temperature for FA in 1M NaCl at pH 5.

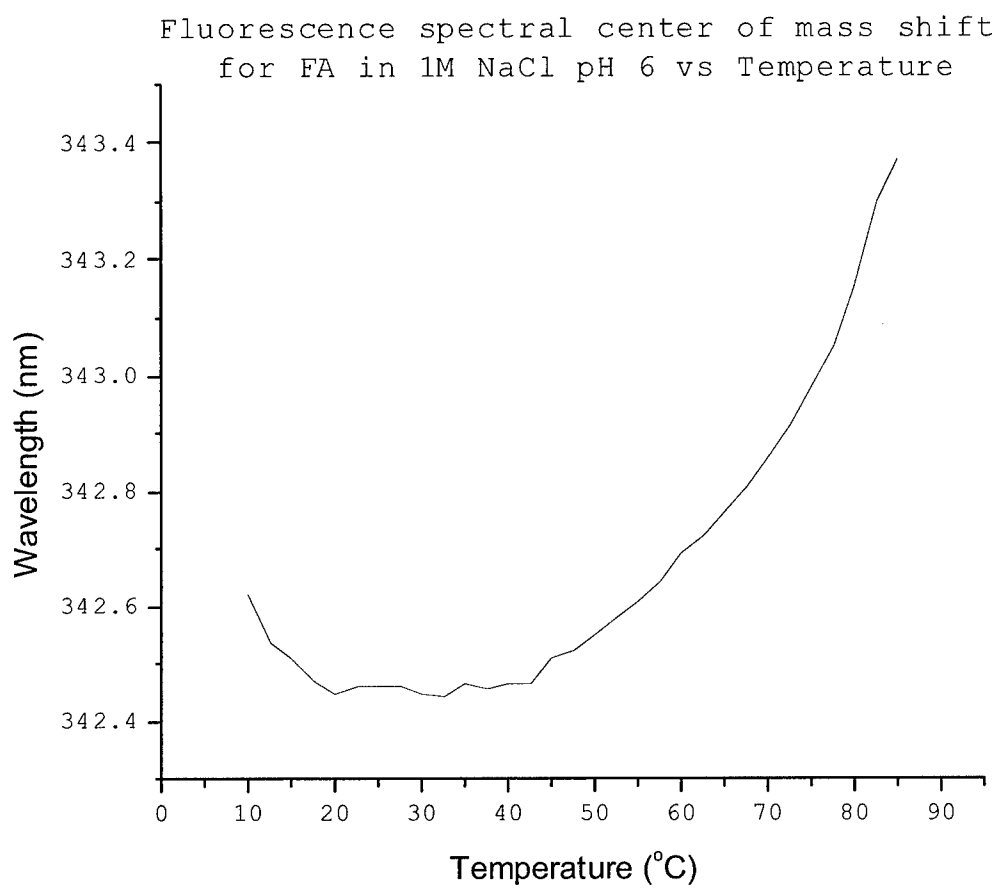


Figure 58. Fluorescence spectral center of mass as a function of temperature for FA in 1M NaCl at pH 6.

Fluorescence intensity at 340 nm  
for FA in 1M NaCl pH 6 vs temperature

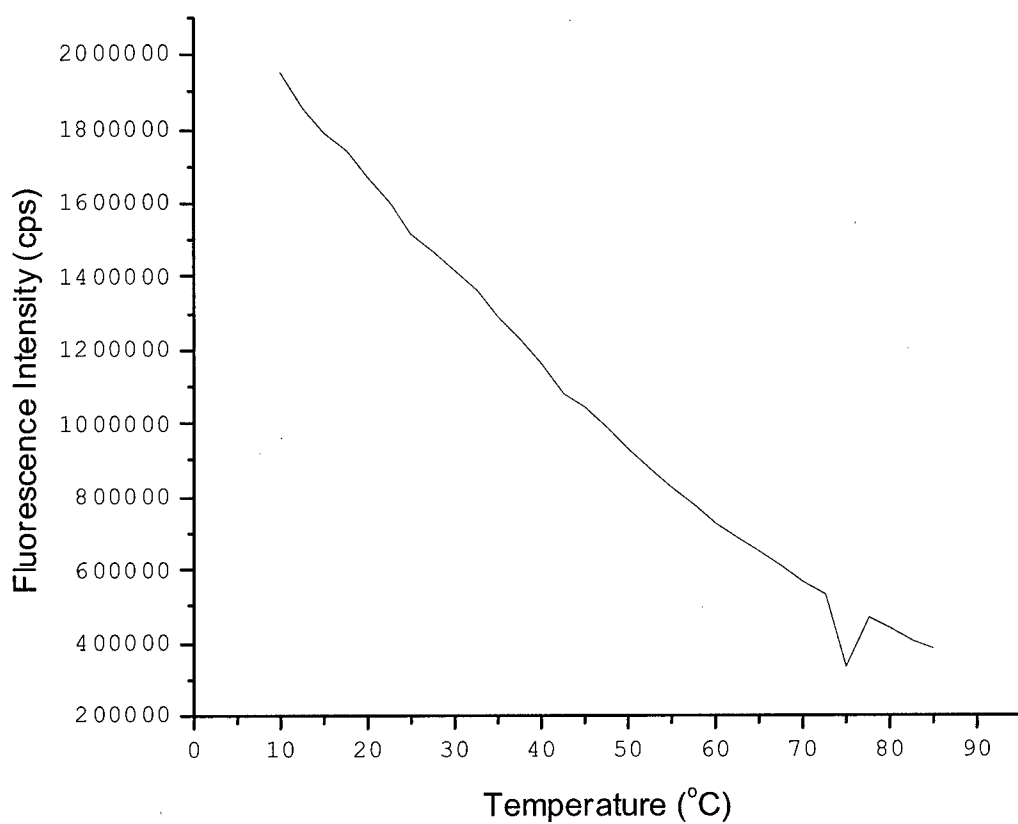


Figure 59. Fluorescence intensity at 340 nm as a function of temperature for FA in 1M NaCl at pH 6.

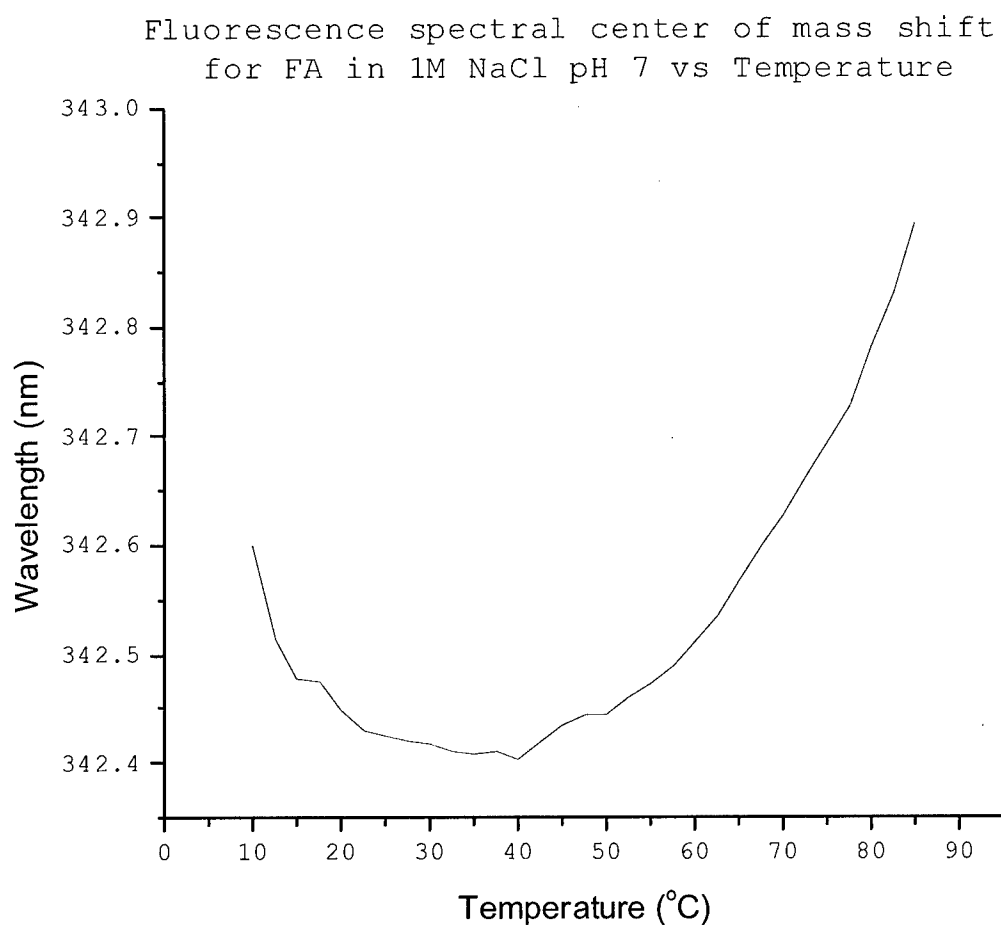


Figure 60. Fluorescence spectral center of mass as a function of temperature for FA in 1M NaCl at pH 7.

Fluorescence intensity at 340nm  
for FA in 1M NaCl pH 7 vs temperature

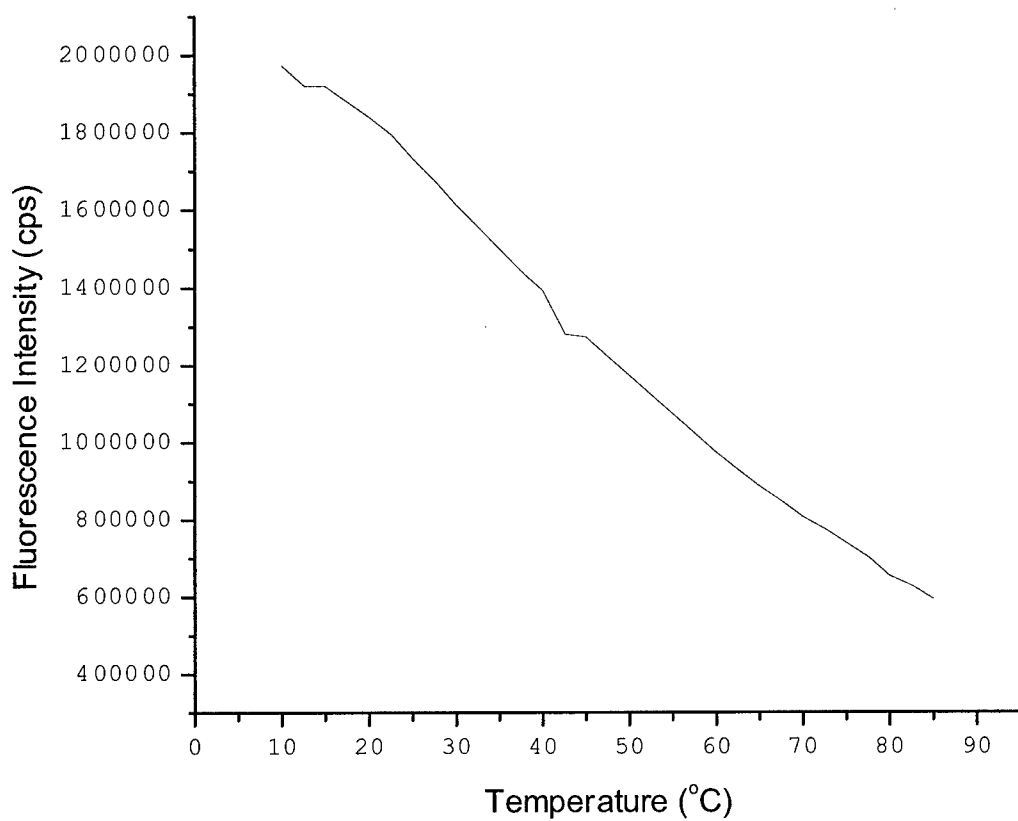


Figure 61. Fluorescence intensity at 340 nm as a function of temperature for FA in 1M NaCl at pH 7.

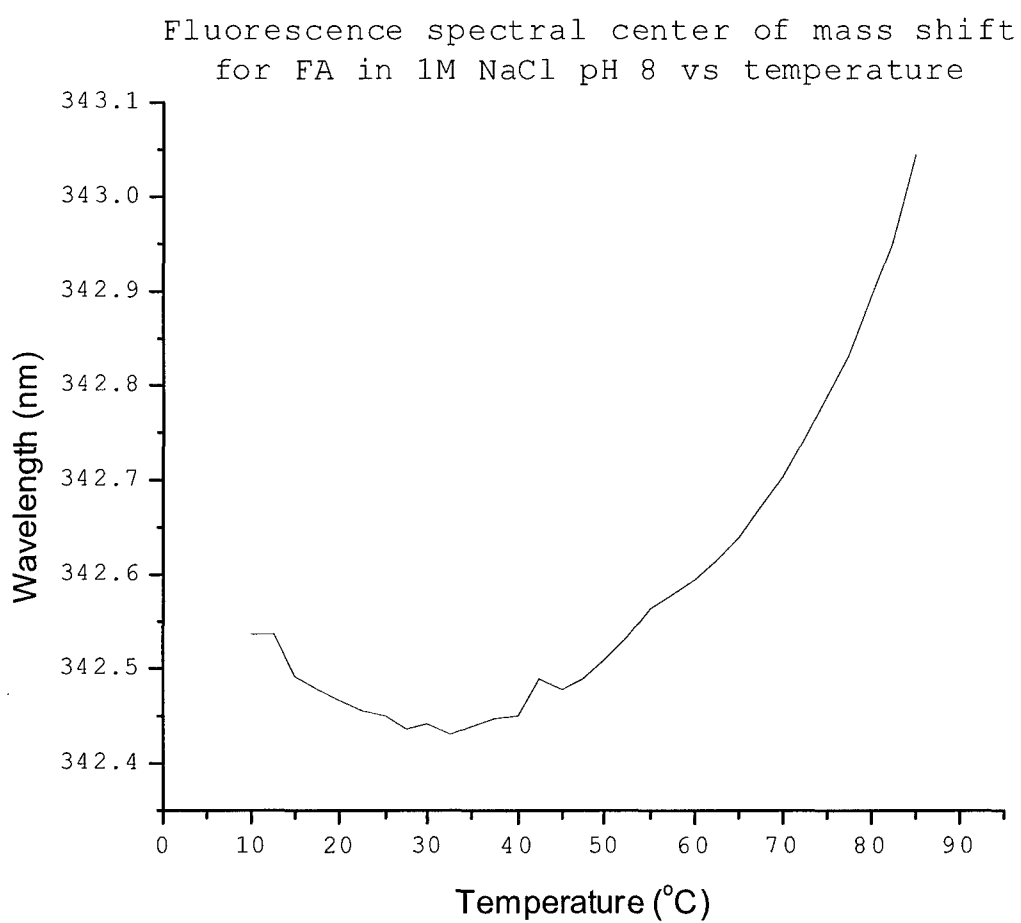


Figure 62. Fluorescence spectral center of mass as a function of temperature for FA in 1M NaCl at pH 8.

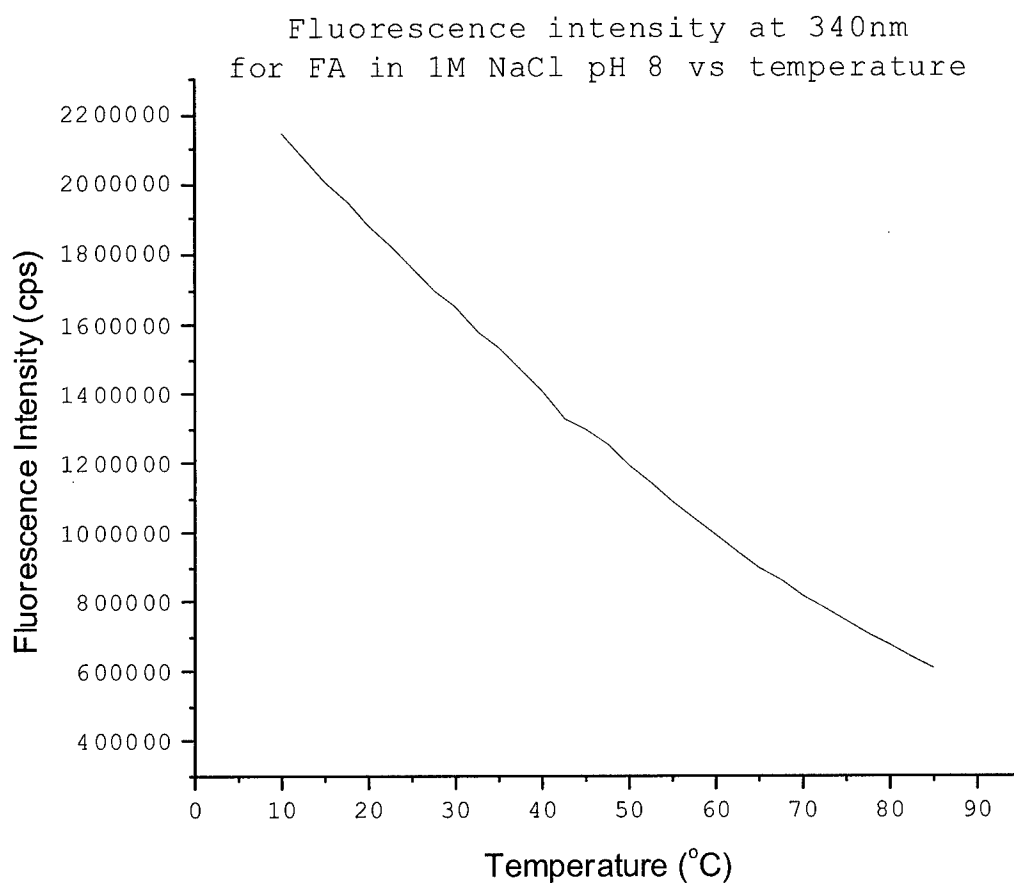
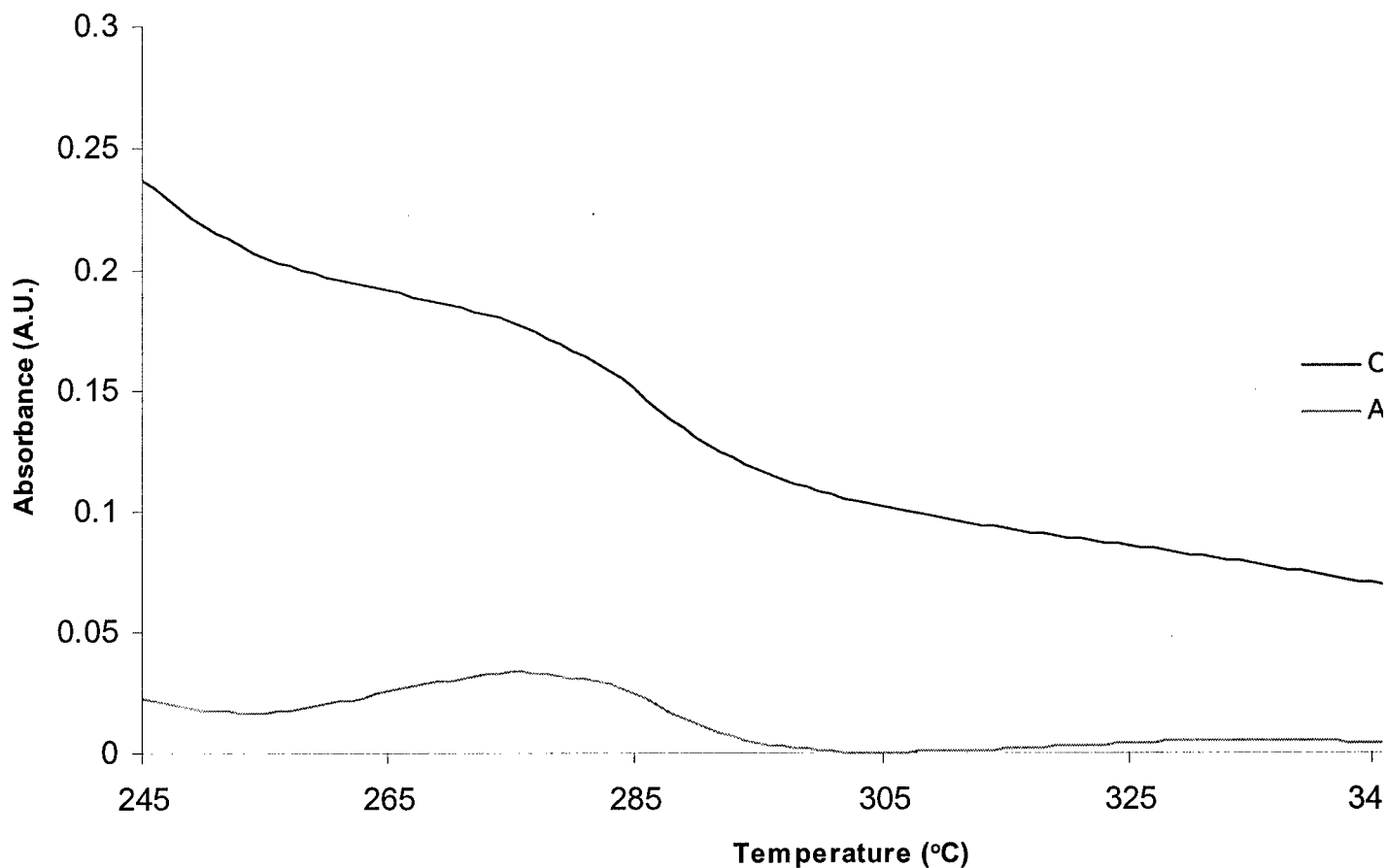


Figure 63. Fluorescence intensity at 340 nm as a function of temperature for FA in 1M NaCl at pH 8.

**UV Absorption Spectroscopy of Reverse Construct FA (as received) 041904**



**Figure 64.** Optical density and light scattering-corrected absorbance spectra of rFA.

**Reverse Fusion Antigen**  
**Optical density at 350 nm as a function of temperature**

041904

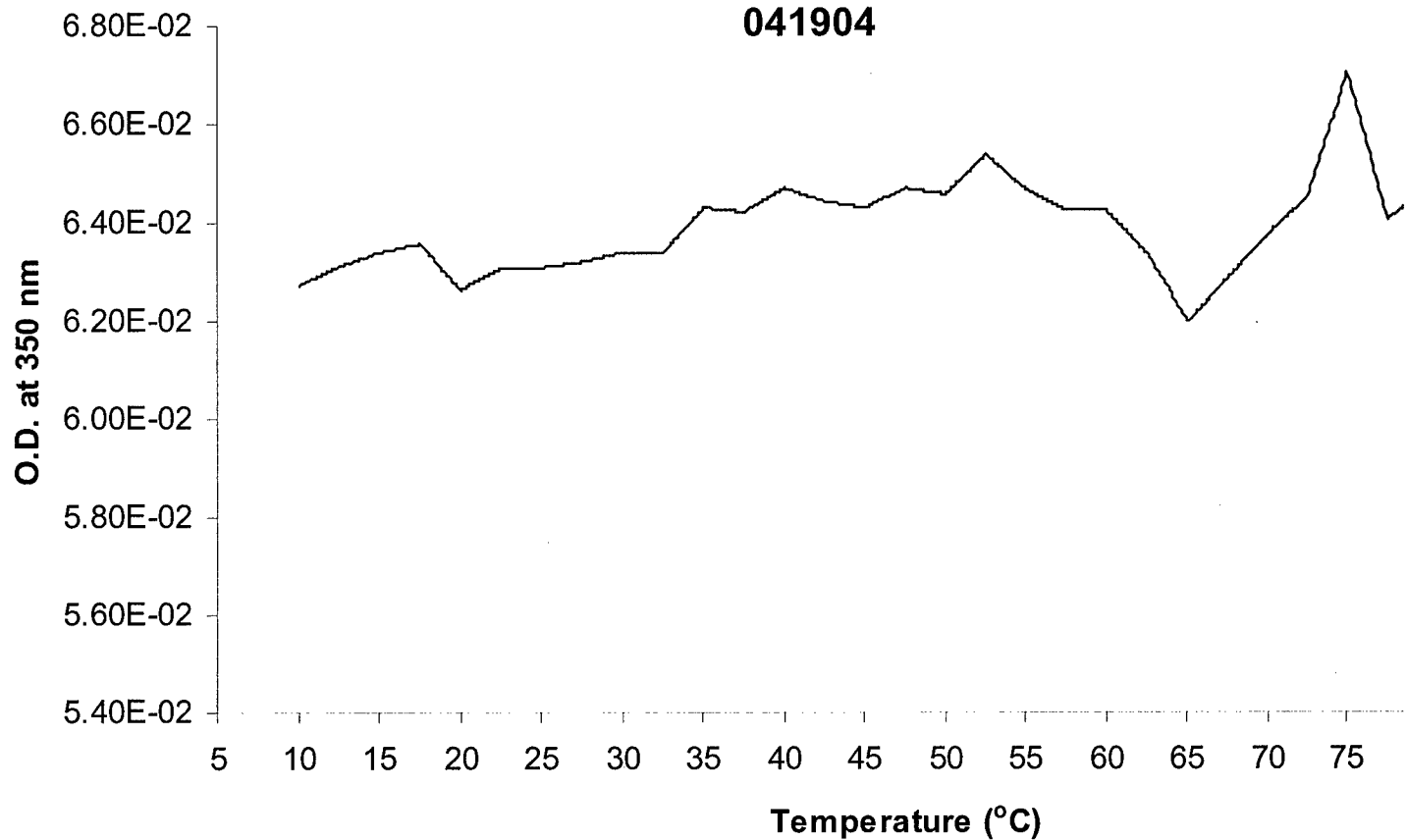


**Figure 65.** rFA optical density at 350 nm as a function of temperature.

Reverse Fusion Antigen  
5mM citrate, 5mM phosphate, pH 7. 041904.

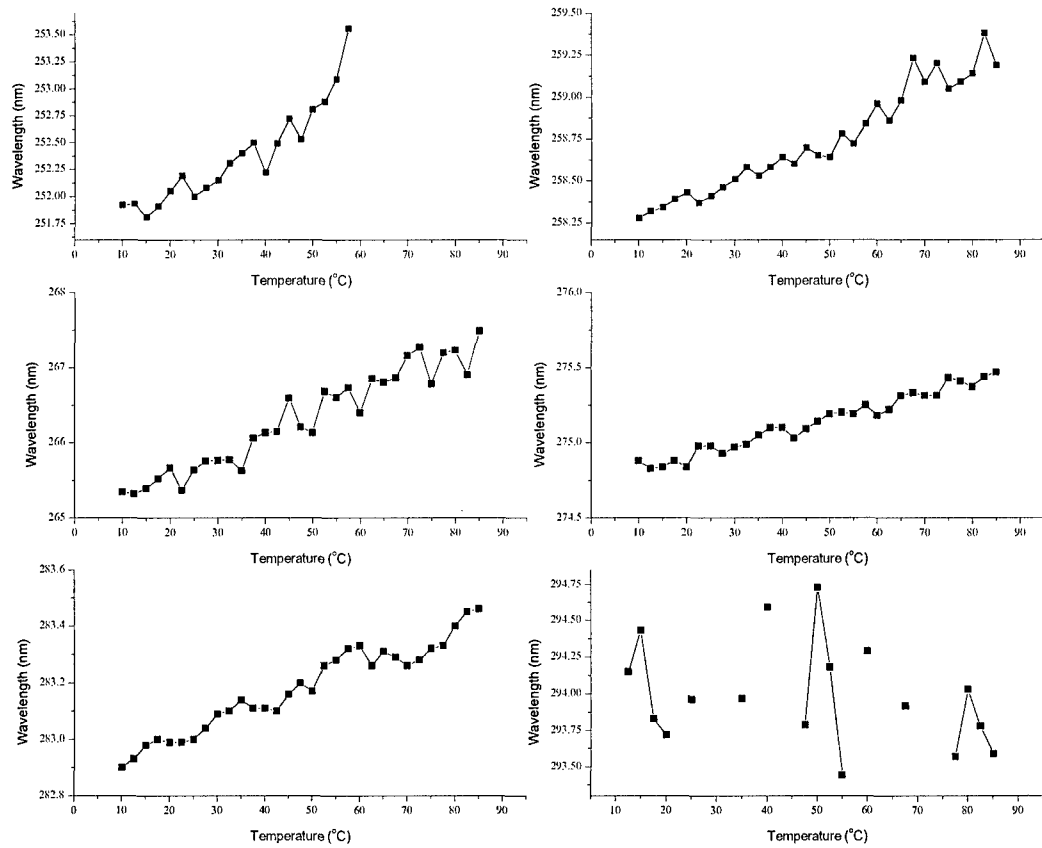


**Figure 66.** 2<sup>nd</sup> derivative UV peak position plots versus temperature of rFA.

## Intrinsic fluorescence spectra of reverse fusion antigen

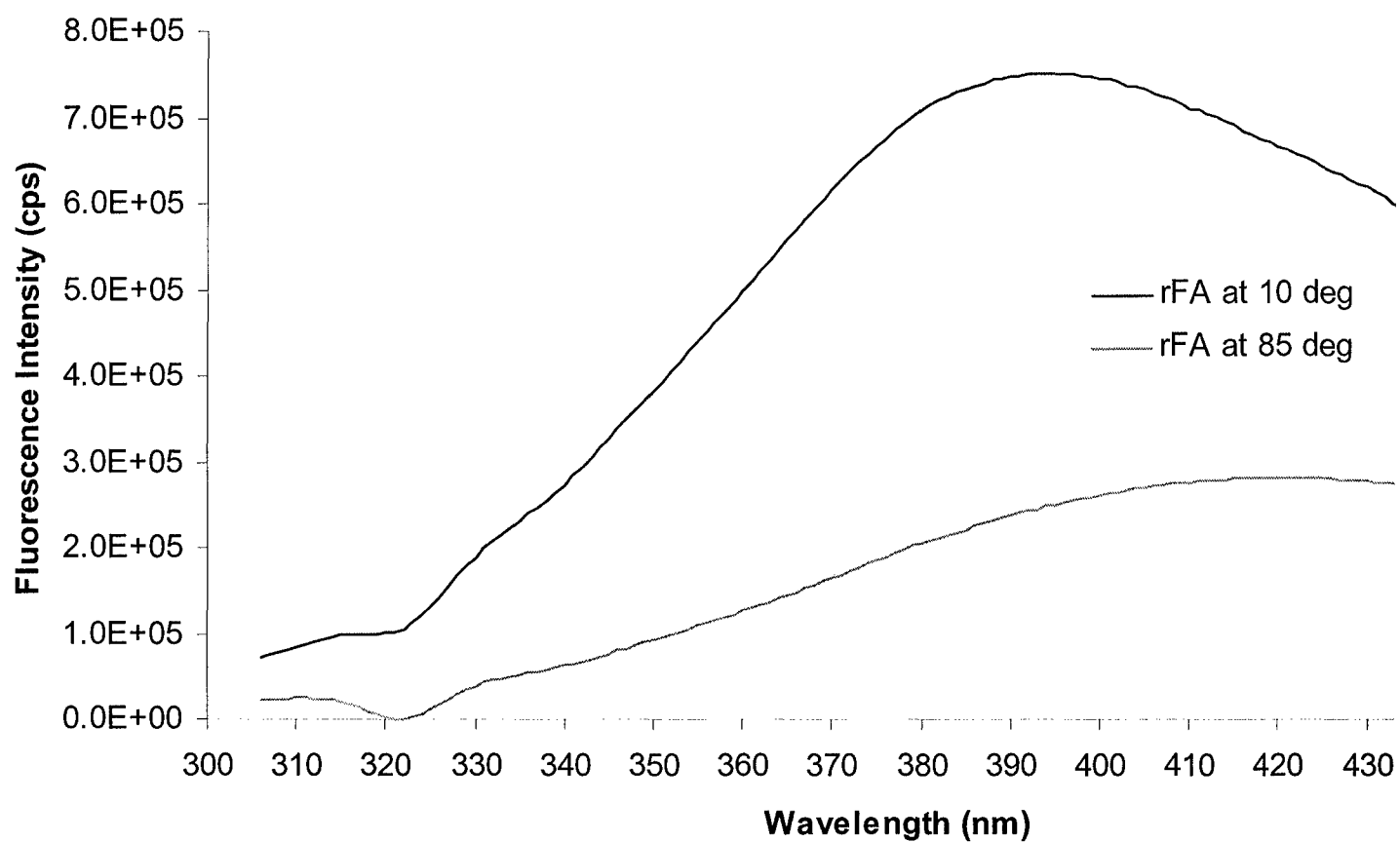


**Figure 67.** rFA intrinsic fluorescence spectra at 10 and 85° C.

**Reverse fusion antigen**  
 **$\lambda_{\text{max}}$  as a function of temperature**

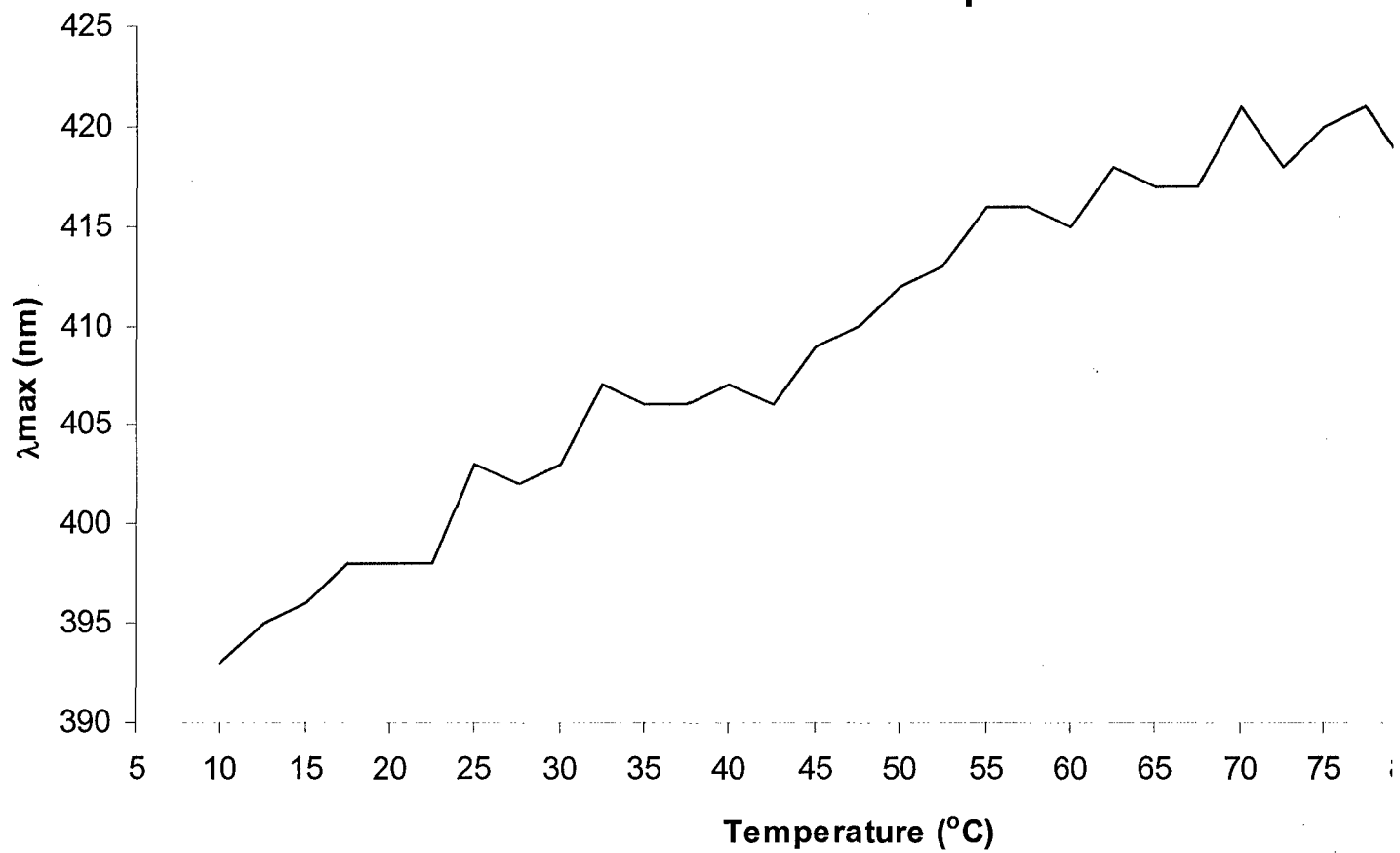


**Figure 68.** rFA intrinsic fluorescence spectroscopy peak position ( $\lambda_{\text{max}}$ ) versus temperature.

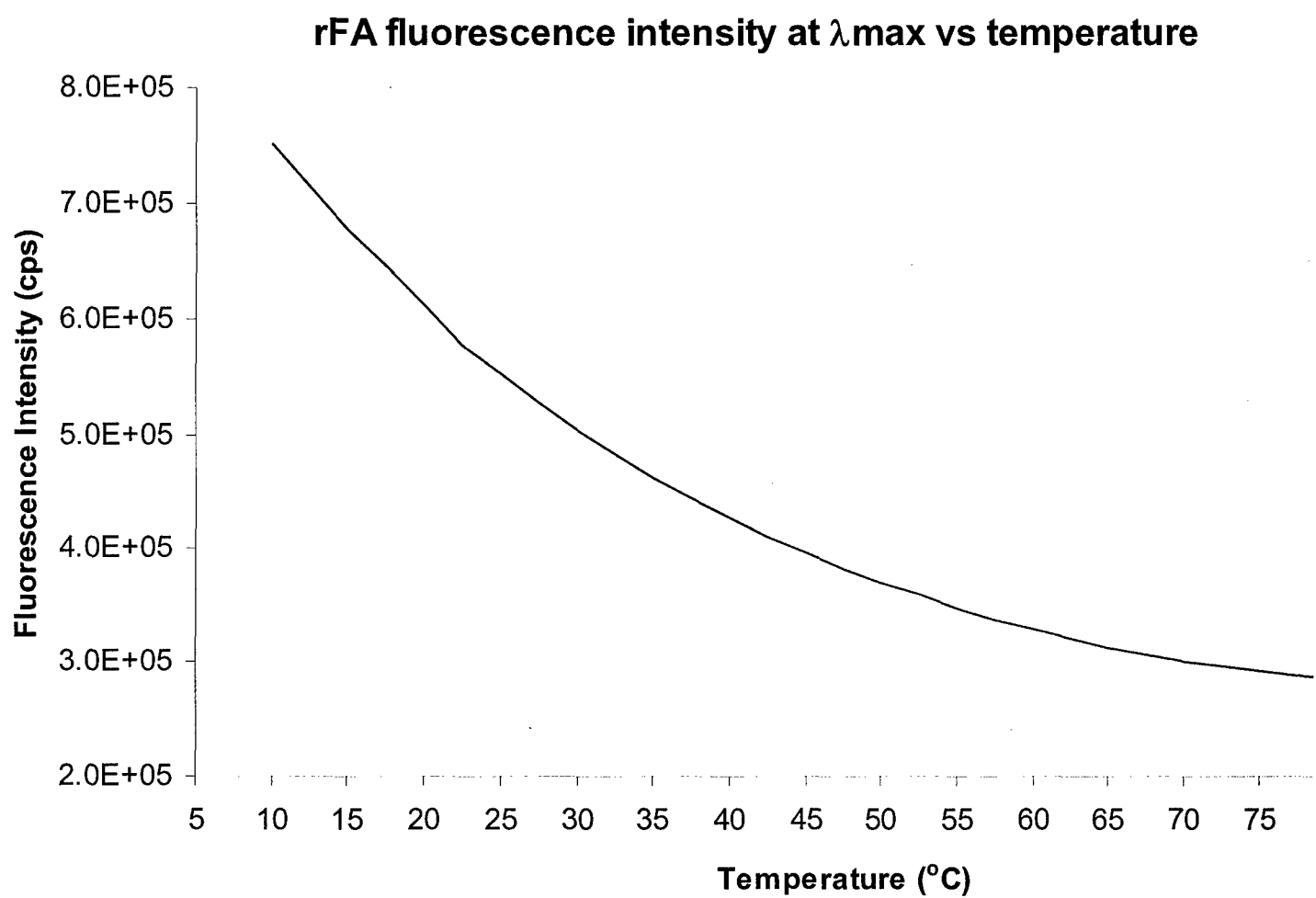


**Figure 69.** rFA intrinsic fluorescence intensity at  $\lambda_{\max}$  versus temperature.

CD spectra of reverse fusion antigen  
5mM citrate, 5mM phosphate, pH 7  
042204

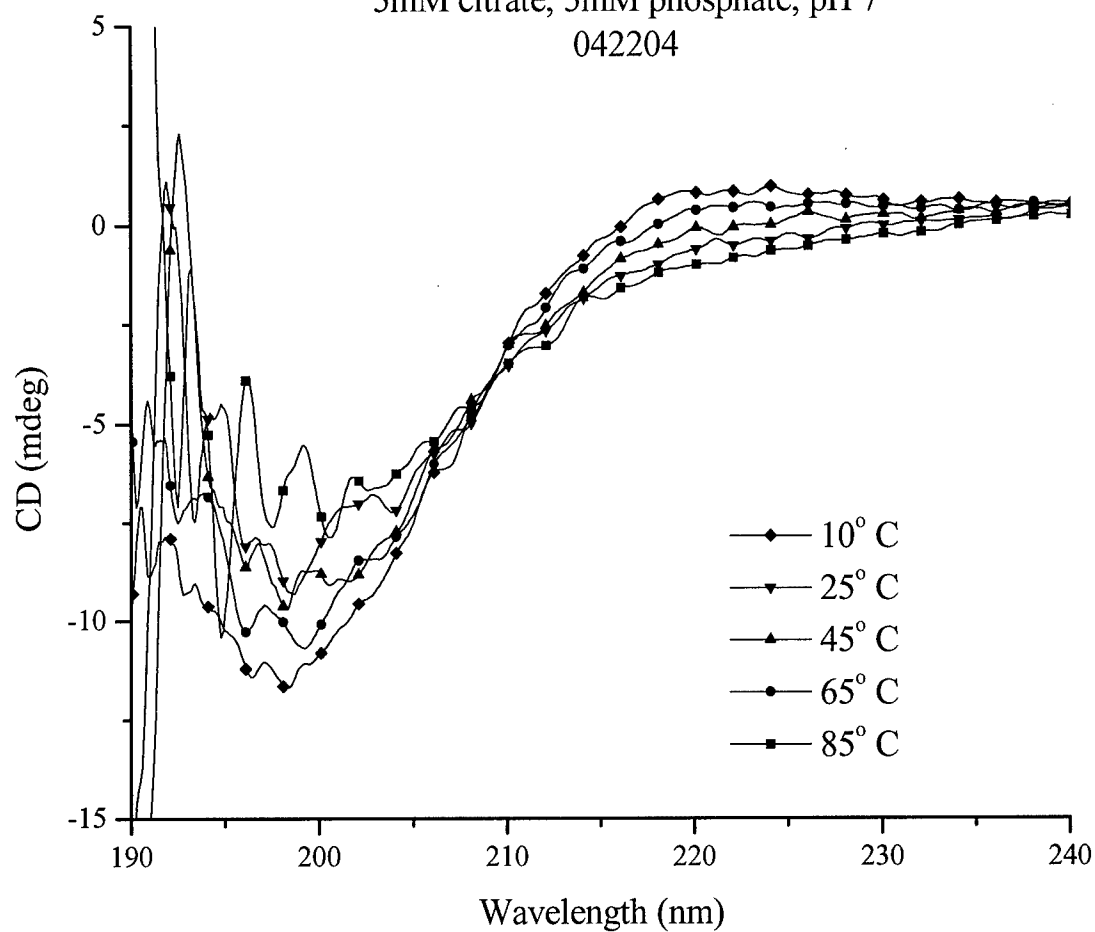


**Figure 70.** rFA CD spectra.

**CD at 200 nm of reverse Fusion Antigen  
042204**

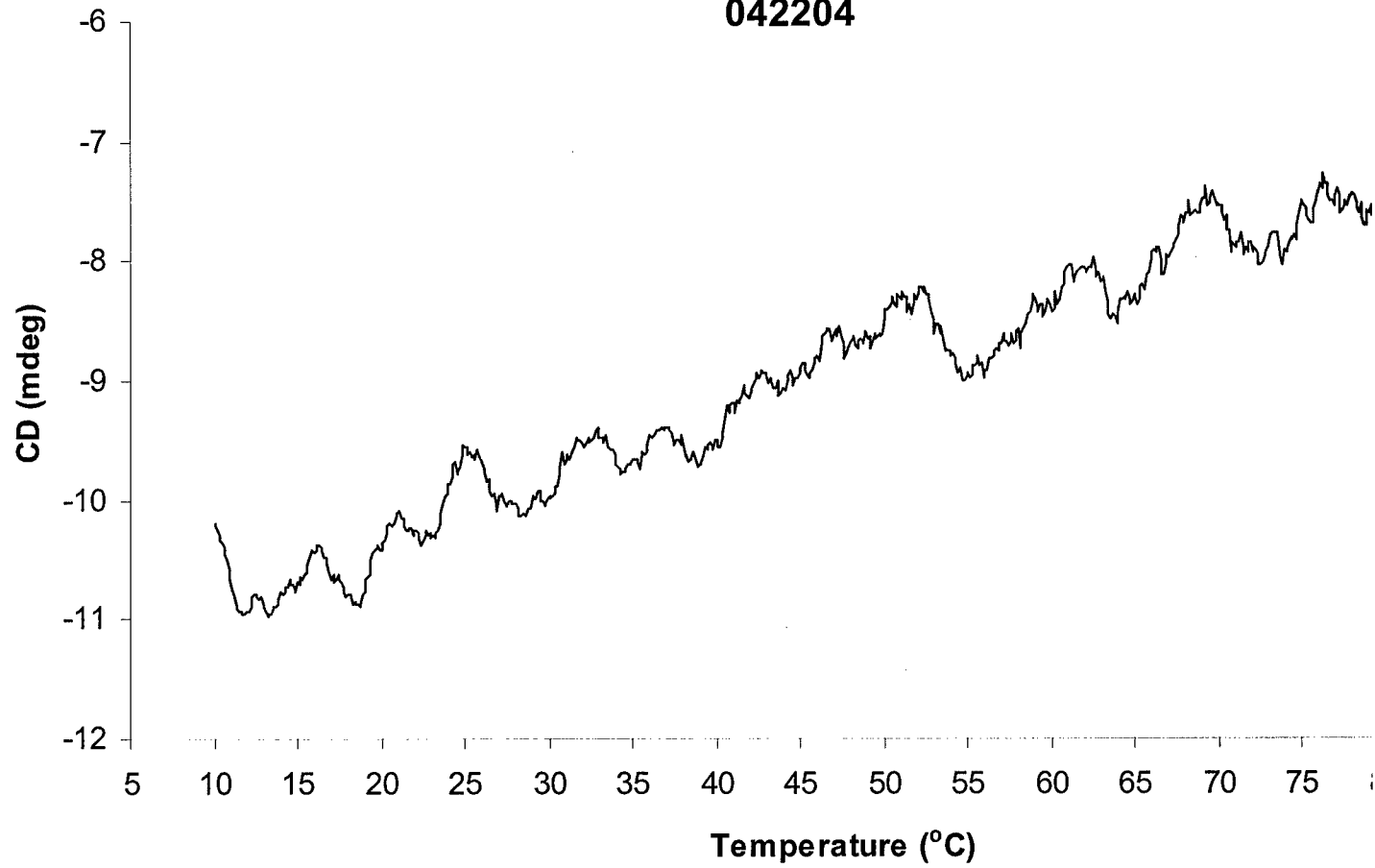


**Figure 71.** rFA CD at 200 nm as a function of temperature.

## **Adenovirus type 5 (Ad5)**

To characterize Ad5 obtained from Merck, various biophysical techniques (e.g. high-resolution second derivative UV, intrinsic and extrinsic fluorescence, CD spectroscopies) as function of pH (3 to 8) over the temperature range 10 to 85°C were employed.

By plotting peak positions of 2<sup>nd</sup> derivative UV spectroscopy data versus temperature, it is possible to assess the tertiary structural stability of the viral particles by monitoring the average environment of aromatic amino acids in the viral particles and comparing the transition temperatures as a function of pH. Initial data obtained by 2<sup>nd</sup> derivative UV absorption as well as the optical density at 350nm suggest that Ad5 is more stable at higher pH. More specifically, 2<sup>nd</sup> derivative UV analysis reveals that transitions occur at higher temperatures for Ad5 in buffer at relatively high pH values suggesting decreased stability at low pH (Figures 72-77 and Table 4). Additionally, the optical density at 10°C and 350nm is maximal for Ad5 at pH 3 and 4 with starting values of 1.0 and 1.1, respectively, also suggesting increased lability and significant aggregation at lower pH (Figures 78-84). Decreases in optical density near 40°C are observed at all pH values. This decrease in scattered light is followed by an increase in the optical density at higher temperatures (near 77°) and is probably a result of aggregation of the viral proteins. On the other hand, decreases in the optical density at even higher temperatures (above 80°C) may be a consequence of massive aggregation and settling of the precipitates formed. Previous studies of Ad5 employing dynamic light scattering revealed an increase in the effective hydrodynamic diameter near 40°C with a concomitant decrease in the quantity of light scattered. Although more data are needed to determine the precise reason for this phenomenon, a change in the refractive index of the particles to more closely match that of the solvent could theoretically account for such observations.

*Intrinsic fluorescence spectroscopy* was also employed to evaluate the tertiary structural stability of Ad5 at pH values 3-8 over the temperature range 10-85°C (Figures 85-90). In agreement with 2<sup>nd</sup> derivative UV spectroscopy data, tertiary structural transitions detected by intrinsic fluorescence spectroscopy suggest that Ad5 is more stable at the higher pH values studied. Shifts in peak positions to higher wavelengths occur near 37 and 40°C for Ad5 at pH values 7 and 8

(Figures 89 and 90), respectively, suggesting an average increase in the solvent accessibility of tryptophan, tyrosine, and phenylalanine residues. A blue shift (shift to lower wavelengths) in the intrinsic fluorescence peak position is observed at pH 3 near 47°C and pH 5 near 55°C (Figures 85 and 87); however these transitions are most likely a result of the domination of the fluorescence spectrum by light scattering following aggregation and precipitation of adenoviral proteins.

*Extrinsic Fluorescence Studies.* TOTO-1 is a polynucleotide intercalating dye that exhibits a significant fluorescence enhancement upon binding (up to 1000-fold). This dye was therefore employed to investigate capsid integrity (quaternary structural stability) over the pH range 5-8 as a function of temperature. Ad5 stability was not examined at pH values 3 and 4 since TOTO-1 is not functional at lower pH. Ad5 displays a significant enhancement in TOTO-1 fluorescence near 42°C at pH values 5-7 suggesting that structural transitions occur which begin to compromise capsid integrity near this temperature (Figures 91-93). At pH 8, however, Ad5 undergoes a more gradual “loosening” of the capsid beginning near 25°C with a maximum TOTO-1 fluorescence observed near 45°C (Figure 94). The highest temperature at which TOTO-1 has a maximum fluorescence over the pH range studied is 50°C at pH 7 suggesting that TOTO-1 does not gain complete access to the viral DNA until 50°C. On the other hand, the maximum fluorescence of TOTO-1 and, thus, the complete DNA intercalation of TOTO-1, occur at lower temperatures for the other pH values studied. These data suggest Ad5 quaternary structure is most stable near neutral pH.

*Circular Dichroism Spectroscopy (CD).* CD was employed as a function of temperature to assess the secondary structural stability of Ad5 over the pH range 3-8. Histidine (His), one component of the Ad5 buffer, absorbs strongly in the region of interest. Since it is known that histidine is an antioxidant that confers an insignificant stabilizing effect to physical structure of Ad5, the His was removed by dialysis at the appropriate pH prior to obtaining CD measurements.

The CD data suggests that the secondary structure of Ad5 is significantly perturbed at low pH since the CD signal is near zero from ~205-225 nm (Figs. 95 and 96). The CD spectra at higher pH values suggest that Ad5 has a mixture of alpha helix and beta sheet secondary structure (bottom of Figs. 97-100). At pH 3, the CD signal at 208 nm remains relatively constant from 10 to

approximately 45° C. An increase in the intensity at 208 nm is observed from ~57-72° C followed by a dramatic decrease in the intensity above 75° C (bottom Fig. 95). Analysis of the Ad5 spectrum at 90° C reveals a negative peak near 208 nm which suggests that the Ad5 proteins have adopted a “cross beta-sheet” structure (top Fig. 95, dashed line). Although these types of secondary structures typically have minima around 202-206 nm, it is possible that the peak is shifted as a result of absorption flattening caused by large Ad5 protein aggregates. A similar type of phenomenon is observed at pH 4 although the increase in CD intensity from ~57-72° C that occurred at pH 3 is not observed (Fig. 96).

A slight loss in secondary structure is observed at pH 5 over the temperature range 10-40° C (Fig. 97, top). This gradual loss is followed by two distinct transitions: one near 45° C and the second above 70° C. These two transitions are also observed in the CD data at other pH values and have also been observed in other studies we have conducted (extrinsic fluorescence and second derivative UV spectroscopies). These structural changes in Ad5 are thought to be a result of an initial loosening of the capsid (near 45° C) which is followed by complete disruption of the proteinaceous viral coat (near 70° C). The pH 5 Ad5 CD spectrum at 90° C suggests that a significant percentage (~66%) of the CD intensity is lost due to thermal perturbation (bottom Fig. 97). Similar losses in Ad5 secondary structure occur due to thermal stress at all higher pH values studied (Figs. 98-100).

*Dynamic Light Scattering (DLS).* A significant stabilizing effect on the tertiary and quaternary structure of Ad5 by 1M NaCl has been previously observed in our lab. Thus, DLS was employed at low and high concentrations of NaCl to assess the quaternary structural stability of Ad5. Although 1M NaCl fails to prevent aggregation and structural perturbation at pH 3 (Fig. 101), a significant stabilizing effect on the quaternary structure of Ad5 is observed at all higher pH values (Figs. 102-106). The most prominent effect is observed at pH 5, where a significant change in the quaternary structure of Ad5 is not observed until 65° C in 1 M NaCl. In comparison, significant aggregation of Ad5 is observed when in the presence of 75 mM NaCl suggesting that 1M NaCl

prevents aggregation as well as thermophysically stabilizes the Ad5 virions. A stabilizing effect of at least 10° C is observed at other pH values with pH5 showing the best quaternary structural stability (*i.e.*, the transition temperature is the highest).

A manuscript entitled, "Effect of pH and ionic strength on the physical stability of adenovirus type 5" is accepted by Journal of Pharmaceutical Sciences (see appendices).

Ad5 pH 3 010804

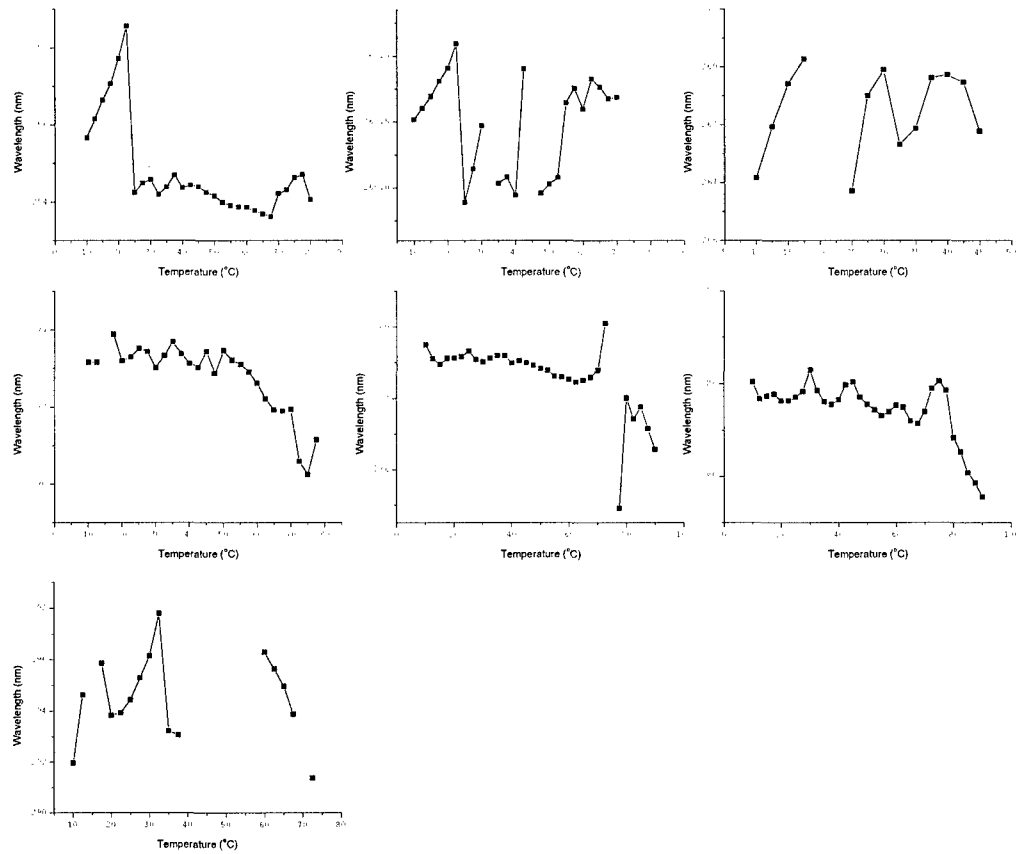


Figure 72. 2<sup>nd</sup> derivative UV peak position as a function of temperature for Ad5 pH 3.0.

Ad5 pH 4 010804

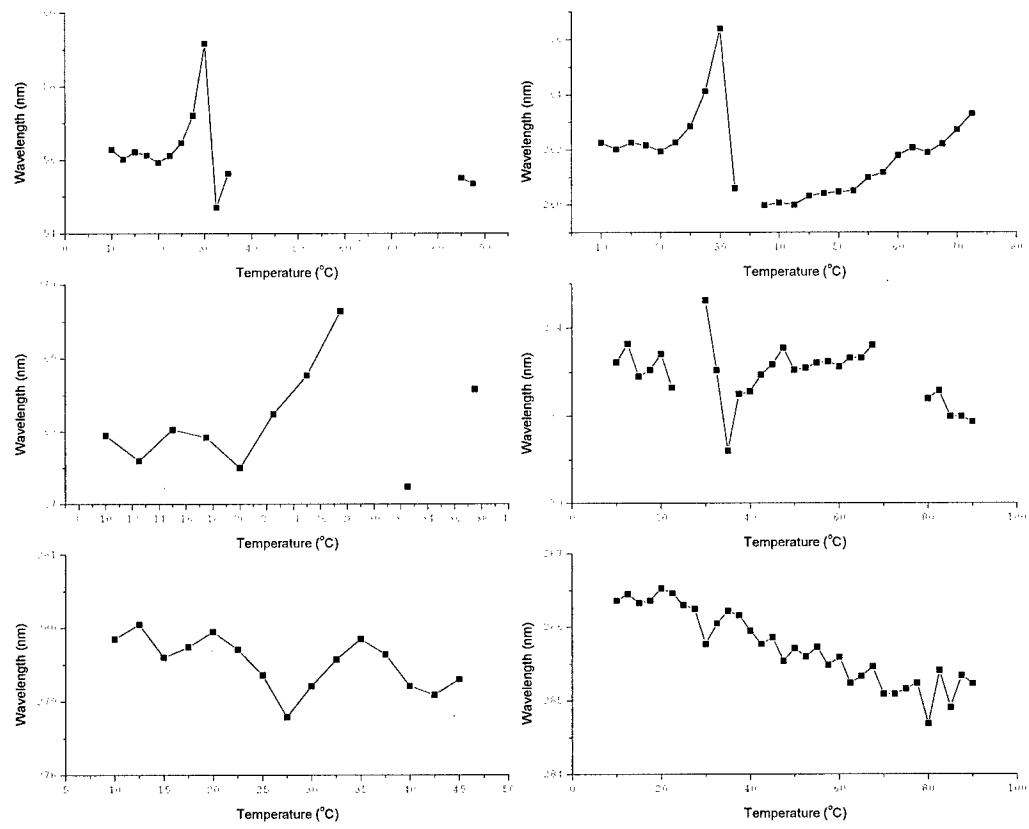


Figure 73. 2<sup>nd</sup> derivative UV peak position as a function of temperature for Ad5 pH 4.0.

Ad5 pH 5 011304 (2nd run)

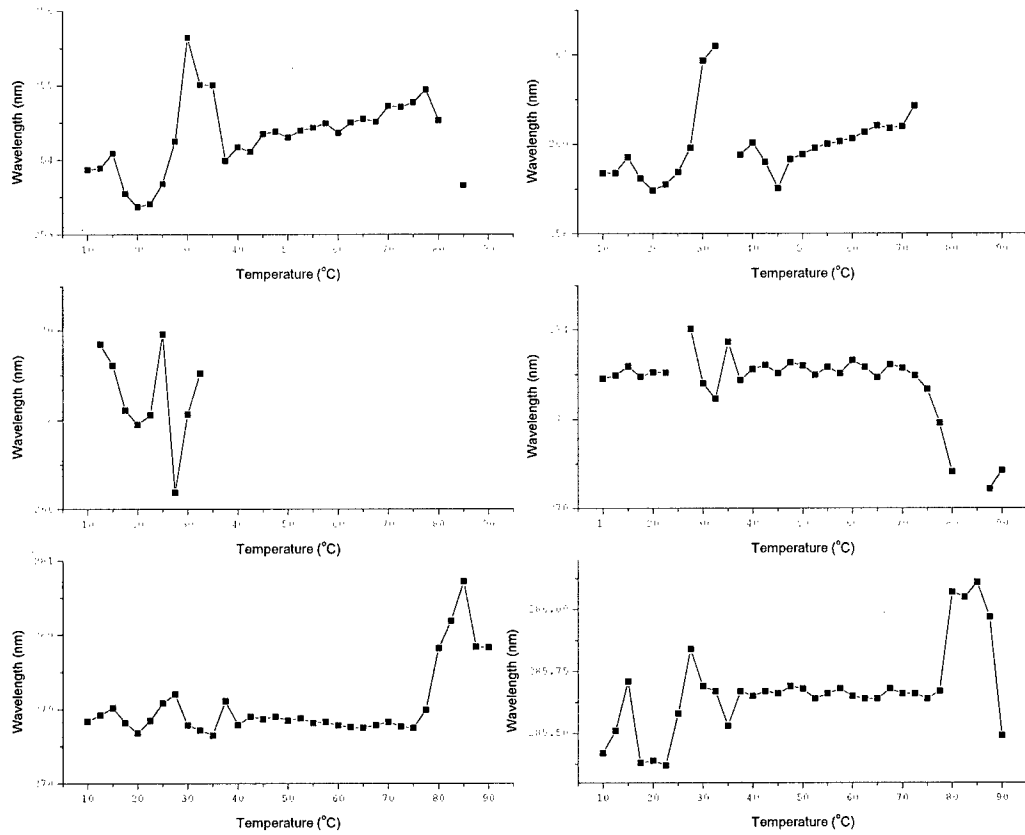


Figure 74. 2<sup>nd</sup> derivative UV peak position as a function of temperature for Ad5 pH 5.0.

Ad5 pH 6 010604

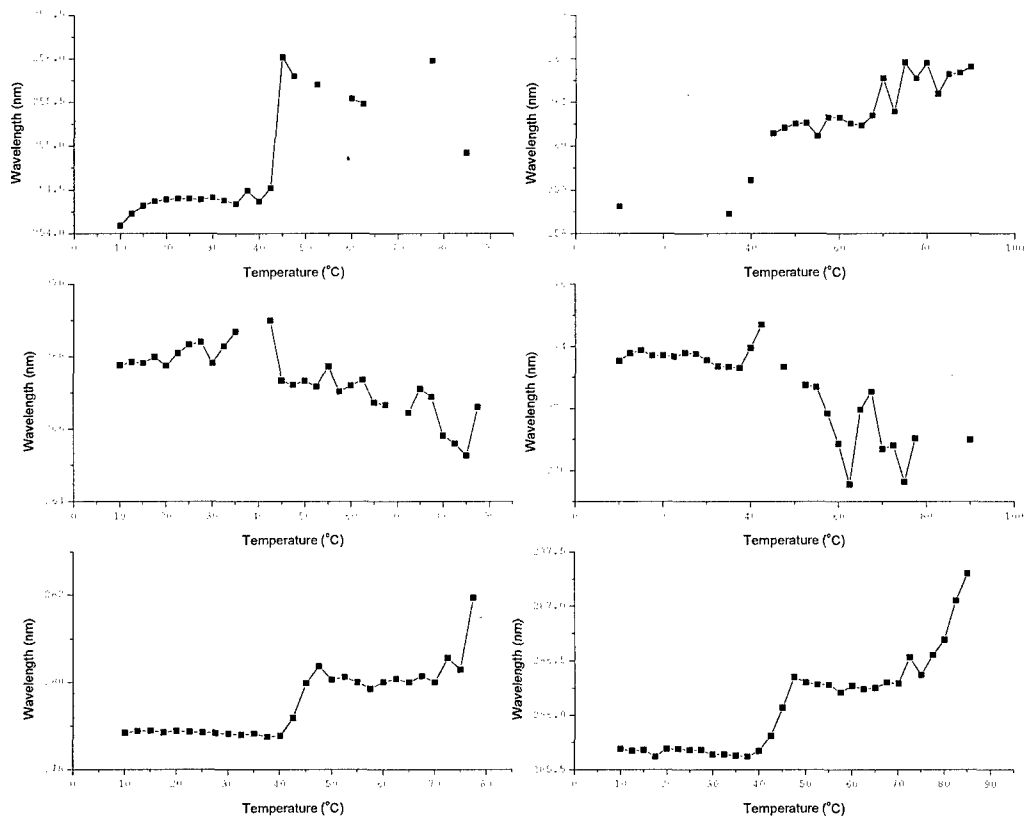


Figure 75. 2<sup>nd</sup> derivative UV peak position as a function of temperature for Ad5 pH 6.0.

Ad5 pH 7 010504

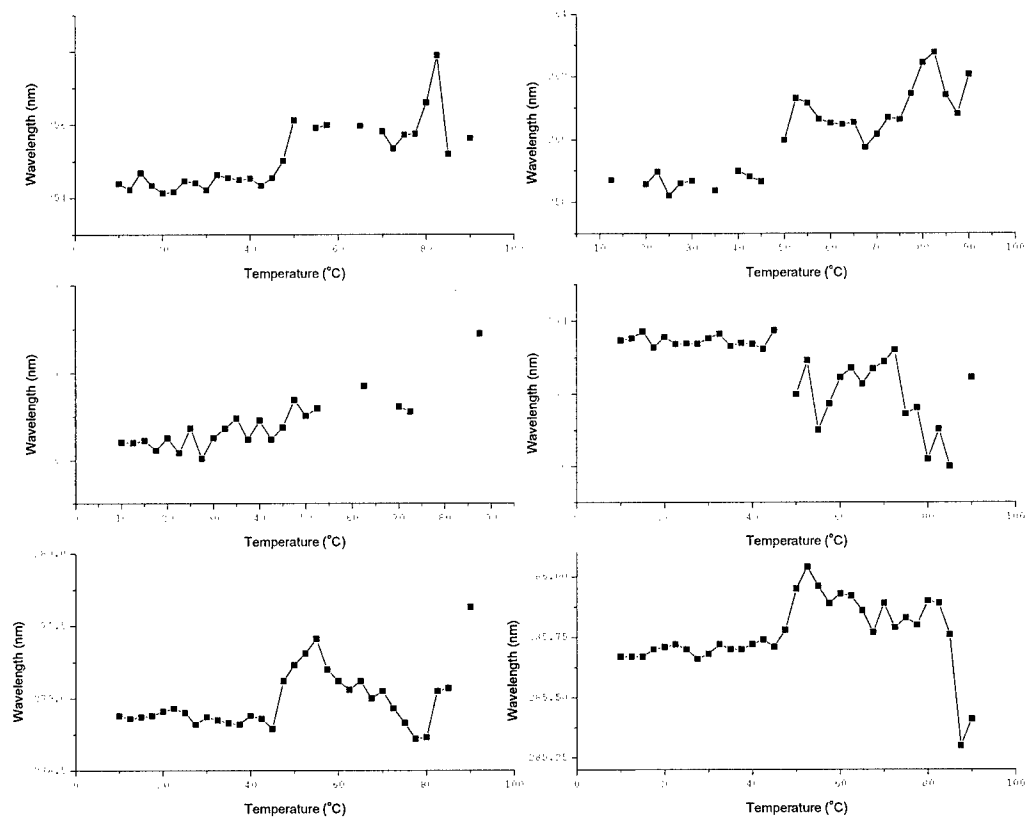


Figure 76. 2<sup>nd</sup> derivative UV peak position as a function of temperature for Ad5 pH 7.0.

Ad5 pH 8 011204 (2nd run)

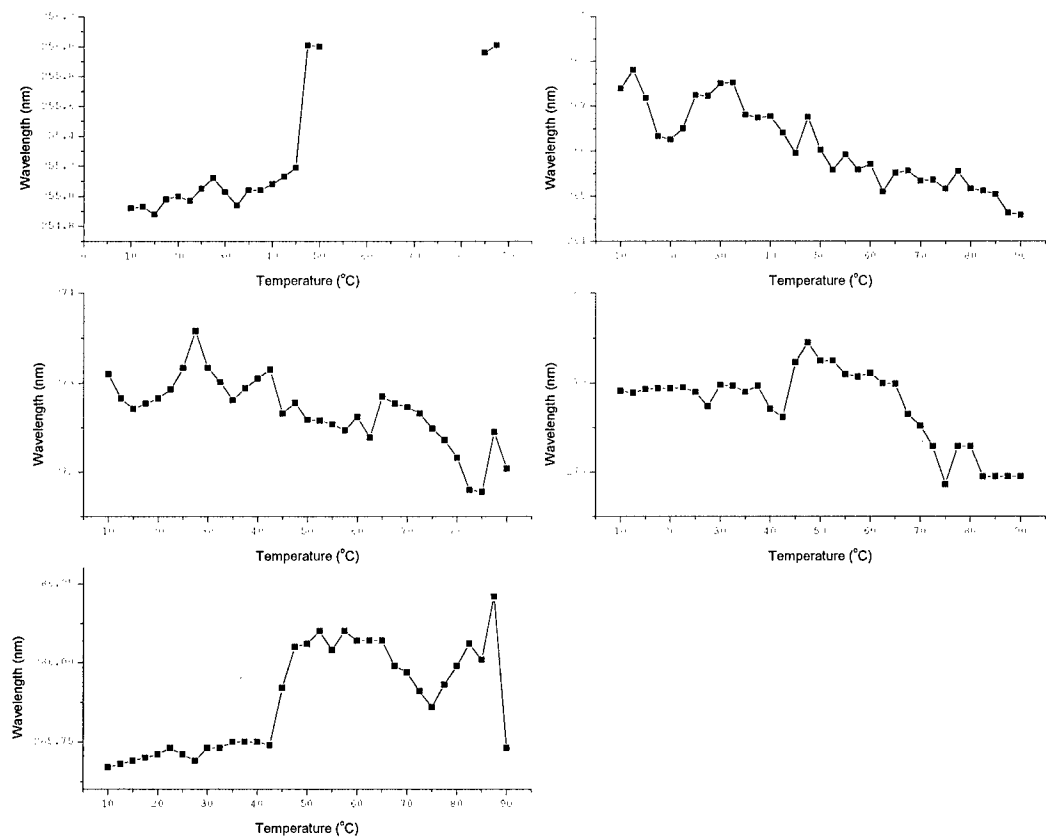


Figure 77. 2<sup>nd</sup> derivative UV peak position as a function of temperature for Ad5 pH 8.0.

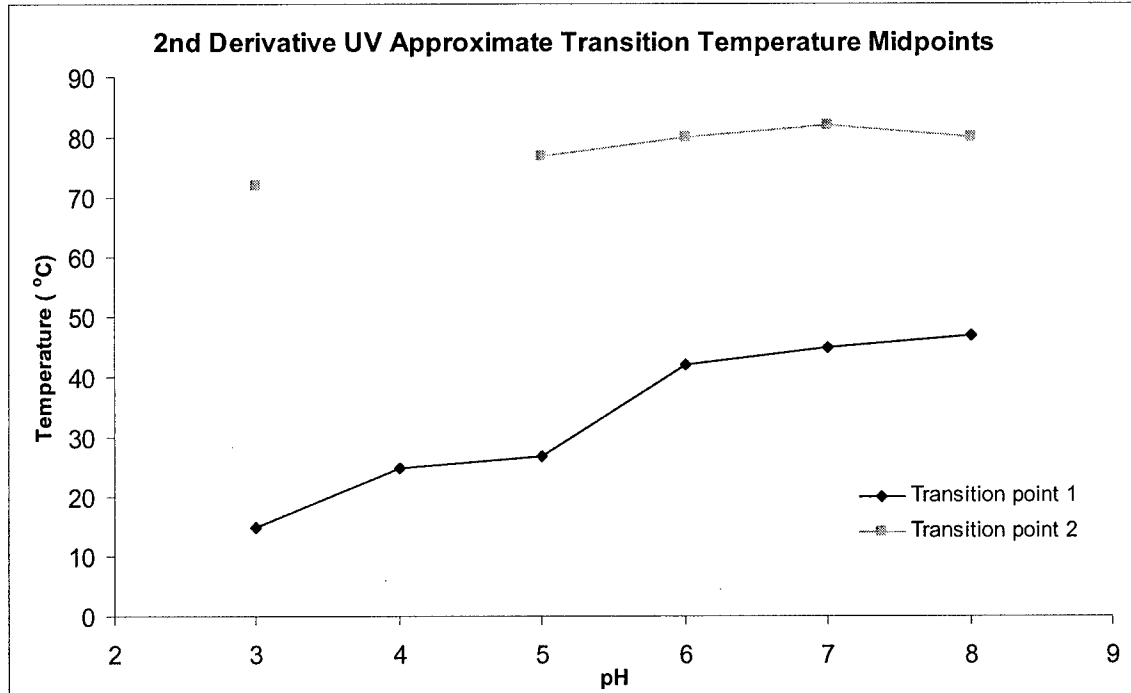


Figure 78. Approximate 2<sup>nd</sup> derivative UV spectroscopy transition temperature midpoints as a function of pH (a second transition midpoint was not assigned at pH 4).

Ad 5 pH 3 010804

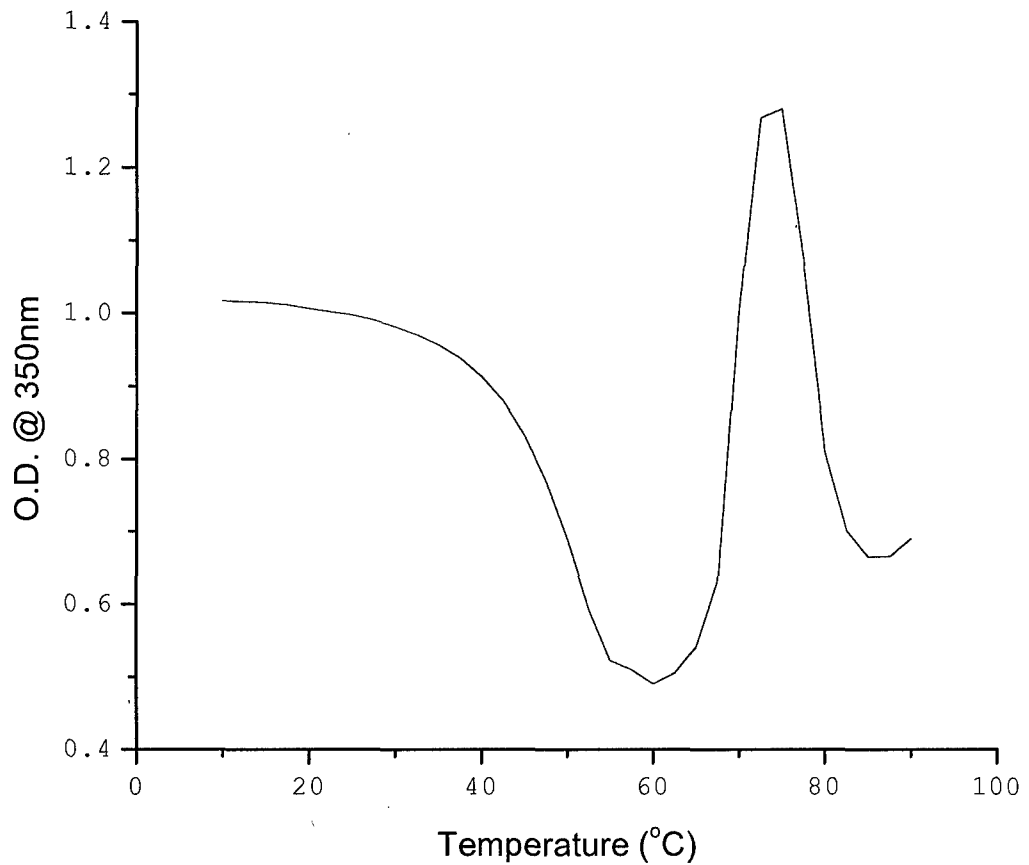


Figure 79. Optical density at 350nm as a function of temperature for Ad5 pH 3.

Ad5 pH 4 010804

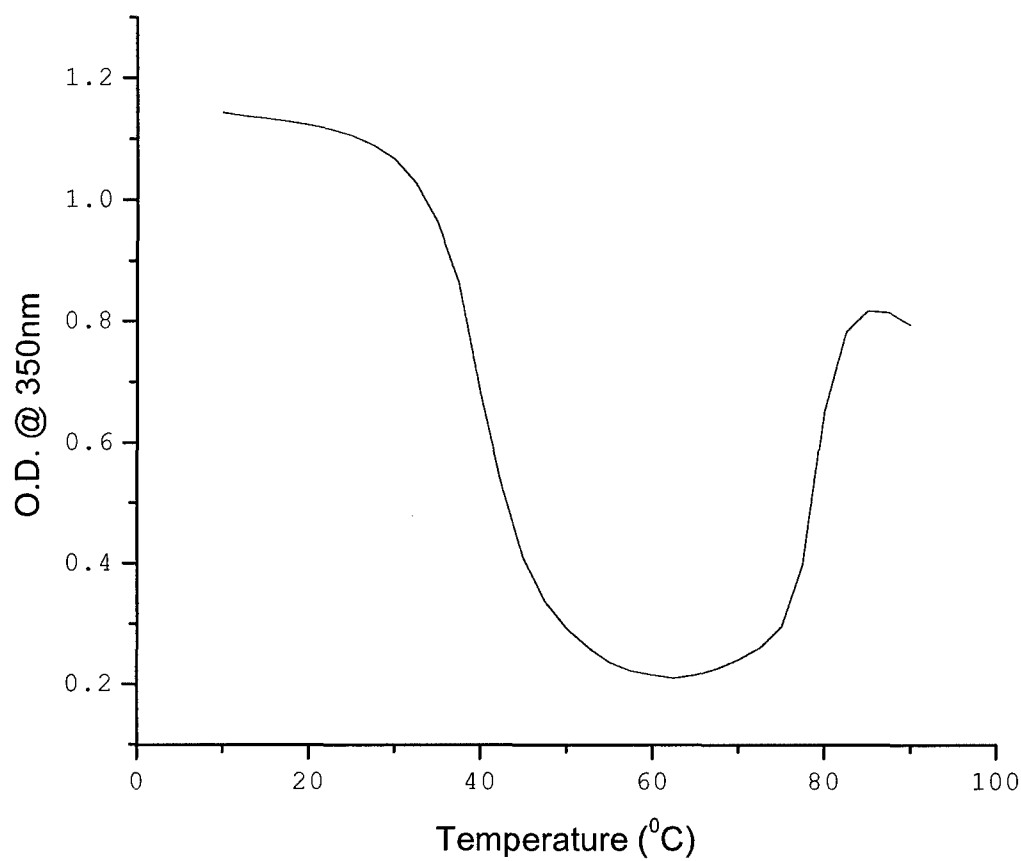


Figure 80. Optical density at 350nm as a function of temperature for Ad5 pH 4.

Ad5 pH 5 011304 (2nd run)

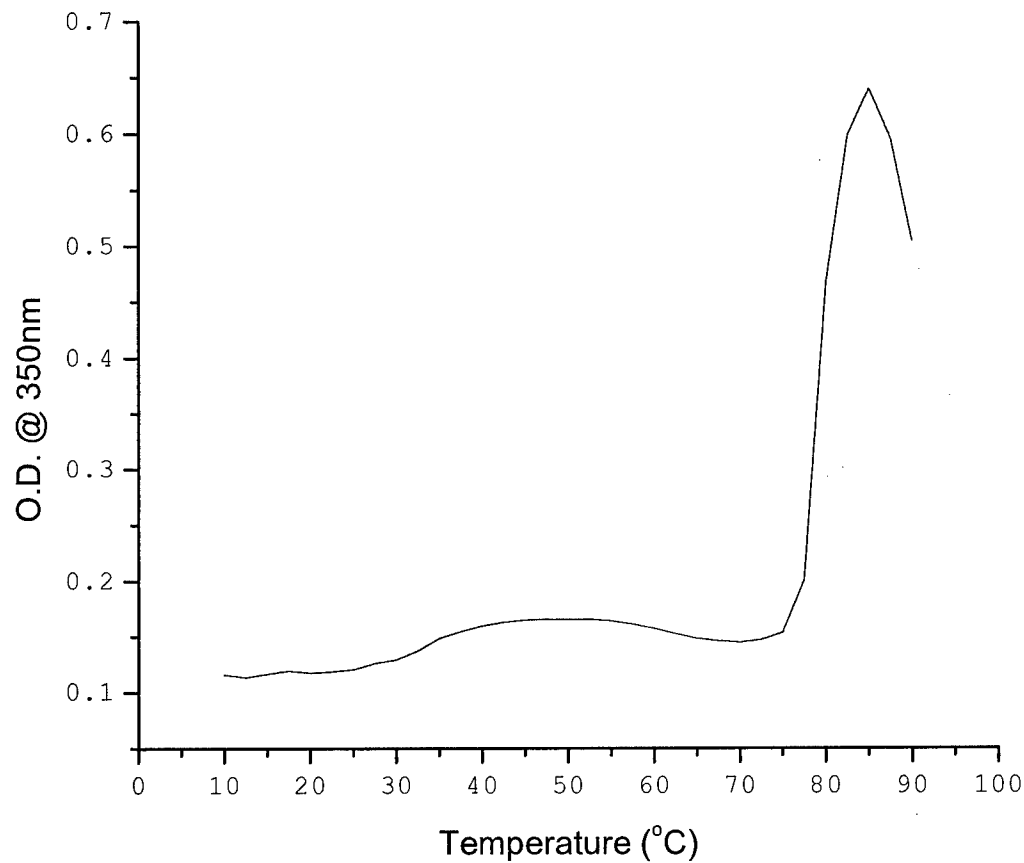


Figure 81. Optical density at 350nm as a function of temperature for Ad5 pH 5.

Ad5 pH 6 010604

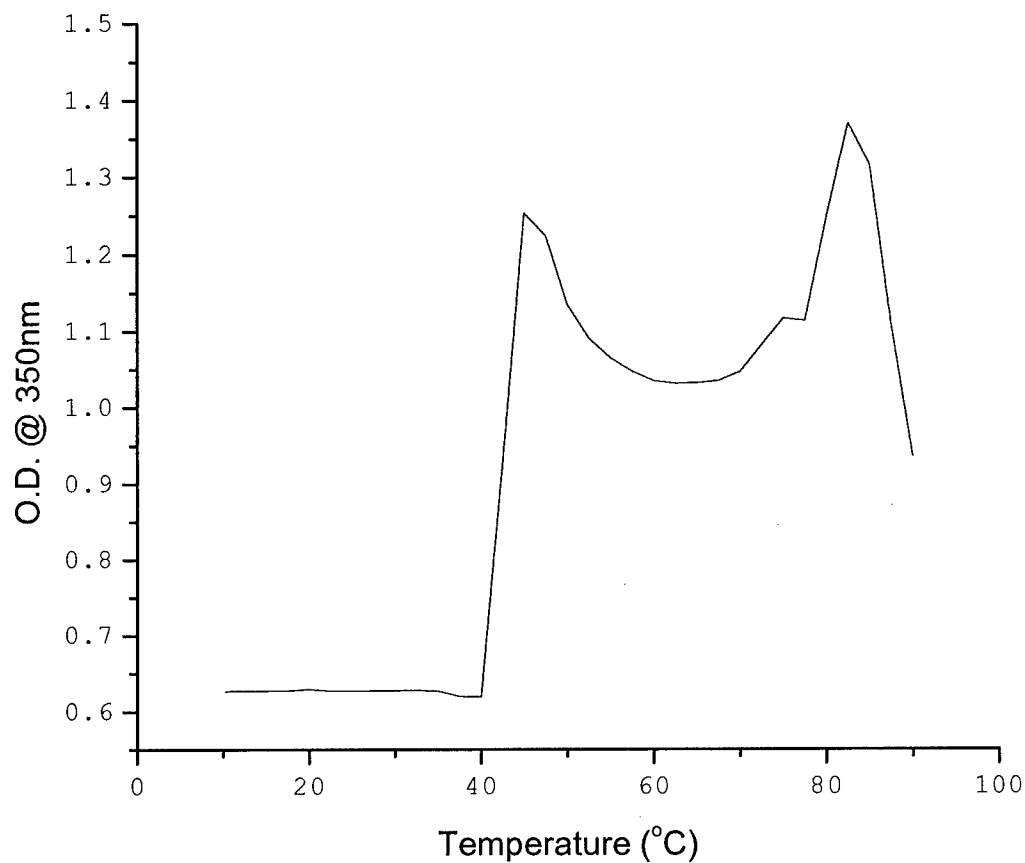


Figure 82. Optical density at 350nm as a function of temperature for Ad5 pH 6.

Ad5 pH 7 010504

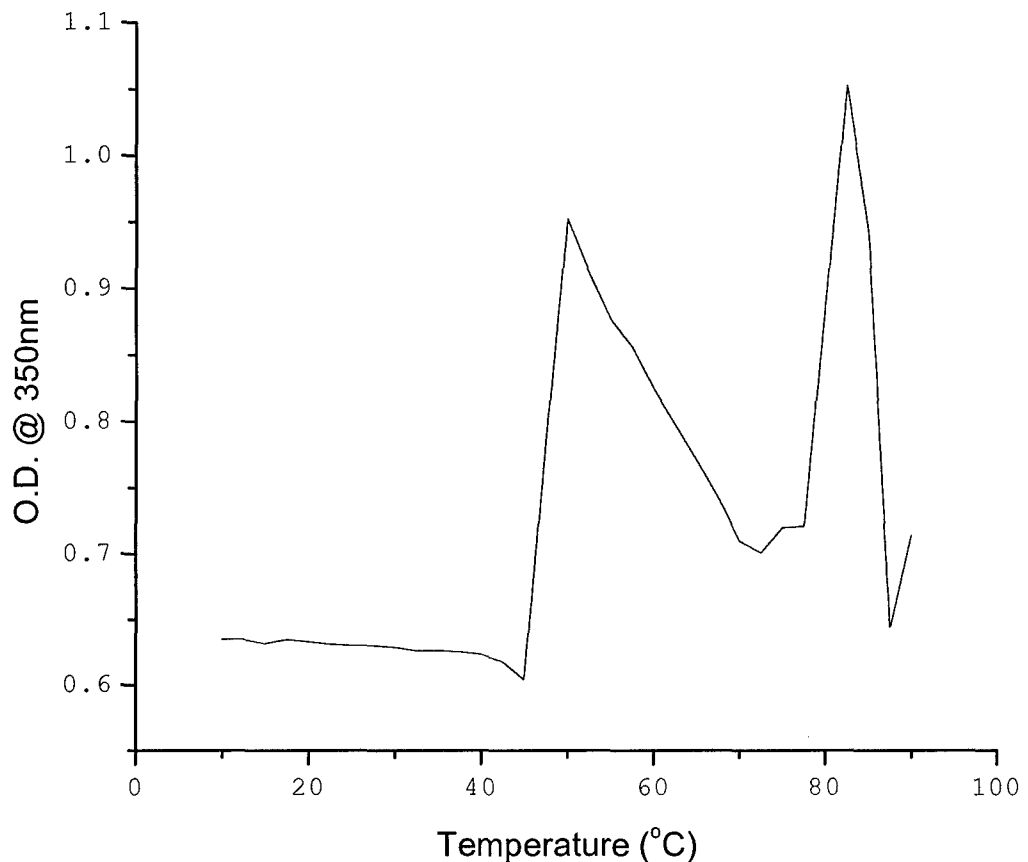


Figure 83. Optical density at 350nm as a function of temperature for Ad5 pH 7.

Ad5 pH 8 011204 (2nd run)

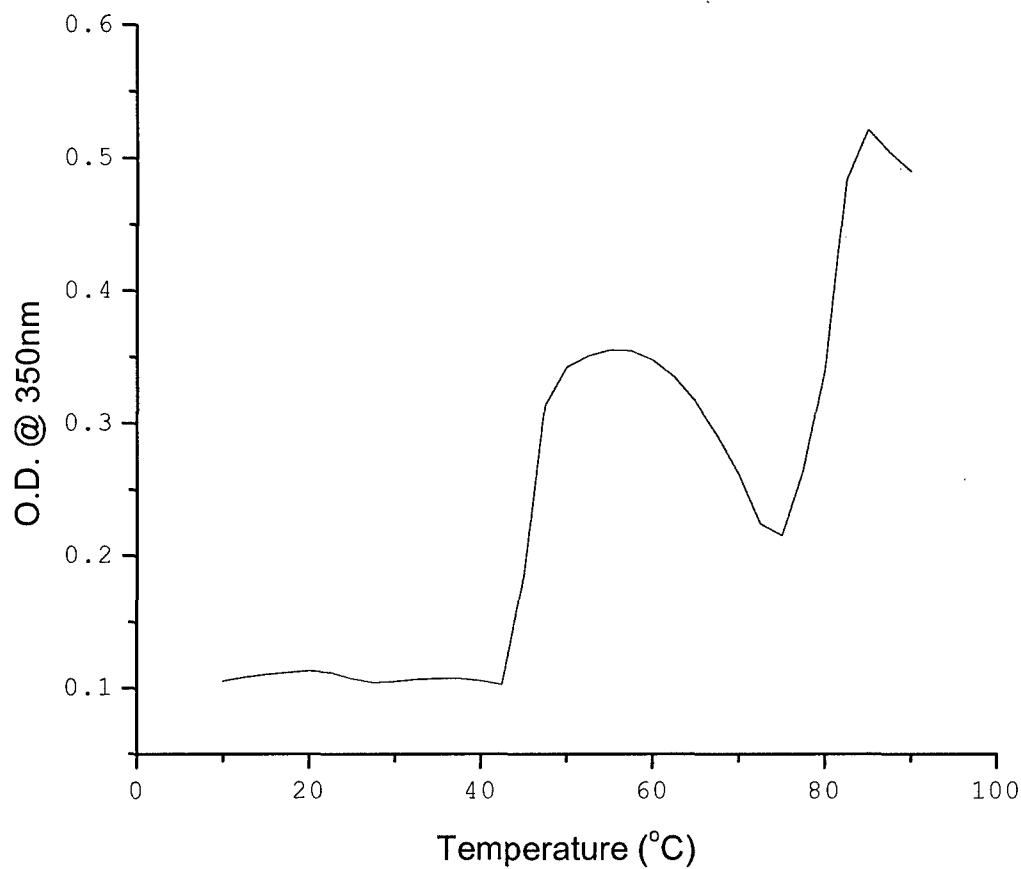


Figure 84. Optical density at 350nm as a function of temperature for Ad5 pH 8.

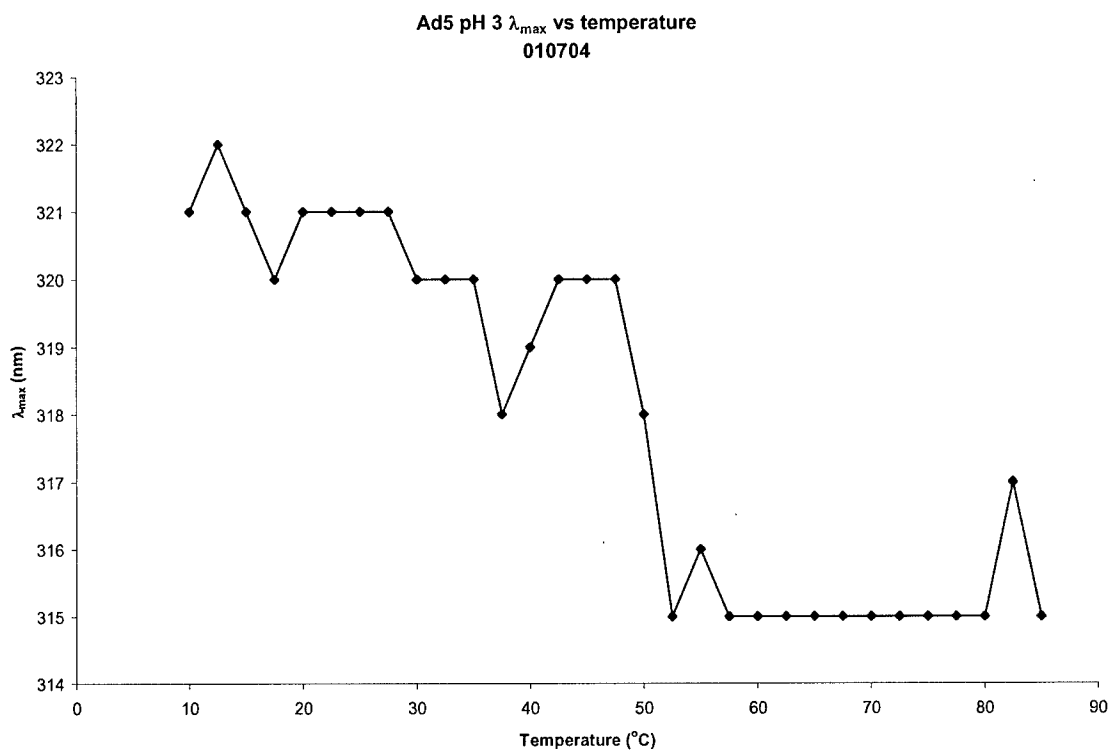


Figure 85. Wavelength of maximum intrinsic fluorescence intensity versus temperature for Ad5 at pH 3.

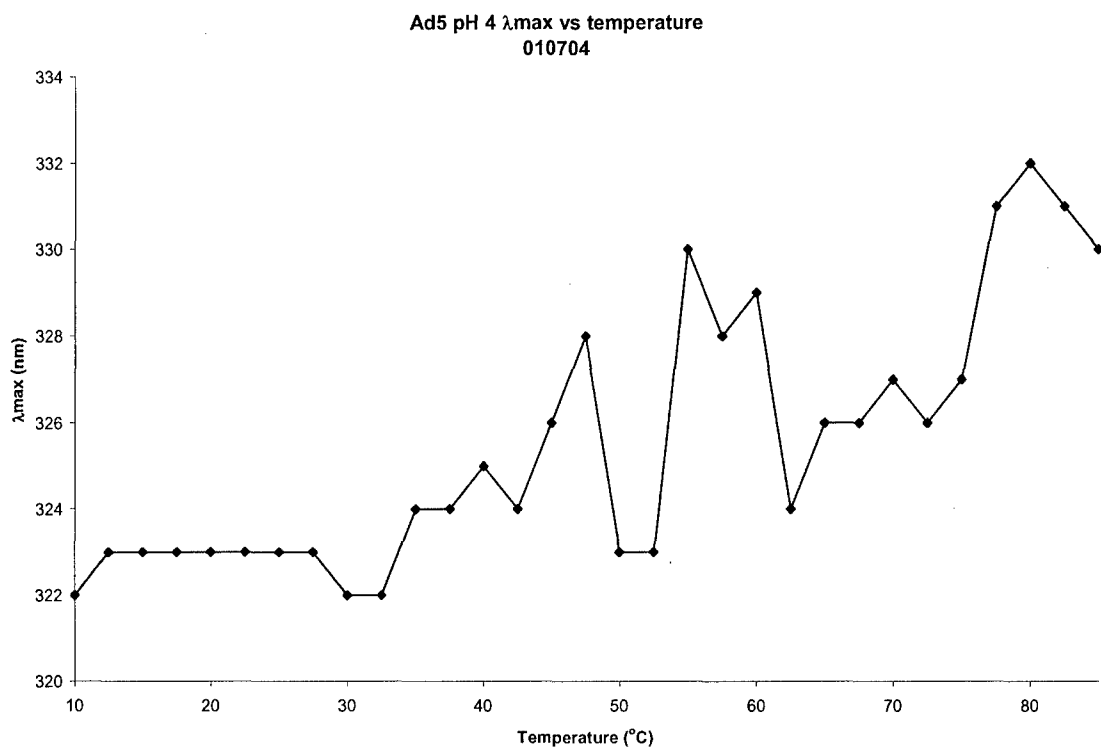


Figure 86. Wavelength of maximum intrinsic fluorescence intensity versus temperature for Ad5 at pH 4.

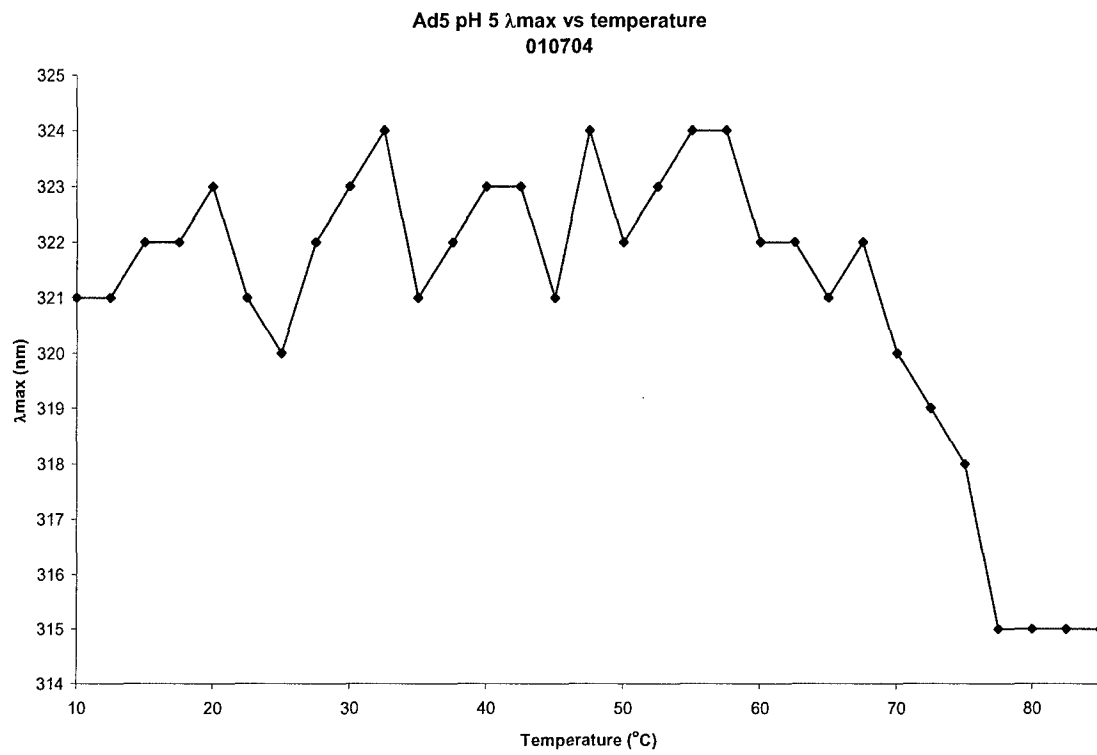


Figure 87. Wavelength of maximum intrinsic fluorescence intensity versus temperature for Ad5 at pH 5.

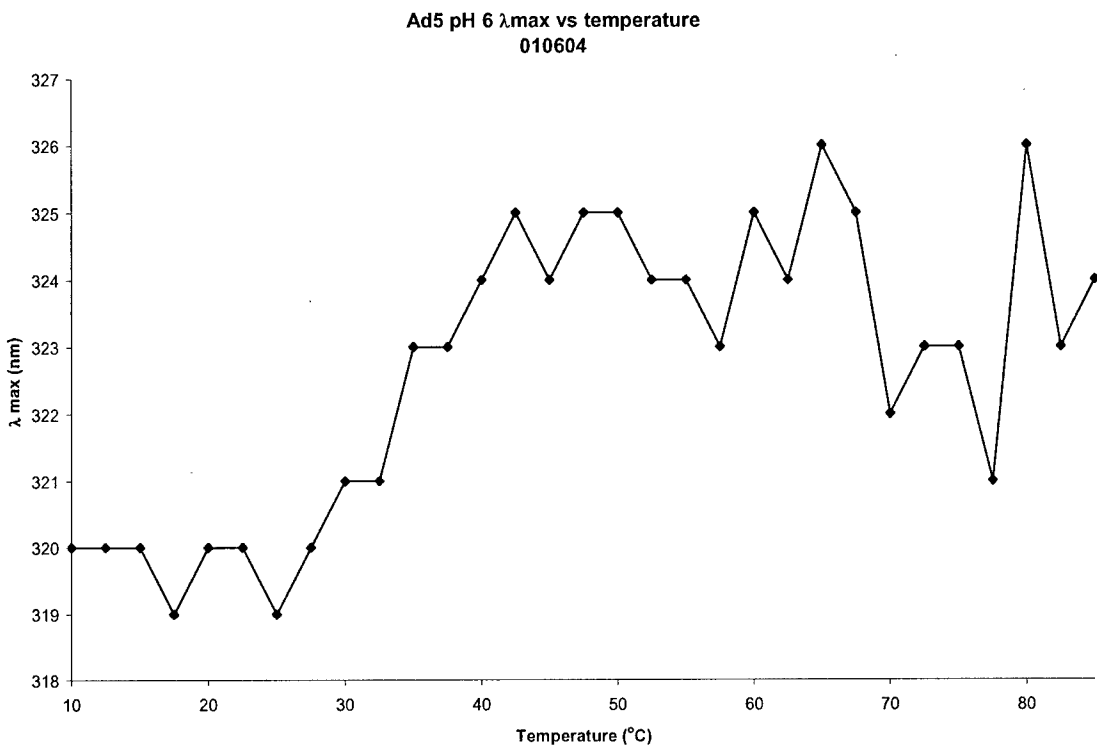


Figure 88. Wavelength of maximum intrinsic fluorescence intensity versus temperature for Ad5 at pH 6.

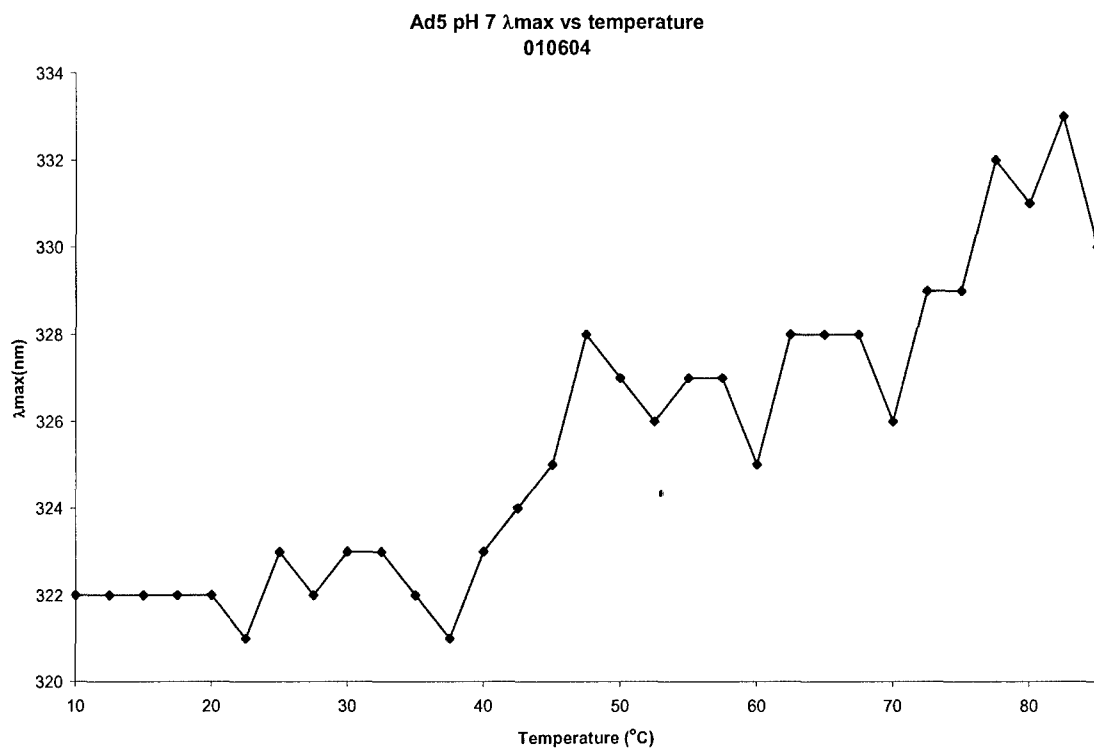


Figure 89. Wavelength of maximum intrinsic fluorescence intensity versus temperature for Ad5 at pH 7.

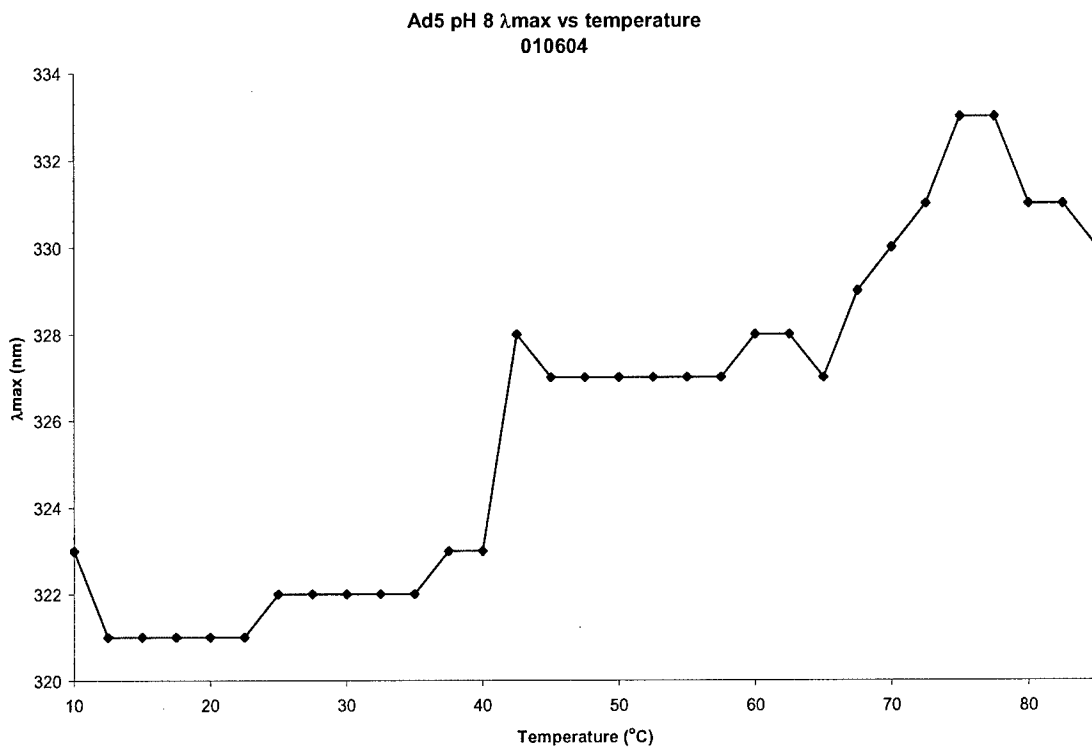


Figure 90. Wavelength of maximum intrinsic fluorescence intensity versus temperature for Ad5 at pH 8.

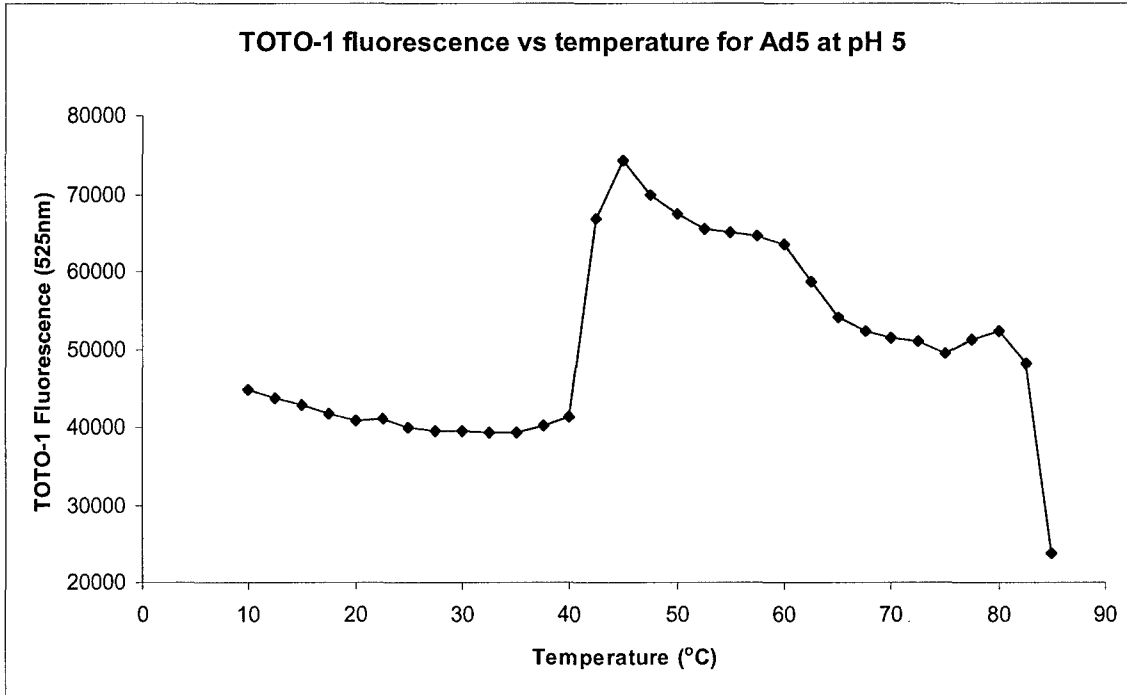


Figure 91. Analysis of Ad5 quaternary structural stability employing TOTO-1 at pH 5.

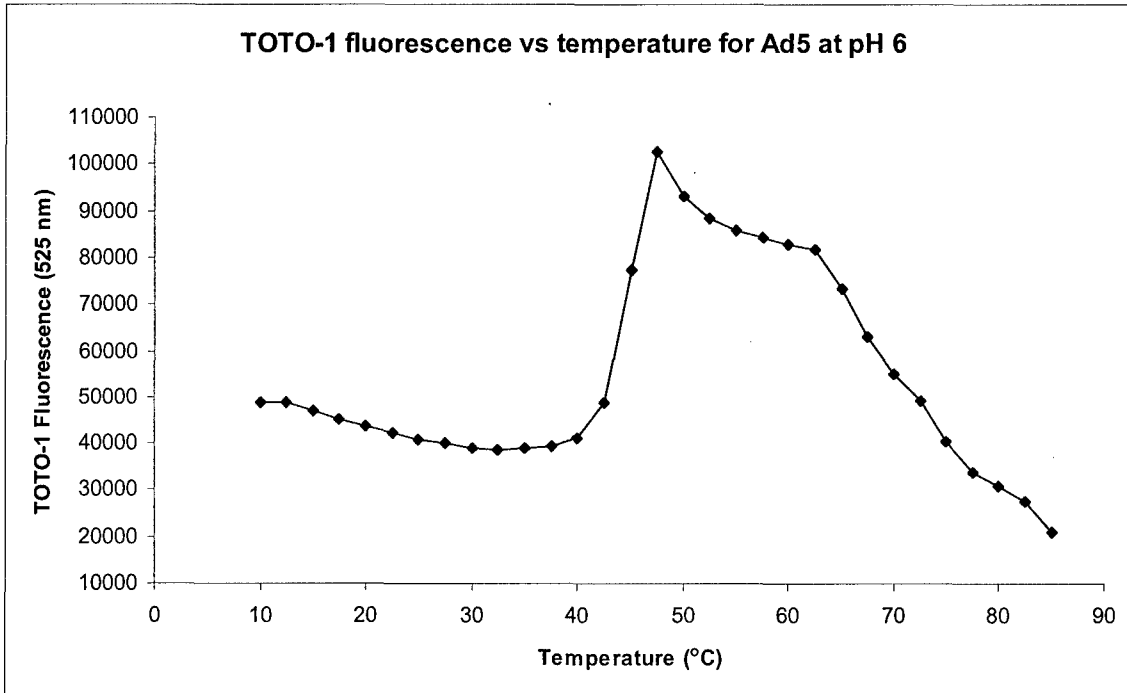


Figure 92. Analysis of Ad5 quaternary structural stability employing TOTO-1 at pH 6.

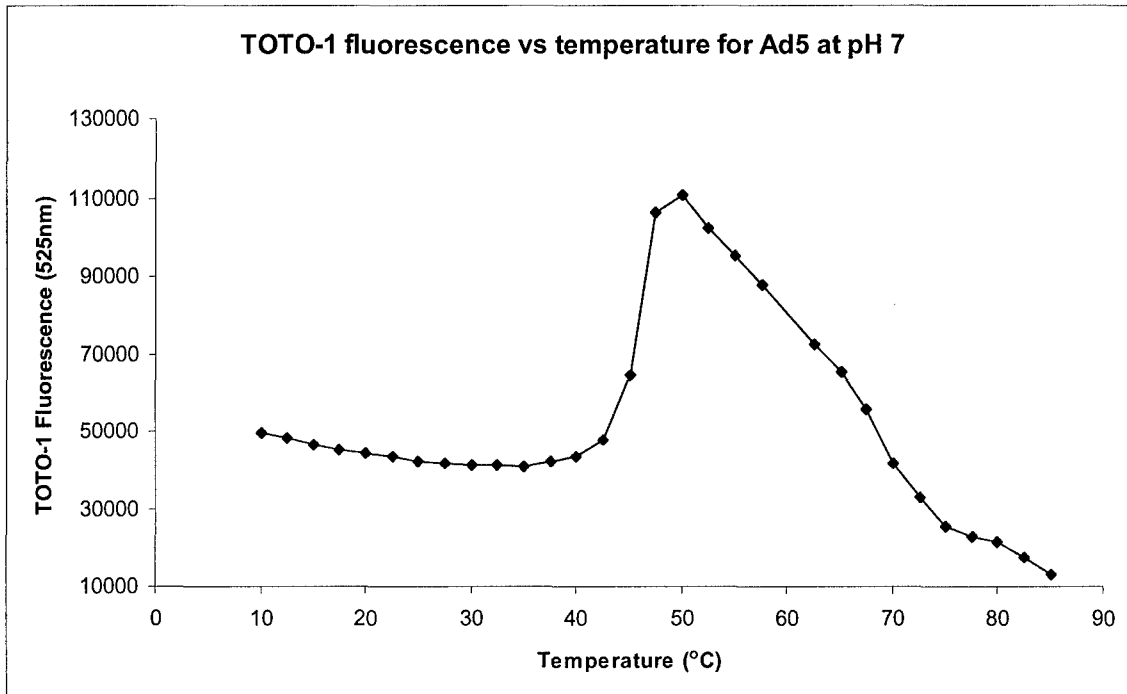


Figure 93. Analysis of Ad5 quaternary structural stability employing TOTO-1 at pH 7.

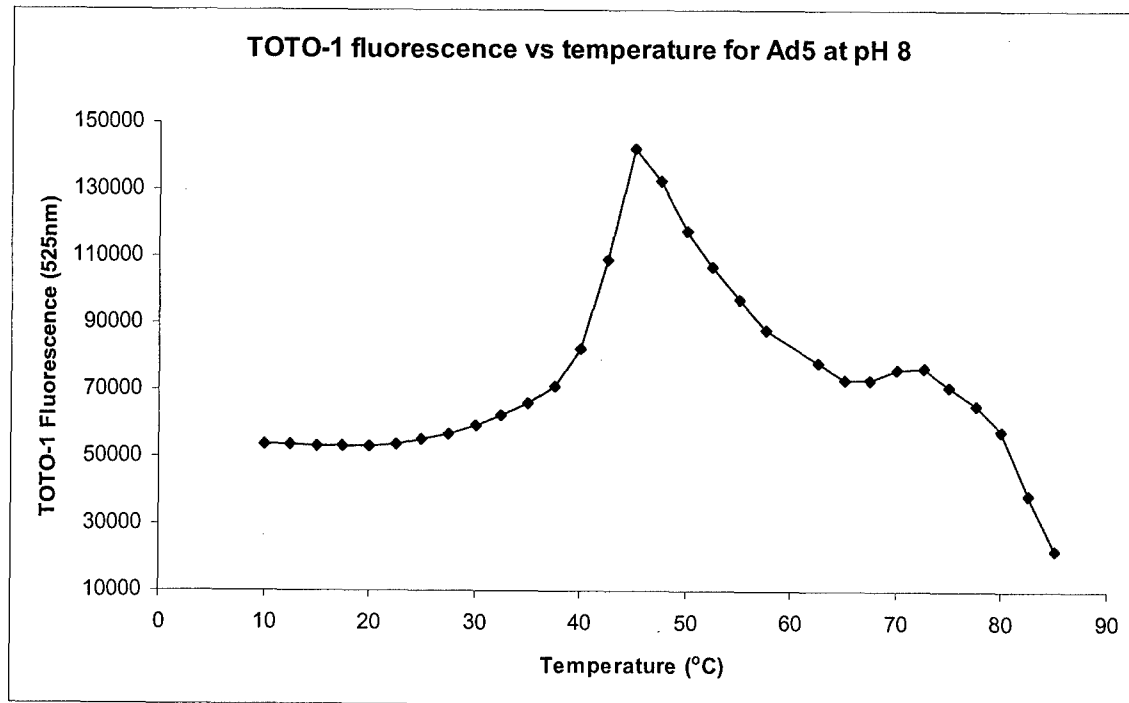
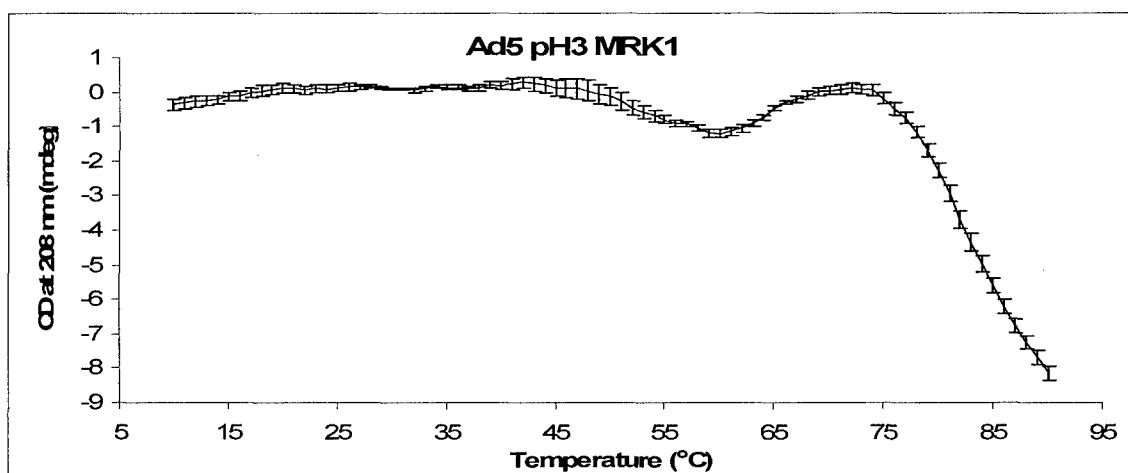
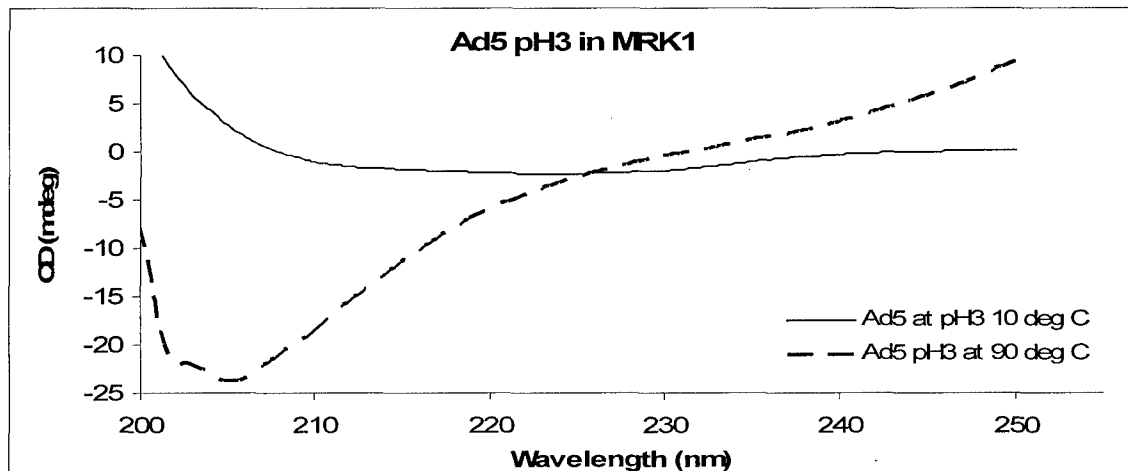
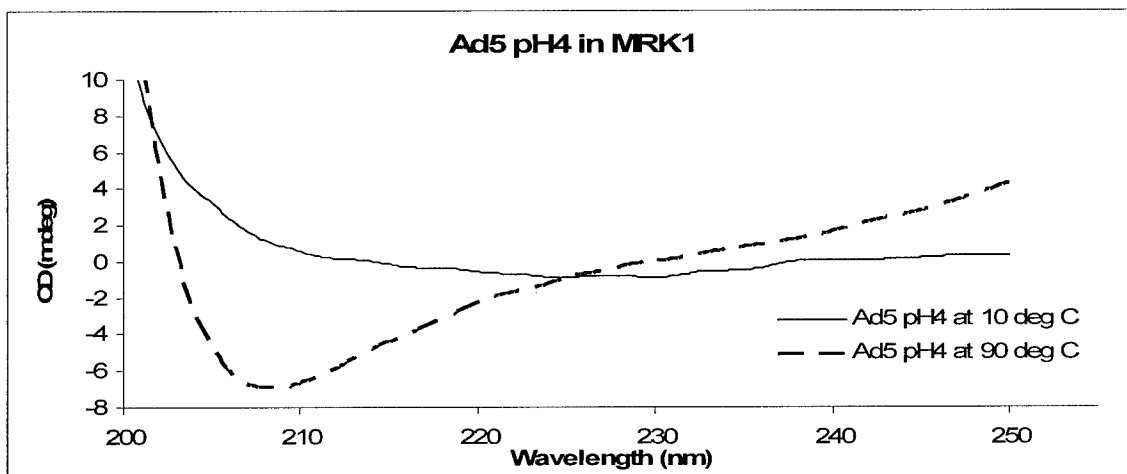
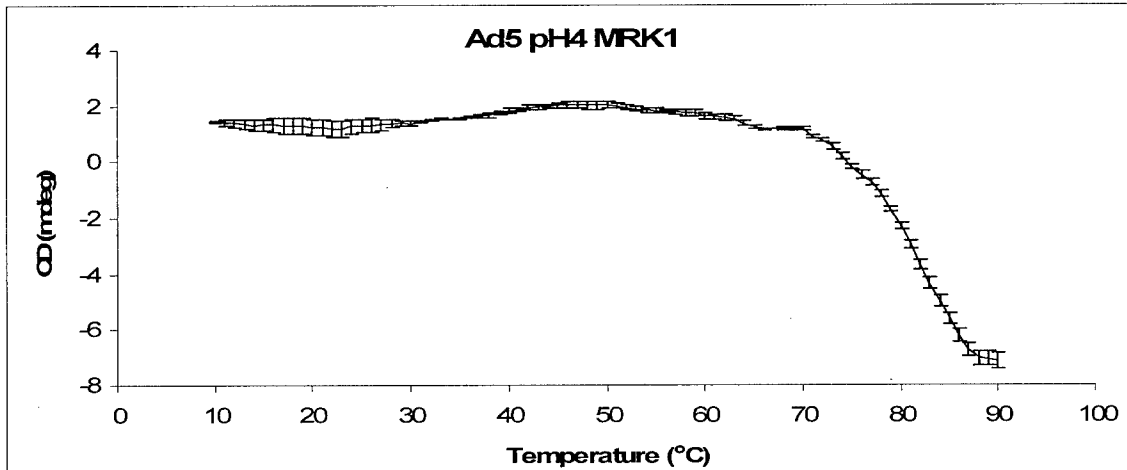


Figure 94. Analysis of Ad5 quaternary structural stability employing TOTO-1 at pH 8.



**Figure 95.** Top: CD spectra of pH 3 Ad5 at 10 (solid line) and 90° C (dashed line). Bottom: CD signal at 208 nm of Ad5 at pH 3 versus temperature.



**Figure 96.** Top: CD signal at 208 nm of Ad5 at pH 4 versus temperature. Bottom: CD spectra of pH 4 Ad5 at 10 (solid line) and 90° C (dashed line).

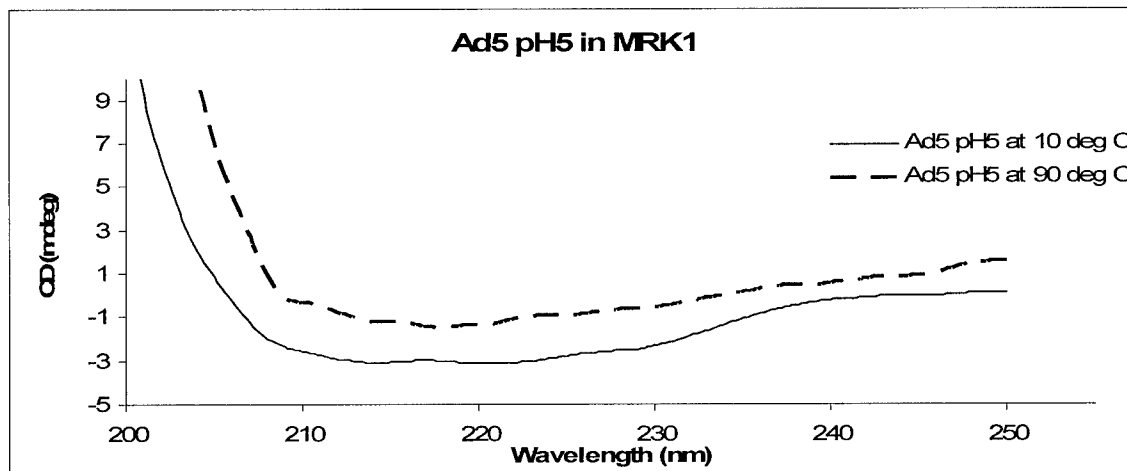
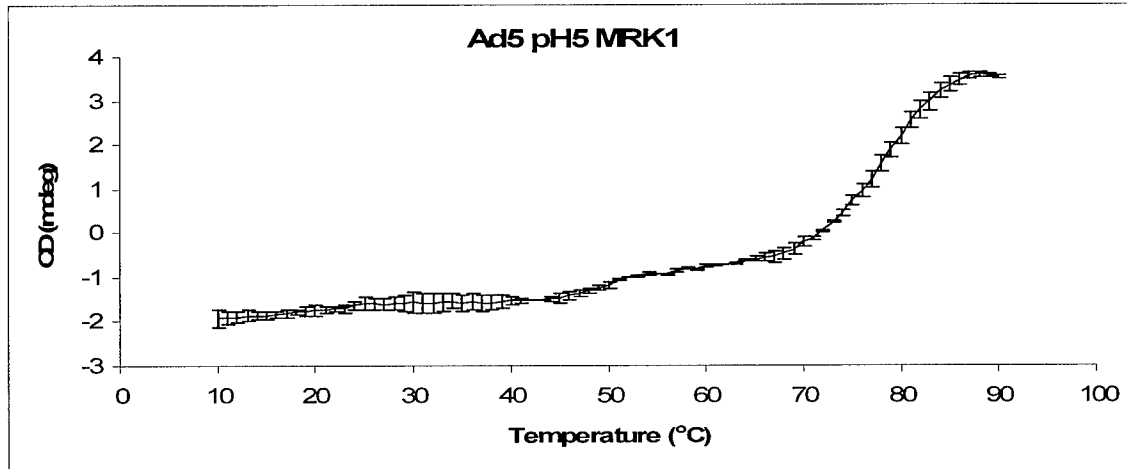


**Figure 97.** Top: CD signal at 208 nm of Ad5 at pH 5 versus temperature. Bottom: CD spectra of pH 5 Ad5 at 10 (solid line) and 90° C (dashed line).

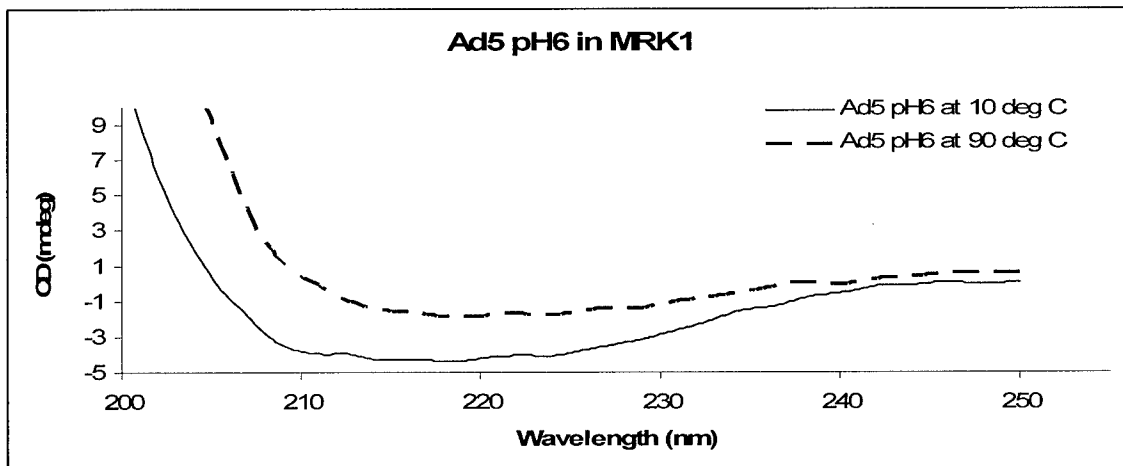
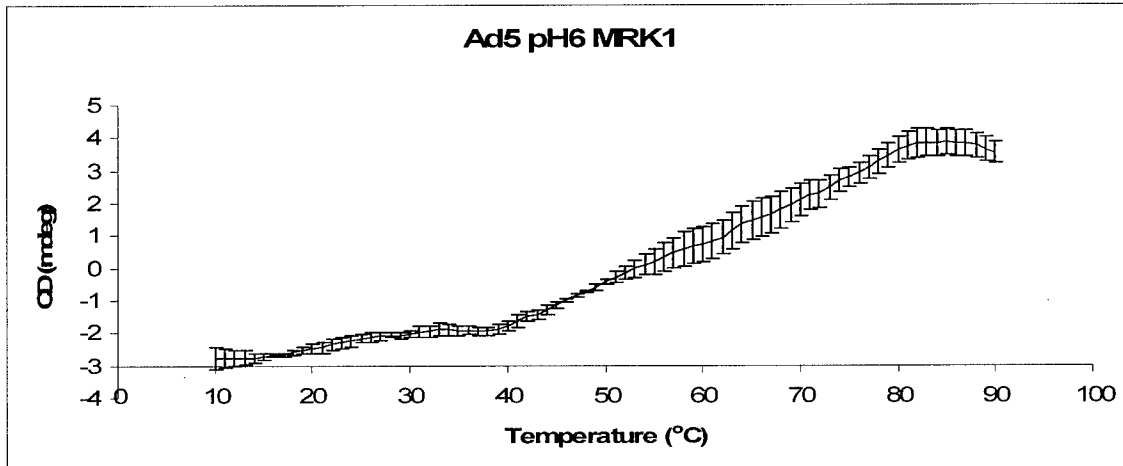


**Figure 98.** Top: CD signal at 208 nm of Ad5 at pH 6 versus temperature. Bottom: CD spectra of pH 6 Ad5 at 10 (solid line) and 90° C (dashed line).

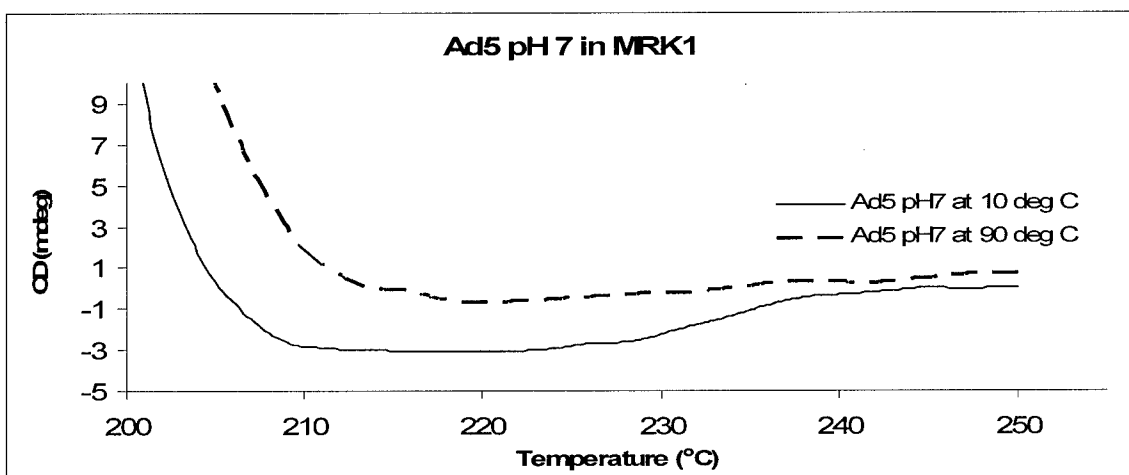
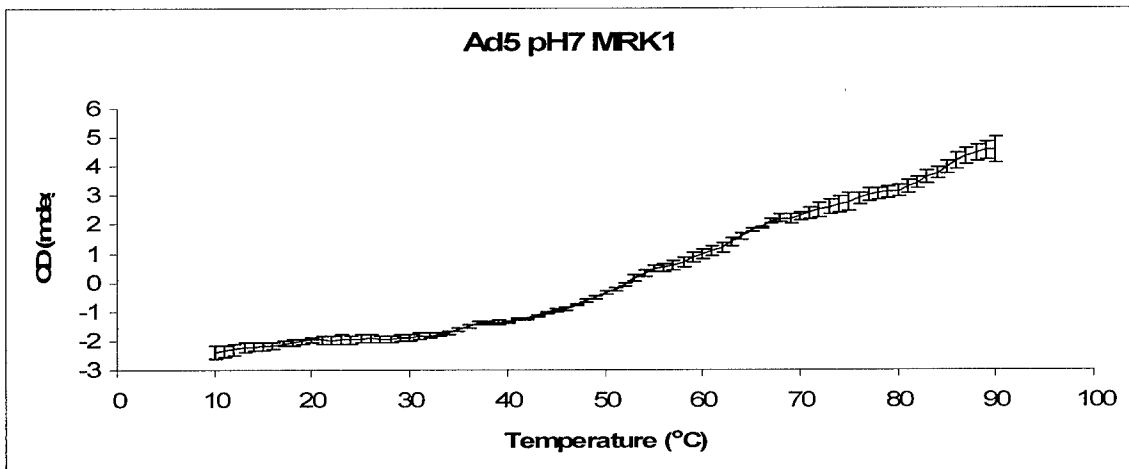


**Figure 99.** Top: CD signal at 208 nm of Ad5 at pH 7 versus temperature. Bottom: CD spectra of pH 7 Ad5 at 10 (solid line) and 90° C (dashed line).

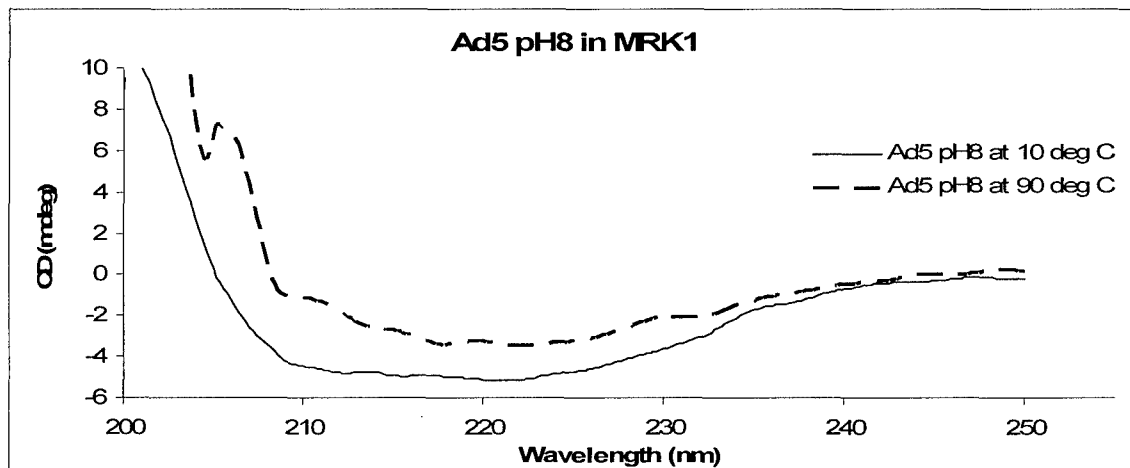
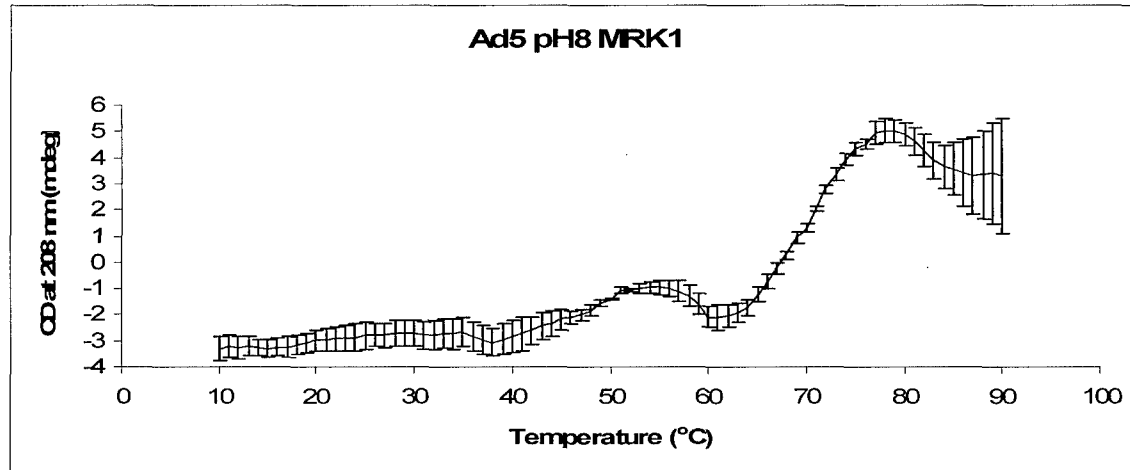


**Figure 100.** Top: CD signal at 208 nm of Ad5 at pH 8 versus temperature. Bottom: CD spectra of pH 8 Ad5 at 10 (solid line) and 90° C (dashed line).

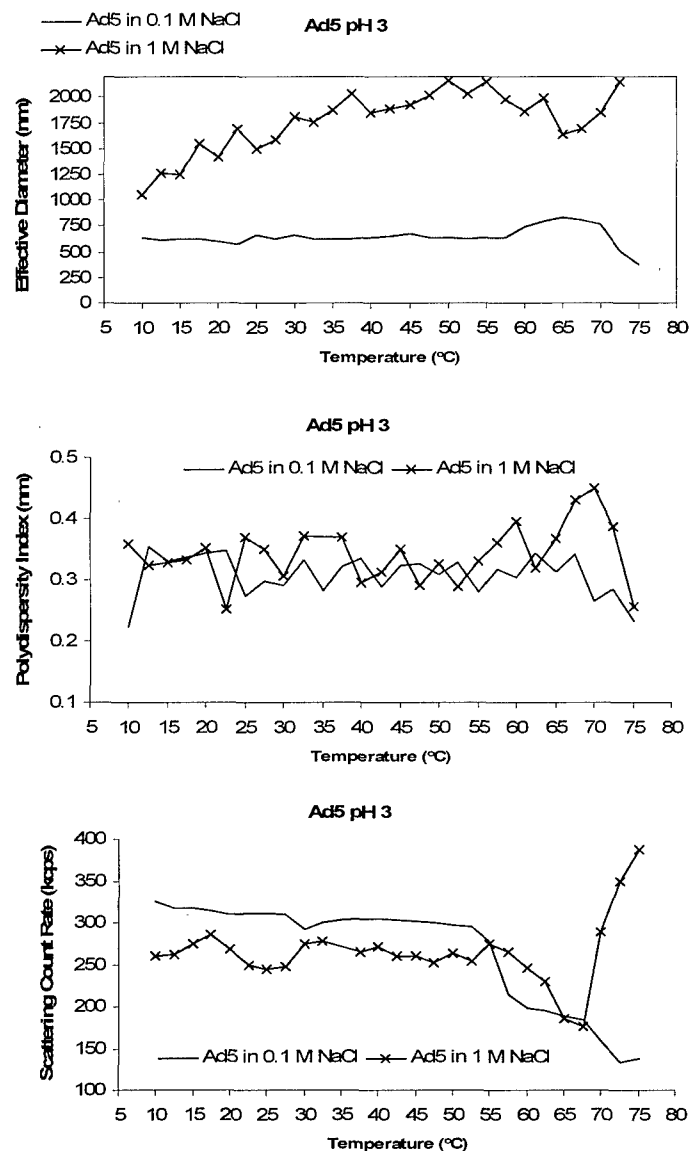


**Figure 101.** Dynamic light scattering measurements of Ad5 at pH 3 versus temperature.

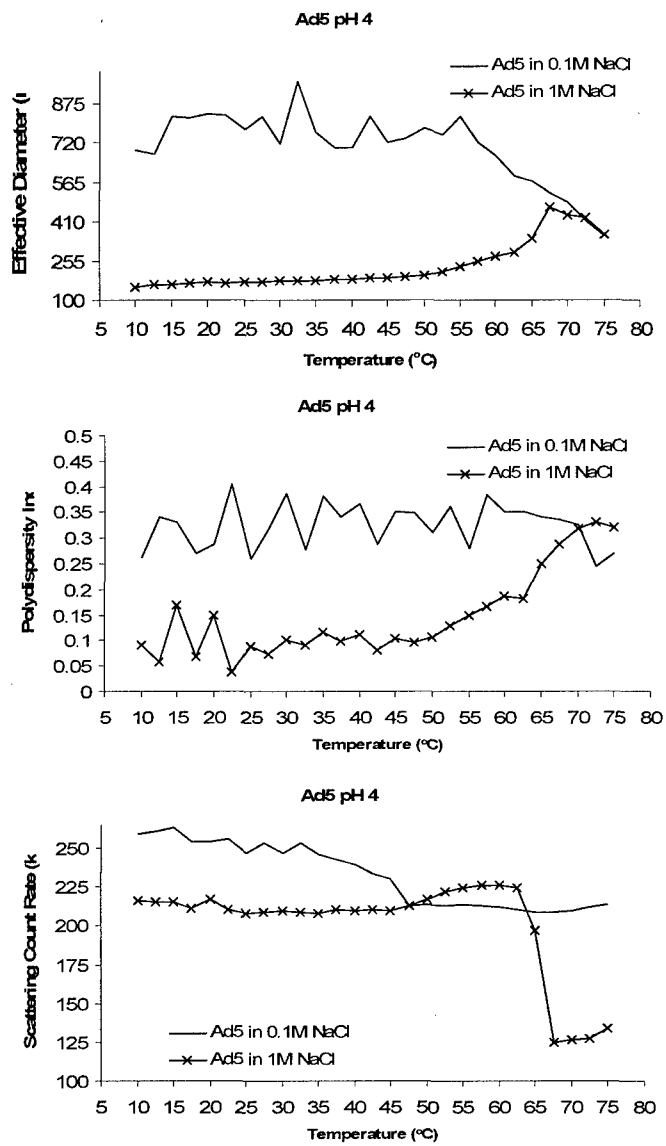


**Figure 102.** Dynamic light scattering measurements of Ad5 at pH 4 versus temperature.

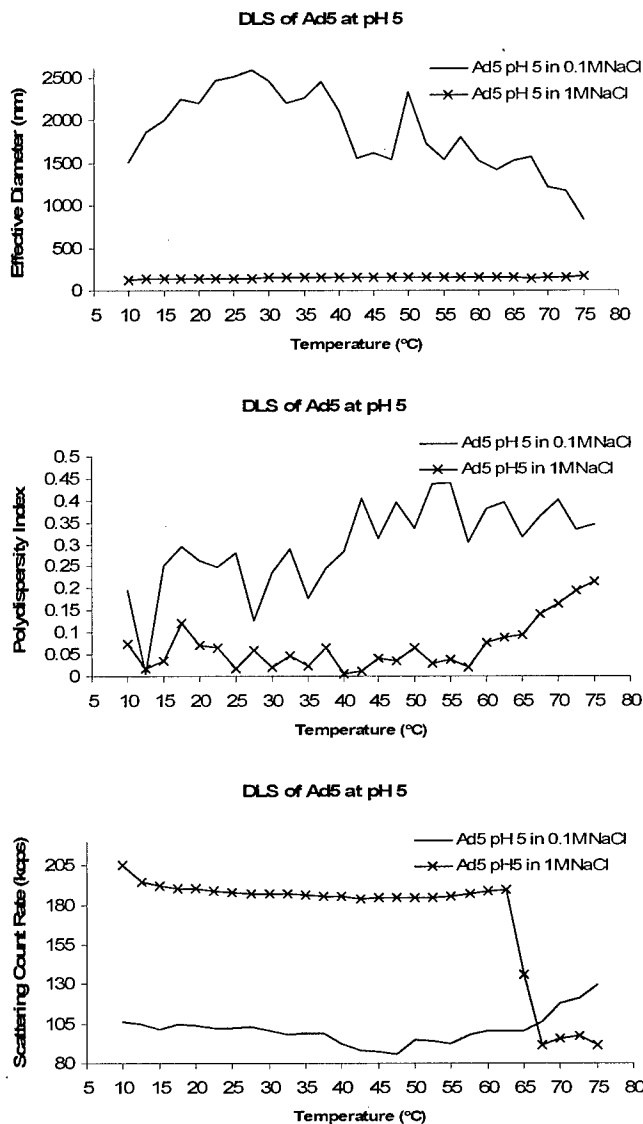


**Figure 103.** Dynamic light scattering measurements of Ad5 at pH 5 versus temperature.

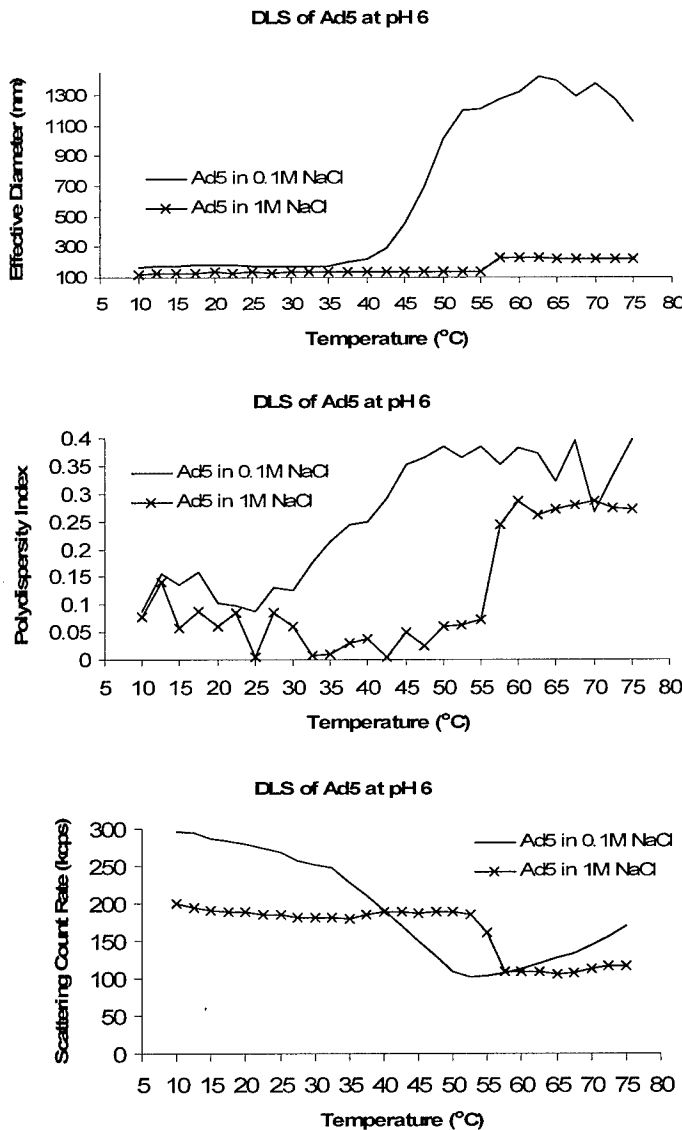


**Figure 104.** Dynamic light scattering measurements of Ad5 at pH 6 versus temperature.

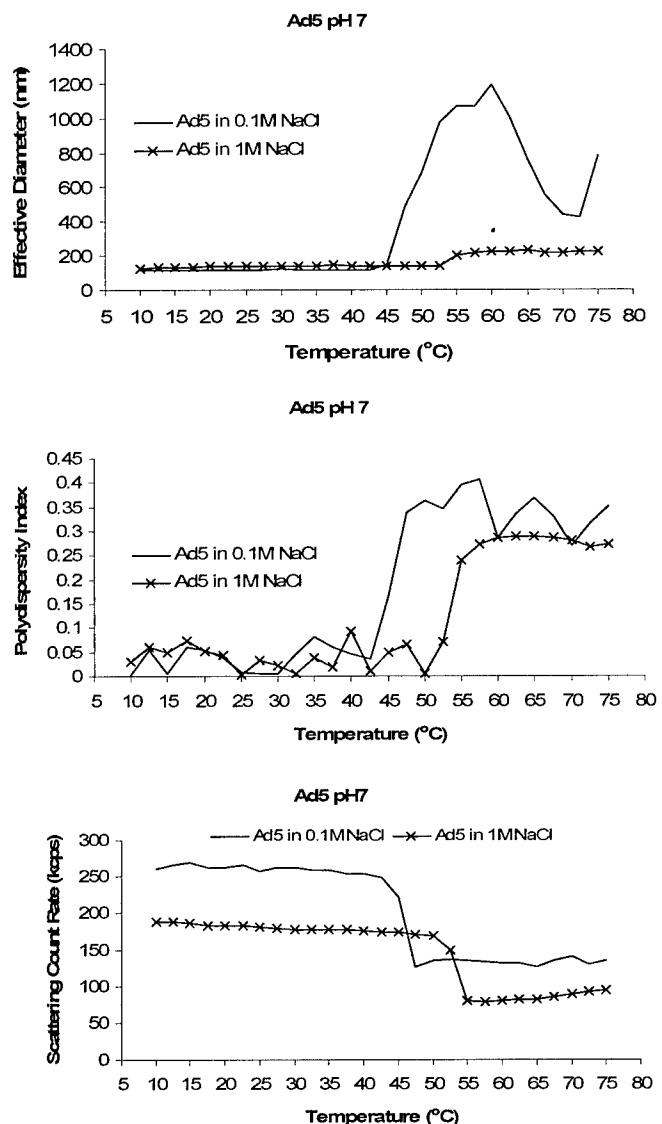


**Figure 105.** Dynamic light scattering measurements of Ad5 at pH 7 versus temperature.

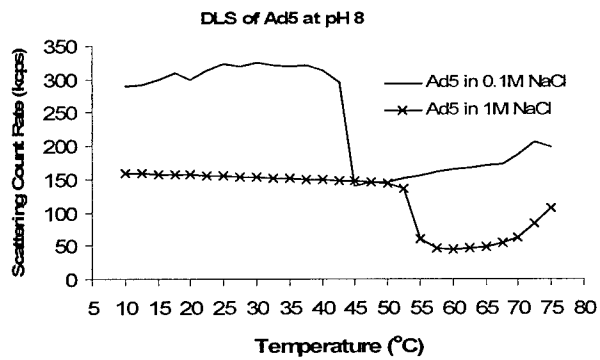
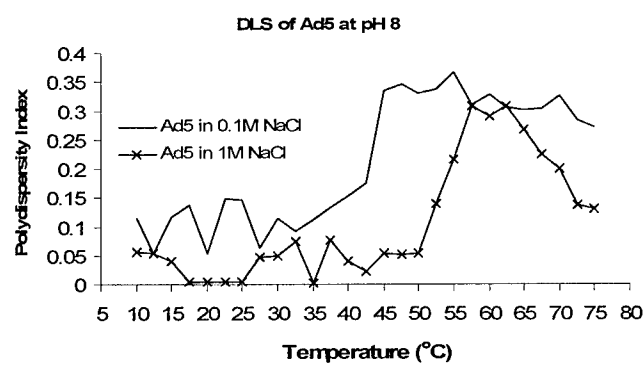
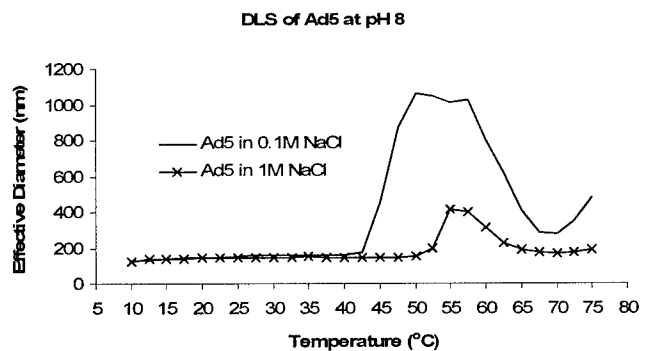


**Figure 106.** Dynamic light scattering measurements of Ad5 at pH 8 versus temperature.

<b>pH</b>	<b>2nd Derivative UV (°C)</b>	<b>Optical Density at 350nm (°C)</b>
3	15, 72	45, 72, 80
4	25	42, 80
5	27, 77	32, 77
6	42, 80	45, 57, 82
7	45, 82	45, 60, 80
8	47, 80	45, 60, 82

Table 4. Approximate 2<sup>nd</sup> derivative UV spectroscopy and optical density at 350nm transition temperature midpoints.

## **Adenovirus type 2 (Ad2)**

Adenovirus type 2 (Ad2) from Genzyme, Inc. was characterized employing a variety of biophysical techniques to assess its physical stability. Structural lability of the viral proteins will ultimately affect the physical and possibly chemical stability of the virus. The thermal stability of the virus, a potential indicator of this lability, was therefore examined by monitoring changes in circular dichroism (CD), UV absorption (UV), and fluorescence spectroscopies as a function of temperature to evaluate the secondary, tertiary, and quaternary structural stability of Ad2 over the pH range 3-8. Complex structural changes were seen and are described in detail in this report and the data is summarized in the form of empirical phase diagrams.

### **Experimental Procedures**

*Adenovirus Type 2 Concentration* – To conserve sample, Ad2 was diluted to  $5 \times 10^{11}$  vp/mL upon receipt with 10mM phosphate, 10% sucrose, 0.5 M NaCl, pH 7.4 and stored at -70° C.

*Ad2 Buffer Exchange* – Two buffer compositions over the pH range 3-8 were employed during these studies: 1.) CP: 10mM citrate, 10mM phosphate, 100mM sodium chloride; 2.) CPS: 10mM citrate, 10mM phosphate, 100mM sodium chloride, 10% sucrose. Buffer pH was adjusted at ambient temperature with HCl or NaOH. Aliquots ranging from 1-3 mL were dialyzed overnight at 4° C using 7k MWCO Pierce Slide-A-Lyzer® dialysis cassettes in the appropriate buffer.

*UV Absorption Spectroscopy* – UV absorption spectra were obtained employing a Hewlett-Packard 8453 diode-array spectrophotometer. A baseline was obtained with the appropriate buffer and baseline-corrected spectra were obtained every 2.5° C from 10-85° C. Calculated second derivative spectra were fit to a spline function with 99 points of interpolation using software supplied with the instrument. Negative peak positions were determined and plotted as a function of temperature using Microcal Origin® version 7. Additionally, the optical density at 350 nm (OD) was monitored as a function of temperature concomitant with absorption spectra.

*Circular Dichroism Spectroscopy* – CD data were obtained employing a Jasco 810 spectropolarimeter equipped with a Peltier temperature control device and a 6-position sample holder. CD spectra were acquired at 10° C and single wavelength CD measurements at 208 nm were taken over the temperature range 10-85° C. Ad2 samples were contained in sealed 0.1 cm path length cells at a concentration of  $\sim 5 \times 10^{11}$  vp/mL. A resolution of 0.2 nm and a scanning speed of 20 nm/min with a 2-s response time were employed. Spectra presented are an average of three consecutive scans. CD at 208 nm was measured at 0.2° C intervals using a 15° C/h temperature ramp rate and a 2-s response time. Data was normalized to correct for minor changes in concentration during dialysis and smoothed using software supplied with the instrument; plotting was performed in Microcal Origin®.

*Fluorescence Spectroscopy* – Fluorescence emission spectra were obtained in 2.5° C increments from 10-85° C using a QuantaMaster™ spectrofluorometer (Photon Technology International, Inc.) equipped with a 4-position cell holder and Peltier temperature control device. A 5-minute equilibration time was used at each temperature before data acquisition. The intrinsic fluorescence spectra were collected by exciting samples at 280 nm and emission was monitored between 305 and 450 nm using excitation and emission slit widths of 4 nm. The spectra were corrected for the Raman band of water by subtraction of the buffer spectrum at each corresponding temperature. Spectra were smoothed using the software included with the instrument; buffer subtraction and plotting were performed in Microsoft Excel®.

Extrinsic fluorescence spectroscopy was conducted to determine the accessibility of Ad2 DNA as the temperature was varied using 7.5 µM propidium iodide (Molecular Probes, #P1304MP) and an Ad2 concentration of  $\sim 2.5 \times 10^{11}$  vp/mL. Sample volumes of 1 mL were excited at 535 nm and emission was monitored from 550 to 650 nm using excitation and emission slit widths of 6 nm. The fluorescence intensity near the wavelength of maximum fluorescence intensity for each spectrum (607 nm) was plotted as a function of temperature in Microsoft Excel®.

*Generation of Phase Diagrams* – Phase diagrams were generated using the data points at 2.5° intervals from 10-85° C. The data used to construct the phase diagrams are: second derivative UV peaks at 259, 285, and 291 nm, CD at 208 nm, optical density at 350 nm, the intrinsic

fluorescence peak position, the intrinsic fluorescence peak position intensity, and propidium iodide fluorescence intensity at 607 nm. Data from these techniques were formatted in Microsoft Word® and copied into Mathematica® version 4.2 (Wolfram Research, Inc.) for phase diagram generation. Phase diagrams represent the physical stability of the virus as a multicomponent vector with the components defined by the measurements indicated and the most influential three components represented as colors in a RGB-based scheme. Details of this method are described elsewhere.<sup>1</sup>

## Results and Discussion

*Optical Density and Second Derivative UV Spectroscopy* – The UV spectrum of Ad2 in CP, pH 7 at 10° C is shown in Figure 107 and an absorption maximum near 260 nm is observed. Due to the relatively large size of the Ad2 particles, a significant quantity of scattered light is observed above 300 nm as indicated by the non-zero slope. At pH 3, 10° C, however, the OD at 350 nm is more than two fold higher suggesting that the virus self-associates (aggregates) at low pH (Fig. 108). This aggregation is most likely a result of small changes in tertiary structure that lead to self-association due to pH-induced structural changes in the viral proteins (see below). The data suggests that the addition of 10% sucrose does not prevent aggregation at pH 3, but does produce inhibition at pH 4 (fig 109). The OD at all other pH values at 10° C is relatively constant suggesting that 10% sucrose does not have a direct effect on the aggregation state of Ad2 at low temperatures at higher pH values.

At pH values 3 and 4 (Figs. 108 and 109), a slight increase in OD is observed with increasing temperature below 20° C followed by a dramatic decrease in light scattering above this temperature. This data suggests that the species seen at low temperatures dissociate with this initial increase in temperature. The OD for Ad2 at pH 3 reaches a minimum near 60° C and culminates in an OD near 0.1 at 85° C for both solutions. On the other hand, the decrease in OD near 20° C for Ad2 at pH 4 reaches a minimum of approximately 0.8 between 25 and 37°C. The OD value over this temperature range at pH 4 is similar to the starting OD values at the other pH values studied suggesting that the initial aggregation observed is reversible with a minor increase in temperature. An increase in OD near 40° C takes place at pH 4; however, this transition is

delayed by approximately 5° C in CPS. The OD at pH 5 remains constant until ~45° C for both formulations where a dramatic increase in the OD is observed (Fig. 110). Sucrose, therefore, has little effect on the aggregation of Ad2 with increasing temperature at pH 5; however, the lack of change in the OD below 45° C is quite distinct compared to the other pH values studied. Transitions below the major transition near 45° C at pH 6, 7, and 8 are preceded by a decrease in the OD at 350 (Figs. 111-113). This decrease in optical density may be due to a change in the refractive index of the viral particles that results in an increase in size (decrease in density) and a decrease in the amount of scattered light<sup>4</sup>, but this hypothesis has not yet been rigorously tested. A transition near this temperature has also previously been shown to be related to the dissociation of the adenovirus capsid<sup>5</sup>. The constant OD below 45° C at pH 5 is an interesting observation since the pI of the main capsid protein, hexon, is 5.06. It would thus not be surprising if aggregation and significant increases in the OD were observed even at 10° C, but this is not the case. The lack of change in the OD at pH 5 with increasing temperature is reproducible and has also been observed with a different serotype of adenovirus (unpublished results).

Ad2 in CPS at pH 6 leads to an increase in OD at lower temperatures compared to the formulation without sucrose. Furthermore, the final OD reached at 85° C is higher than that of the Ad2 solution without sucrose suggesting that sucrose is deleterious to the physical stability of Ad2 at pH 6. At pH 7, the addition of sucrose delays the initial decrease in OD; however, the significant increase in the OD begins near 42° C for both formulations. Furthermore, the maximum OD reached at higher temperatures for pH 7 is higher for the Ad2 formulation containing sucrose. Together, the OD data at pH 7 suggests that the addition of sucrose may delay the decrease in scattering near 37° C, but the transition leading to capsid dissociation occurs at the same temperature in the presence and absence of sucrose. Additionally, the addition of sucrose also results in more aggregation at higher temperatures at this pH. Sucrose has the most potent stabilizing effect at pH 8 where a significant increase in OD is observed near 30° C for Ad2 in CP although this transition does not occur until approximately 40° C for Ad2 in the presence of sucrose.

Figure 107 illustrates the second derivative spectrum of Ad2 in CP, pH 7 at 10° C. The negative peaks between 250 and 275 nm arise from the overlapping absorbance of Ad2 DNA and aromatic

amino acids (phenylalanine and tyrosine). Peaks near 279, 285, and 292 nm are attributed to absorbance from tyrosine, a combination of tyrosine and tryptophan, and tryptophan, respectively. The positions of these peaks are environmentally sensitive and shifts with increasing temperature suggest changes aromatic side chains' immediate environment. As aromatic residues become more exposed to the polar solvent (water), they preferentially absorb light of lower wavelengths. The position of second derivative peaks near 279, 285, and 292 nm for Ad2 in CP at pH 3 (Fig. 114) suggest that the aromatic amino acids Tyr and Trp are more exposed in CP compared to Ad2 in CPS at 10° C since they are generally significantly blue-shifted. As the temperature is increased, however, a common value is reached near 47° C for all three peaks suggesting that protein tertiary structure becomes similar for Ad2 in CP and CPS at pH 3 near this temperature. Since the OD at 10° C, pH 3 is not significantly different for Ad2 in CP and CPS, the conformation of the virus involved in the associative process may be different in CP versus CPS, but the nature of any such alterations remains unclear.

In general, second derivative data for Ad2 at pH 4-8 (with the exception of pH 7) also show significant differences between CP and CPS suggesting that sucrose stabilizes the overall tertiary structure of the viral proteins since transitions occur at lower temperatures in the absence of sucrose (Figs. 115-119). Shifts in the peak positions at pH 4 and 5 suggest that Tyr and Trp residues are being exposed to a less polar environment (more buried) as the temperature increases since peak positions shift to higher wavelengths; this could also be a result of aggregation of viral proteins since the optical density also increases at higher temperatures. Conversely, shifts in Tyr and Trp peak positions with increasing temperature show an opposite trend at pH values 6-8. At these higher pH values the peaks shift to lower wavelengths suggesting that the solvent environment of the Tyr and Trp residues is changing to a more polar one. This is probably a result of perturbations in tertiary structure with increasing temperature. Note that transitions at pH values 4-8 occur over the temperature range 35-45° C (within the physiological temperature range).

*Intrinsic Fluorescence Spectroscopy* – Intrinsic fluorescence spectroscopy should detect changes in the tertiary structure of the adenovirus proteins as a direct consequence of alterations in the polarity of the local environment of tryptophan in the virus. This makes it a complementary

technique to second derivative UV spectroscopy. As expected, the fluorescence emission spectrum is indeed dominated by tryptophan emission. Under all pH conditions the emission maximum is located near  $322 \pm 1$  nm indicating a highly buried environment for the majority of the proteins' Trp residues. Figures 120-125 show that, in general, an increase in the wavelength of the emission maximum ( $\lambda_{\text{max}}$ ) occurs between  $35-50^\circ \text{ C}$  suggesting that the Trp indole side chains are becoming more solvent exposed. These changes in tertiary structure are also confirmed by the distinct changes in slope in temperature-dependent fluorescence intensity at the  $\lambda_{\text{max}}$  near the temperature of peak position shift. At pH 3, aggregation and precipitation of the Ad2 protein components results in spectral dominance by light scattering and a shift of the peak position to lower wavelengths. This same phenomenon also occurs at temperatures above  $80^\circ \text{ C}$  at pH 6-8 for CPS and/or CP. Data obtained by intrinsic fluorescence spectroscopy agrees well with the data obtained by UV spectroscopy although only a slight enhancement in the tertiary structural stability is detected in the presence of sucrose at the two lower pH values. Of particular interest is the observation that although an apparently reversible aggregation results at low temperatures, the tertiary structural stability of Ad2 proteins is maximized at pH 4 (*i.e.*, the Tm is the highest) in the presence of 10% sucrose.

*Circular Dichroism Spectroscopy* – CD was employed to monitor the thermal perturbation of the secondary structure of the viral proteins. No signal from the viral genome was seen at the concentration employed in these experiments. Figures 126 and 127 show the normalized CD spectra of Ad2 at  $10^\circ \text{ C}$  in the presence and absence of sucrose. The secondary structure of Ad2 in the absence of sucrose appears highly disrupted at pH 3; in the presence of the sugar, the spectrum is also altered, but significant structure is present with some hint of new beta sheet being present. A similar mixture of alpha helix and beta structure is observed at all other pH values suggesting that the secondary structure is preserved regardless of the change in pH over the pH range 4-8. The ellipticity at 208 nm (Figs. 128 and 129) shows that an abrupt loss in Ad2 secondary structure occurs near  $45^\circ \text{ C}$  for CP at pH 4 and occurs near  $47^\circ \text{ C}$  at pH 5-7. At pH 8, the first transition occurs near  $40^\circ \text{ C}$  suggesting that the secondary structure is more labile at this pH. The addition of sucrose at pH 8 does not appear to enhance the stability of the secondary structure of Ad2. A second, more prominent transition occurs near  $70^\circ \text{ C}$  at pH 4-8 for Ad2 in CP indicating that an additional significant loss in secondary structure occurs at higher temperatures. Although the

distinct loss in secondary structure that occurs near 45° C for pH 4-7 in the absence of sucrose also occurs near the same temperature in CPS, the transition is less pronounced and occurs over a broader temperature range. The loss in secondary structure detected at higher temperatures for Ad2 in CPS occurs near 80° C at pH 4 and the transition temperature decreases as the pH is increased to pH 8. Overall, the data suggests that the stability of the overall secondary structure of the viral proteins may be slightly enhanced in the presence of sucrose since the transition near 45° C occurs over a broader temperature range. Furthermore, the loss of secondary structure that occurs above 70° C is delayed as the pH is decreased from pH 8 to 4 in the presence of sucrose suggesting that the secondary structure is thermally more stable at lower pH.

*Extrinsic Fluorescence Spectroscopy* – Propidium iodide (PI), an extrinsic fluorescent probe, was employed to assess the quaternary structural stability of the Ad2 capsid (Figs. 130-131). PI is a DNA intercalating dye whose fluorescence is enhanced ~20-30-fold upon binding DNA. The fluorescence of PI is therefore quenched until the viral capsid is compromised and the DNA becomes accessible. The fluorescence of PI in Ad2 at pH 3 remained relatively constant over the entire temperature range studied. The reason for this lack of fluorescence intensity change is not established, but a plausible explanation is that the DNA is inaccessible due to aggregation. The data suggests that the stability of the quaternary structure of the Ad2 capsid is maximized at pH 4 in CP and pH 5 in CPS since the increase in PI fluorescence occurs near 52° for both buffer compositions. Perhaps surprisingly, the PI fluorescence in CPS at pH 4 is enhanced at 10° C suggesting that the viral particles are completely disrupted at pH 4 in the presence of sucrose. On the other hand, sucrose does appear to have a stabilizing effect on the quaternary structure of Ad2 at pH 7 and 8 since the increase in PI fluorescence intensity occurs at lower temperatures in the absence of sucrose at these pH values. The best quaternary structural stability, however, is seen at pH 4 in CP and at pH 5 in CPS.

*Ad2 Empirical Phase Diagrams* – Phase diagrams are shown in Figures 132-133. When the data are combined and summarized in the form of phase diagrams, it becomes evident that Ad2 is thermally most stable near pH 5 in the presence of 10% sucrose. Although a phase transition does not occur until approximately 60° C in the absence of sucrose, the color of the phase below the transition temperature is slightly different when compared to pH 6-8 at low temperatures (regions

where adenovirus is known to be biologically active). Whether this difference in color reflects an effect on the activity of Ad2 is not known. The phase diagrams also indicate that the thermal stability of Ad2 is decreased at pH 8 in CP and CPS. Aggregation and anomalies in the extrinsic fluorescence spectroscopy measurements result in distinct phase behavior at pH 3 and 4 compared to the other pH values studied.

*GRAS excipients screening* – A 96-well microplate containing Ad2 in the presence of 32 different GRAS compounds at various concentrations was analyzed in the fluorescence mode employing the extrinsic fluorescent dye propidium iodide (PI). The fluorescence of PI is quenched when not bound to DNA, however, upon DNA intercalation, its fluorescence is enhanced up to 100-fold. This dye was therefore employed to assess the capsid integrity of Ad2 at pH 6 over a 2h time period at 55 °C. Initial results are listed in Figures 134-143. Based on the data in Figures 134-143, the increase in PI fluorescence intensity was significantly inhibited by eleven excipients. Although Asp, Glu, lactic acid, 20% lactose and 20% glycerol delay the onset of PI fluorescence enhancement, the best capsid stability of Ad2 is observed in the presence of 10% lactose, 0.2M sodium citrate, malic acid, Lys, Gly, sorbitol and sucrose. Based on these results, the secondary, tertiary, and quaternary structural stability of Ad2 will be characterized in the presence of these excipients alone and in combination with one another.

*Conclusions* – The data obtained suggests that the thermal stability of Ad2 under the conditions studied is maximal at pH 5 in the presence of 10% sucrose. Whether formulating Ad2 at pH 5 would have an impact on its activity is unknown at this point; however, if physical changes in the conformation of the virus are prevented, time-dependent activity may be enhanced.

A manuscript entitled, “Thermal Stability of Adenovirus Type 2 as a Function of pH” has been submitted to the Journal of Pharmaceutical Sciences (see appendices).

### **Effect of 10% Sucrose on Ad2 OD at 10° C**

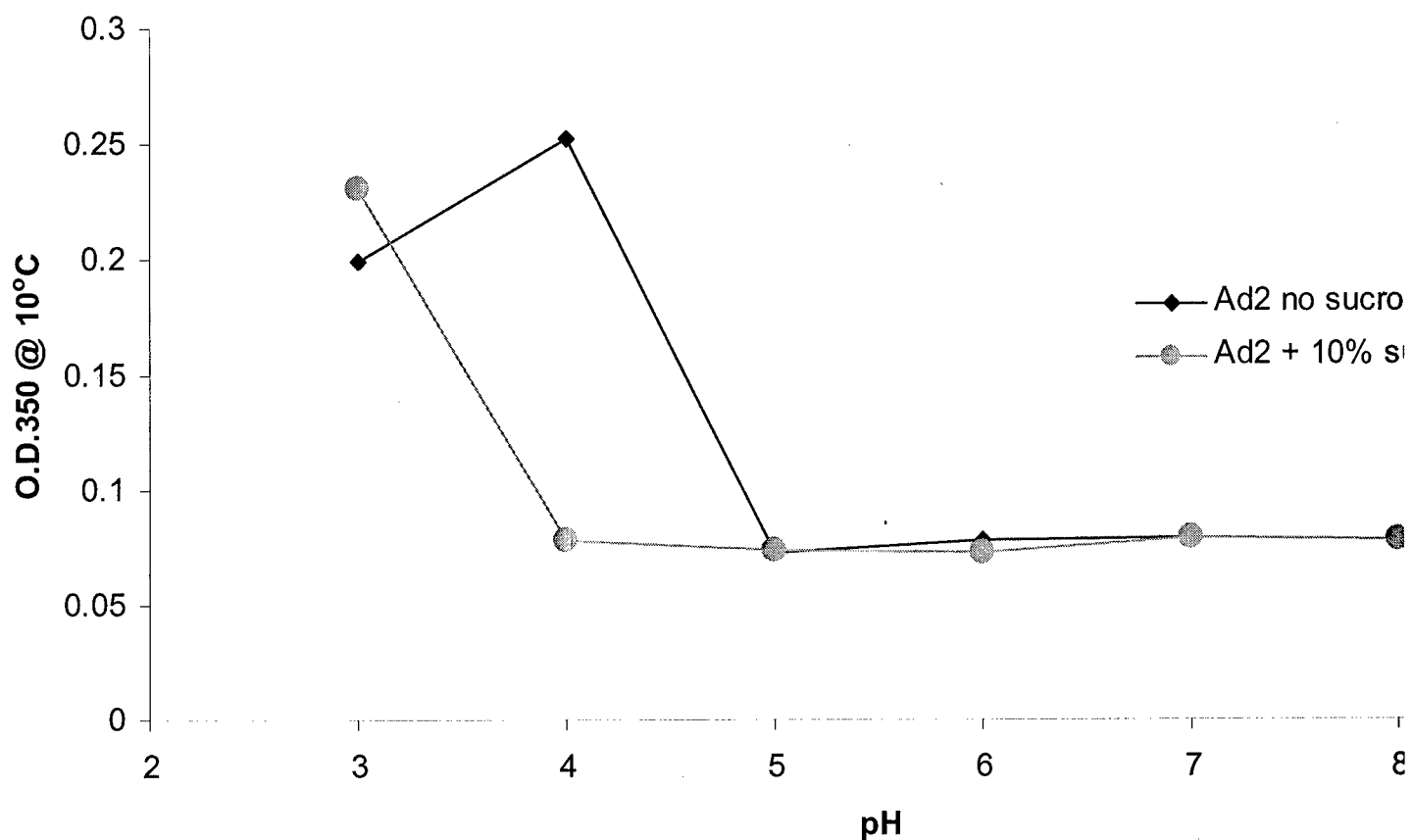


**Figure 107.** Effect of 10% sucrose on the optical density at 350 nm of Ad2 at 10° C, pH 7.

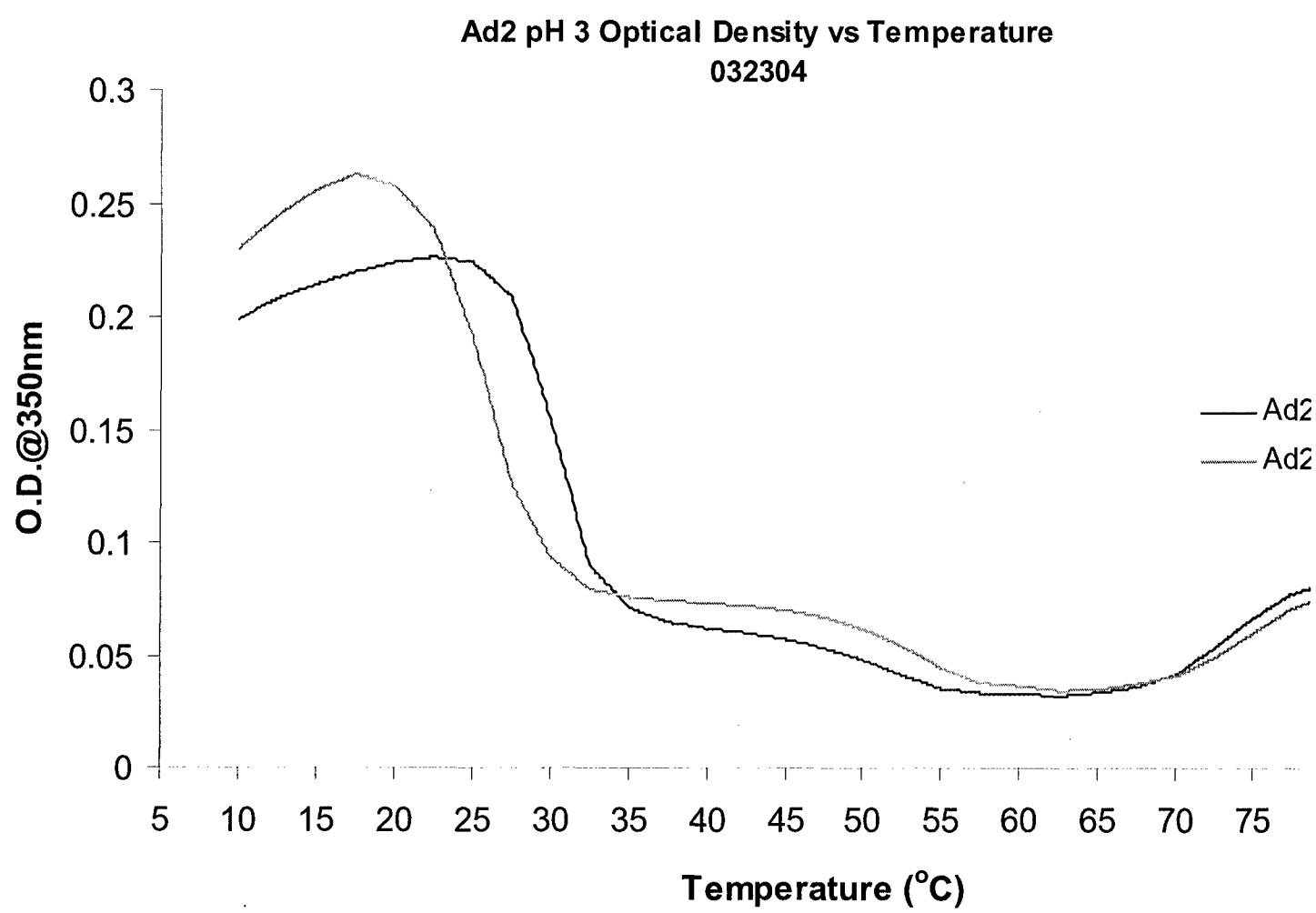


**Figure 108.** Interpolated heating trace of optical density at 350 nm for Ad2, pH 3.

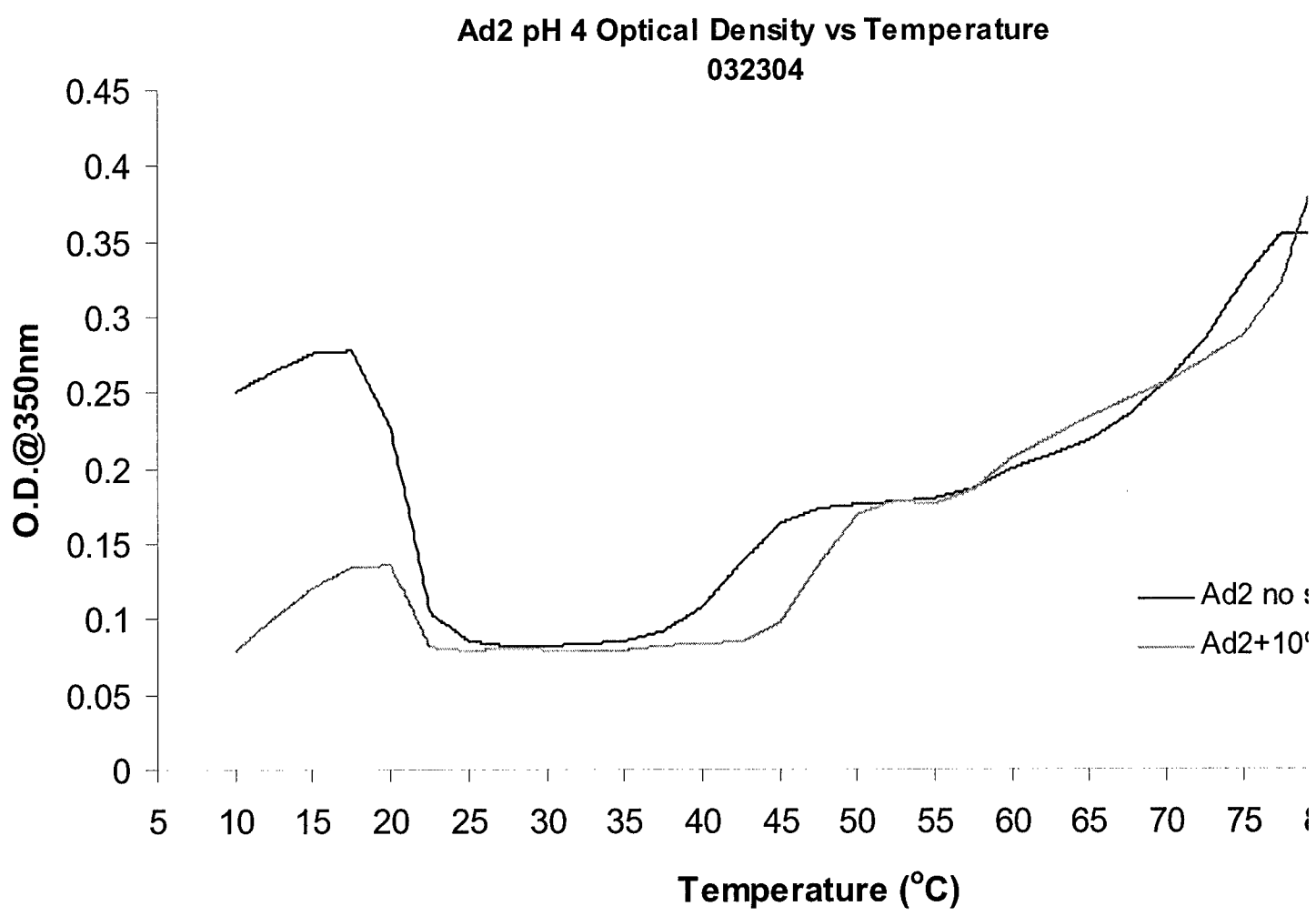


**Figure 109.** Interpolated heating trace of optical density at 350 nm for Ad2, pH 4.

**Ad2 pH 5 OD @ 350nm  
032404**

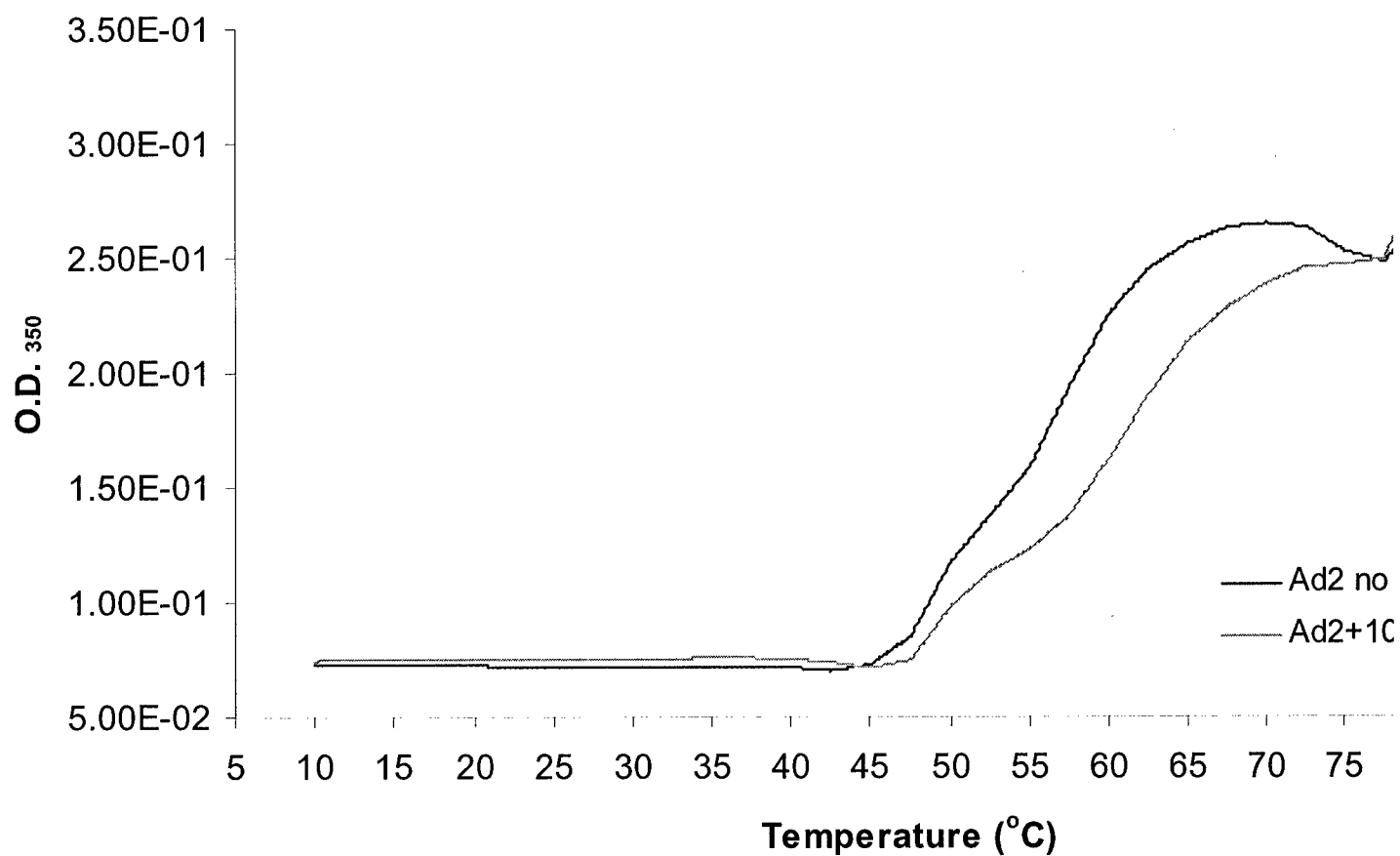


**Figure 110.** Interpolated heating trace of optical density at 350 nm for Ad2, pH 5.

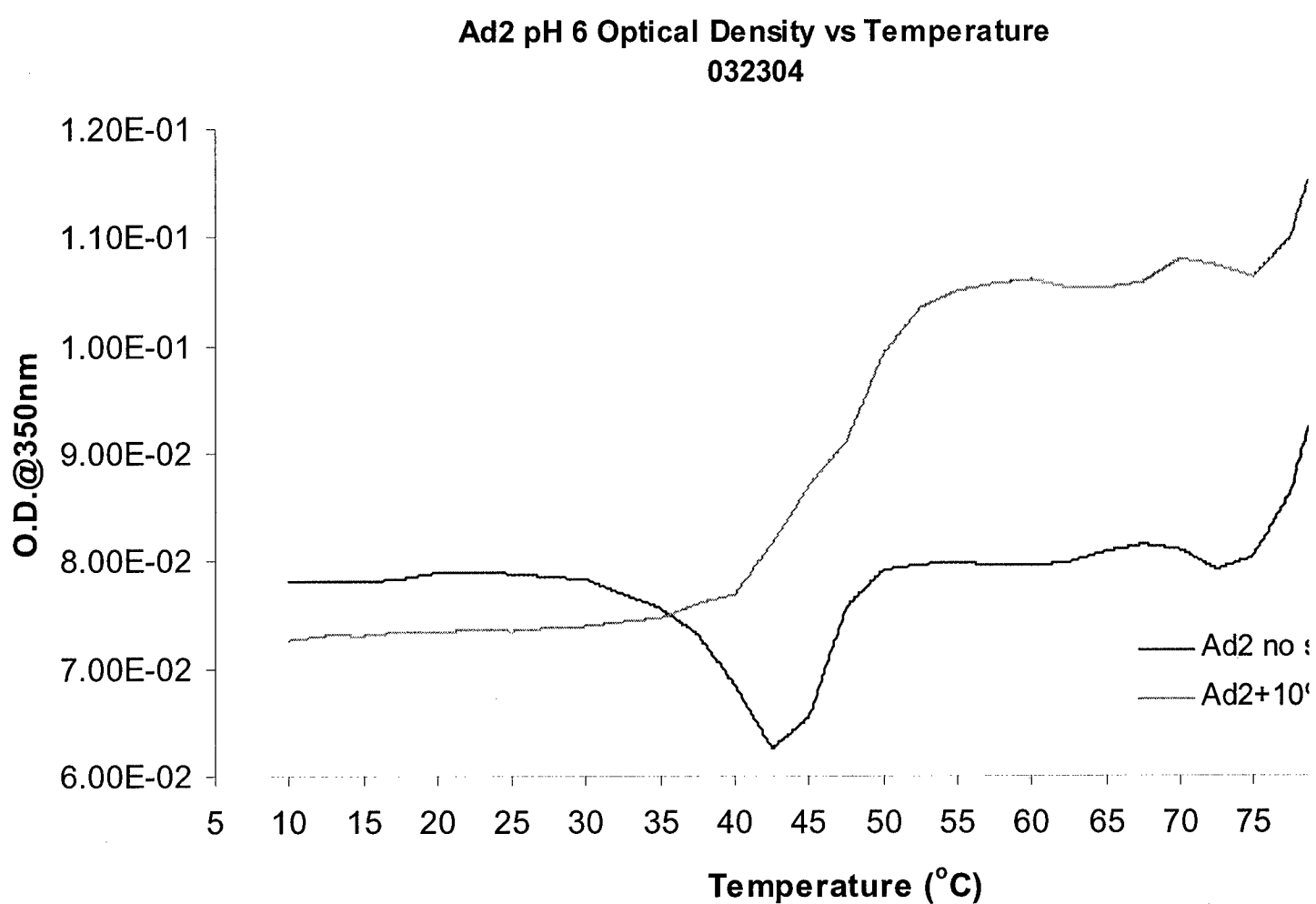


**Figure 111.** Interpolated heating trace of optical density at 350 nm for Ad2, pH 6.

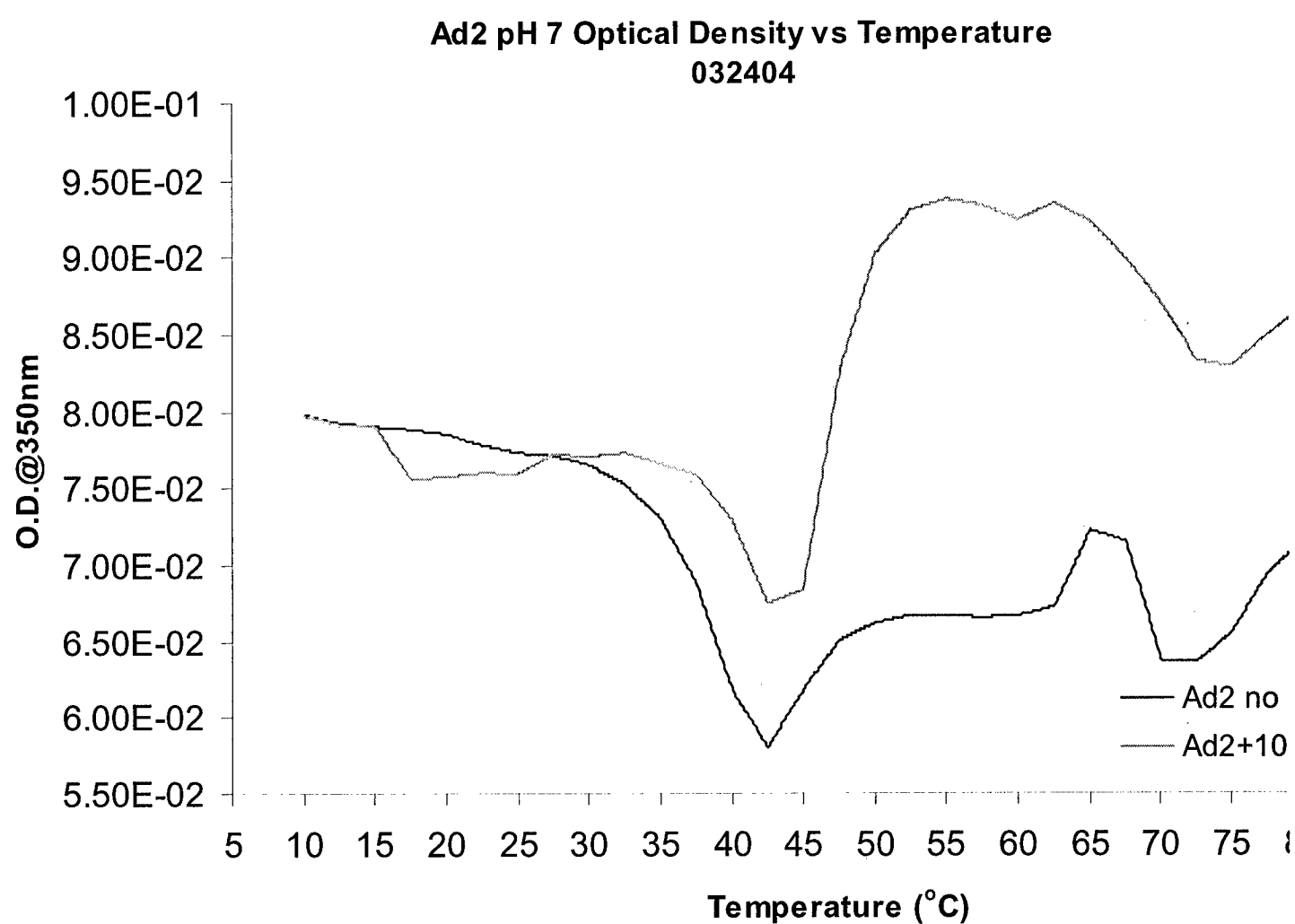


**Figure 112.** Interpolated heating trace of optical density at 350 nm for Ad2, pH 7.

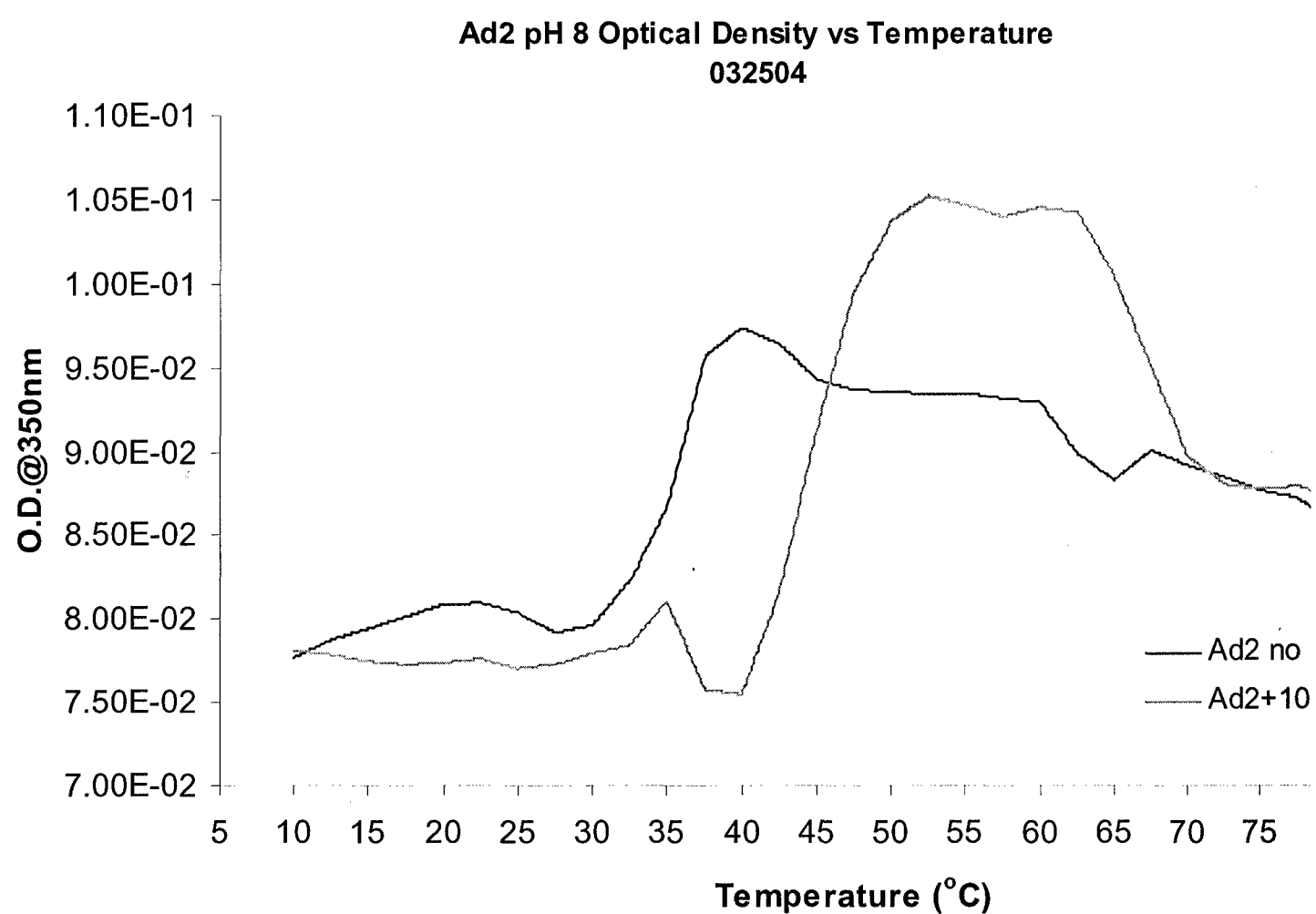


**Figure 113.** Interpolated heating trace of optical density at 350 nm for Ad2, pH 8.

### Second Derivative UV of Ad2 pH 3

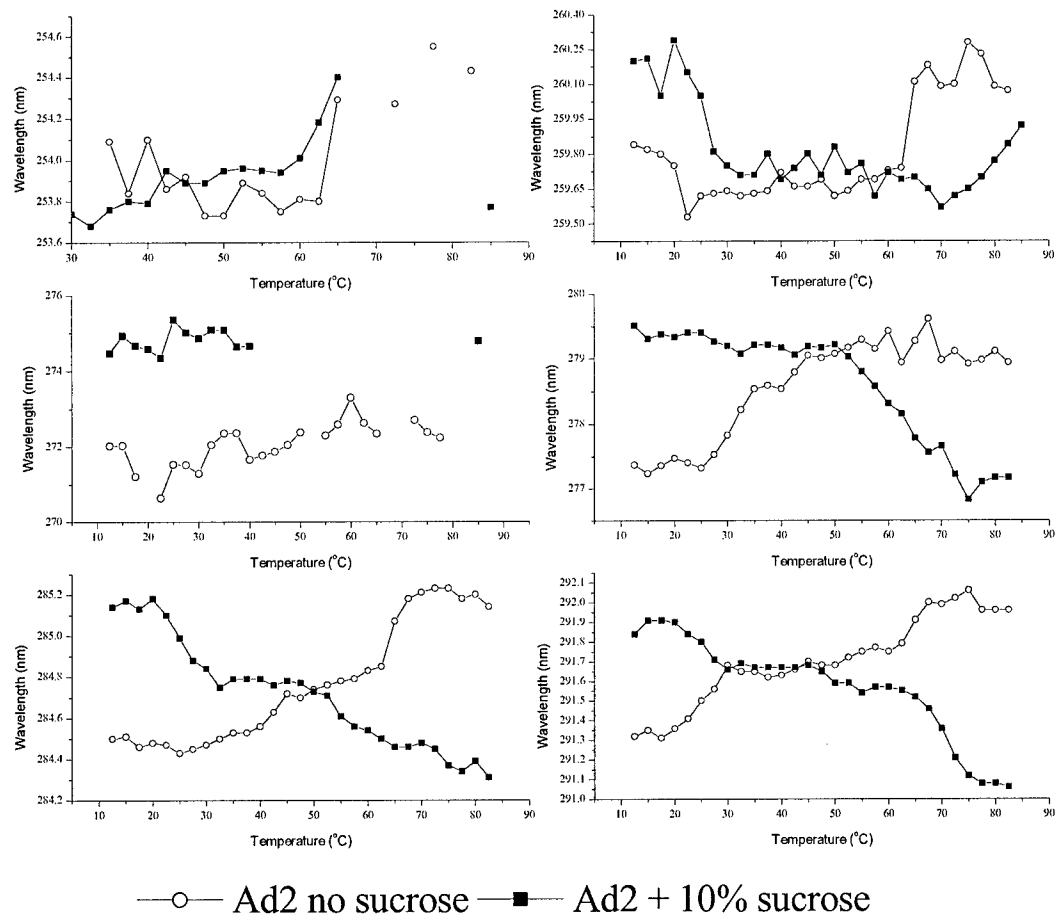


**Figure 114.** 2<sup>nd</sup> derivative UV peak position plots versus temperature of Ad2 at pH 3.

### Second Derivative UV of Ad2 pH 4

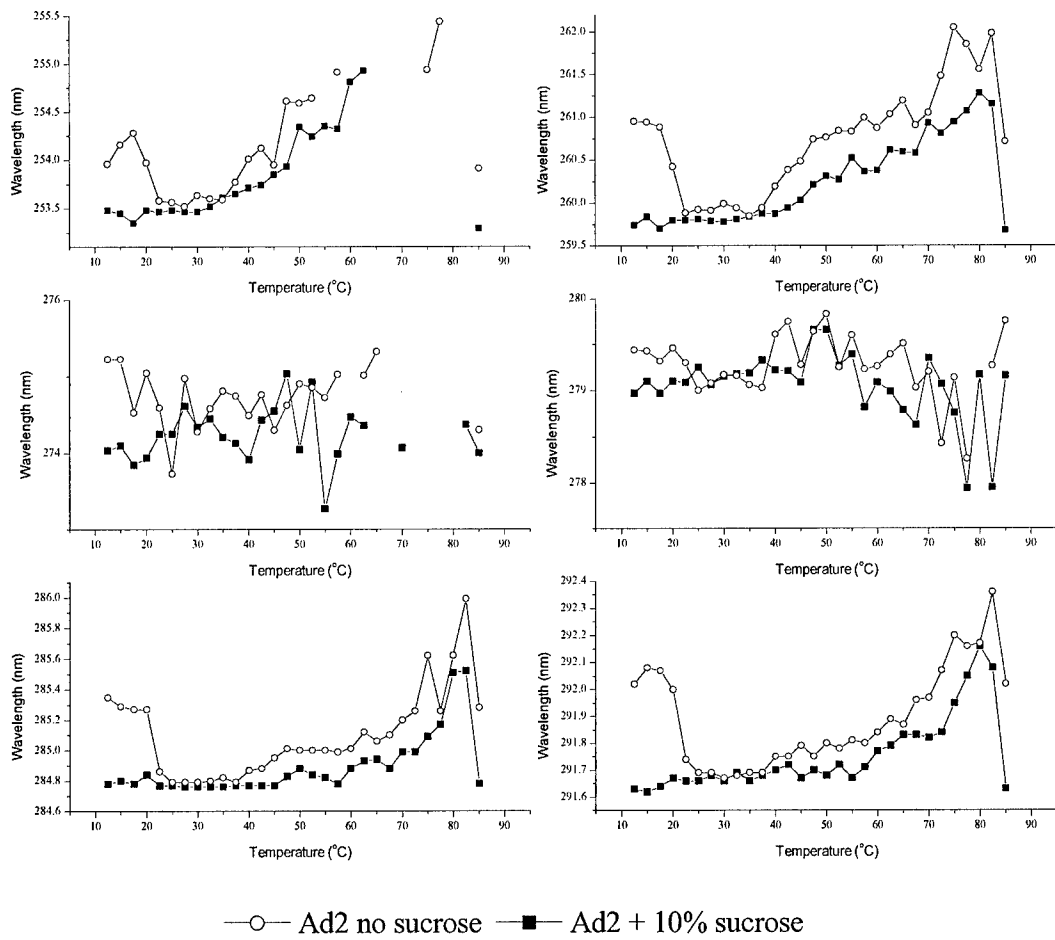


**Figure 115.** 2<sup>nd</sup> derivative UV peak position plots versus temperature of Ad2 at pH 4.

### Second Derivative UV of Ad2 pH 5

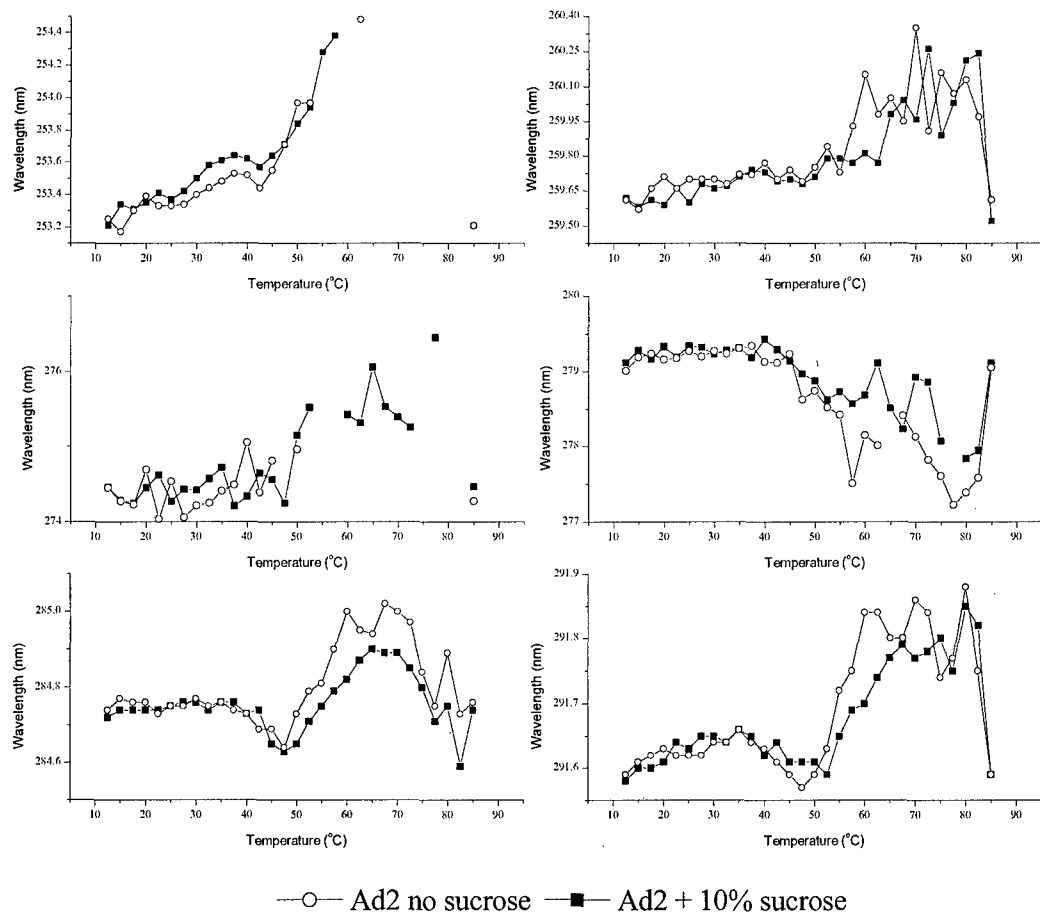


**Figure 116.** 2<sup>nd</sup> derivative UV peak position plots versus temperature of Ad2 at pH 5.

### Second Derivative UV of Ad2 pH 6

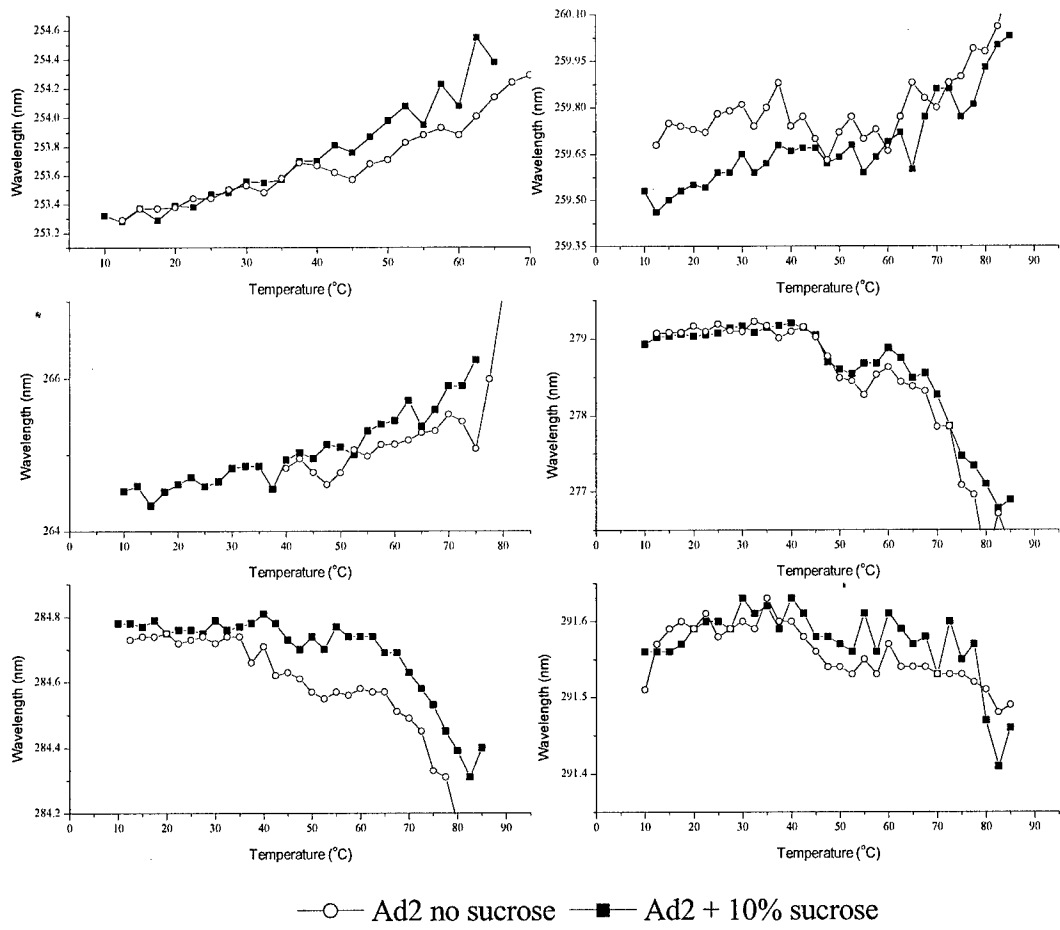


**Figure 117.** 2<sup>nd</sup> derivative UV peak position plots versus temperature of Ad2 at pH 6.

### Second Derivative UV of Ad2 pH 7

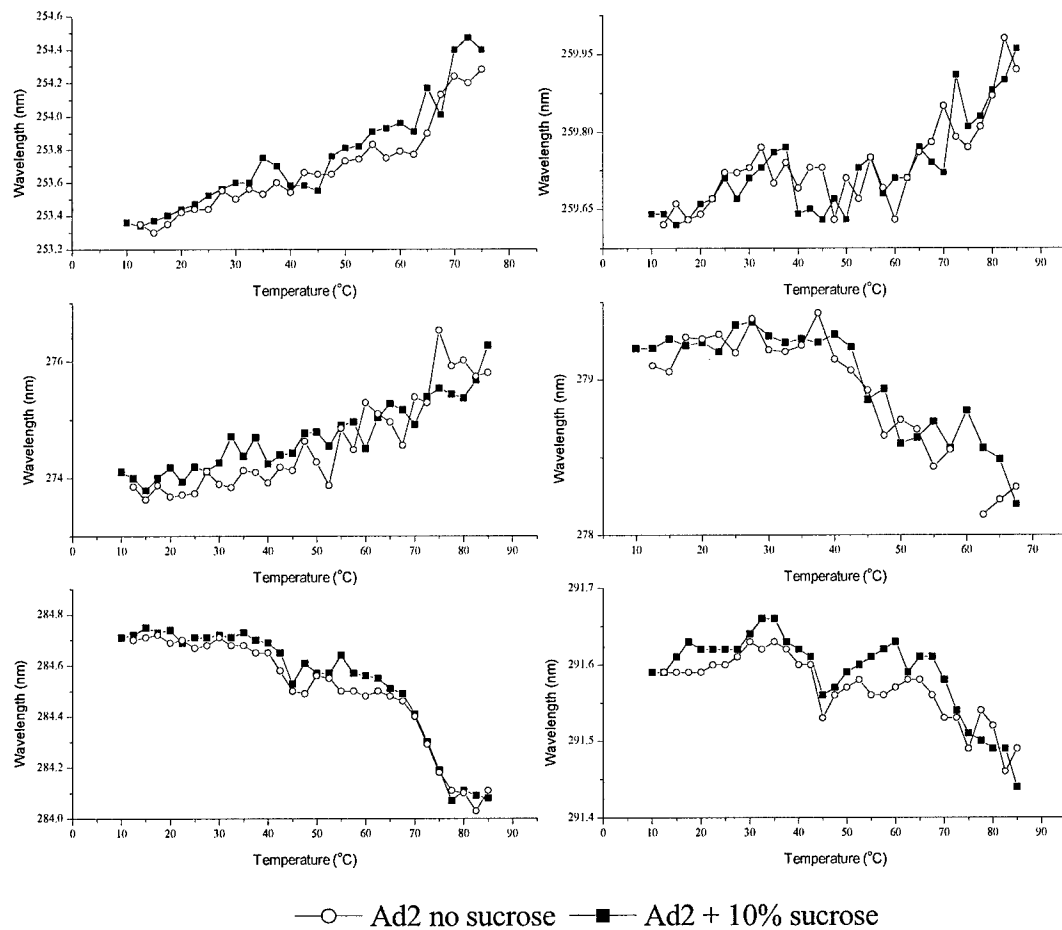


**Figure 118.** 2<sup>nd</sup> derivative UV peak position plots versus temperature of Ad2 at pH 7.

### Second Derivative of Ad2 pH 8

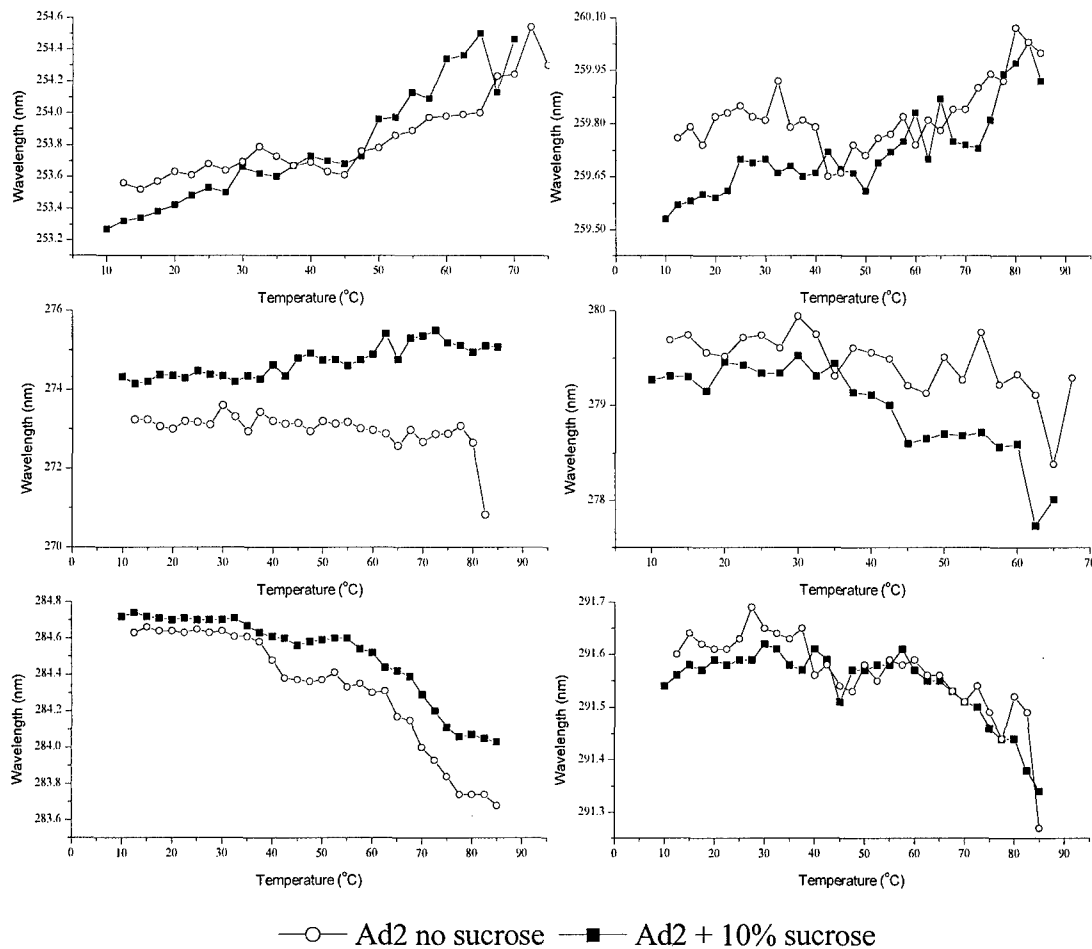
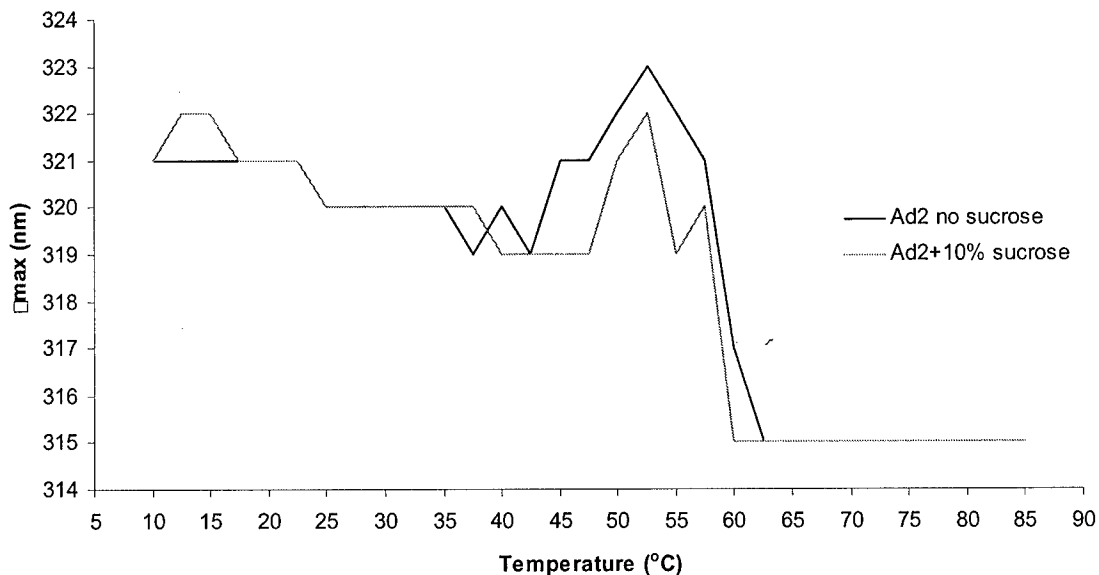


**Figure 119.** 2<sup>nd</sup> derivative UV peak position plots versus temperature of Ad2 at pH 8.

### Ad2 pH 3 Intrinsic Fluorescence Peak Position vs Temperature



### Ad2 pH 3 Normalized Intrinsic Fluorescence Intensity at $\lambda_{\text{max}}$ vs Temperature

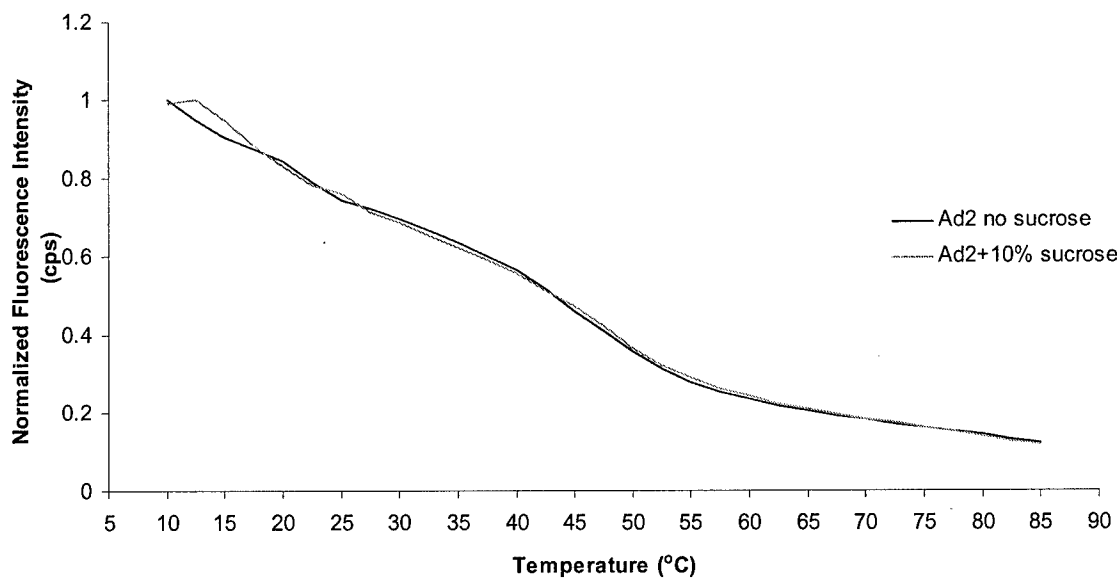


**Figure 120.** Top: intrinsic fluorescence spectroscopy peak position versus temperature of Ad2 at pH 3. Bottom: normalized intrinsic fluorescence intensity at  $\lambda_{\text{max}}$  versus temperature for Ad2 at pH 3.

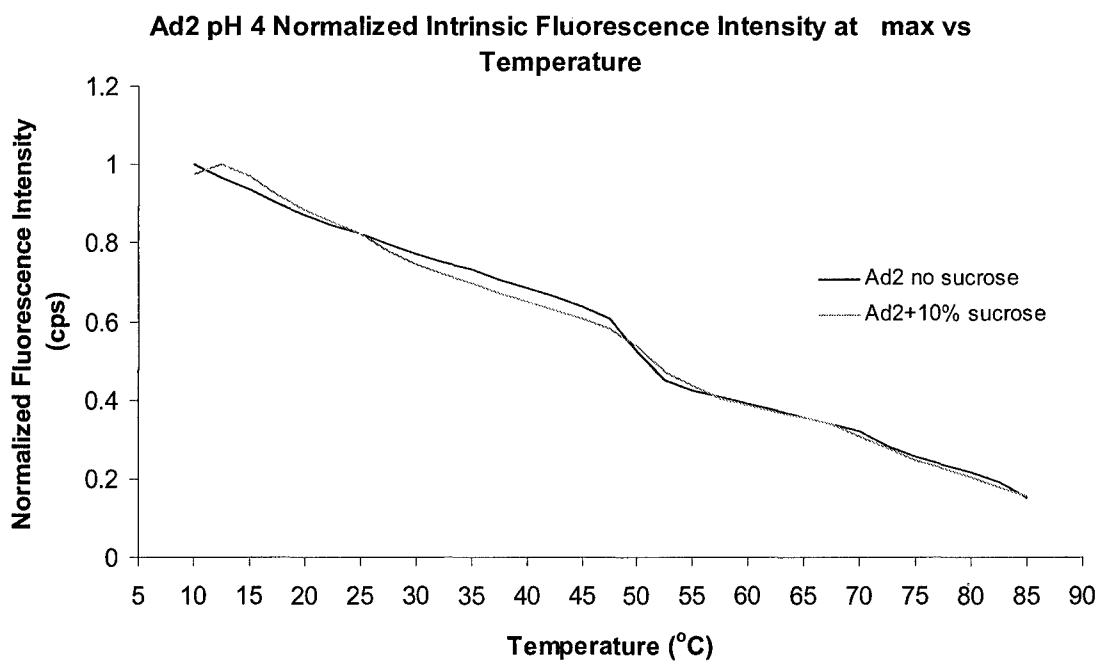
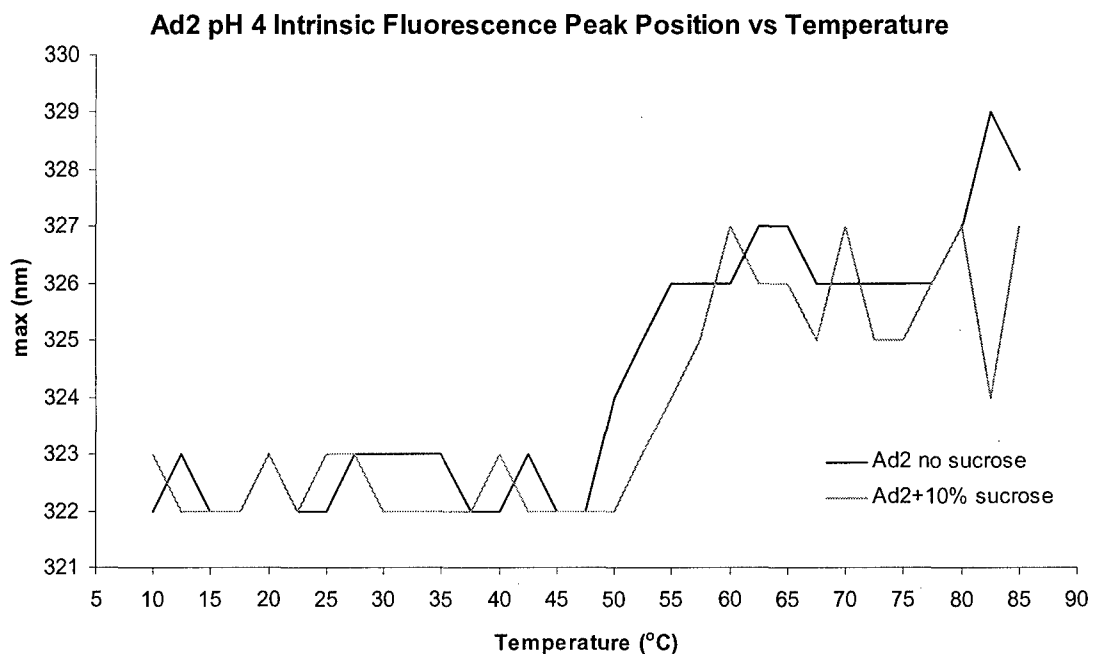


**Figure 121.** Top: intrinsic fluorescence spectroscopy peak position versus temperature of Ad2 at pH 4. Bottom: normalized intrinsic fluorescence intensity at  $\lambda_{\text{max}}$  versus temperature for Ad2 at pH 4.

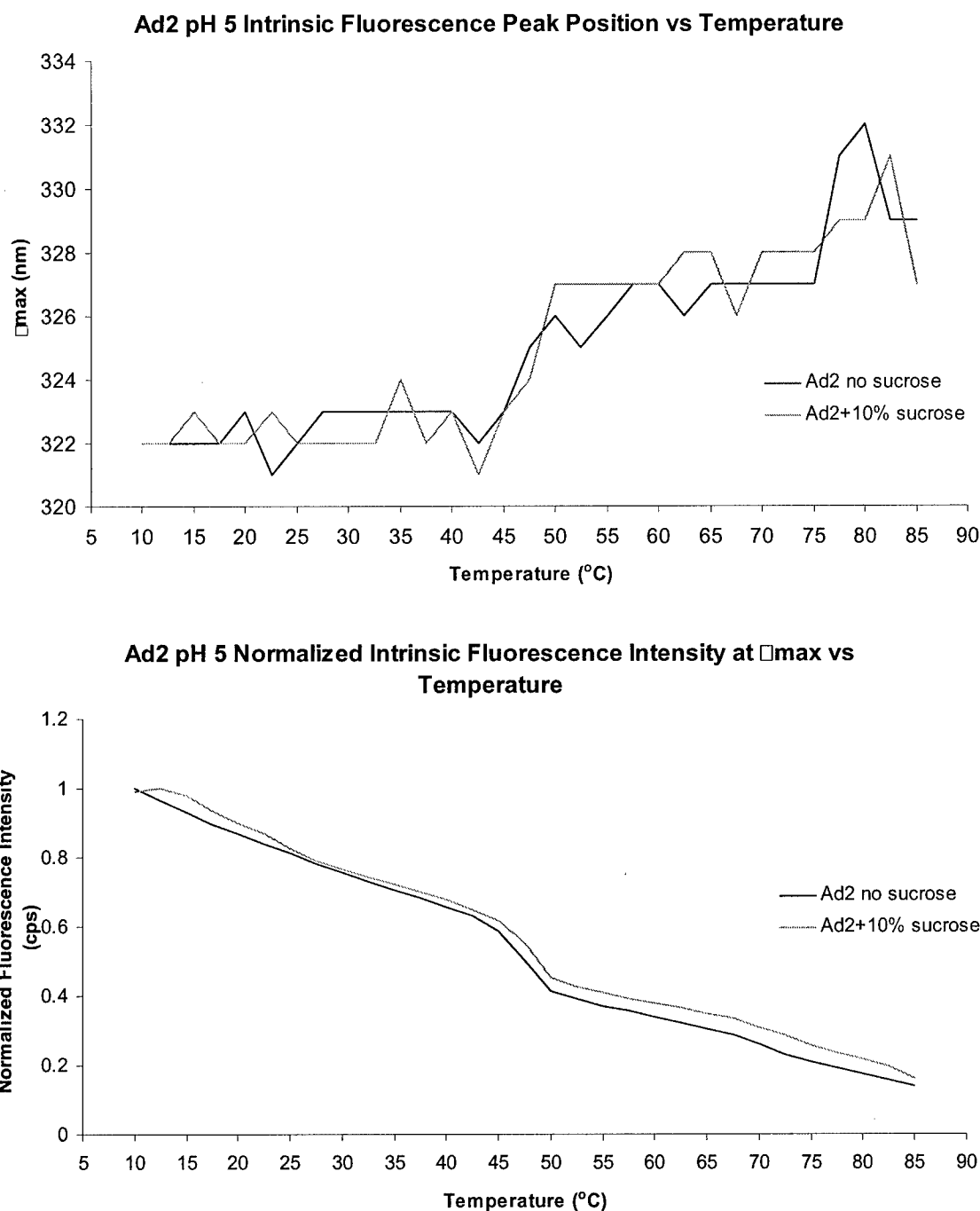
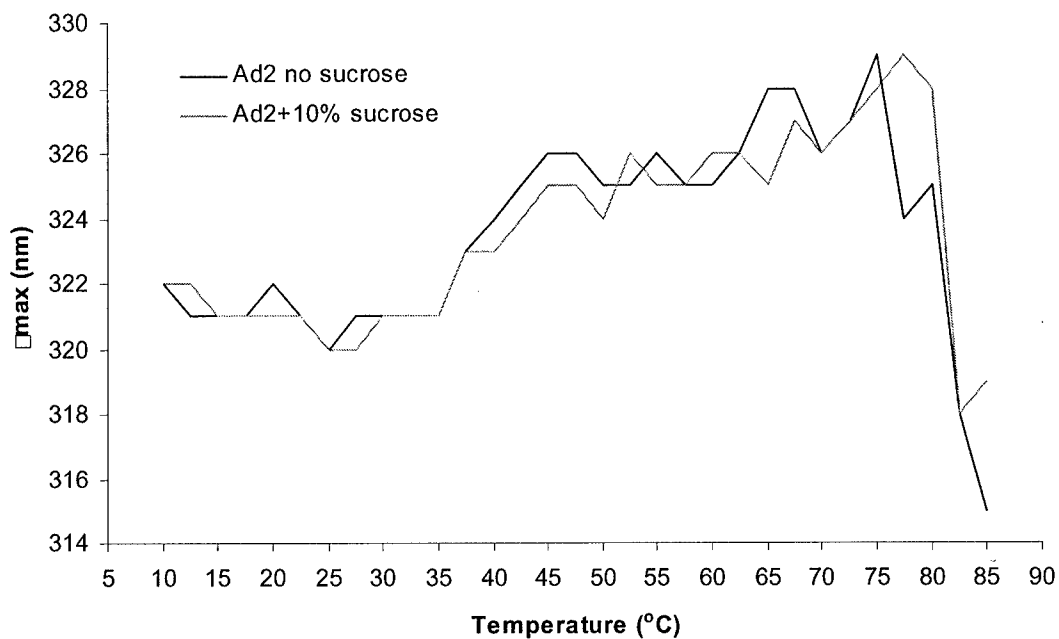


**Figure 122.** Top: intrinsic fluorescence spectroscopy peak position versus temperature of Ad2 at pH 5. Bottom: normalized intrinsic fluorescence intensity at  $\lambda_{max}$  versus temperature for Ad2 at pH 5.

### Ad2 pH 6 Intrinsic Fluorescence Peak Position vs Temperature



### Ad2 pH 6 Normalized Intrinsic Fluorescence Intensity at $\lambda_{max}$ vs Temperature

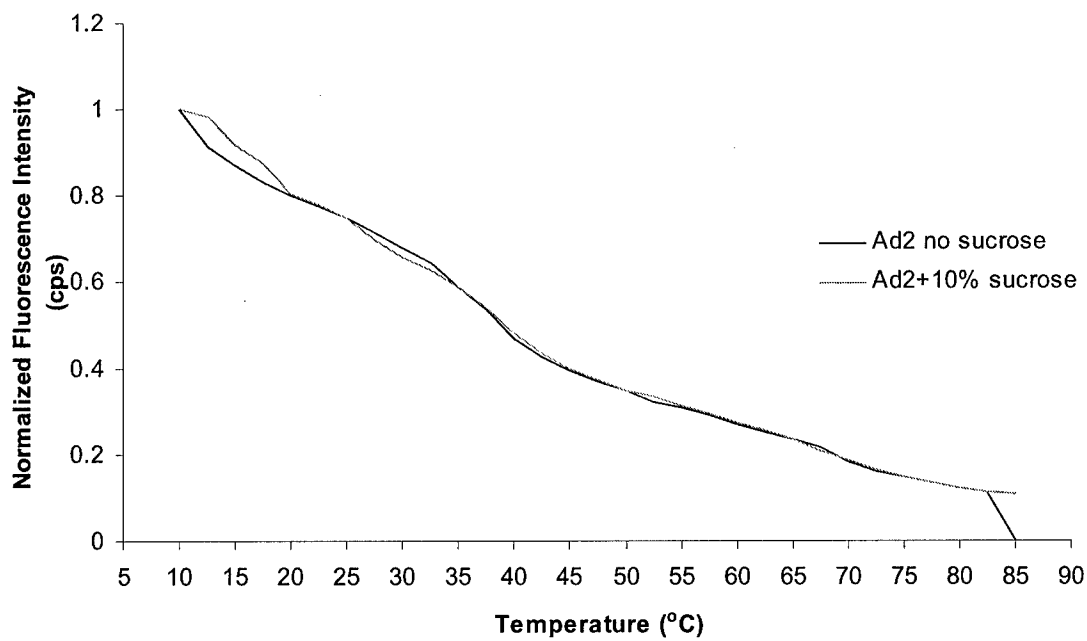


**Figure 123.** Top: intrinsic fluorescence spectroscopy peak position versus temperature of Ad2 at pH 6. Bottom: normalized intrinsic fluorescence intensity at  $\lambda_{max}$  versus temperature for Ad2 at pH 6.

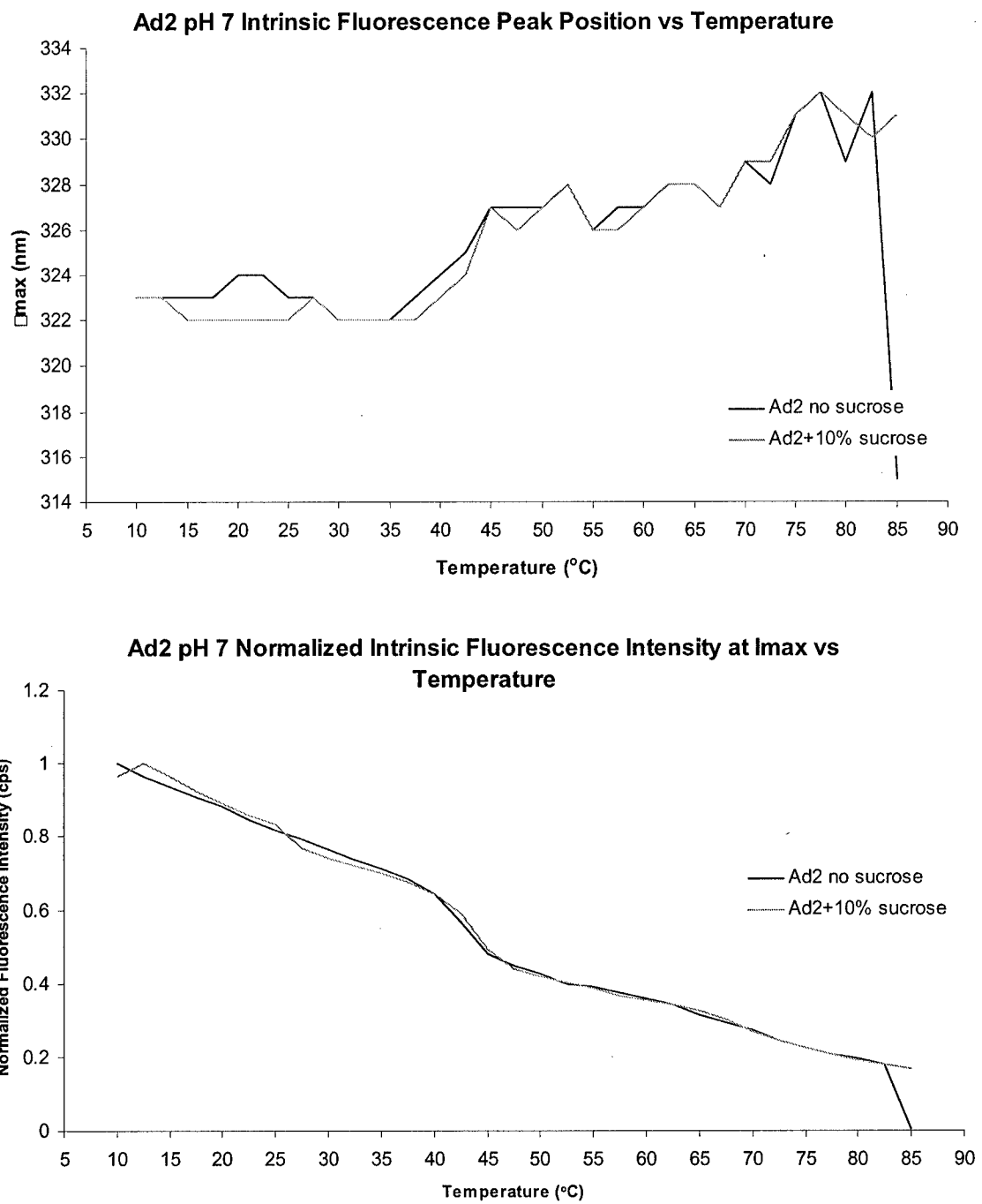


**Figure 124.** Top: intrinsic fluorescence spectroscopy peak position versus temperature of Ad2 at pH 7. Bottom: normalized intrinsic fluorescence intensity at  $\lambda_{max}$  versus temperature for Ad2 at pH 7.

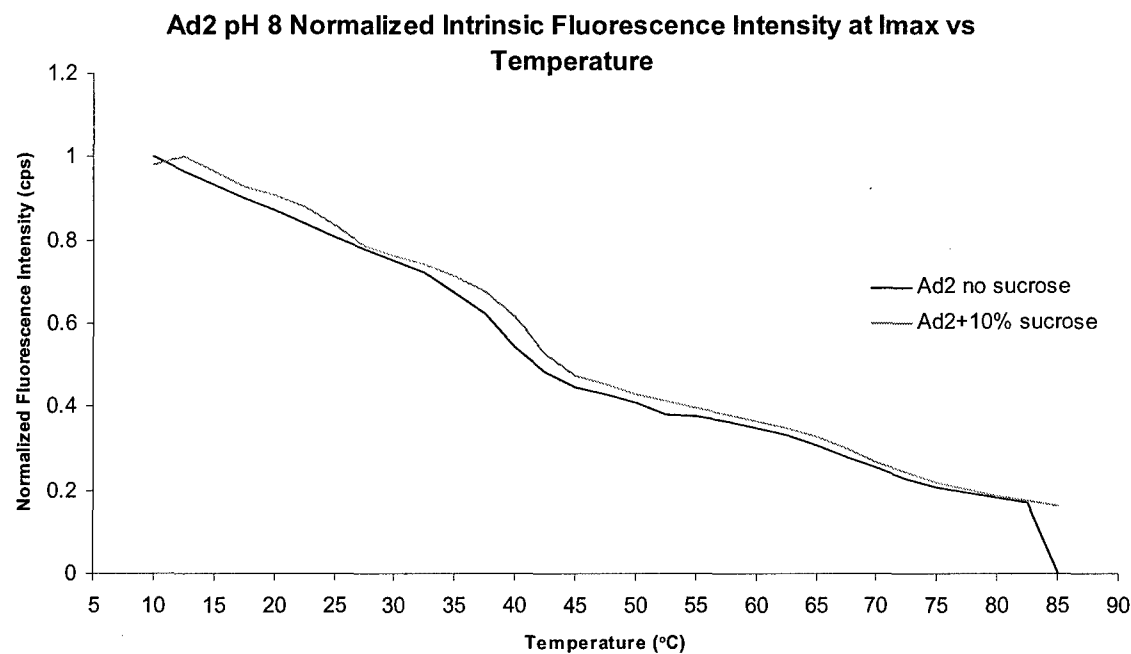
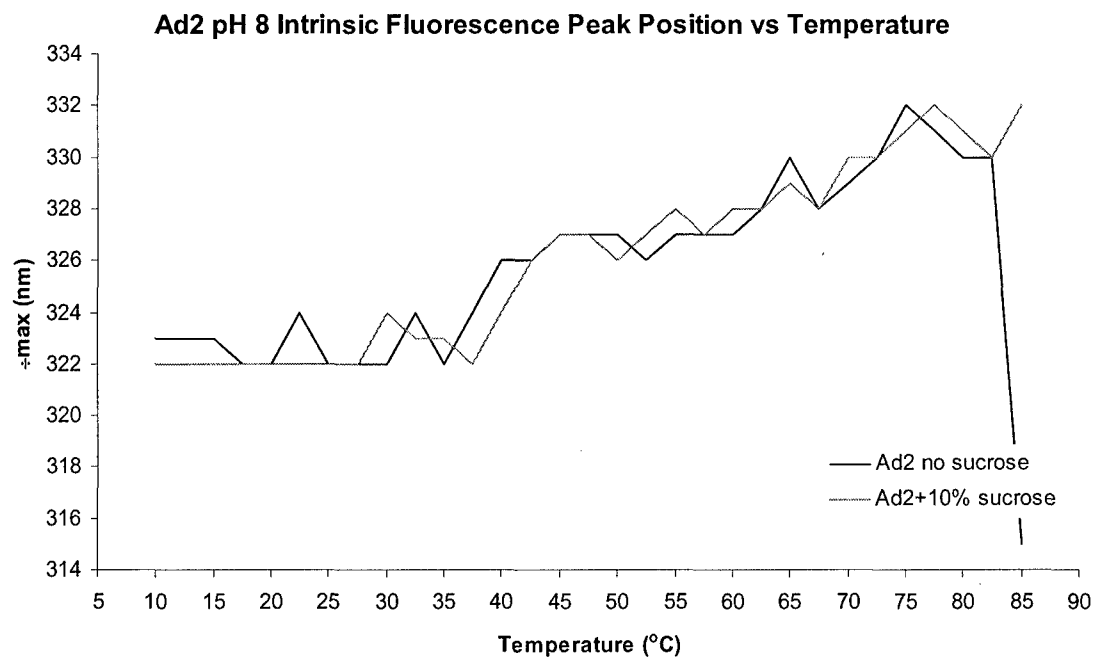


**Figure 125.** Top: intrinsic fluorescence spectroscopy peak position versus temperature of Ad2 at pH 8. Bottom: normalized intrinsic fluorescence intensity at  $\lambda_{\text{max}}$  versus temperature for Ad2 at pH 8.

### Normalized Ad2 CD Spectra at 10° C (no sucrose)

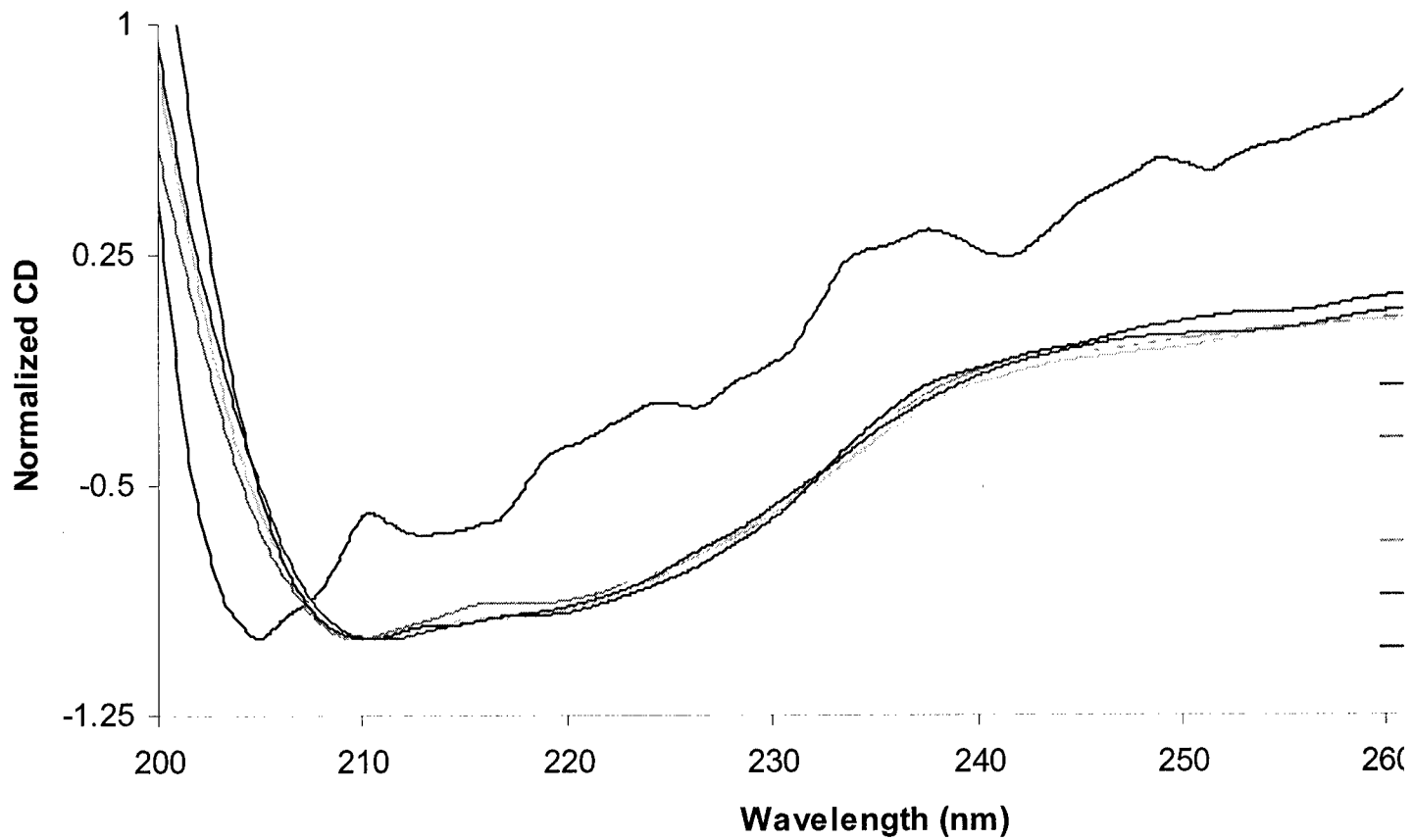


**Figure 126.** Normalized CD spectra of Ad2 in CP (no sucrose) at 10° C.

### Normalized Ad2 CD Spectra at 10° C in 10% Sucrose

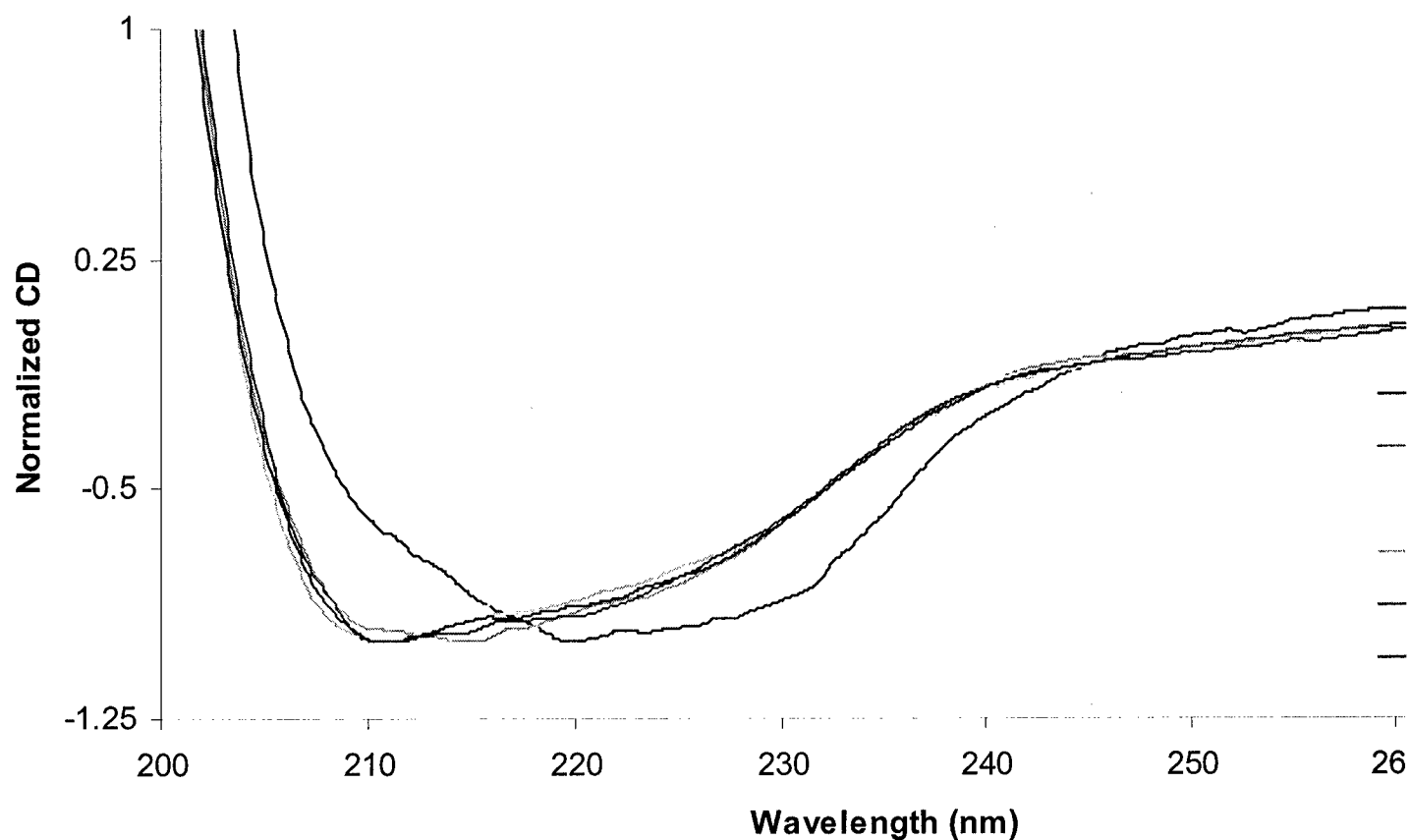


**Figure 127.** Normalized CD spectra of Ad2 in CPS at 10° C.

Normalized CD at 208 nm of Ad2 vs Temperature (no sucrose)

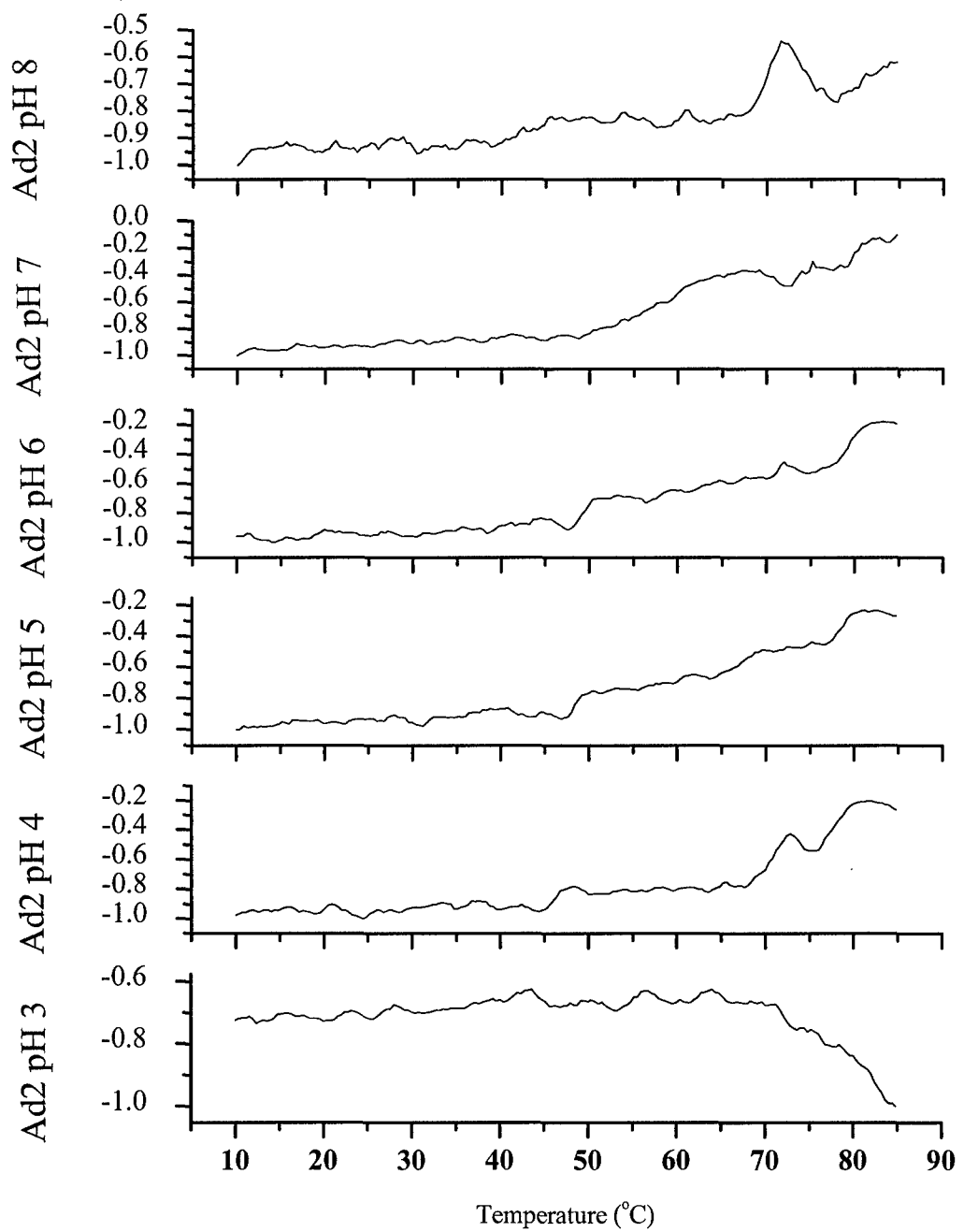


**Figure 128.** Normalized CD at 208 nm of Ad2 as a function of temperature in CP (no sucrose).

Normalized CD at 208 nm of Ad2 in 10% Sucrose vs Temperature

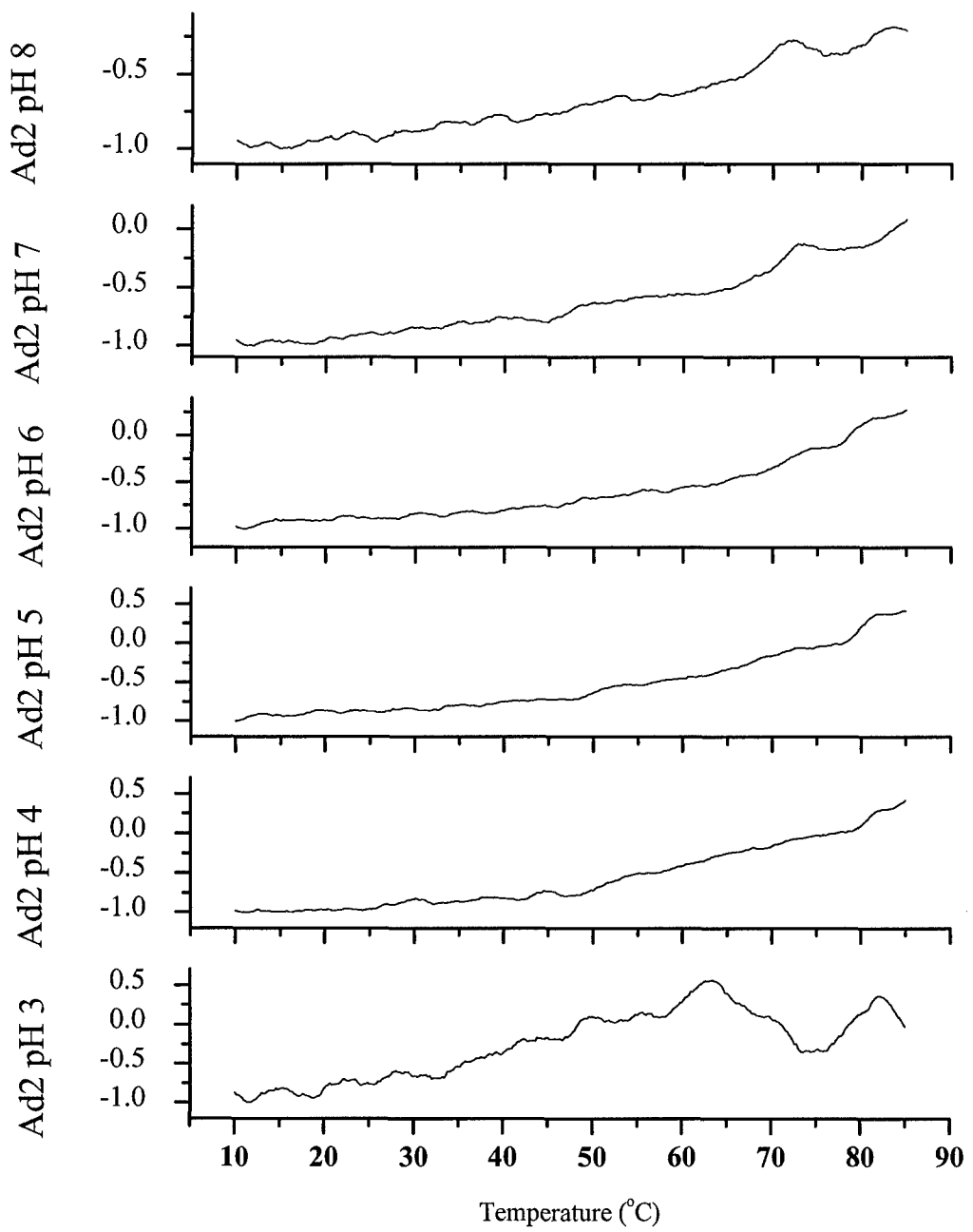


**Figure 129.** Normalized CD at 208 nm of Ad2 as a function of temperature in CPS.

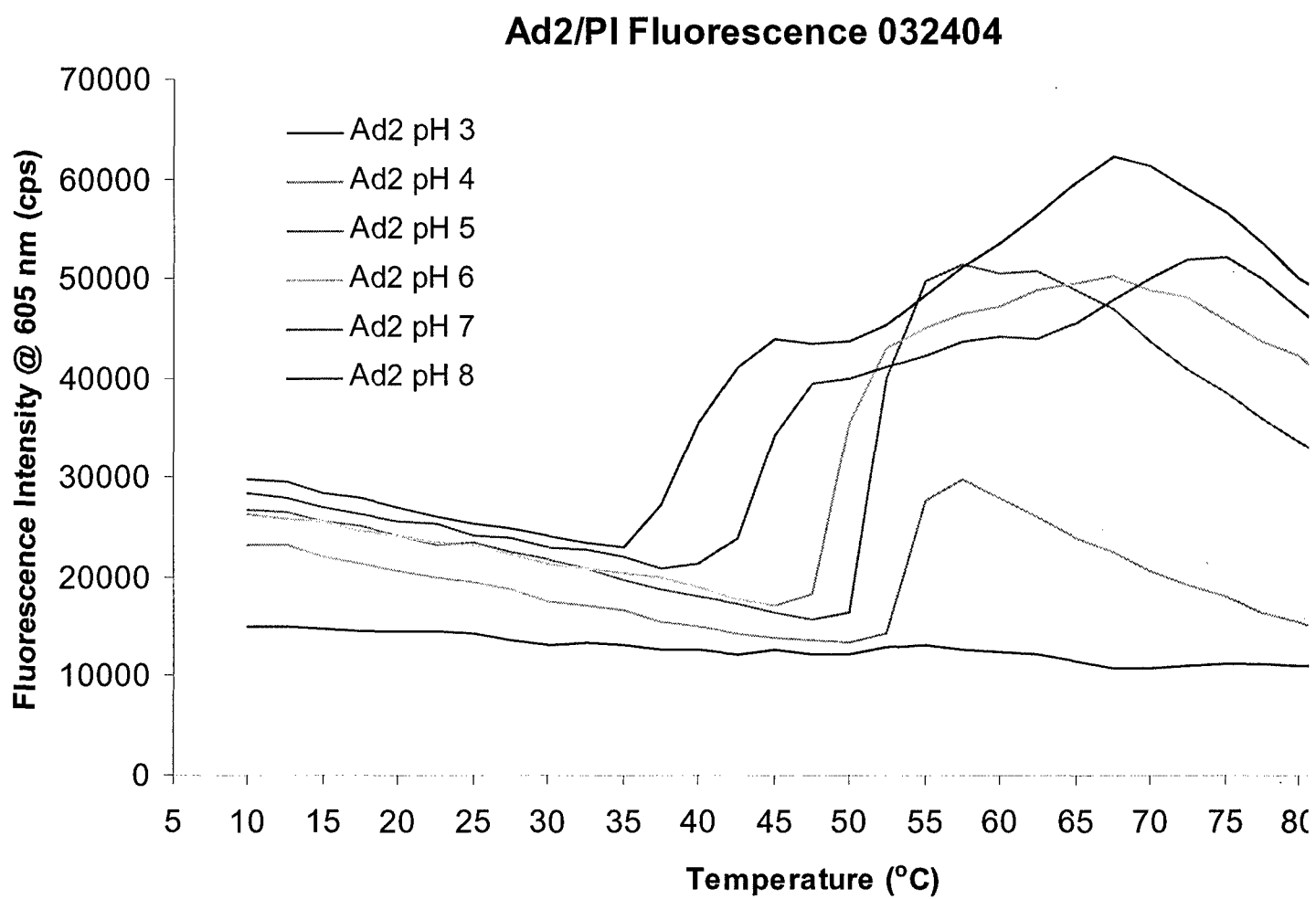


**Figure 130.** Extrinsic fluorescence spectroscopy of Ad2 (no sucrose) as a function of temperature.

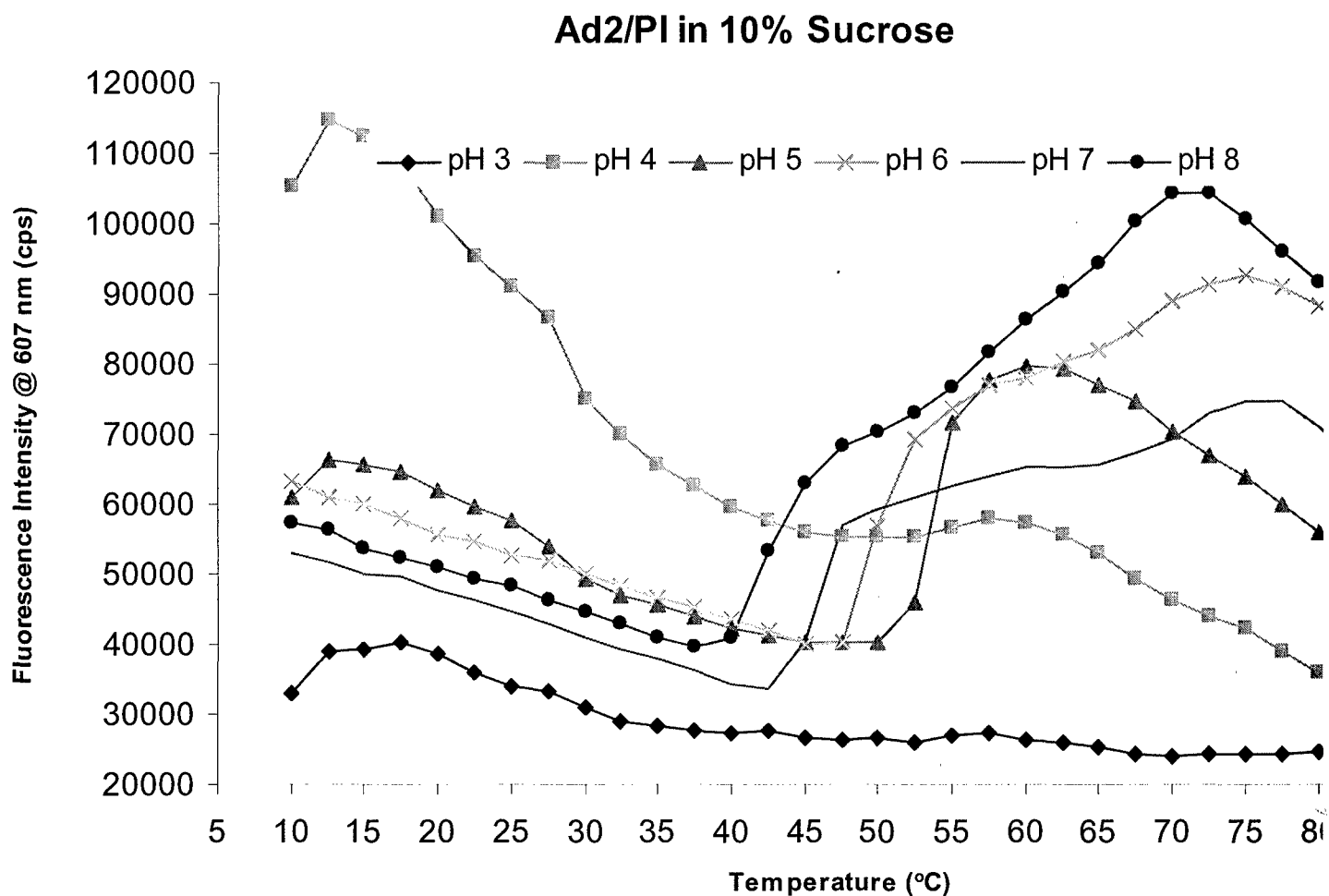


**Figure 131.** Extrinsic fluorescence spectroscopy of Ad2 in the presence of 10% sucrose as a function of temperature.

### *Ad2 Phase Diagram (no sucrose)*

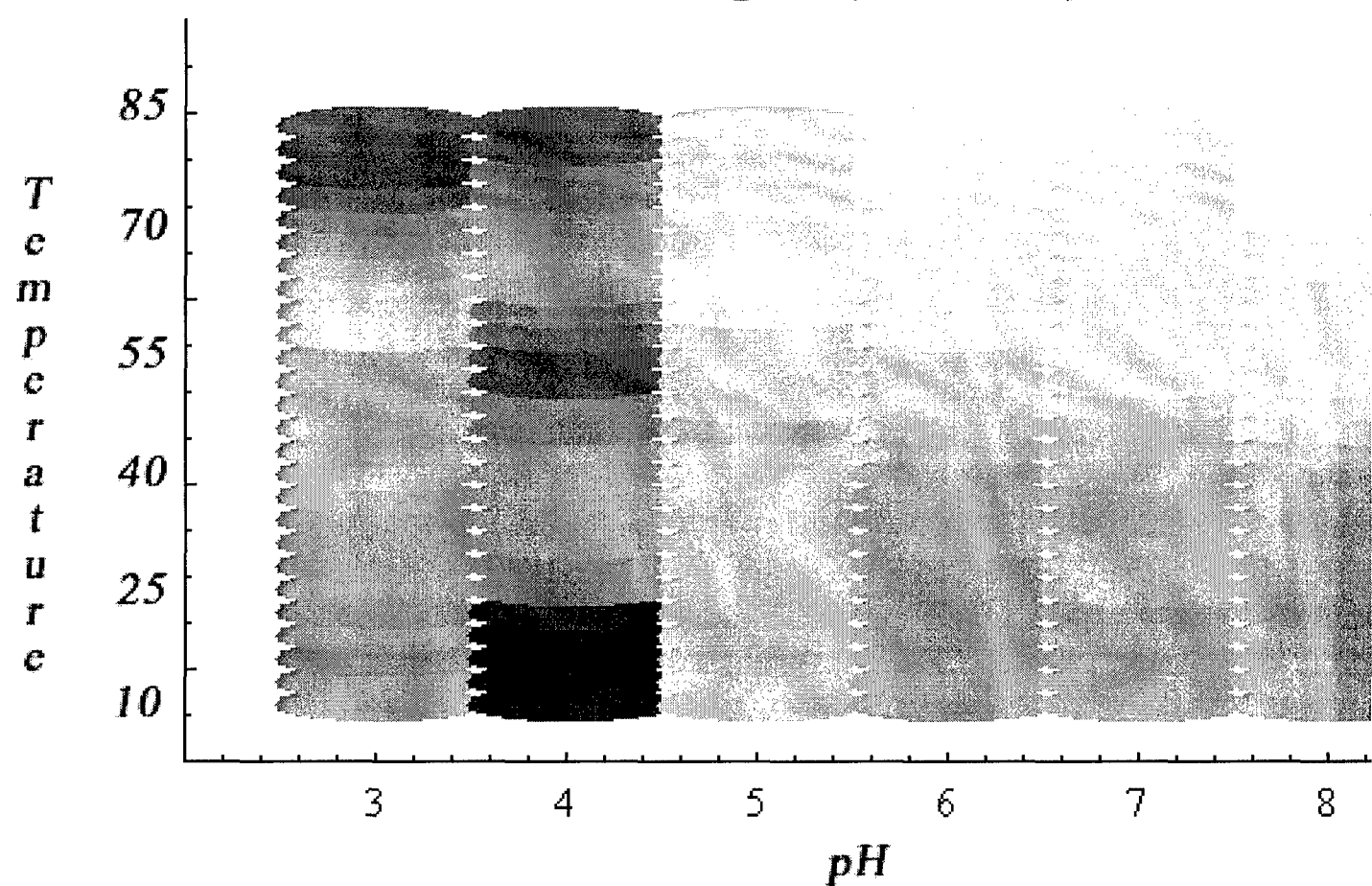


**Figure 132.** Empirical phase diagram of Ad2 as a function of temperature and pH in CP.

### *Ad2 in 10% Sucrose Phase Diagram*

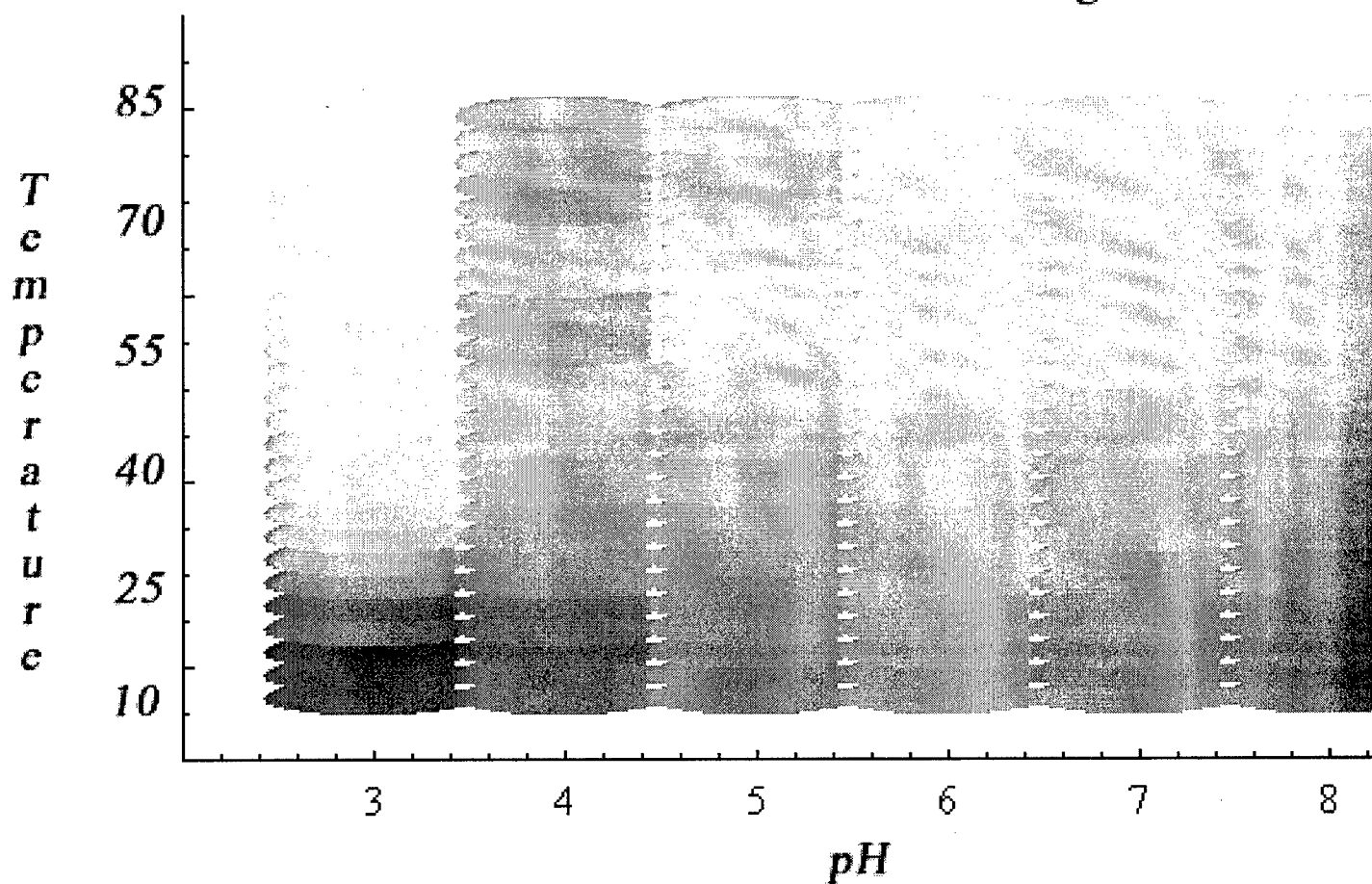


**Figure 133.** Empirical phase diagram of Ad2 as a function of temperature and pH in CPS.

	H	G	F	E	D
12	buffer	ascorbic acid (0.15M)	Na citrate (0.1M)	Pluronic F-68 (0.05%)	sucrose (20%)
11	buffer	aspartic acid (0.15M)	Na citrate (0.2M)	Pluronic F-68 (0.1%)	mannitol (10%)
10	buffer	glutamic acid (0.15M)	Brij 35 (0.01%)	Albumin (1%)	sorbitol (10%)
9	Ad2 alone	lactic acid (0.15M)	Brij 35 (0.05%)	Albumin (2.5%)	sorbitol (20%)
8	Ad2 alone	malic acid (0.15M)	Brij 35 (0.1%)	Albumin (5%)	glycerol (10%)
7	Ad2 alone	Arg (0.3M)	Tween 20 (0.01%)	lactose (10%)	glycerol (20%)
6	dextran sulfate (0.0003mM)	diethanolamine (0.3M)	Tween 20 (0.05%)	lactose (20%)	$\alpha$ -cyclodextrin (2.5%)
5	dextran sulfate (0.003mM)	guanidine (0.3M)	Tween 20 (0.1%)	trehalose (10%)	2-OH propyl b-CD (5%)
4	dextran sulfate (0.0075mM)	His (0.3M)	Tween 80 (0.01%)	trehalose (20%)	2-OH propyl b-CD (10%)
3	dextran T40 (0.0003mM)	Lys (0.3M)	Tween 80 (0.05%)	dextrose (10%)	2-OH propyl g-CD (5%)
2	dextran T40 (0.003mM)	Pro (0.3M)	Tween 80 (0.1%)	dextrose (20%)	2-OH propyl g-CD (10%)
1	dextran T40 (0.0075mM)	Gly (0.3M)	Pluronic F-68 (0.01%)	sucrose (10%)	Empty

**Table 5.** 96-well microplate layout. The wells contain ~1E11 vp/mL Ad2 at pH 6, 7.5  $\mu$ M propidium iodide, and the designated GRAS excipients. The numbers in parentheses indicate the concentration of excipients.

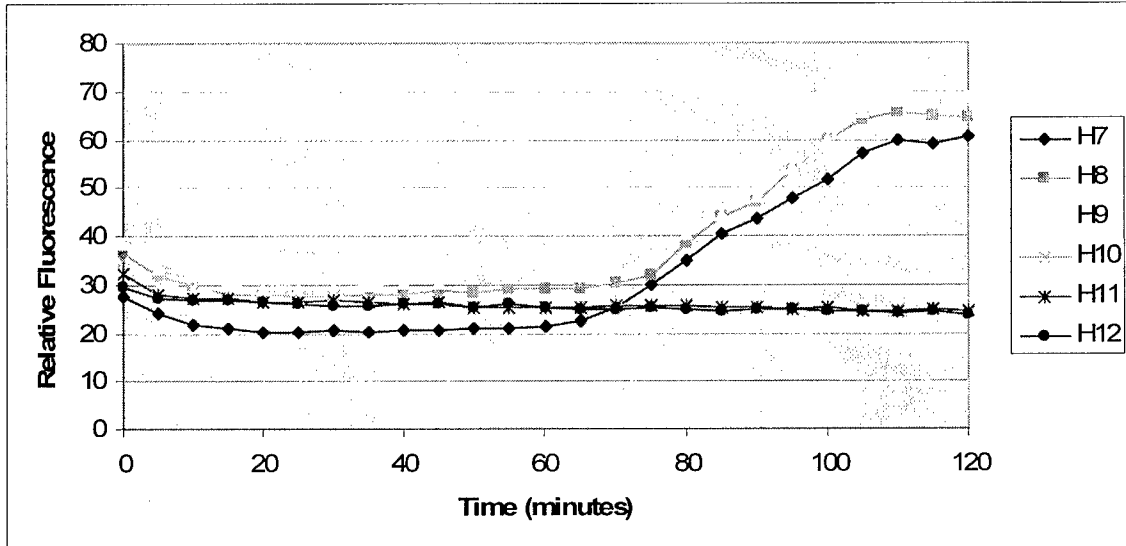


**Figure 134.** H 7-9 contain Ad2 at pH 6 (no excipients present). H 10-12 contain buffer alone.

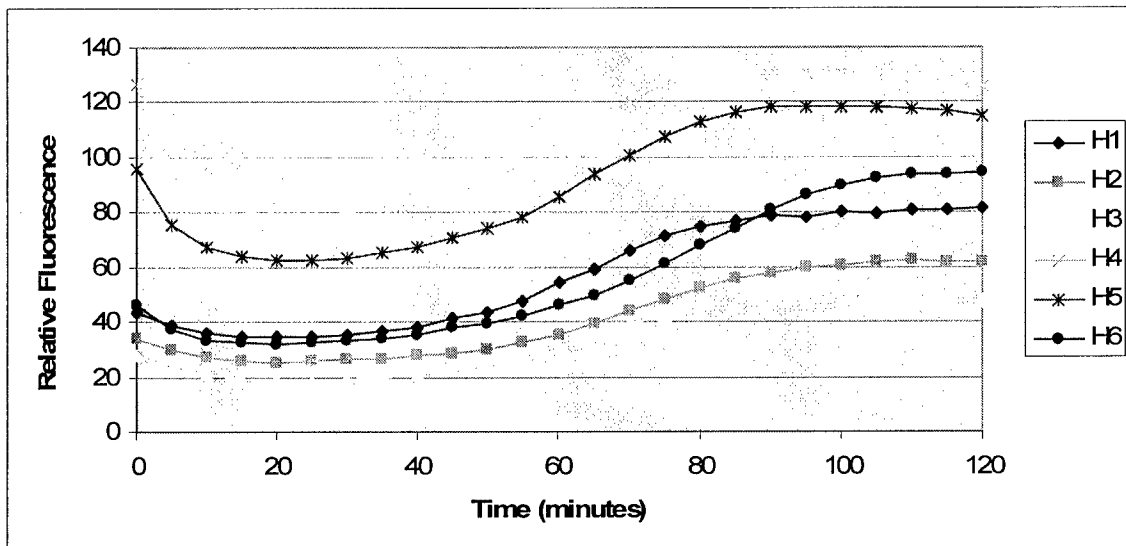


**Figure 135.** H 1-3 contain Ad2 in the presence of dextran T40 at different concentrations. H 4-6 contain Ad2 in the presence of dextran sulfate at various concentrations.

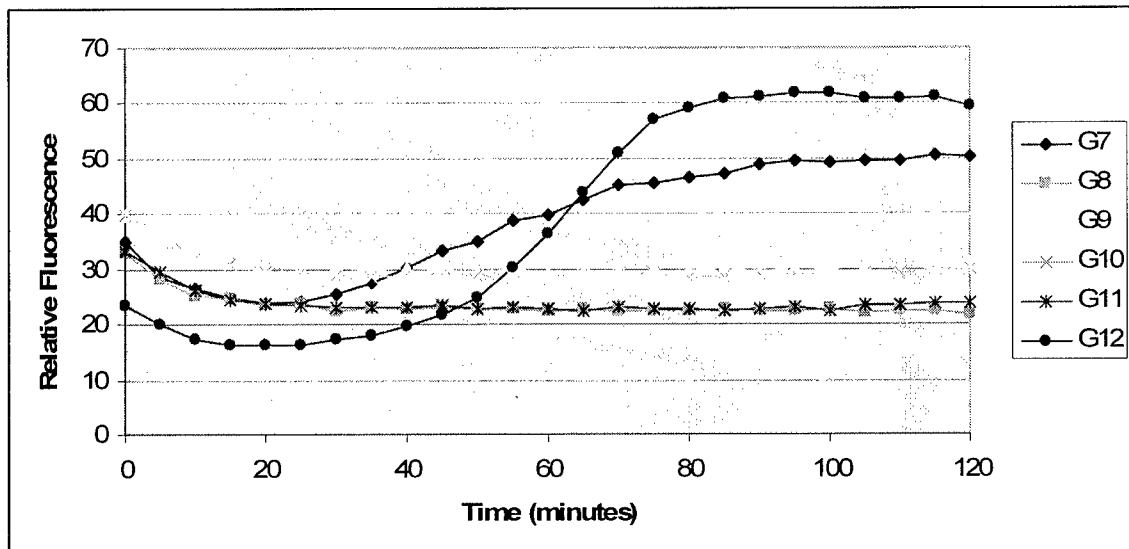


**Figure 136.** G7: Arg, G8: malic acid, G9: lactic acid, G10: Glu, G11: Asp, G12: ascorbic acid.

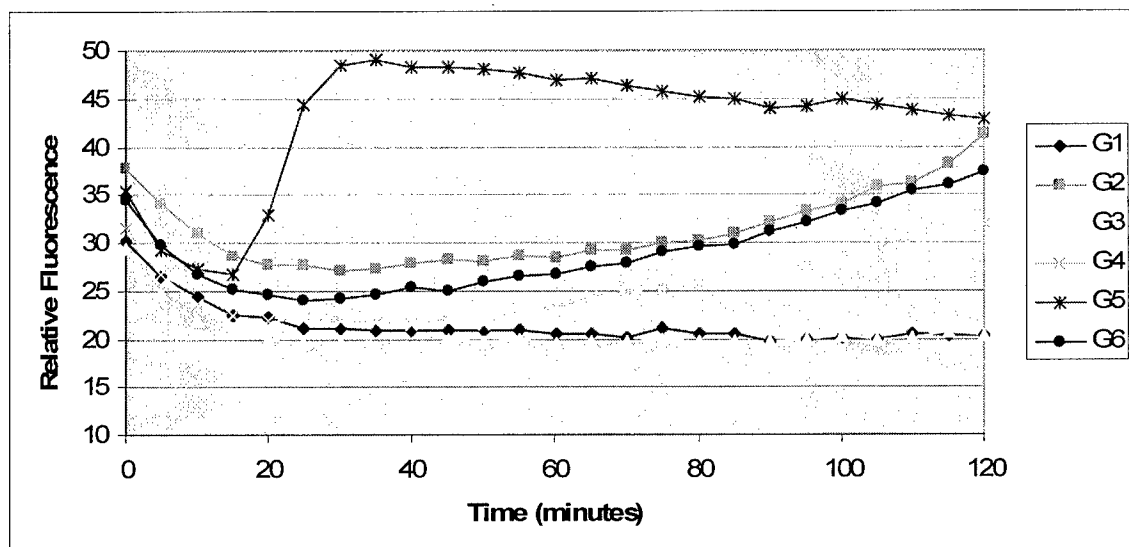


**Figure 137.** G1: Gly, G2: Pro, G3: Lys, G4: His, G5: guanidine, G6: diethanolamine.

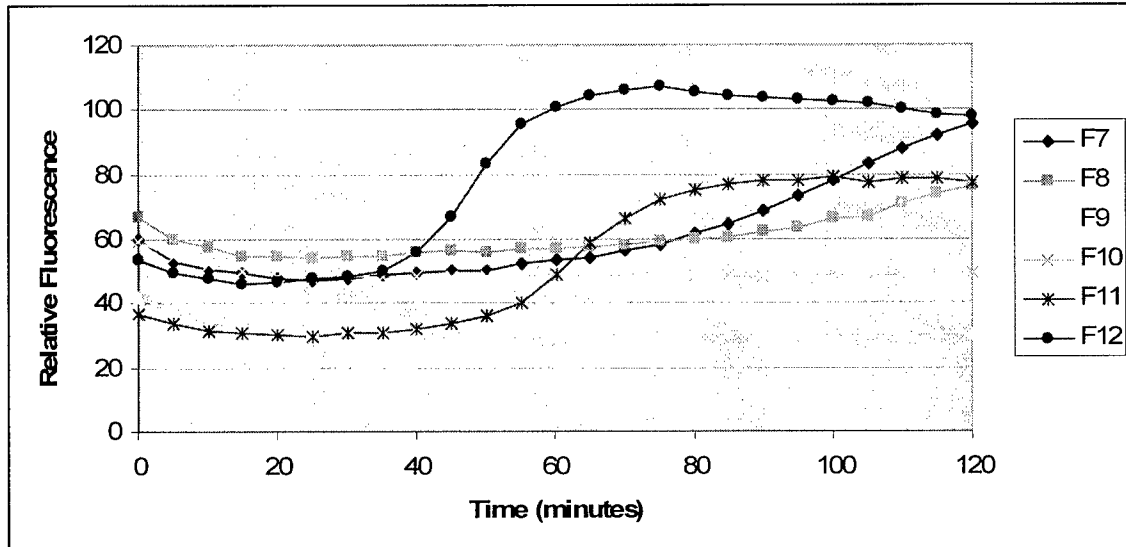


**Figure 138.** F7: Tween 20 (0.01%), F8: Brij 35 (0.1%), F9: Brij 35 (0.05%), F10: Brij 35 (0.01%), F11: sodium citrate (0.2M), F12: sodium citrate (0.1M).

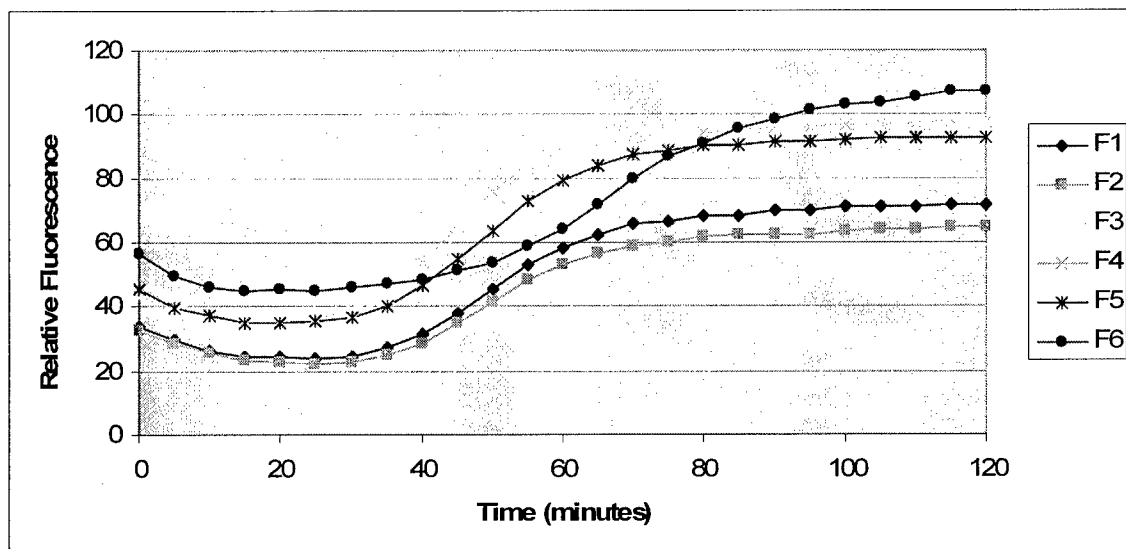


**Figure 139.** F1: Pluronic F-68 (0.01%), F2: Tween 80 (0.1%), F3: Tween 80 (0.05%), F4: Tween 80 (0.01%), F5: Tween 20 (0.1%), F6: Tween 20 (0.05%).

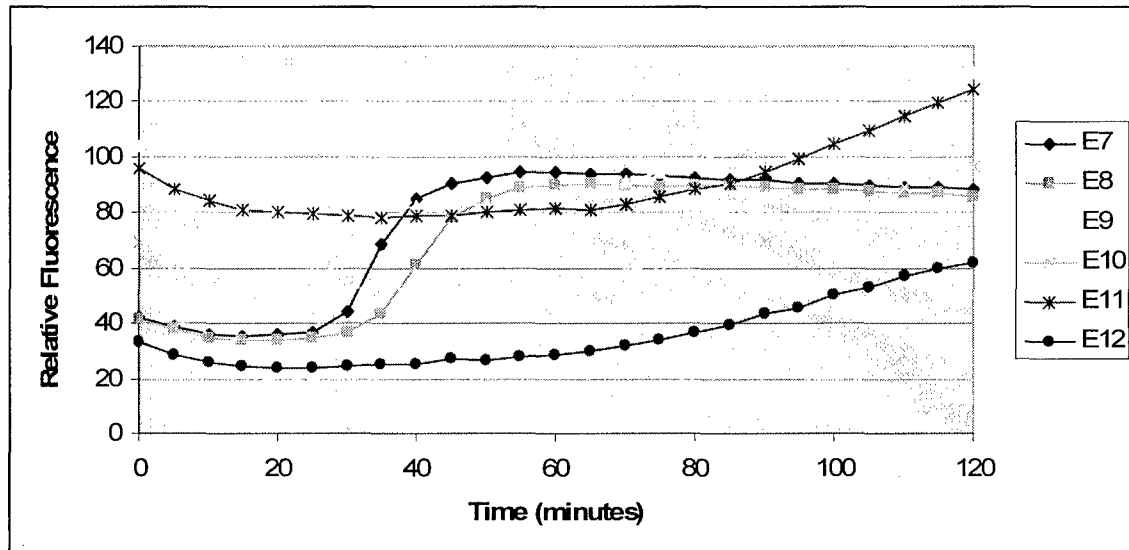


**Figure 140.** E7: lactose (10%), E8: albumin (5%), E9: albumin (2.5%), E10: albumin (1%), E11: Pluronic F-68 (0.1%), E12: Pluronic F-68 (0.05%).

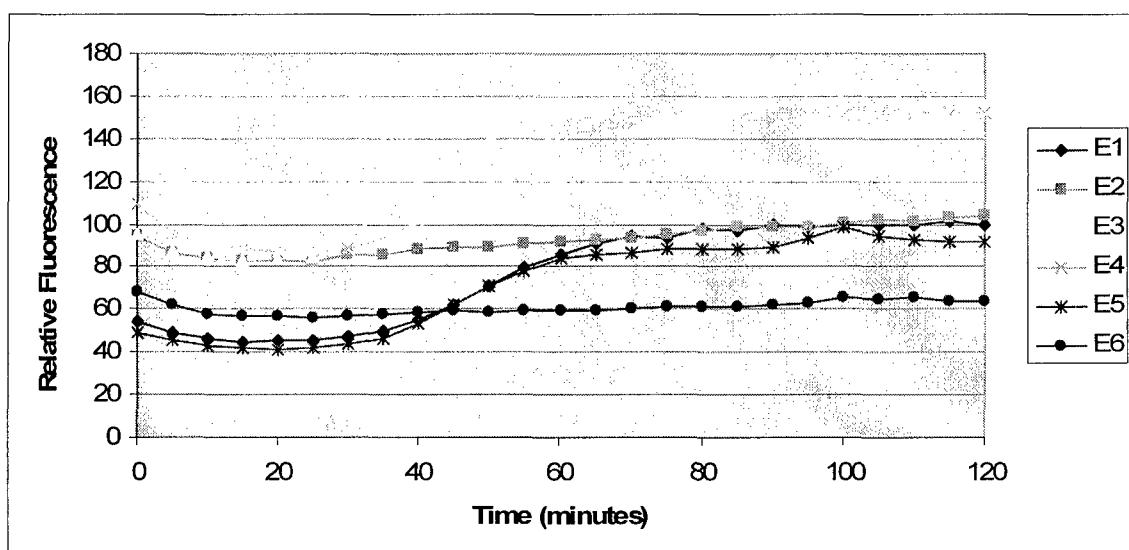


**Figure 141.** E1: sucrose (10%), E2: dextrose (20%), E3: dextrose (10%), E4: trehalose (20%), E5: trehalose (10%), E6: lactose (20%).

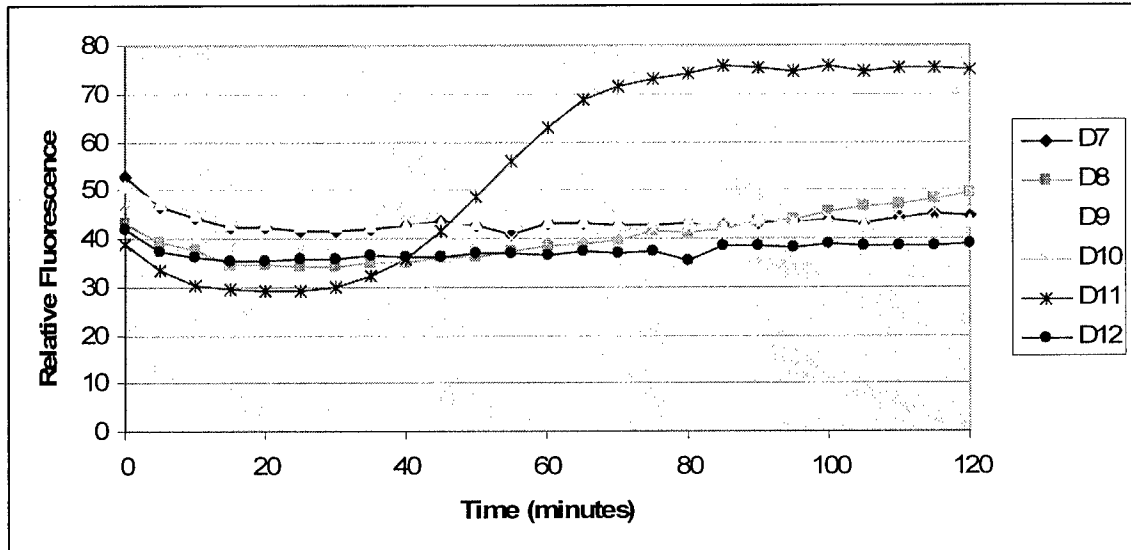


**Figure 142.** D7: Glycerol (20%), D8: glycerol (10%), D9: sorbitol (20%), D10: sorbitol (10%), D11: mannitol (10%), D12: sucrose (20%).

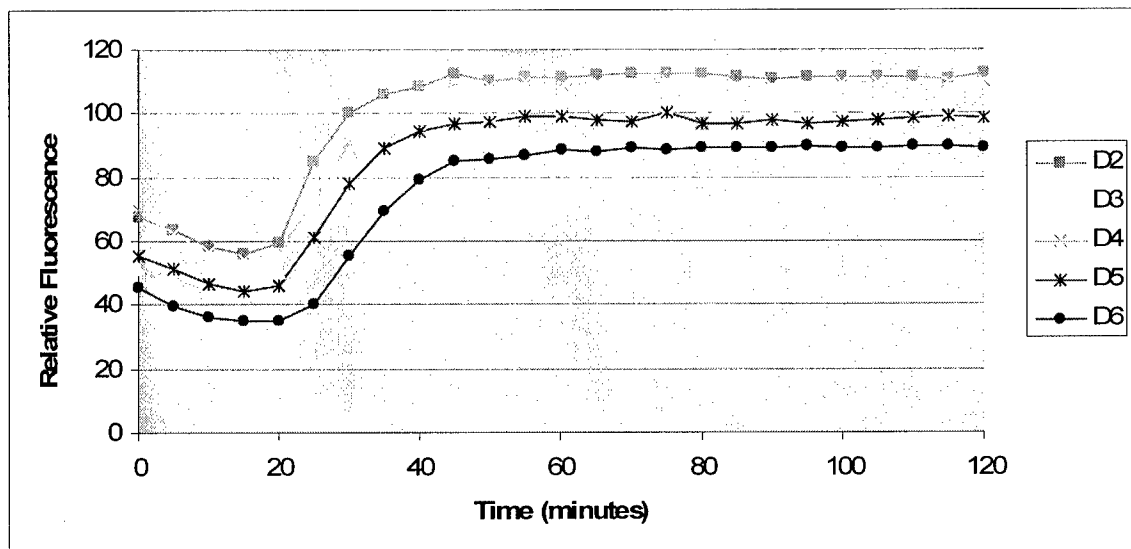


**Figure 143.** D2: 2-OH propyl  $\gamma$ -cyclodextrin (10%), D3: 2-OH propyl  $\gamma$ -cyclodextrin (5%), D4: 2-OH propyl  $\beta$ -cyclodextrin (10%), D5: 2-OH propyl  $\beta$ -cyclodextrin(5%), D6:  $\alpha$ -cyclodextrin (2.5%).

## **Key Research Accomplishments:**

- A manuscript entitled, “Anthrax vaccine powder formulations for nasal mucosal delivery” is accepted by Journal of Pharmaceutical Sciences (see appendices).
- A manuscript entitled, “Effect of pH and ionic strength on the physical stability of adenovirus type 5” is accepted by Journal of Pharmaceutical Sciences (see appendices).
- A manuscript entitled, “Thermal Stability of Adenovirus Type 2 as a Function of pH” has been submitted to the Journal of Pharmaceutical Sciences (see appendices).
- Stabilization projects involving botulinum toxin (Allergan), A ricin vaccine (DOR Biopharma) and a vaccine against Norwalk virus (Ligocyte) were also initiated and are in various stages of development. This work will be reported in the future and is not described in this report.

## **Reportable Outcomes:**

- A poster entitled, “Development and evaluation of anthrax vaccine powder formulations for nasal mucosal delivery” was presented at the ACS 2004 conference, Philadelphia, PA, August 22-26, 2004.
- A poster entitled, “A Systematic Approach to the Biophysical Characterization and Vaccine Pre-formulation of Recombinant Protective Antigen” was presented at Colorado Protein Stability Conference, July 15, 2005
- A Ph.D. degree was awarded to Jason Rexroad, a student in Dr. Middaugh’s lab, in May 2005. His dissertation work involved the studies on Valley fever antigens and adenovirus reported above.
- List of personnel receiving/received pay from the research effort:
  - Dr. Russ Middaugh
  - Dr. Duane Brandau
  - Dr. Sangeeta Joshi
  - Dr. Laura Lucas
  - Dr. Jason Rexroad
  - Dr. Chad Braun

## **Conclusions:**

In conclusion, we have established that the empirical phase diagram approach to the physical stabilization of macromolecules and their complexes is an effective and rapid method for the preformulation and formulation of vaccines and therapeutic proteins. This methodology has been shown to be effective for characterizing both viruses and recombinant proteins as demonstrated by our studies on adenovirus types 2 and 5, valley fever (coccidioidomycosis) fusion antigen and the recombinant protective antigen (rPA) of anthrax. In the case of rPA a vaccine has been developed

and will shortly enter phase 1 trials. New projects involving botulinum toxin, a ricin vaccine and a virus-like particle vaccine for Norwalk virus have been initiated.

## References:

1. Kueltzo LA, Ersoy B, Ralston JP, Middaugh CR. 2003. Derivative absorbance spectroscopy and protein phase diagrams as tools for comprehensive protein characterization: a bGCSF case study. *J Pharm Sci.* 92 (9): 1805-20.
2. Fan, H., Ralston, J., DiBase, M., Faulkner, E., and Middaugh, C.R. 2005. The solution behavior of IFN- $\beta$ -1a: An empirical phase diagram approach. *J. Pharm Sci.*(*in press*)
3. Tiyaboonchai W, Woiszwillo J, Sims RC and Middaugh CR. (2003). Insulin containing polyethylenimine-dextran sulfate nanoparticles. *Int J Pharm* **255**:139-151.
4. van Holde KE, Johnson WC, Ho PS. 1998. Scattering from Solutions of Macromolecules. In: Challice J, editor. *Principals of Physical Biochemistry*. Upper River Saddle, NJ: Prentice Hall, Inc., pp. 312-23.

5. Rexroad J, Wiethoff CM, Green AP, Kierstead TD, Scott MO, Middaugh CR. 2003. Structural stability of adenovirus type 5. *J Pharm Sci.* 92(3):665-78.

## **Appendices:**

### **Appendix I: rPA manuscript**

## **Anthrax vaccine powder formulations for nasal mucosal delivery**

Ge Jiang<sup>1</sup>, Sangeeta B. Joshi<sup>2</sup>, Laura J. Peek<sup>2</sup>, Duane T. Brandau<sup>2</sup>, Juan Huang<sup>1</sup>, Matthew S. Ferriter<sup>1</sup>, Wendy D. Woodley<sup>1</sup>, Brandi M. Ford<sup>1</sup>, Kevin D. Mar<sup>1</sup>, John A. Mikszta<sup>1</sup>, C. Robin Hwang<sup>1</sup>, Robert Ulrich<sup>3</sup>, Noel G. Harvey<sup>1</sup>, C. Russell Middaugh<sup>2</sup>, Vincent J. Sullivan<sup>1</sup>

1 BD Technologies, 21 Davis Dr., RTP, NC 27709

2 University of Kansas, Department of Pharmaceutical Chemistry

3 US Army Medical Research Institute of Infectious Diseases

Corresponding author:

Vince Sullivan, Ph.D.

BD Technologies

21 Davis Dr.

Research Triangle Park, NC 27709 Tel: 919-

597-6173

Fax: 919-597-6402

Email: [vince\\_Sullivan@bd.com](mailto:vince_Sullivan@bd.com)

## INTRODUCTION

Anthrax, the zoonotic disease caused by the Gram-positive spore-forming bacterium, *Bacillus anthracis*, can infect humans via cutaneous, gastrointestinal, and pulmonary routes. The inhaled form is of particular concern considering its demonstrated use as a bioweapon<sup>1-4</sup>. Inhalational anthrax is difficult to diagnose since the symptoms of infection are not always detected in time for antibiotic treatment to be effective; therefore, prophylactic vaccination is critical to elicit protection for individuals at risk of exposure<sup>5,6</sup>.

*B. anthracis* produces a three component exotoxin (anthrax toxin complex), which consists of protective antigen (PA, 83 kDa), edema factor (EF, 89 kDa) and lethal factor (LF, 90 kDa)<sup>7-9</sup>. While all three proteins are nontoxic individually, the combination of PA and LF (designated lethal toxin) causes systemic shock and death associated with hyperoxidative burst and cytokine release from macrophages<sup>10,11</sup>. A combination of PA and EF, known as edema toxin, induces an increase in intracellular cAMP and also elicits edema at the site of infection<sup>12,13</sup>. PA is regarded as the most important molecule within the anthrax toxin complex since it plays an essential role in anthrax pathogenesis involving transport of LF and EF into the cytoplasm. When PA binds to a target cell membrane receptor, it is cleaved and a 20-kDa fragment is released, exposing the LF and EF binding sites. The remaining 63-kDa protein forms a heptameric pore through which LF and EF can be internalized into the cytosol<sup>4,14,15</sup>. PA is also the primary immunogenic

molecule that confers protection against anthrax<sup>16,17</sup>. The current licensed anthrax vaccines for human use are produced from the sterile culture supernatant fraction of *B. anthracis* and are adsorbed on aluminum hydroxide for intramuscular (IM) injection<sup>18</sup> in the United States and precipitated with aluminum phosphate for subcutaneous (SC) injection in the United Kingdom<sup>19</sup>. These vaccines contain varying amounts of natural PA and also small amounts of LF and EF<sup>20</sup>. A limited duration of protection and a consequent need for frequent boosts to maintain immunity have resulted in recent efforts to develop alternative vaccines such as those that employ recombinant PA (rPA) to improve the immunogenicity, safety and pharmaceutical consistency<sup>2,21,22</sup>.

A second generation anthrax vaccine consisting of a recombinantly produced PA antigen is currently under clinical investigation where it is being administered by IM injection<sup>23</sup>, despite a lack of evidence that the IM administration is the optimal route. Delivery of vaccine to the respiratory mucosa may offer an attractive alternative to parenteral delivery for protection against pulmonary anthrax infection. Intranasal (IN) immunization is efficient at eliciting mucosal immunity in the lungs<sup>24-26</sup>, and has been shown in animals to be an effective means of immunizing against pulmonary anthrax infection<sup>2</sup>. IN vaccination offers advantages, as it is non-invasive route of delivery, with potential for self-administration. Nasal immunization with rPA could be further facilitated by the use of stable powder formulations delivered via a unit dosed disposable device. Nasal powder delivery may have several advantages over conventional liquid formulations for parenteral routes including protection from hydrolysis in bulk solution, potential

elimination of the need for refrigeration, increased portability, and better suitability for mass immunization campaigns through an all-in-one prefilled device.

Previously, we reported that IN delivery of a powder formulation of rPA provides complete protection against inhalational anthrax in a rabbit model<sup>27</sup>. These results are summarized in Table 1. *In vivo* protective efficacy was reflected by animal survival after aerosol anthrax spore challenge. The IN powders elicited similar or slightly higher protection compared to liquid formulations administered IM or IN (Table 1). In the present study, we describe the pre-formulation work including investigation of the biophysical stability of rPA and the subsequent formulation and characterization of such IN rPA vaccine powders. The stability of rPA in solution as a function of pH and temperature was assessed and interpreted by an empirical phase diagram approach<sup>28</sup>. In addition, stabilizers were examined in order to identify a range of optimal formulation conditions. Under the conditions selected, rPA solutions were prepared and further processed to produce powder forms. The impact of powder processing on the intrinsic stability of rPA as well as on its long term storage stability was also investigated.

## MATERIAL AND METHODS

### Materials

rPA was obtained from two different sources, the US Army Medical Research Institute of Infectious Diseases (USAMRIID, Fredrick, MD) and List Biological Laboratories (Campbell, CA). rPA from both sources was expressed and purified from *Bacillus*

*anthracis* and was equivalent based on the criteria of size exclusion chromatography (SEC) and SDS-PAGE analysis. The CpG-containing oligonucleotide (#1826, TCCATGACGTTCTGACGTT) was purchased from Proligo, LLC (Boulder, CO). Chitosan (MW 50,000-190,000) was purchased from Sigma (St. Louis, MO). All other reagents including buffers and salts were purchased from Sigma (St. Louis, MO) and were of analytical grade.

## **Experimental Methods**

### **Physical characterization of rPA stability**

rPA sample preparation: rPA solution was prepared at a concentration of 2.4  $\mu$ M for UV absorption and CD studies or 1.2  $\mu$ M for fluorescence studies in 50 mM citrate phosphate buffer containing 0.1 M NaCl at six different pH values from 3-8 at one pH unit intervals. UV Optical Density Measurements: The effect of temperature on rPA aggregation was determined by monitoring turbidity at 360 nm at each pH value using an Agilent 8453 UV-Visible spectrophotometer over a temperature range of 10-90°C at 2.5°C intervals. A 5-min equilibration time was employed at each temperature interval to ensure equilibrium conditions.

Circular Dichroism (CD): CD studies were performed using a Jasco J-810 spectropolarimeter equipped with a 6-position Peltier temperature controller to measure changes in the secondary structure of rPA as a function of temperature. Each sample was examined in a 0.1 cm pathlength cuvette sealed with a Teflon stopper, and the CD signal of rPA at 222 nm was monitored as a function of temperature from 10-90°C, collecting

data every 0.5°C. The CD signal was converted to molar ellipticity using the Jasco Spectra Manager software.

Intrinsic Tryptophan (Trp) fluorescence: Intrinsic fluorescence measurements were performed to assess perturbations in the tertiary structure of rPA as a function of temperature and pH. Fluorescence emission spectra of rPA (1.2 μM) were recorded from 10 to 85°C using a PTI Quanta Master Spectrofluorometer equipped with a turreted, four-cell thermostatically controlled holder. An excitation wavelength of 295 nm (>95% Trp Emission) was employed and emission spectra were collected from 305 to 440 nm. Excitation and emission slits were set at 4 nm and a 1 cm pathlength quartz cuvette was used in all experiments. Spectra were collected at 2.5°C intervals with a 5-min equilibration time at each temperature. Buffer baselines were subtracted from each spectrum prior to data analysis using Felix™ (PTI) software. Emission peak positions were obtained by a “center of spectral mass” method, which calculates the zero moment of the entire spectral curve from 305 to 440 nm. Typically, the “center of spectral mass” values do not correspond to observed peak maxima ( $\lambda_{\text{max}}$ ), but do accurately reflect the trend in actual peak position changes.

ANS dye binding studies: The apolar dye, 8-Anilino-1-naphthalene sulfonate (ANS), often binds to hydrophobic regions on proteins as their conformation is altered. This usually results in enhanced fluorescence as well as a blue shift in the emission peak position. Thus, the association of ANS with rPA (1.2 μM) was monitored as a function of temperature (10-85°C) and pH (3-8) using a PTI Quanta Master Spectrofluorometer. ANS was added in a 20-fold molar excess over rPA. An excitation wavelength of 375 nm was used, and spectra were collected from 400-600 nm. The temperature ramping profile

and instrument settings were the same as those used for the intrinsic Trp fluorescence experiments. Blanks of buffer containing ANS were subtracted from each spectrum prior to data analysis.

### **Constructing Empirical Phase Diagram**

An empirical phase diagram was constructed as described previously<sup>28</sup> but in this case using CD molar ellipticity, intrinsic Trp fluorescence center of mass and ANS fluorescence intensity data sets. By the phrase “phase diagram”, we refer to an empirical determination of regions of control variables, such as pH and temperature, in which the structural data are substantially uniform and coherent. These phase diagrams are created by a multicomponent vector approach in which the peaks that most reflect structural changes are represented by red, blue or green colors. Thus, each final color in the diagram, which is a summation of the three input experimental results, represents a different physical state of the protein.

### **Screening for Stabilizers**

An initial high-throughput screen for stabilizers was performed utilizing the susceptibility of rPA to aggregation by monitoring the turbidity of the solution with an optical density measurement at 360 nm using a 96-well plate reader (BMG Labtechnologies, Germany). To identify potential stabilizers, more than thirty “Generally Regarded As Safe” (GRAS) excipients including buffers, sugars, amino acids and surfactants were screened for their ability to inhibit the aggregation of rPA. In a 96-well plate, rPA (0.25 mg/ml) was added to wells containing each compound from the GRAS library at selected concentrations in

citrate-phosphate buffer at pH 5. The samples were incubated at 37°C, and the optical density of the solutions in each well was monitored at 360 nm ( $_{OD360}$ ) for 70 min with readings obtained at 5-min intervals. Controls of rPA solution without excipient were examined simultaneously. The final  $_{OD360}$  observed at 70 min was used to calculate the percent inhibition of rPA aggregation produced by each compound.

Several effective inhibitors of rPA aggregation were further studied to determine their effect on the conformational stability of rPA upon thermal denaturation, using the CD and intrinsic fluorescence methods described previously. Titration experiments were performed with the selected stabilizer by monitoring turbidity, as described above, to obtain the optimal concentration range of the stabilizer.

### **Formulation of anthrax dry powder vaccine**

The anthrax dry powder was formulated by freeze drying (FD) or spray freeze drying (SFD) with rPA, trehalose and an adjuvant comprising the CpG-containing oligonucleotide (#1826, TCCATGACGTTCTGACGTT) (abbreviated herein as CpG). rPA was supplied at pH 8 in either ammonium acetate solution (USAMRIID material) or in a freeze dried form (List Lab material) containing HEPES buffer salts. The rPA solution was mixed with CpG and trehalose solutions to obtain the final concentrations of 0.5 mg/ml rPA, 0.5 mg/ml CpG, 99.0 mg/ml trehalose (with trace amount of salts from the rPA material). Part of this solution was stored at -70° C for stability testing and the remainder was aliquotted for FD and SFD. To produce SFD powder, the solution was first sprayed into liquid nitrogen using a BD Accuspray® nozzle. The frozen particles

obtained were collected into lyophilization vials and then transferred to a freeze drier (Dura-Stop/Dura-Dry, FTS Systems, Stonebridge, NY) precooled to -40°C. Finally, both FD and SFD samples underwent a lyophilization cycle in which the primary drying was performed at -10°C (shelf temperature) for 16 hr, followed by a gradual ramping of the shelf temperature to 20°C for secondary drying. The vials were stoppered under a nitrogen backfill. The FD cake was milled by ball milling (Wig-L-Bug Grinding Mill, Reflex Analytical Corp, Ridgewood, NJ) for 1 min at 3000 RPM to generate the final powder. These rPA/CpG/trehalose powders can be filled into the capsule of an IN delivery device previously described<sup>27,29</sup>. Additionally, to determine if a bioadhesive further enhances immunity, aliquots of the above powders were blended with a chitosan powder prior to device filling.

#### **Determination of rPA stability during the SFD process**

The integrity of rPA throughout the SFD process was determined by SD S-PAGE under both reducing and non-reducing conditions and by SEC-HPLC. Samples were collected at each step of the SFD process, i.e., after mixing of rPA with CpG and trehalose, after the solution was sprayed from the nozzle, after the sprayed droplets were frozen in liquid nitrogen, and after the final lyophilization. The final dried powder was also reconstituted in water for SEC-HPLC analysis for comparison to freshly prepared rPA/CpG/trehalose solution.

#### **Storage stability studies of anthrax vaccine formulations under accelerated conditions**

The SFD anthrax vaccine powder was aliquotted into 2 ml serum vials (Wheaton, Millville, NJ) in a dry box (Terra Universal, Anaheim, CA) under nitrogen purge. Each vial contained ~25 mg of powder. The vials were sealed with rubber stoppers and aluminum crimp seals. The liquid formulation containing the same composition as the SFD powder was also included in the stability study. After storage at 25°C or 40°C , powder samples were reconstituted in ~0.25 ml water for analysis. Ten microliters of each sample were used for SDS-PAGE analysis and the remaining solution was filtered through a 0.22 µm centrifugal filter (Millipore, Bedford, MA) prior to SEC-HPLC.

### **Size exclusion chromatography (SEC)**

SEC was performed using a Waters HPLC instrument equipped with a binary pump (Waters 1525, Milford, MA), an autosampler (Waters 717 plus) and UV spectrophotometric detector (Waters 2487) interfaced to a Waters Breeze software package. Two size exclusion columns were used (Shodex®, JM Science Inc, Grand Island, NY), a KW-803 (cutoff 700,000) column coupled to a KW-802.5 (cutoff 150,000) column to enhance resolution. Samples (75 µl) were analyzed by UV detection ( $\epsilon=220$  nm) employing a mobile phase consisting of 50 mM NaCl, 5 mM HEPES, 200 ppm sodium azide and a flow rate of 0.5 ml/min. After passing through the UV detector, the samples were additionally analyzed using a multi-angle light scattering detector (Wyatt Technology Optilab DSP, Santa Barbara, CA) for molecular weight measurement. The light scattering data were analyzed using Wyatt Astra software.

## **SDS-PAGE**

SDS-PAGE was performed with a pre-cast NuPAGE 4-20% TrisGly gel (Invitrogen, Carlsbad, CA). Protein samples and standards were mixed with 2X Tris-Glycine SDS sample buffer (Invitrogen) containing 2% SDS. For reducing conditions, dithiothreitol (1M) and 2-Mercaptoethanol were added at 5% (v/v) each in the samples. Samples were incubated for 8 min at 95°C, and electrophoresis was performed at a constant voltage of 125 V and 8 mA. The gel was stained with Colloidal Blue (Invitrogen) and destained with distilled water.

## **RESULTS AND DISCUSSION**

### **Physical characterization of rPA stability as a function of pH and temperature**

The effect of pH and temperature on the physical stability of rPA was analyzed using a number of biophysical approaches. First, aggregation of rPA was both temperature and pH dependent as observed by monitoring the turbidity at 360 nm (Figure 1A). Between pH 4 and 7, the temperature at which aggregation began increased with pH. At pH 8, aggregation of rPA began at slightly lower temperature than at pH 7 with more substantial reductions in aggregation onset temperature at lower pH. Additionally, the extent of temperature-induced aggregation as indicated by the maximum OD was lower for rPA at pH 7-8 than at pH 4-6. The subsequent decline of OD is indicative of extensive protein precipitation. At pH 7-8, turbidity onset occurred at higher temperatures suggesting that rPA is thermally more stable in this pH range. At pH 3, aggregation of

rPA was only detected at temperatures above 80° C, indicating that the aggregation mechanism may differ from that at pH 4-8.

The CD spectra of rPA display minima at about 206-208 nm with a shoulder at 216-217 nm at all pH values (Figure 1B). This suggests that rPA primarily consists of a mixture of secondary structure moieties (e.g.  $\alpha$ -helix and  $\beta$ -sheet). The calculated secondary structure from the CD spectra is comparable to that of PA reported previously<sup>30</sup>. At 10°C, the CD spectrum of rPA at pH 3 remained distinct from that at other pH values with a significantly lower molar ellipticity, indicating that the secondary structure of rPA in solution is altered at very low pH. The secondary structure of rPA underwent significant pH and temperature-dependent transitions, suggesting a loss of secondary structure as evidenced by a decrease in the negative ellipticity (Figure 1C). The opposite is seen, however, at pH 3. Thermally induced ellipticity changes occurred at significantly lower temperatures at acidic pH values (e.g. pH 4) suggesting that rPA is structurally more labile in an acidic environment. The different behavior seen at pH 3 suggests that rPA undergoes a different type of structural alteration compared to that which occurs at higher pH values (Figure 1C). This is consistent with the altered CD spectrum seen even at low temperature at this pH (Figure 1B). No major thermally induced changes were seen at pH 7-8, implying higher thermal stability under these conditions; this is also consistent with the temperature/turbidity studies (Figure 1A).

Intrinsic (Trp) fluorescence studies were performed to detect changes in the tertiary structure of rPA. The shift in fluorescence emission peak position as a function of

temperature at various pH values is shown in Figure 1D. At all pH values, the peak position displays a red shift at elevated temperatures. This corresponds to an increase in exposure of the Trp residues to a more polar environment implying protein unfolding. Again, the onset temperature for red shift increased with increasing pH. Thus, these experiments also suggest that the most stable environment for rPA is within the pH range of 7-8.

At pH 4 and 5, changes in the tertiary structure of rPA were detected in fluorescence spectra at approximately 20-25°C. In contrast, CD thermal transitions began at higher temperatures, i.e., 33°C and 37°C for pH 4 and 5, respectively (Table 2). This suggests that a range of temperatures exist in which rPA possesses a retention of pronounced secondary structure and compactness, but a partial loosening of the native, tightly packed tertiary structure. Similar characteristics are also observed for rPA at pH 6-8. This suggests the appearance of molten globule-like states<sup>31,32</sup> between these temperatures. Such states are often prone to protein aggregation<sup>33,34</sup>. The turbidity profiles for rPA (Figure 2A) support this idea since the temperature at which aggregation begins for rPA at pH 4-8 falls within the temperature range of molten globule-like states as determined by intrinsic fluorescence and CD.

The hydrophobic dye, ANS, was utilized as an extrinsic fluorescent probe to further investigate alterations in rPA tertiary structure. As a protein begins to unfold, the increased accessibility of the dye to the protein's apolar interior often results in an enhanced fluorescence signal. In some cases, however, the negative charge on ANS is

also thought to be involved in its interaction with proteins. ANS is also believed to have a much stronger affinity for protein “molten globule states” than for native and severely structurally disrupted conformational states<sup>35-37</sup>. The change in ANS fluorescence intensity as a function of temperature and pH is shown in Figure 1E. Conformational transitions appear to follow the same patterns observed in the previous data. For example, at pH 3.0, rPA displayed significant apolar character even at 10°C, signified by a high ANS fluorescence intensity. This suggests that the protein is already structurally altered, perhaps to a molten globule state. At pH 4-8, the onset of increase in fluorescence intensity shifted to a higher temperature as pH increased. Also noteworthy is the decrease in the amplitude of fluorescence intensity as the pH increased, suggesting less binding of ANS to rPA at increasing pH. These findings again demonstrate that the optimal pH range for rPA stability is 7-8. Moreover, the ANS fluorescence results are consistent with the presence of molten globule states at intermediate temperatures (Table 2).

### An empirical phase diagram

A phase diagram was constructed using the results of ANS fluorescence intensity, the intrinsic tryptophan fluorescence center of mass and the CD intensity. Such a color map provides information regarding the state of rPA’s secondary and tertiary structures as a function of both pH and temperature. This mathematical approach provides a useful tool with which to interpret large quantities of data from different biophysical techniques for wide pH and temperature ranges. Each color represents a different physical state of the protein. Thus, a region of consistent color corresponds to an identifiable state while abrupt color differences correspond to changes in protein states (i.e. phase boundaries).

The nature of each phase can be identified by simultaneously looking at the original CD and fluorescence thermal melt spectra. We emphasize the empirical nature of such diagrams (no equilibrium between states is implied) and their primarily practical utility as representations of protein behavior in solution.

In the phase diagram for rPA (Figure 2), drastic color contrast clearly reflects changes in conformational stability over a variety of pH and temperature ranges. According to the previous discussion, the red-colored region in the lower, right-hand corner of the diagram can be identified as the phase of maximum stability (i.e. the “native” state of the protein). A second phase (blue/purple) is observed at pH 3 at temperatures below 45°C and also

appears to encompass pH 4 & 5 at temperatures between 25-40°C and 30-45°C, respectively. As discussed previously, this state possesses significant molten globule character. At higher temperatures at pH 3, rPA rapidly enters another state reflected by the dark brown color. This phase represents a severely structurally altered state of the protein. In the pH range of 4-7 at high temperatures (> 50°C) and pH 8 (50-65°C), the light purple to light brown zone corresponds to the structurally altered and aggregated states which were identified previously in the UV turbidity studies. At pH 8, yet another phase exists at >65°C which we speculate may correspond to an even further structurally disrupted form. This phase diagram serves to identify the boundaries at which changes occur and can be used to select conditions for the development of a high-throughput stabilizer screening assay and for formulation optimization.

## **Screening for Stabilizers**

As shown in Figure 1A, aggregation is a prominent pathway of physical degradation for rPA. Therefore, a turbidity-based high throughput screening assay was developed to examine the ability of various GRAS excipients to inhibit the aggregation of rPA. Based on the phase diagram, screening was performed at pH 5 and 37°C. These conditions were chosen based on the intrinsic marginal stability of rPA at this pH and temperature. The conditions serve well the requirements of accelerated stability testing since the protein readily aggregates at this pH and temperature. At the same time, they are sufficiently moderate to be relevant to phenomena occurring under typical pharmaceutical storage conditions. Figure 3 shows a representative plot of aggregation versus time for rPA at 37°C with and without the presence of three stabilizing excipients (malic acid, Tween-20 and sodium citrate). Thirty-two GRAS excipients, including carbohydrates, amino acids, surfactants, inorganic salts and organic acids, were screened at various concentrations. Eighteen compounds exhibited a significant (>50%) ability to suppress rPA aggregation (complete list not shown). For example, sodium citrate, malic acid and Tween 20 reduced rPA aggregation by 94%, 83%, and 16%, respectively. The disaccharide trehalose was found to be one of the most effective aggregation inhibitors. The extent of inhibition of rPA aggregation was also concentration dependent (Figure 4). In this case, 5% or higher concentrations of trehalose elicited  $\pm$  50% inhibition of rPA aggregation.

After certain aggregation inhibitors were identified, a number were further studied for their effects on the conformational stability of rPA using CD (Figure 5A) and intrinsic Trp fluorescence (Figure 5B). The data indicate that citrate, mannitol and trehalose

stabilize both the secondary and tertiary structure of rPA against thermal perturbation while Brij 35 has little effect. Trehalose produced the greatest stabilization, as demonstrated by a significant elevation in  $T_m$  of 10°C in both CD and intrinsic fluorescence studies.

### **Formulation of anthrax dry powder vaccine**

Having identified certain conditions that lead to enhanced stability of rPA in the liquid state, we prepared and characterized dry powder formulations based on these findings. These powders have been previously shown to protect rabbits from inhalational anthrax challenge<sup>27</sup> (Table 1). The powders were produced by either FD or SFD processes. The lyophilized cakes did not display any evident collapse or obvious shrinkage. The SFD powder consisted of highly porous particles with an uneven surface (Figure 6) and a bulk density of approximately 0.04g/cc. The average particle size was approximately 70  $\mu\text{m}$ , a size appropriate for deposition in the nasal cavity, and large enough to avoid lung deposition. The lyophilized cake was converted into a powder by ball milling. Additionally, to study the potential utility of bioadhesion, selected formulations were prepared containing dry chitosan, which was blended with rPA/CpG/trehalose powders prior to filling into IN delivery devices for the animal testing described previously<sup>27</sup>.

### **Effect of SFD on rPA stability**

In an attempt to determine any changes in rPA integrity that might occur due to the SFD process, samples were collected at various stages, including solution preparation, spraying, instant freezing of sprayed droplets, and SFD. The dried powder was

reconstituted for SDS-PAGE analysis (Figure 7), and SEC-HPLC (Figure 8). Under both reducing and non-reducing conditions, samples from all four stages appeared as a predominant, intense 83 kDa band identical to the fresh rPA standard. The CpG oligonucleotide did not have any noticeable effect. A variety of physical studies also found no evidence of interaction between the protein and oligonucleotide (data not shown). Two weaker bands of lower molecular weight appeared at approximately 65 kDa and 58 kDa. Comparing the intensity of the bands, these impurities represent a concentration of less than 5% of rPA monomer and exist equally in the rPA standard and all processed samples. No aggregation bands were observed under non-reducing conditions, suggesting that covalent disulfide linkages were not formed as a result of the large air-liquid interface present during the spaying process. Thus, this analysis suggests that rPA is robust and stable during the entire SFD procedure.

In SEC chromatograms (Figure 8), rPA and CpG peaks were well resolved and accurately quantified. The SFD powder and the liquid prior to the SFD process showed comparable rPA and CpG retention times as well as similar peak areas. No additional aggregation or degradation was detected. Therefore, retention of rPA integrity was also supported by SEC-HPLC studies.

#### **Storage stability studies of anthrax vaccine formulations under accelerated conditions**

Stability testing was conducted under accelerated conditions at 25 and 40°C. The desirable long-term storage temperature for powder formulations is 4°C, and most

preferably ambient temperature for convenient use. The SFD powder anthrax vaccine consists of rPA, CpG, trehalose and trace amounts of neutral buffer salts. The liquid formulation was of the same composition and was tested along with the powder for comparison and as a control. During incubation at both 25 and 40°C, powder samples maintained their physical appearance as a light powder and could be rapidly reconstituted into clear solutions at each time point.

At 25°C (Figure 9A), the stability of the powder rPA was not adversely affected throughout the fifteen days of incubation since over 90% intact monomer content was found at each time point by SEC. The molecular weight (83 kDa) of the monomer peak was confirmed by light scattering. In contrast, the liquid formulation displayed significant degradation over the course of the study. The residual stability of the liquid at day 15 was found to be only 15% (Figure 9A).

At 40°C (Figure 9B), the powder retained over 90% stability during the entire time course of 29 days. The liquid formulation, however, completely lost its monomer content in one day. The intact rPA monomer peak was below the low level of quantification of the SEC method after only 24 hr incubation and remained undetectable throughout the study. Retention of stability in the powder formulation at 40°C suggests that the powder may be successfully stored for long periods at room temperature. Removal of the need for the cold chain during storage and transportation along with the potential for self-administration using IN delivery may provide significant advantages for biodefense mass immunization.

The SEC results correlate closely with the findings of SDS-PAGE under reducing conditions. For example, on day 0, both liquid and powder formulations were identical to the fresh rPA standard (Figure 10A). On day 1, at 40°C, the intact rPA monomer band in the liquid formulation was much lighter than the rPA standard in intensity and more prominent degradation bands appeared between 30 and 42 kDa (Figure 10B). It should be noted that the total intensity of all bands for the solution sample was still lower than that of the standard, indicating that additional smaller fragments less than 4 kDa may have been generated. The liquid formulation continued to degrade further after day 1. On day 3, the 83 kDa rPA monomer band was completely absent and only a few bands of faded intensity at 40 kDa and lower were apparent (Figure 10C). For the SFD powder formulation under the same conditions, the samples appear unaltered compared to the rPA standard (Figure 10 A, B, C). This pattern persisted through day 29. At 25°C, the degradation of rPA in the liquid formulation appeared to follow the same pattern as that at 40°C except that the deterioration process was more gradual, i.e., it took longer to reach the same degree of degradation at 25°C than at 40°C. As expected, the powder at 25°C retained the same characteristics as the intact standard.

To gain a better understanding of the effect of temperature on the liquid stability of rPA and to estimate whether the liquid could be stored refrigerated instead of frozen, additional liquid stability testing was performed at 20°C and 30°C. Figure 1 1A shows loss of intact rPA for the liquid formulation as a function of time at four temperatures (20°C, 25°C, 30°C and 40°C) as determined by SEC-HPLC. As predicted, the rate of

deterioration increased as the temperature was elevated, and decreased with time. The stability profile was fitted using a first order model (Figure 1 1B) where the log percentage of intact rPA remaining was plotted against time. This simple model fits reasonably well for the experimental data at 20°C and 25°C with an  $R_2 > 0.96$ . The 30°C profile had only three time points during the period of rPA degradation, which could account for the poorer fit ( $R_2 = 0.82$ ). Based on these results, the liquid formulation should be kept frozen during long-term storage, at least under these formulation conditions.

## SUMMARY AND CONCLUSIONS

We previously reported that IN anthrax vaccine powders provided complete protection of rabbits against anthrax lethal aerosol challenge. The formulation development for this vaccine powder is comprehensively described in this study. This work first investigated the physical stability of rPA in solution as a function of pH and temperature. The stabilizing effect of GRAS excipients on rPA aggregation and loss of conformational stability was determined. Based on these findings, anthrax vaccine powders including SFD or FD dosage forms were prepared at pH 7-8 with trehalose as a stabilizer and bulking agent. The stability of rPA was retained after powder processing. The dry powder also maintained protein integrity under both ambient and accelerated aging temperatures for approximately one month while the liquid formulation showed rapid degradation. Such degradation appears to follow first order kinetics.

Based on these studies, stable IN powder formulations of rPA were developed as a potential alternative to heat-labile liquid formulations and conventional parenteral delivery by injection. Combination of this powder formulation with the non-invasive delivery platform described previously<sup>27,29</sup> could greatly improve the viability of mass immunization for this important pathogen.

#### **ACKNOWLEDGEMENT**

The authors thank Harry Sugg for performing electron microscopy on powder samples, and Pat McCutchen and Linda Tingen for administrative assistance in preparing the manuscript. Financial support was provided by funding from the U.S. Army Medical Research and Material Command, agreement number DAMD17-03-2-0037.

## **FIGURE LEGEND**

**Figure 1.** Physical stability of rPA as a function of pH and temperature in citrate phosphate buffer as determined by aggregation (A); CD spectra of rPA at 10°C (B); CD thermal melts monitored at 222 nm (C); intrinsic Trp fluorescence spectra center of mass; ANS dye binding fluorescence intensity (E).

**Figure 2.** Phase diagram of rPA based on intrinsic, ANS dye-binding fluorescence and CD results. Distinct phases are observed: (1) most stable phase [red-colored region in the lower, right-hand corner]; (2) molten globule-like state [blue/purple area at pH 3, <45°C, pH 4, 25-40°C and pH 5, 30-45°C]; (3) severely structurally altered phase [dark brown area at pH 3, >45°C]; (4) structurally altered and aggregated state [light purple ~ light brown region at pH 4-7, >50°C and pH 8, 50-65°C]; (5) Highly structurally disrupted form [green area at pH 8, >65°C]. Blocks of continuous color represent single phases, conditions under which the raw data-derived vectors behave similarly.

**Figure 3.** Aggregation of rPA in the presence and absence of excipients including 0.15 M malic acid, 0.0 1% Tween 20 and 0.2% sodium citrate.

**Figure 4.** Protection against rPA aggregation by trehalose at six different concentrations: 0%, 2.5%, 5%, 10%, 15% and 20%.

**Figure 5.** Increase in rPA thermal transition temperature in the presence of trehalose compared to several other excipients as determined by CD (A) and Trp fluorescence (B). **Figure 6.** SEM of spray freeze dried rPA anthrax vaccine powder.

**Figure 7.** Retention of rPA integrity throughout the spray freeze drying process as determined by SD S-PAGE under reducing conditions (A) and non-reducing conditions

(B). Lanes 1&8, MW Marker; Lane 2, CpG Std; Lane 3, rPA Std; Lane 4, rPA/CpG/trehalose solution; Lane 5, solution sprayed from nozzle; Lane 6, instant freezing of sprayed droplets in liquid nitrogen; Lane 7. Reconstituted spray freeze dried powder .

**Figure 8.** Retention of rPA stability after spray freeze drying as determined by SECHPLC.

**Figure 9.** Storage stability of rPA liquid and spray freeze dried powder at 25°C (A) and 40°C (B) determined by SEC-HPLC.

**Figure 10.** Degradation of the liquid formulation at 40°C determined by SDS-PAGE under reducing conditions on day 0 (Fig A; lane 1, 2ug rPA Std; Lane 2, MW Marker; Lane 3, 2ug CpG Std; Lane 4&5, liquid formulation containing rPA 2  $\mu$ g and 0.5  $\mu$ g, respectively; Lane 5&6, SFD powder formulation containing rPA 2  $\mu$ g and 0.5  $\mu$ g, respectively), day 1 and day 3 (Fig B and C; Lane 1, MW Marker; Lane 2, rPA Std 1.5ug; Lane 3, CpG Std 1 .5ug; Lane 4, liquid formulation containing rPA 1.5  $\mu$ g; Lane 5, SFD powder formulation containing rPA 1.5  $\mu$ g ).

**Figure 11.** Degradation profiles of the liquid formulation at 20, 25, 30 and 40°C as determined by SEC-HPLC (A) and the data fit to 1<sub>st</sub> order kinetics (B).

**Table 1.** Protective effect from intranasal dry powder formulations in rabbits receiving anthrax inhalational challenge (each rabbit received 50 µg of rPA, n=6 for each group) <sup>27</sup>

Formulation & Administration Route	Animal survival (%)	Form
Positive control (rPA/CpG liquid, IM)	83%	
rPA/CpG liquid, IN	67%	
rPA/CpG/trehalose SFD powder, IN	83%	
rPA/CpG/trehalose SFD powder + chitosan, IN	100%	
rPA/CpG/trehalose FD powder, IN	100%	
rPA/CpG/trehalose FD powder + chitosan, IN	100%	
Negative control (CpG)	0%	

**Table 2.** Thermal transition onset temperatures of rPA characterized by optical density ( $OD_{360\text{nm}}$ ), CD, intrinsic Trp fluorescence and ANS dye-binding fluorescence.

PH	Biophysical approaches			
	$OD_{360}$	CD	Trp fluorescence	ANS dye-binding
				fluorescence
3	81.7°C	16.4°C	16.5°C	10.0°C
4	30.4°C	32.8°C	22.5°C	21.5°C
5	36.4°C	36.5°C	25.2°C	30.1°C
6	43.7°C	43.0°C	37.5°C	42.3°C
7	46.8°C	48.0°C	42.1°C	45.0°C
8	47.9°C	46.3°C	40.0°C	40.8°C

Standard Errors for all runs were  $0 \pm 0.5^\circ\text{C}$ .

## **References:**

1. Oncu S, Sakarya S 2003. Anthrax--an overview. *Med Sci Monit* 9(1 1):RA276-283.
2. Flick-Smith HC, Eyles JE, Hebdon R, Waters EL, Beedham RJ, Stagg TJ, Miller J, Alpar HO, Baillie LWJ, Williamson ED 2002. Mucosal or parenteral administration of microsphere-associated *Bacillus anthracis* protective antigen protects against anthrax infection in mice. *Infection and Immunity* 70(4):2022-2028.
3. Gupta P, Singh S, Tiwari A, Bhat R, Bhatnagar R 2001. Effect of pH on stability of anthrax lethal factor: correlation between denaturation and activity. *Biochem Biophys Res Commun* 284(3):568-573.
4. Bhatnagar R, Batra S 2001. Anthrax toxin. *Crit Rev Microbiol* 27(3):167-200.
5. Quinn CP, Turnbull PC. 1998. Anthrax. In Collier L, Barlow A, Sussman M, editors. *Topley and Wilson's microbiology and microbial infections*, ed., London, United Kingdom: Arnold.
6. Tan Y, Hackett NR, Boyer JL, Crystal RG 2003. Protective immunity evoked against anthrax lethal toxin after a single intramuscular administration of an adenovirusbased vaccine encoding humanized protective antigen. *Hum Gene Ther* 14(17): 1673-1682.
7. Abrami L, Lindsay M, Parton RG, Leppla SH, van der Goot FG 2004. Membrane insertion of anthrax protective antigen and cytoplasmic delivery of lethal factor occur at different stages of the endocytic pathway. *J Cell Biol* 166(5): 645-651.
8. Arora N, Klimpel KR, Singh Y, Leppla SH 1992. Fusions of anthrax toxin lethal factor to the ADP-ribosylation domain of *Pseudomonas* exotoxin A are potent cytotoxins which are translocated to the cytosol of mammalian cells. *J Biol Chem* 267(22):15542-15548.
9. Chauhan V, Bhatnagar R 2002. Identification of amino acid residues of anthrax protective antigen involved in binding with lethal factor. *Infect Immun* 70(8):4477-4484.
10. Pezard C, Berche P, Mock M 1991. Contribution of individual toxin components to virulence of *Bacillus anthracis*. *Infect Immun* 59(10):3472-3477.
11. Hanna P 1999. Lethal toxin actions and their consequences. *J Appl Microbiol* 87(2):285-287.
12. Leppla SH 1982. Anthrax toxin edema factor: a bacterial adenylyl cyclase that increases cyclic AMP concentrations of eukaryotic cells. *Proc Natl Acad Sci U S A* 79(10):3 162-3 166.
13. Hoover DL, Friedlander AM, Rogers LC, Yoon IK, Warren RL, Cross AS 1994. Anthrax edema toxin differentially regulates lipopolysaccharide-induced monocyte production of tumor necrosis factor alpha and interleukin-6 by increasing intracellular cyclic AMP. *Infect Immun* 62(10):4432-4439.
14. Collier RJ, Young JA 2003. Anthrax toxin. *Annu Rev Cell Dev Biol* 19:45-70.
15. Mogridge J, Cunningham K, Collier RJ 2002. Stoichiometry of anthrax toxin complexes. *Biochemistry* 41(3): 1079-1082.

16. Prokupek K, Dvorak R, Polacek R 1981. Immunogenic effect of anthrax protective antigen. *Vet Med (Praha)* 26(5):279-290.
17. Ivins BE, Fellows PF, Nelson GO 1994. Efficacy of a standard human anthrax vaccine against *Bacillus anthracis* spore challenge in guinea-pigs. *Vaccine* 12(10):872-874.
18. Jendrek S, Little SF, Hem S, Mitra G, Giardina S 2003. Evaluation of the compatibility of a second generation recombinant anthrax vaccine with aluminum-containing adjuvants. *Vaccine* 21(21 -22):301 1-3018.
19. Baillie L, Hebdon R, Flick-Smith H, Williamson D 2003. Characterisation of the immune response to the UK human anthrax vaccine. *FEMS Immunol Med Microbiol* 36(1-2):83-86.
20. Reuveny S, White MD, Adar YY, Kafri Y, Altboum Z, Gozes Y, Kobiler D, Shafferman A, Velan B 2001. Search for correlates of protective immunity conferred by anthrax vaccine. *Infect Immun* 69(5):2888-2893.
21. Ivins BE, Welkos SL 1986. Cloning and expression of the *Bacillus anthracis* protective antigen gene in *Bacillus subtilis*. *Infect Immun* 54(2):537-542.
22. Singh Y, Ivins BE, Leppla SH 1998. Study of immunization against anthrax with the purified recombinant protective antigen of *Bacillus anthracis*. *Infect Immun* 66(7):3447-3448.
23. . Clinicaltrials.gov website ([www.clinicaltrials.gov/ct/show/NCT00057525](http://www.clinicaltrials.gov/ct/show/NCT00057525))T. ed.
24. Tebbey PW, Scheuer CA, Peek JA, Zhu D, LaPierre NA, Green BA, Phillips ED, Ibraghimov AR, Eldridge JH, Hancock GE 2000. Effective mucosal immunization against respiratory syncytial virus using purified F protein and a genetically detoxified cholera holotoxin, CT-E29H. *Vaccine* 18(24):2723-2734.
25. Papp Z, Babiuk LA, Baca-Estrada ME 1999. Antigen-specific cytokine and antibody isotype profiles induced by mucosal and systemic immunization with recombinant adenoviruses. *Viral Immunol* 12(2):107-1 16.
26. Isaka M, Yasuda Y, Taniguchi T, Kozuka S, Matano K, Maeyama J, Morokuma K, Ohkuma K, Goto N, Tochikubo K 2003. Mucosal and systemic antibody responses against an acellular pertussis vaccine in mice after intranasal co-administration with recombinant cholera toxin B subunit as an adjuvant. *Vaccine* 21(1 1-12):1 165-1173.
27. Mikszta JA, Sullivan VJ, Dean C, Waterston AM, Alarcon JB, Dekker JP, Brittingham JM, Huang J, Hwang CR, Ferriter M, Jiang G, Mar K, Saikh KU, Stiles BJ, Roy CJ, Ulrich RG, Harvey NG Protective Immunization Against Inhalational Anthrax: A Comparison of Minimally-Invasive Delivery Platforms. *J Infect Dis* 191:278-288.
28. Kueltzo LA, Ersoy B, Ralston JP, Middaugh CR 2003. Derivative absorbance spectroscopy and protein phase diagrams as tools for comprehensive protein characterization: a bGCSF case study. *J Pharm Sci* 92(9): 1805-1820.
29. Huang J., Garmise R.J., Crowder T.M., Mar K.M., Hwang C.R., Hickey A.J., Mikszta J.M., 2004 SVJ 2004. A novel dry powder influenza vaccine and intranasal delivery technology: induction of systemic and mucosal immune responses in rats. *Vaccine* 23:794-801.
30. Radha C, Salotra P, Bhat R, Bhatnagar R 1996. Thermostabilization of protective antigen--the binding component of anthrax lethal toxin. *J Biotechnol* 50(2-3):235-242.
31. Buchner J, Renner M, Lilie H, Hinz HJ, Jaenicke R, Kiehabel T, Rudolph R 1991. Alternatively folded states of an immunoglobulin. *Biochemistry* 30(28) :6922-6929.

32. Mayo KH, Barker S, Kuranda MJ, Hunt AJ, Myers JA, Maione TE 1992. Molten globule monomer to condensed dimer: role of disulfide bonds in platelet factor-4 folding and subunit association. *Biochemistry* 31(48): 12255-12265.
33. Tanksale A, Ghatge M, Deshpande V 2002. Alpha-crystallin binds to the aggregation-prone molten-globule state of alkaline protease: implications for preventing irreversible thermal denaturation. *Protein Sci* 11(7):1720-1728.
34. Karlsson M, Martensson LG, Olofsson P, Carlsson U 2004. Circumnavigating misfolding traps in the energy landscape through protein engineering: suppression of molten globule and aggregation in carbonic anhydrase. *Biochemistry* 43(21):6803-6807.
35. Asghari SM, Khajeh K, Ranjbar B, Sajedi RH, Naderi-Manesh H 2004. Comparative studies on trifluoroethanol (TFE) state of a thermophilic alpha-amylase and its mesophilic counterpart: limited proteolysis, conformational analysis, aggregation and reactivation of the enzymes. *Int J Biol Macromol* 34(3):173-179.
36. Mazon H, Marcillat O, Forest E, Smith DL, Vial C 2004. Conformational dynamics of the GdmHCl-induced molten globule state of creatine kinase monitored by hydrogen exchange and mass spectrometry. *Biochemistry* 43(17):5045-5054.
37. Almstedt K, Lundqvist M, Carlsson J, Karlsson M, Persson B, Jonsson BH, Carlsson U, Hammarstrom P 2004. Unfolding a folding disease: folding, misfolding and aggregation of the marble brain syndrome-associated mutant H107Y of human carbonic anhydrase II. *J Mol Biol* 342(2):619-633.

Figure 1E.

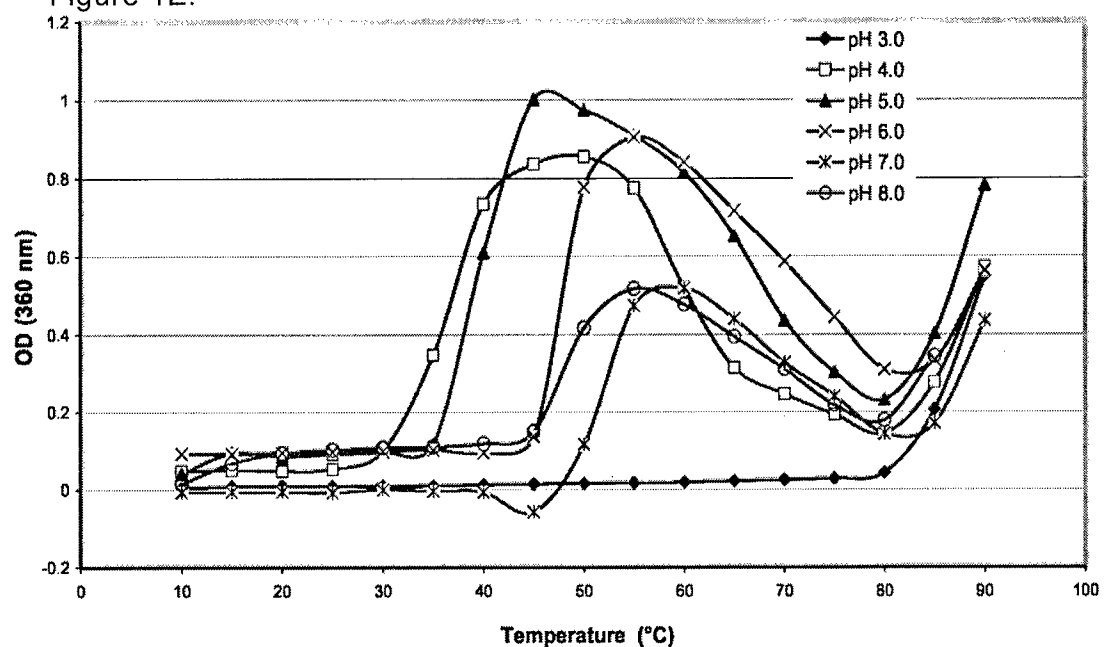


Figure 1B.

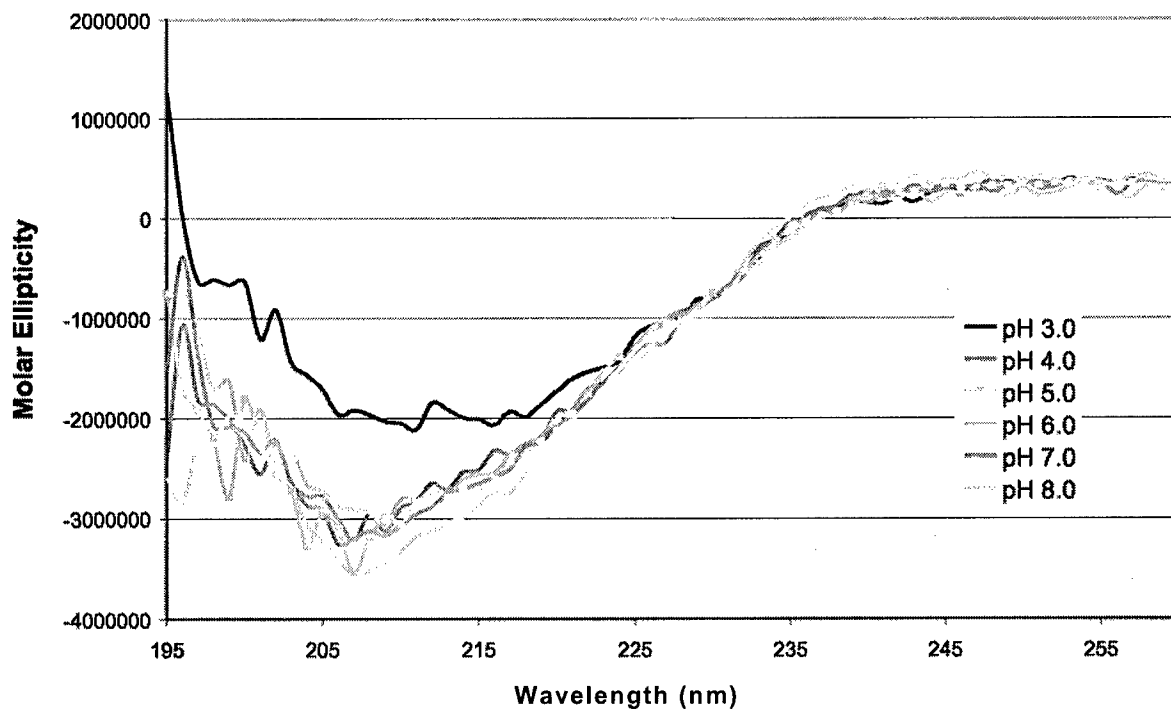


Figure 1E.

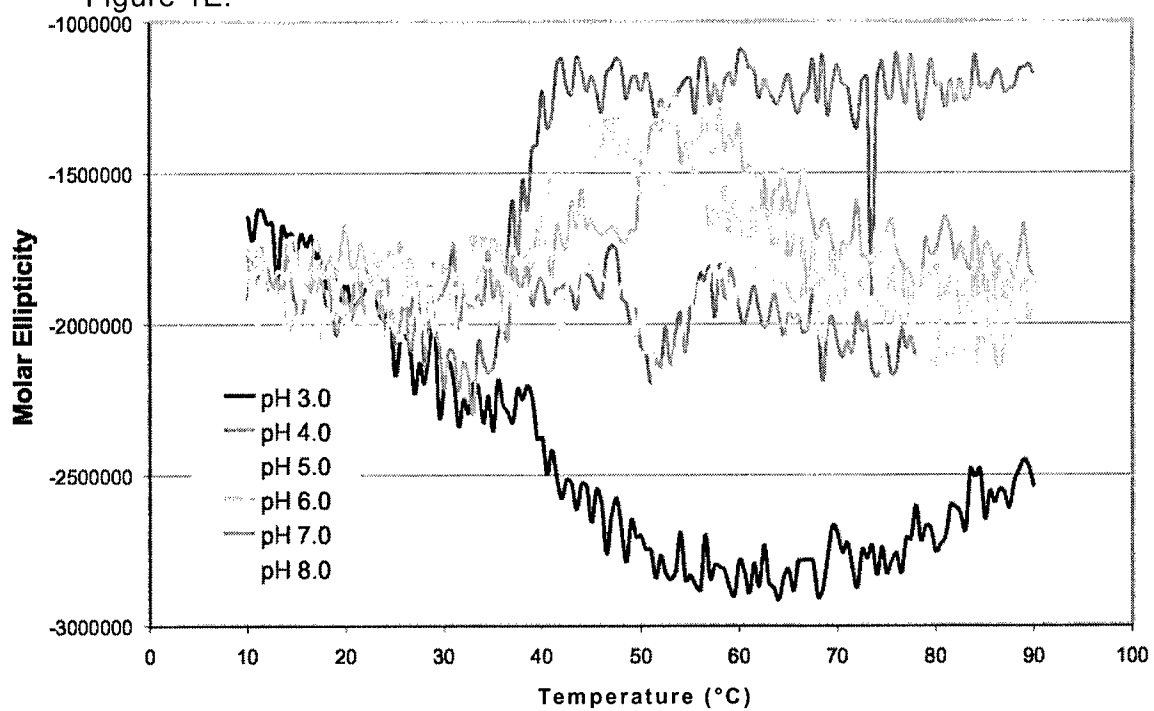


Figure 1D.

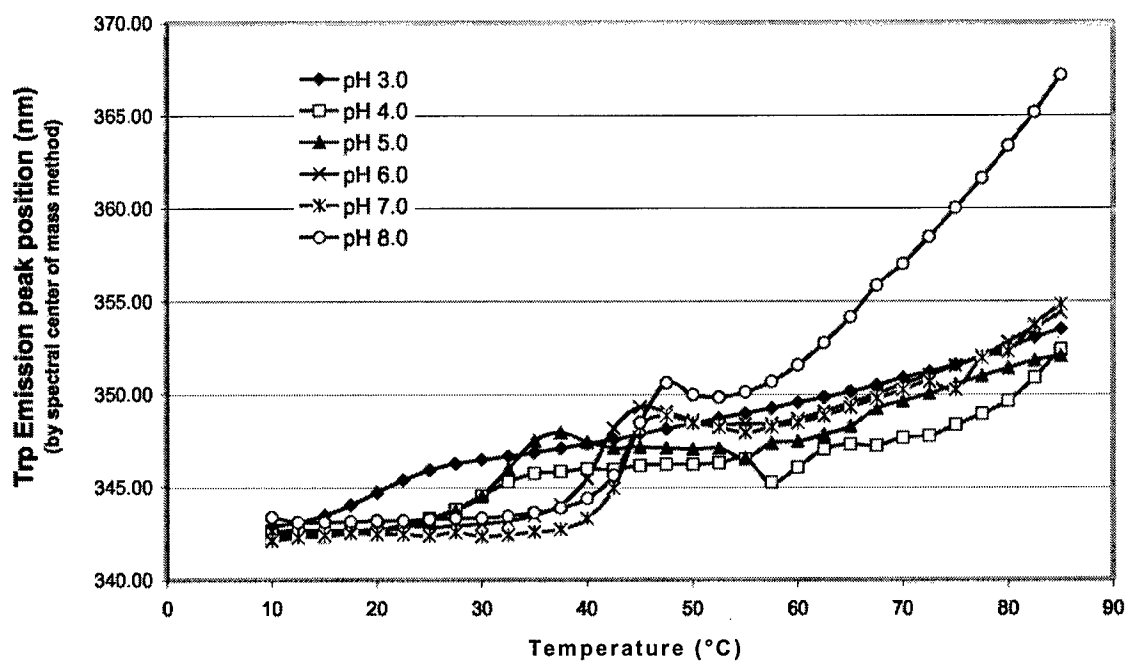


Figure 1E.

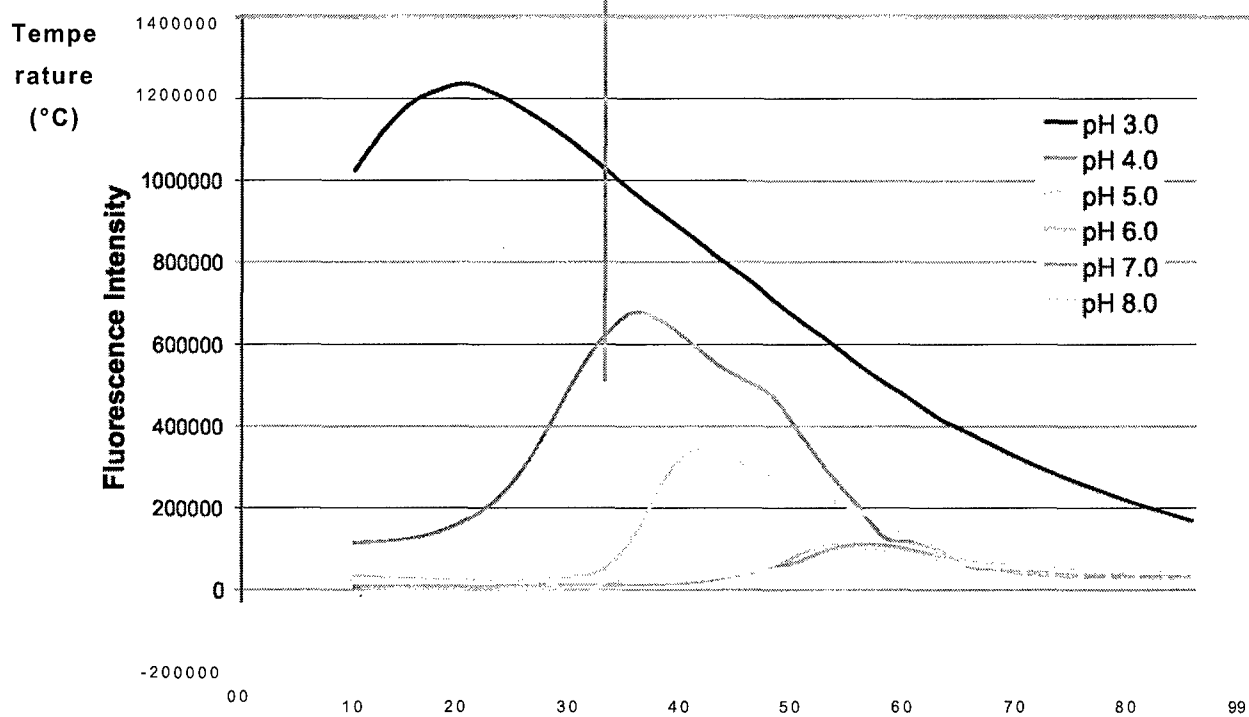


Figure 2.

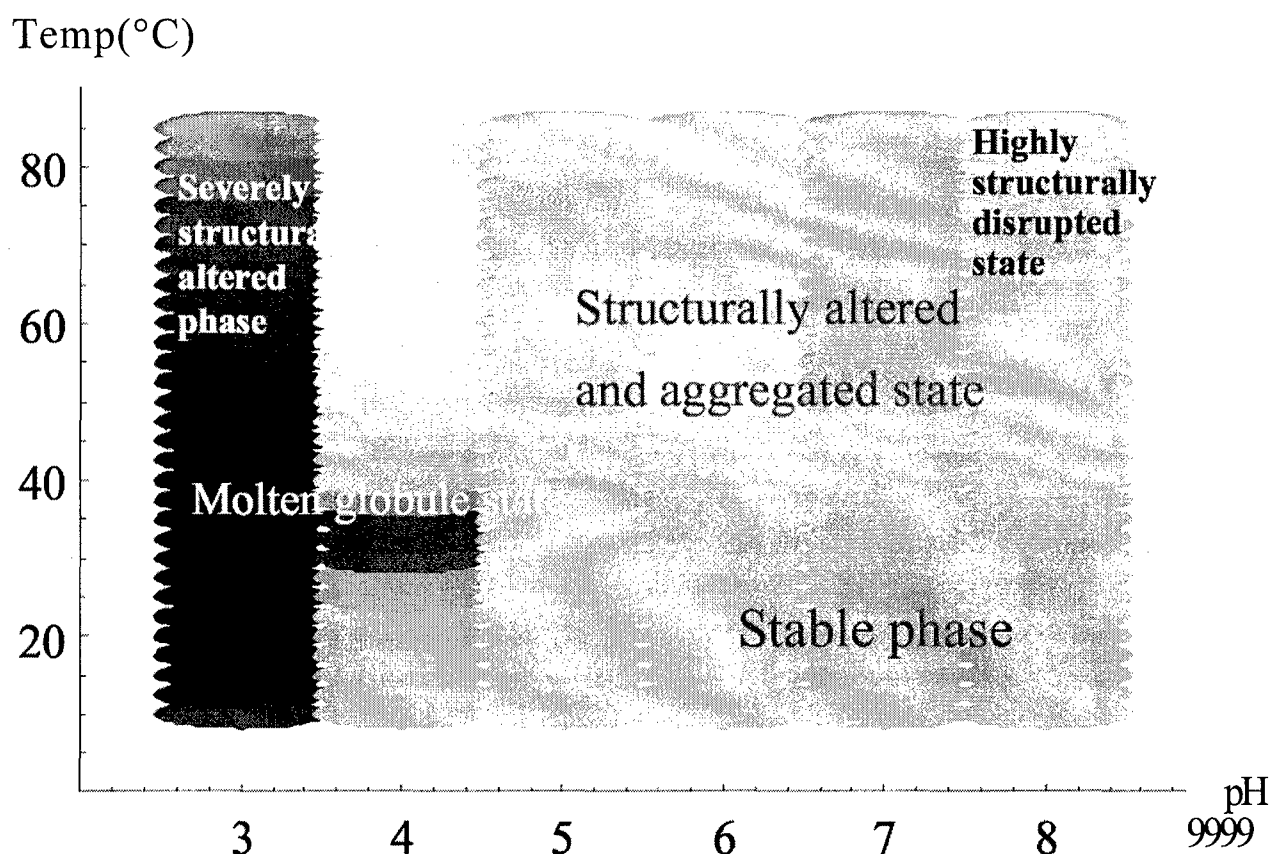


Figure 3.

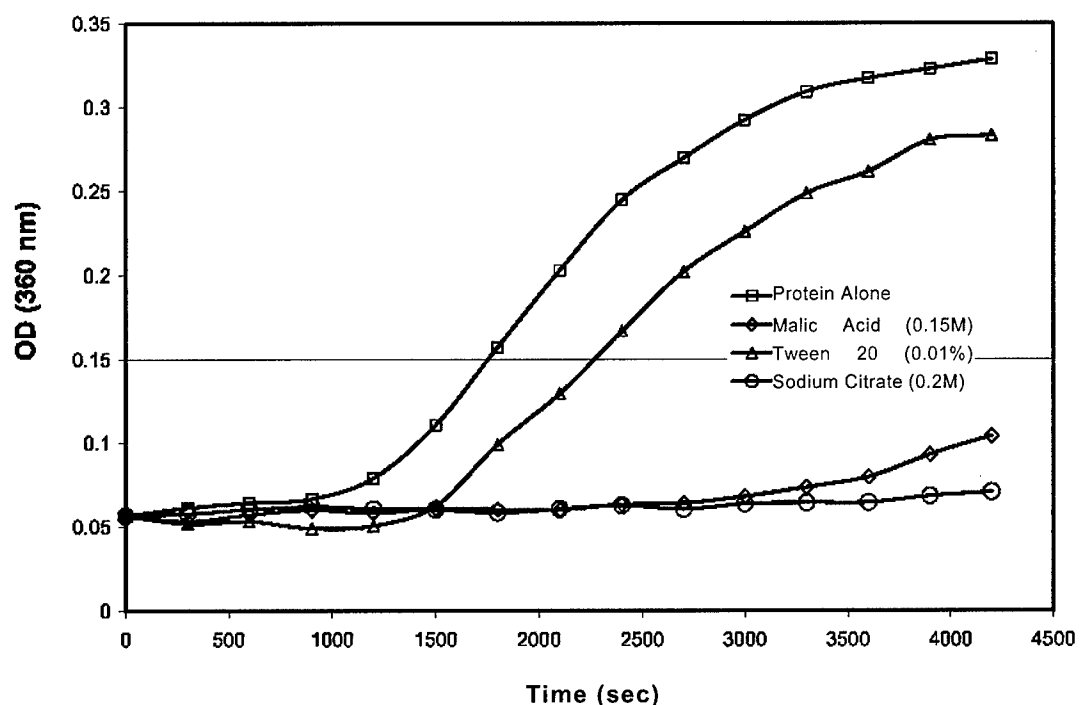
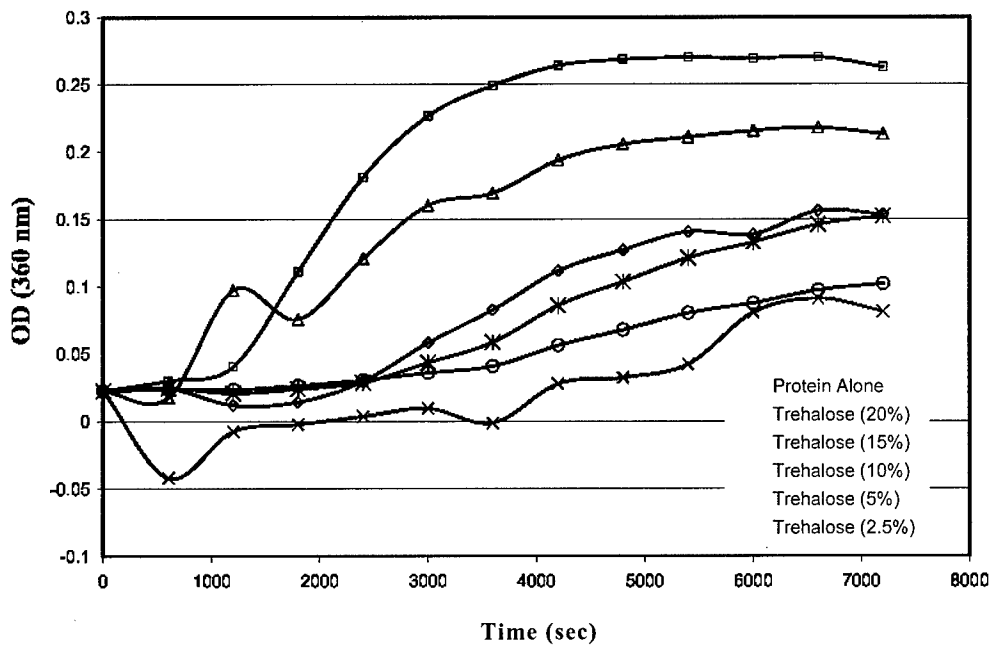


Figure 4.



5A.

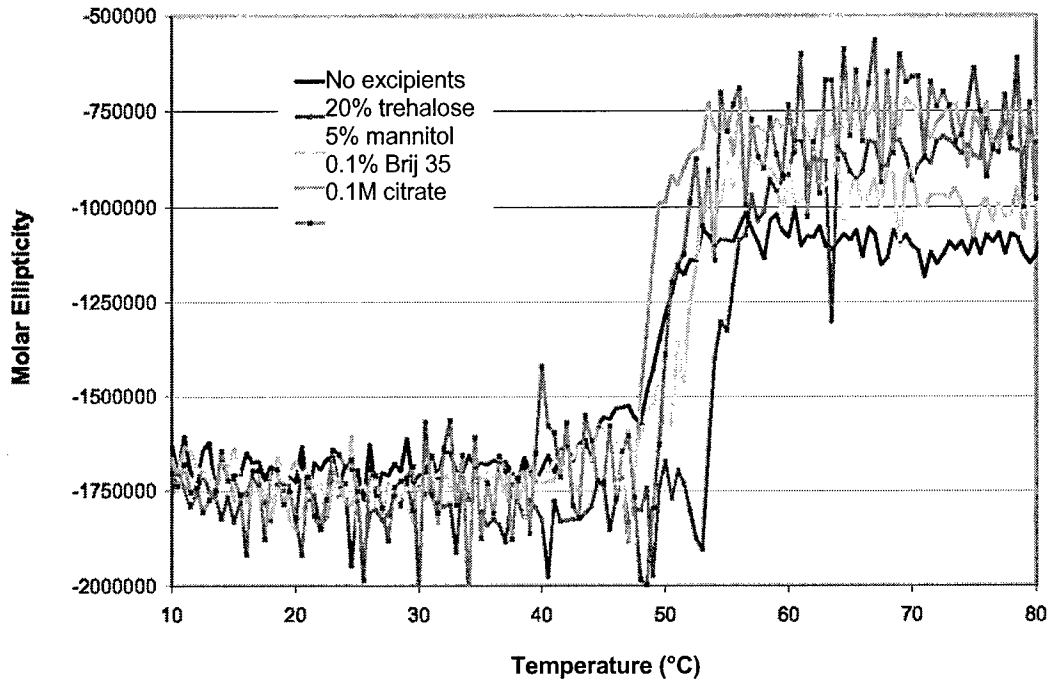


Figure 5B.

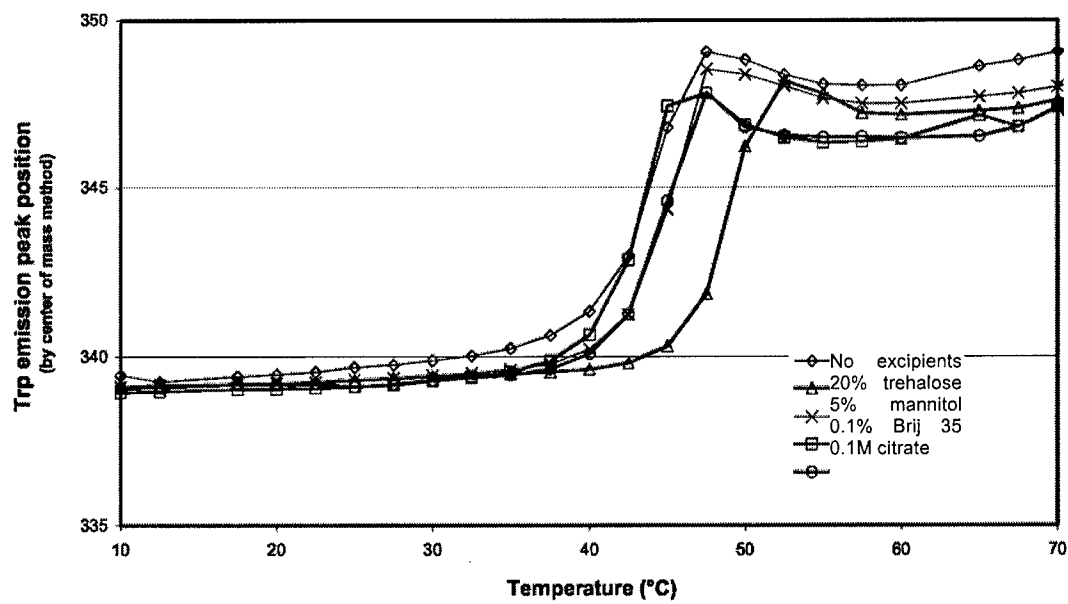
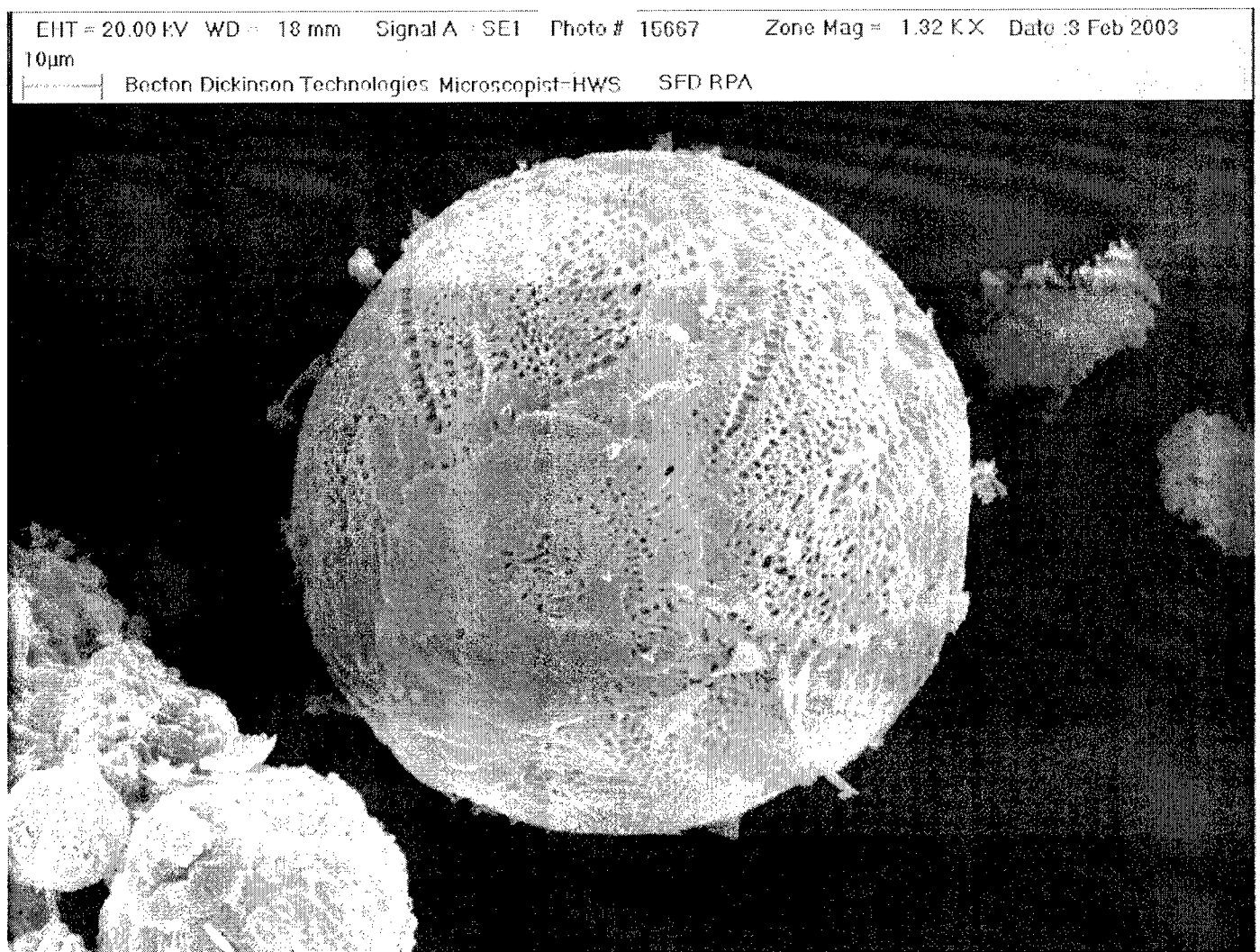


Figure 6.



igure 7.

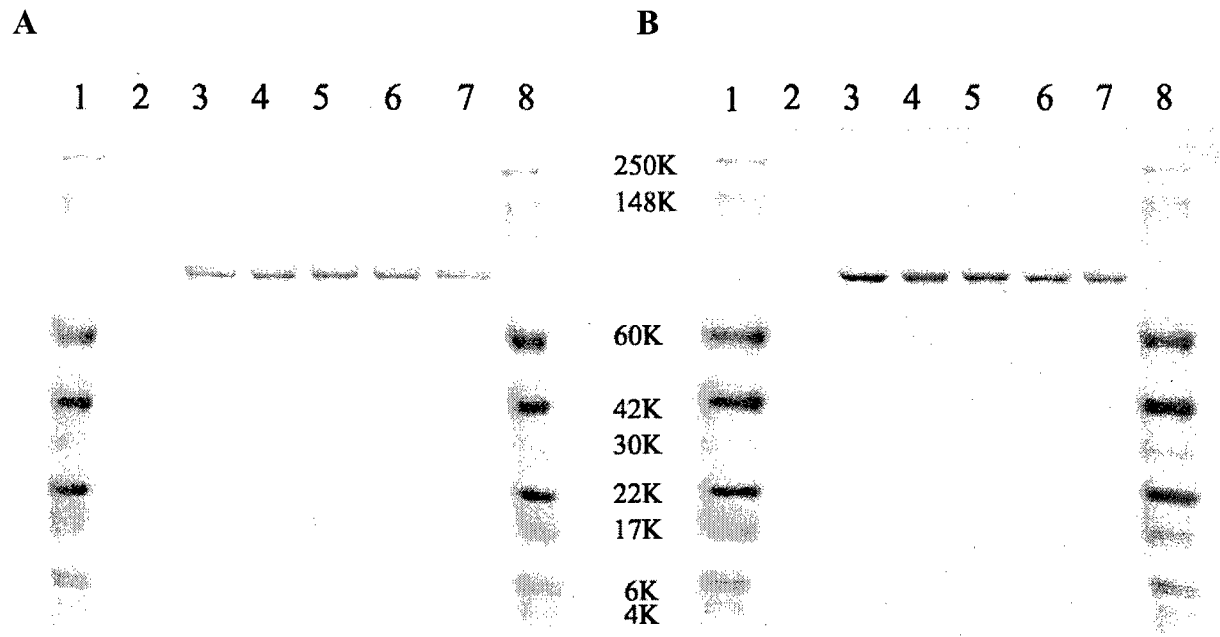


Figure 8.

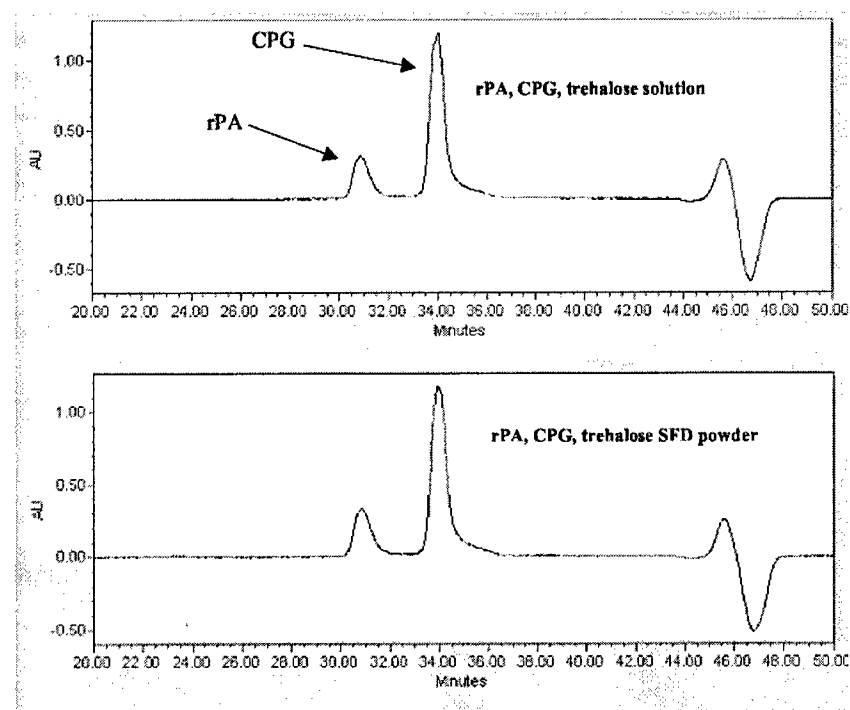
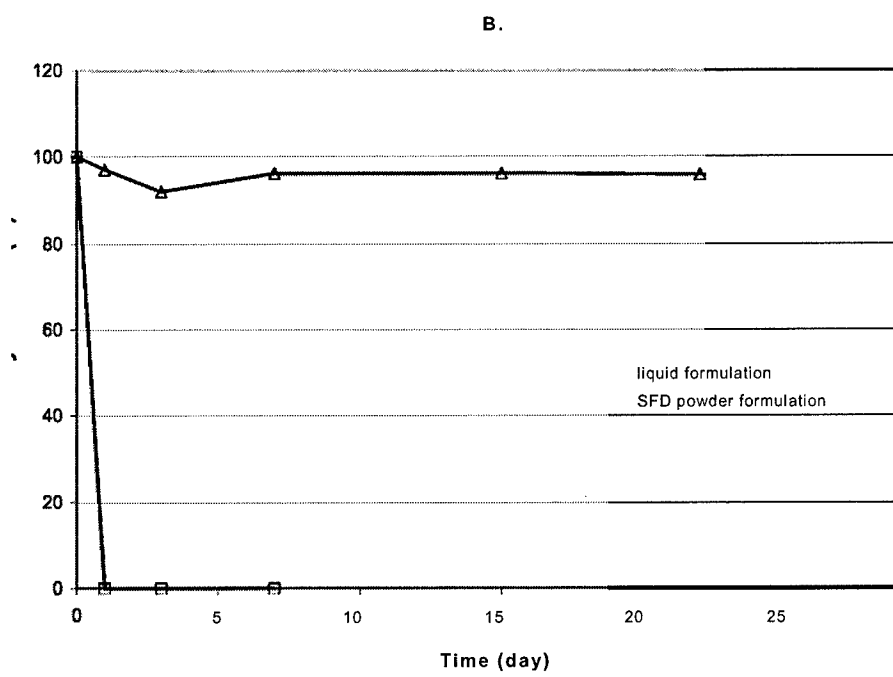
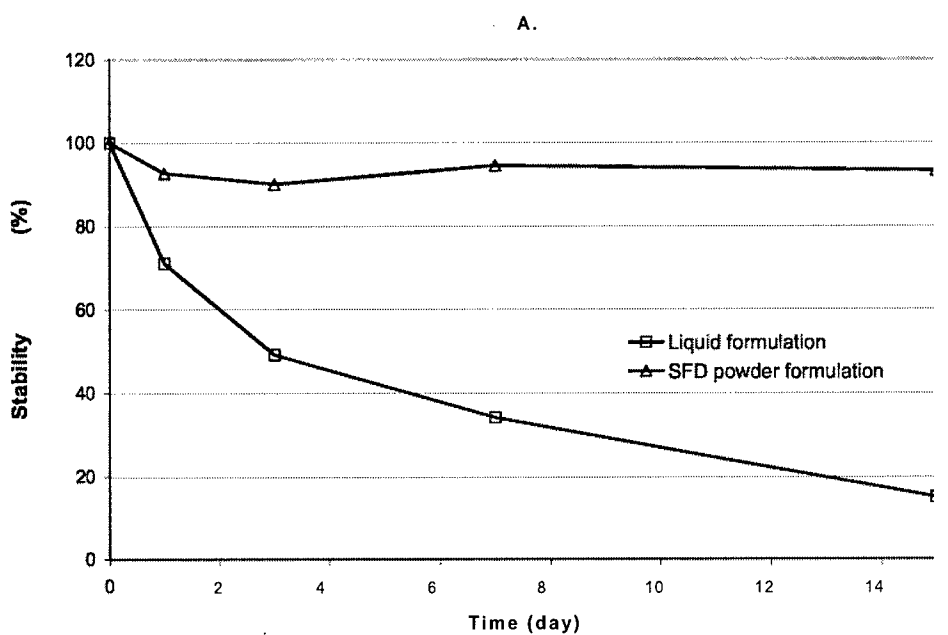


Figure 9.



**Figure 10.**

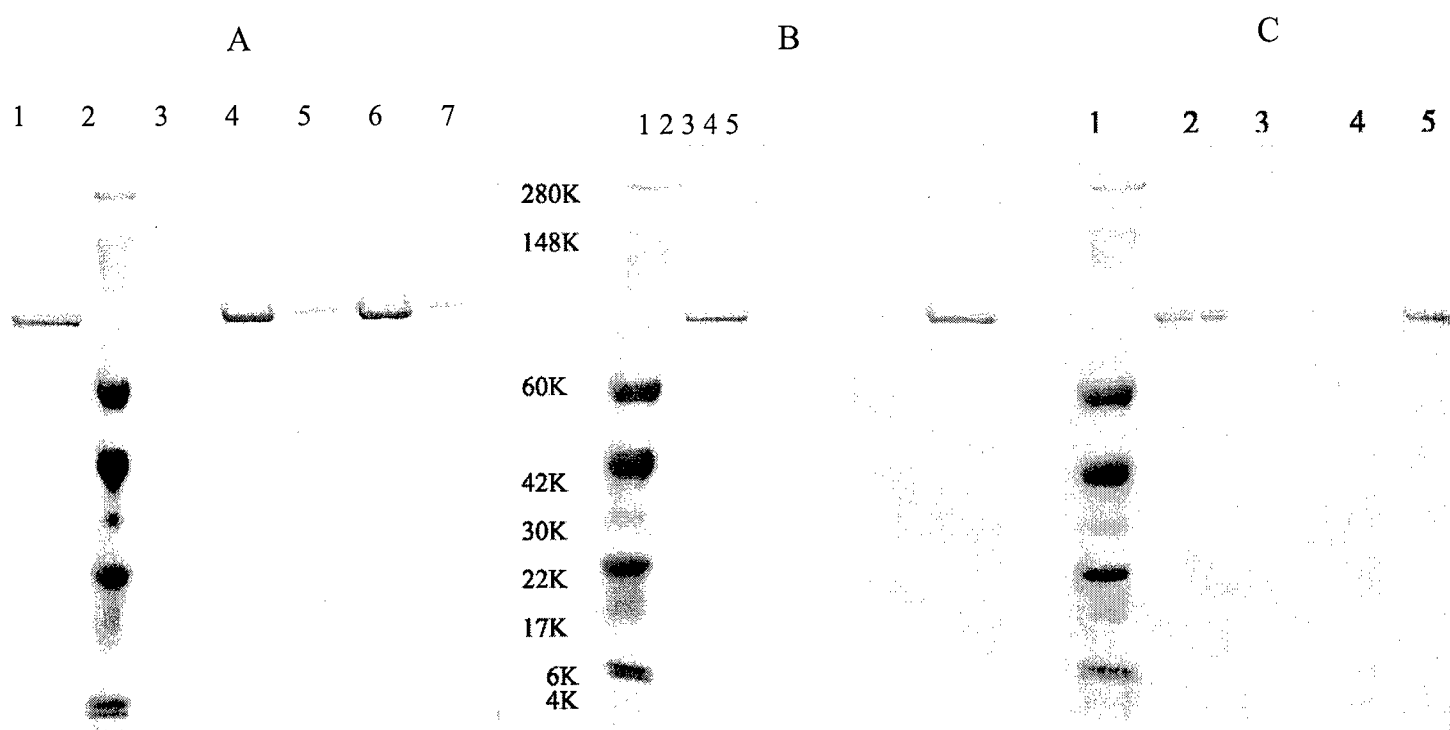
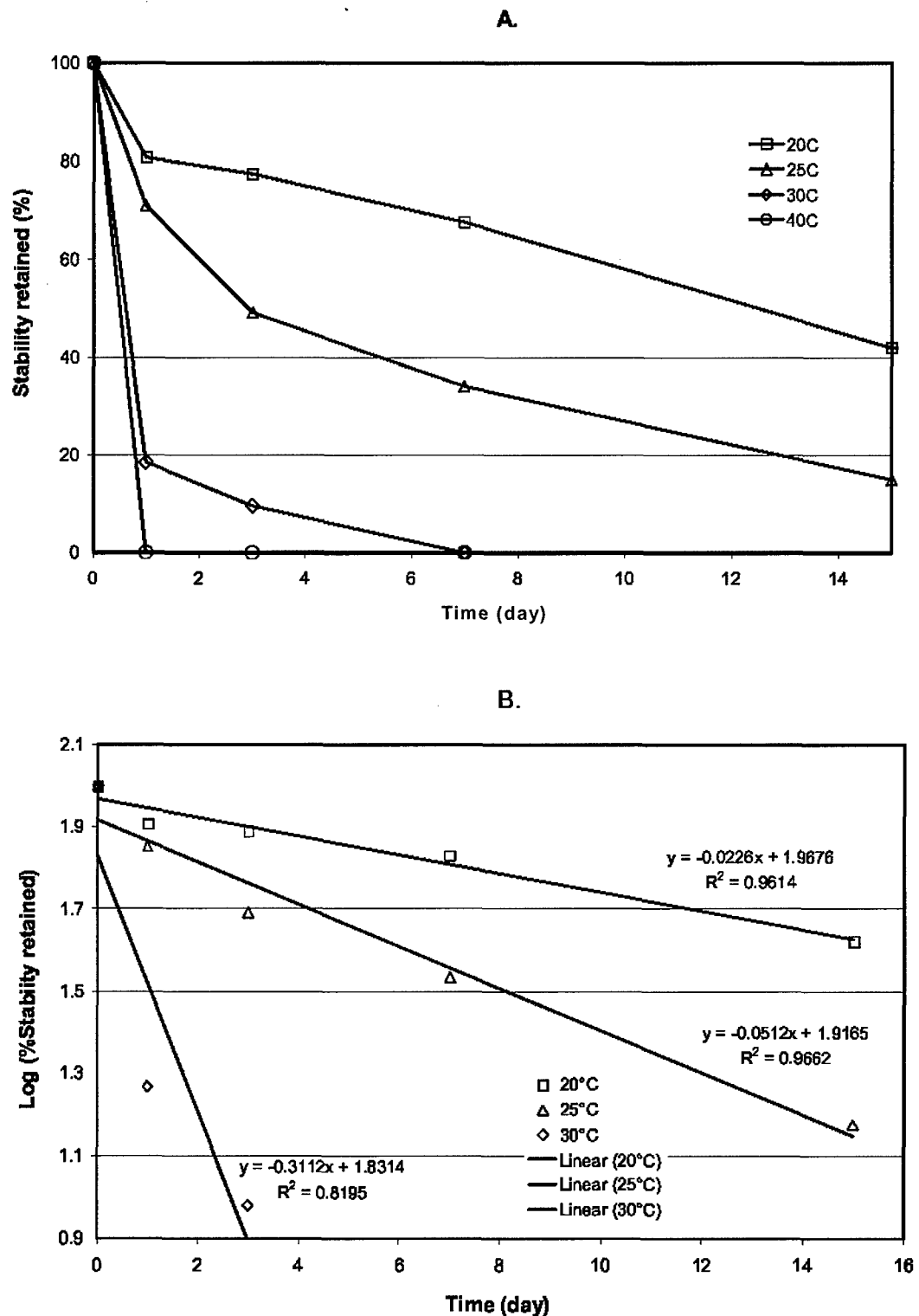


Figure 11.



## **Appendix II: Adenovirus 5 manuscript**

### **Effect of pH and Ionic Strength on the Physical Stability of Adenovirus Type 5**

*Jason Rexroad<sup>1</sup>, Robert K. Evans<sup>2</sup>, Carl J. Burke<sup>2</sup>, and C. Russell Middaugh<sup>1\*</sup>*

<sup>1</sup>*Department of Pharmaceutical Chemistry, University of Kansas,  
Lawrence, KS 66047*

<sup>2</sup>*Department of Vaccine Pharmaceutical Research, Merck Research Laboratories, WP78-302,  
Sumneytown Pike, West Point, Pennsylvania 19486*

\*To whom correspondence should be addressed

Department of Pharmaceutical Chemistry  
University of Kansas 2095  
Constant Ave Lawrence, KS  
66047 Tel: (785) 864-5813  
Fax: (785) 864-5814  
[middaugh@ku.edu](mailto:middaugh@ku.edu)

**Abstract:**

The thermal stability of adenovirus type 5 (Ad5) was investigated over the pH range 3-8 employing a variety of biophysical techniques. Additionally, the structural stability of Ad5 was compared under conditions of low and high ionic strength. Analysis of the structural stability of Ad5 by dynamic light scattering, intrinsic and extrinsic fluorescence, and second derivative UV absorption spectroscopies suggest that the capsid stability of Ad5 increases with decreasing pH under both sets of ionic strength conditions, however, significant aggregation was observed at pH : 5 under low ionic strength conditions. Furthermore, this study suggests that the physical stability of Ad5 is significantly enhanced under acidic conditions in the presence of 1M NaCl. Evaluation of the quaternary structural stability of Ad5 by dynamic light scattering and extrinsic fluorescence spectroscopy suggest that the Ad5 capsid undergoes a two-step dismantling process. Initially, the viral particles expand in size and a significant exposure of the DNA core to the surrounding solvent is observed near 50 °C. This is followed by complete capsid disassembly and total exposure of the DNA core at higher temperatures. Data generated during these studies were combined employing a multidimensional eigenvector approach that combines data from numerous techniques into a picture termed an "empirical phase diagram." This picture provides an intuitive representation of the physical stability of Ad5 over the pH range 4-8 from 10-85 °C. In addition, this is the first reported application of an empirical phase diagram to a protein/DNA complex such as a virus.

## **Introduction:**

Since their identification more than 50 years ago, extensive research has been directed towards characterizing and exploiting adenoviral systems, especially for their use as vaccines and their employment as delivery vehicles in gene therapy and genetic vaccination. At present, there are more than 160 human clinical trials involving adenoviral vectors<sup>1</sup> and of the more than 50 known human adenovirus serotypes, adenovirus type 5 (Ad5) is one of the most frequently utilized and well-characterized. Despite the enormous potential for these vectors to revolutionize the pharmaceutical industry, extensive efforts to develop more stable adenoviral formulations have been costly and time-consuming. In addition, the stability of adenoviral formulations has ultimately relied on biologically-based assays which can be inaccurate, imprecise, and usually fail to directly elucidate the mechanisms of inactivation. Modern instrumentation, however, can often efficiently analyze the chemical and physical integrity of macromolecular complexes as well as potentially provide details on the mechanisms of inactivation.

Adenovirus has a characteristic morphology<sup>2</sup> with a naked icosahedral capsid that is composed of multiple copies of at least seven different proteins. The viral core contains a linear, double-stranded 35 kb DNA genome which is associated with multiple copies of four different proteins. Together, the protein and nucleic acid give Ad5 a molecular weight of approximately 150 MDa.<sup>3</sup> The complex makeup of Ad5 has made the nature of any inactivation mechanisms difficult to elucidate, although our previous work suggests that thermal inactivation may be a result of lability in proteins III and IIIa.<sup>4</sup> Adenovirus has previously been shown to lose significant activity upon heating above 50 °C.<sup>5,6</sup> In addition, the virus is particularly sensitive to acidic environments and undergoes

significant irreversible aggregation when exposed to low ionic strength conditions (0.005M NaCl).<sup>7</sup> Acidification of endosomes upon adenoviral uptake has been suggested to assist in disassembly of adenoviral particles.<sup>8,9</sup> During storage, loss of Ad5 activity has been attributed to aggregation, oxidation, and freeze-thaw damage.<sup>10</sup> Although this work by Evans et al has resulted in the development of an Ad5 formulation that is stable for 24 months at 4 °C, an ideal formulation would have a shelf life of 24-3 6 months at room temperature.

Efforts to counteract the inactivation of Ad5 have been made by altering its solution environment,<sup>4,10</sup> site-directed mutagenesis,<sup>11</sup> lyophilization,<sup>12,13</sup> or chemical modification of the viral capsid.<sup>14</sup> Like all macromolecules, viral proteins are sensitive to changes in pH, temperature, redox potential and the presence of solutes. Since the activity of Ad5 relies on the maintenance of secondary, tertiary, and quaternary structure of the viral proteins, environmental modifications which inhibit structural changes in the viral proteins also have the potential to enhance its physicochemical stability. To this end, in this study we have employed a number of biophysical techniques to characterize the physical stability of Ad5 over the pH range 4-8. Additionally, because of its reported success in the stabilization of some macromolecular systems,<sup>15-18</sup> we have compared the structural stability of Ad5 at low and high salt concentrations.

The extensive biophysical characterization of any complex molecular entity generates large amounts of data that can be difficult to interpret in a comprehensive manner. Recent work by Kueltzo et al. has reported the development of a multidimensional Eigenvector approach that combines data from numerous techniques into a picture termed an “empirical phase diagram.”<sup>19</sup> The empirical phase diagram provides an intuitive representation of the data that can be used to determine the structural

stability of the entity of interest over a relatively wide range of temperatures and pH. The “phase boundaries” established by this procedure can also be used to develop accelerated stability assays for high throughput screening to identify potential stabilizing excipients. Although the empirical phase diagram approach has already been applied to recombinant proteins, this is the first description of its application to a protein/DNA complex like a viral particle. It is not only anticipated that this work will aid in the development of more stable adenoviral pharmaceutical formulations in an efficient manner, but it may also provide insight on physiologically relevant structural changes that take place upon exposure to acidic conditions such as those experienced by Ad5 during endosomal maturation.

## MATERIALS AND METHODS

**Ad5 formulations.** Purified Ad5 at a concentration of  $7.1 \times 10^{11}$  viral particles/mL (vp/mL) by anion exchange HPLC and  $4.8 \times 10^{11}$  vp/mL by genome quantitation assay<sup>10</sup> was provided by Merck Research Laboratories, Fermentation and Cell Culture Department and Vaccine Bioprocess Engineering Department. A thorough description of Ad5 purification is described elsewhere.<sup>20</sup> Two buffer compositions were employed during these studies: 1.) MRK1: 10mM HEPES, 10mM sodium acetate, 10mM histidine, 5% sucrose, 75 mM NaCl, 1mM MgCl<sub>2</sub>, and 0.006% (w/v) polysorbate-80; 2.) MRK2: 10mM HEPES, 10mM sodium acetate, 10mM histidine, 5% sucrose, 1 M NaCl, 1mM MgCl<sub>2</sub>, and 0.006% (w/v) polysorbate-80. Buffer pH was adjusted at ambient temperature with HCl or NaOH.

**UV absorption spectroscopy (UV).** UV absorption spectra were obtained employing a Hewlett-Packard 8453 diode-array spectrophotometer. The instrument was blanked with the appropriate buffer and spectra of Ad5 at a concentration of  $3 \times 10^{11}$  vp/mL were measured every 2.5 °C from 10-85 °C with an incubation period of 5 minutes at each temperature. Second derivatives of the absorption spectra from 240-370 nm were obtained and fit to a spline function with 99 points of interpolation using software supplied with the instrument. The negative second derivative peak positions were determined and used to follow the average environment of the aromatic amino acids (Phe, Tyr, and Trp) in the viral particles and plotted as a function of temperature using Microcal Origin® version 7. To simultaneously evaluate the aggregation behavior of Ad5 with increasing temperature, an interpolated heating trace of the optical density at 350 nm (OD) was followed as a function of temperature concomitant with absorption spectra determination using HP software. Second derivative UV and optical density data are presented as mean values with standard errors (N=3).

**Fluorescence spectroscopy.** Fluorescence emission spectra were obtained in 2.5 °C increments from 10-85 °C employing a QuantaMaster™ spectrofluorometer (Photon Technology International, Inc.) equipped with a 4-position cell holder and Peltier temperature control device at an Ad5 concentration of  $3 \times 10^{11}$  vp/mL. A 5-minute equilibration time was used at each temperature before data acquisition. The intrinsic fluorescence spectra were collected by exciting samples at 280 nm and emission was monitored between 305 and 450 nm using excitation and emission slit widths of 4 nm. The spectra were corrected for the Raman band of water by subtraction of the buffer spectrum at each corresponding temperature. Spectra were smoothed using the software

included with the instrument; buffer subtraction and plotting were performed in Microsoft Excel® and Microcal Origin 7®, respectively. Ad5 fluorescence data are mean values with standard errors (N=3). The T<sub>m</sub> at each pH was determined by calculating the abscissa (x-axis coordinate) where the second derivatives of the fluorescence intensity versus temperature plots change from negative to positive using Microcal Origin®.

Extrinsic fluorescence spectroscopy was conducted to determine the accessibility of Ad5 M DNA with increasing temperature from 10-85 °C in 2.5 °C increments employing 7.5 propidium iodide (Molecular Probes, #P-1304) and an Ad5 concentration of  $3 \times 10^{11}$  vp/mL. Sample volumes of 1 mL were excited at 535 nm and emission was monitored from 550 to 650 nm using excitation and emission slit widths of 6 nm. The fluorescence intensity at the wavelength of maximum fluorescence intensity for each spectrum (approximately 607 nm) was plotted as a function of temperature in Microsoft Excel®. The T<sub>m</sub> for Ad5 at each pH was determined as described above.

**Dynamic light scattering.** The hydrodynamic diameter of Ad5 as a function of temperature was estimated by dynamic light scattering using a viral concentration of  $3 \times 10^{11}$  vp/mL. Measurements were obtained every 2.5 °C using a light scattering instrument (Brookhaven Instruments Corp, Holtszille, NY) equipped with a 50 mW

diode-pumped laser (=532 nm) incident upon a sample cell immersed in a bath of decalin. Temperature was controlled by a circulating water bath. The scattered light was monitored by a PMT (EMI 9863) at 90° to the incident beam and the autocorrelation function was generated by a digital correlator (BI-9000AT). Data was collected

continuously for five 30-s intervals for each sample and averaged. The autocorrelation function was fit by the method of cumulants to yield the average diffusion coefficient of the complexes. The effective hydrodynamic diameter (Z-average particle size) was obtained from the diffusion coefficient by the Stokes-Einstein equation. In the cases of pH-induced aggregation, the data was fit to a non-negatively constrained least squares algorithm to yield multi-modal distributions on a number average basis.

**Empirical phase diagram generation.** Empirical phase diagrams were generated using the data points at 2.5 °C intervals from 10-85 °C from the following: second derivative UV peaks near 279, 284, and 291 nm, optical density at 350 nm, intrinsic fluorescence peak position, intrinsic fluorescence peak intensity, propidium iodide fluorescence intensity at 607 nm, and hydrodynamic diameter from dynamic light scattering. Data from these techniques were imported into Mathematica® version 4.2 (Wolfram Research, Inc.) and empirical phase diagrams were generated as described elsewhere (REF) although a brief description is provided here. The data generated by the various biophysical techniques employed are initially ordered by parameter (i.e., pH and temperature). These discrete parameters can also be thought of as coordinates that are associated with a set of variables from each technique employed. These variables represent unit vectors that define an n-dimensional vector space with dimensions equal to the number of variables included in the data set. Individual unit vector projectors are then calculated and summed to obtain a density matrix. The eigenvalues and eigenvectors of the density matrix are subsequently calculated and the dimensions are reduced to three based on their relative contributions for the generation of the empirical phase diagram. Each of the three dimensions is then assigned a color (red, green, or blue) to yield a final

color which is a sum of the three component vectors. The images generated not only provide an easily interpreted description of the average physical state of Ad5 over a broad range of temperature and pH, but also define the boundary conditions under which physical changes in Ad5 occur.

## RESULTS

**Stability of Ad5 tertiary structure.** High resolution second derivative UV spectroscopy was employed to assess the tertiary structural stability of the Ad5 proteins. Absorption bands near 254, 280, and 291 nm are attributed to absorbance by phenylalanine, tyrosine, and tryptophan residues, respectively. Additional absorbance bands are due to absorbance by viral DNA (near 260 nm) and an overlapping absorbance at 284 nm reflects contributions from both Tyr and Trp (Figure 1). The positions of such peaks are typically sensitive to changes in polarity of the immediate environment of aromatic amino acid residues. In general, exposure of the apolar aromatic amino acid residues to a more polar environment (e.g., water) is manifested as the preferential absorbance of light of lower wavelengths, whereas shifts to higher wavelengths suggest that the residues are incorporated into a more buried, or less polar environment. Analysis of the second derivative data for Ad5 at pH 3-8 in MRK1 (0.075 M NaCl) reveals complex behavior. A representative plot of negative peak position versus temperature is shown for Ad5 at pH 7 in MRK2 (1 M NaCl) in Figure 2. In particular, shifts in peak positions to lower wavelengths above 50 °C are observed for Ad5 at neutral pH suggesting that a more solvent exposed conformation is adopted by the aromatics residues above this temperature. With the exception of pH 3 where a value for the  $T_m$  is unobtainable due to extensive aggregation, this transition occurs at increasingly higher temperatures with

decreasing pH (Figure 3) suggesting that this perturbation in tertiary structure is inhibited by an increase in protonation level of the viral proteins. The transitions near 50 °C are followed by increases in peak position above 70 °C where thermally-induced aggregation is known to occur (see below).

Although the pH dependence itself is similar, a small, but significant increase in the tertiary structural stability of Ad5 is observed in the presence of 1M NaCl compared to the lower salt concentration at all pH values studied. As an indicator of the overall tertiary structural stability of Ad5, the peak trace near 284 nm was selected since absorbance at this wavelength is attributed to the overlapping absorbance of Tyr and Trp residues. Similar effects are seen in the other peaks, however (not shown).

Intrinsic fluorescence spectroscopy was employed as a complementary technique to second derivative UV spectroscopy to assess changes in tertiary structure with increasing temperature. As expected, the fluorescence emission spectrum is dominated by tryptophan emission. Under all pH conditions for both salt concentrations, the emission maximum is located near  $333 \pm 1$  nm at low temperature suggesting a relatively buried environment for the majority of the proteins' Trp residues. Similar to the results obtained by second derivative UV spectroscopy, the intrinsic fluorescence data as a function of temperature suggests that the stability of the tertiary structure of Ad5 is more stable in the presence of 1M NaCl. Also in agreement with the absorbance studies is the trend of increasing stability with decreasing pH at the higher salt concentration (Figure 4). Changes in tertiary structure are also confirmed by changes in slope in plots of fluorescence intensity versus temperature (data not shown). In general, the data obtained

by intrinsic fluorescence spectroscopy agrees well with the data obtained by absorbance measurements, although second derivative analysis reveals some smaller structural transitions that are not as clearly resolved by intrinsic fluorescence spectroscopy. In contrast, the fluorescence changes initiate at somewhat lower temperatures than the absorbance detected transitions.

**Turbidity (optical density) studies.** Optical density at 350 nm (OD) as a function of temperature was recorded concomitantly with UV absorption spectra to assess gross changes in associative states of the viral particles. The OD values remain relatively constant up to approximately 50 °C. At temperatures above 50 °C, a decrease in the optical density occurs prior to a dramatic increase above 60 °C. Decreases such as those seen prior to OD increases are most often associated with decreases in the refractive index of the scatterer and subsequent lowering of scattering intensities. This might be, for example, associated with the swelling of particles. The more extensive increases in scattering seen at higher temperatures are most consistent with gross particle aggregation. Whatever the explanation, these transitions occur at higher temperatures with decreasing pH (Figure 5). At pH 4, detectable transitions do not occur until approximately 10 °C higher suggesting that changes in capsid conformation that lead to aggregation are inhibited with decreasing pH. Comparisons reveal no significant differences between the aggregation states of Ad5 in MRK1 and MRK2.

**Extrinsic fluorescence spectroscopy.** Propidium iodide (PI) was employed to assess the thermal stability of the quaternary structure of the Ad5 capsid. PI is a DNA intercalating dye whose fluorescence is enhanced up to 30-fold upon binding to DNA. The

fluorescence of PI is therefore quenched until the viral capsid is compromised and the DNA becomes accessible. With the exception of pH3, the temperature at which the nucleic acid core becomes accessible to PI increases with decreasing pH in MRK2, suggesting that the quaternary structural stability of Ad5 increases as the pH is lowered (Figure 6). On the other hand, the greatest capsid stability is observed at pH 7 in MRK1 with the  $T_m$  being near 46 °C. The presence of 1M NaCl, however, increases the  $T_m$  at pH 7 by approximately 4 °C and more than 18 °C at pH 4 relative to Ad5 in MRK1 at the same pH. Similar to results obtained by the second derivative UV, intrinsic fluorescence, and optical density studies, the thermal stability of Ad5's quaternary structure is maximized at pH 4 in MRK2.

The fluorescence of PI in the presence of Ad5 at pH 3 remained relatively constant over the entire temperature range studied suggesting that extensive capsid disruption was not occurring. The reason for this lack of fluorescence intensity change was investigated by adding PI to free DNA at pH 3 at various temperatures. It was observed that although an increase in fluorescence intensity occurs upon addition of PI to free DNA at 10 °C, the intensity of the fluorescence was decreased by ~15% compared to pH 4-8 (data not shown). At 55 °C, however, no detectable increase in the fluorescence intensity of PI was observed upon the addition of PI to DNA suggesting that binding does not occur at elevated temperatures at this pH. Thus, it can be concluded from the pH 3 data that the viral particles are still intact at 10 °C. The temperature at which the capsid is breached, however, is not detectable by the employment of this fluorescent probe. Attempts to employ other DNA binding dyes were not successful and therefore no conclusions are made with regard to the capsid's thermal stability at pH3.

Extrinsic fluorescence measurements also suggest that Ad5 viral particles undergo at least a two-step thermal disruption of the capsid (Figure 7). Initial increases in PI fluorescence intensity are observed near 40 and 37 °C for Ad5 at pH 5 and 6, respectively. A second, less substantial increase in PI fluorescence intensity also occurs at temperatures near 60 °C. This result, along with dynamic light scattering measurements described below suggest that the viral particles undergo an initial “loosening” of the capsid prior to more complete capsid disassembly. The temperatures at which these transitions take place are dependent upon both the pH and buffer components present (i.e., salt concentration).

**Dynamic Light Scattering.** Dynamic light scattering was employed to monitor changes in the size of viral particles with increasing temperature. The effective hydrodynamic radius of Ad5 in two buffers at pH 7 was found to be  $120 \pm 5$  nm at 10 °C which is in close agreement with previous measurements.<sup>4,21</sup> The polydispersity index of the solution under these conditions was  $0.02 \pm 0.01$  suggesting a monodisperse size distribution. Additionally, significant differences between Ad5 dynamic light scattering measurements at 10 °C were not detected for the two formulations from pH 6-8 suggesting that major changes in quaternary structure were not induced by altering the pH from neutrality. Particle sizes greater than 500 nm and polydispersity indices over 0.2 were measured at pH 3-5 for Ad5 in MRK1 suggesting the presence of highly aggregated viral particles. Although the presence of 1M NaCl did not prevent aggregation at pH3, Z-average particle sizes were 148 and 128 nm at pH 4 and 5, respectively, with polydispersity indices below 0.1. To determine whether the increase in Z-average particle size was due to the presence of large aggregates, the data were fit to a non-negatively constrained least squares

algorithm (NNLS). It was determined that particle sizes ranged from 155-205 nm which is smaller than would be expected if higher order aggregates were formed. Together, this data suggests that a monodisperse solution of intact viral particles is present under these solution conditions despite the slight increase in hydrodynamic diameter.

Similar to the results obtained by the other methods, Ad5 demonstrates a thermal stability of its quaternary structure that decreases with increasing pH in MRK2.  $T_m$ s were not obtainable for Ad5 at pH 3-5 in MRK1 and pH3 in MRK2 since significant aggregation occurred during dialysis. A significant enhancement in Ad5 thermal stability was observed, however, in the presence of 1M NaCl (Figure 8). The highest  $T_m$  was calculated for Ad5 in MRK2 at pH 4 ( $T_m = 65.2\text{ }^{\circ}\text{C}$ ), but increases in size, polydispersity index, and scattering intensity were measured with an onset near 50  $^{\circ}\text{C}$  offering further evidence that a “loosening” of the capsid may occur prior to major capsid disruption and aggregation. The same two-step capsid disruption phenomenon was observed under other solution conditions, but they were most pronounced at pH 4 in the presence of 1M salt.

**Ad5 Empirical Phase Diagrams.** Empirical phase diagrams are shown in Figure 9 for Ad5 from pH 4-8. Data at pH 3 were not included due to the lack of extrinsic fluorescence data as well as the extensive aggregation seen under these conditions. When the remaining data are combined and summarized in the form of empirical phase diagrams, it is evident that Ad5 remains structurally similar from pH 6-8 below 40  $^{\circ}\text{C}$  in MRK1 (the blue phase in Figure 9, panel A). Color changes at low temperatures at pH 4 and 5 (pink/blue and orange, respectively in Figure 9, panel A), however, reflect quaternary structural instability and aggregation as revealed by dynamic light scattering

measurements. Although the onset of color changes at pH 6 for Ad5 in MRK1 starts near the same temperature, the transition to light green is not as abrupt as the color changes that take place at pH 7 and 8 near 40 °C. Additionally, close inspection of panel A in Figure 9 at pH6 shows color differences at low temperatures (purple at low temperatures for pH6 versus blue at the same temperatures for Ad5 at pH 7 and 8) revealing physical alterations of Ad5 at low pH. Comparisons of the Figures 9 and 10 suggest a significant stabilizing effect by 1M NaCl, especially at lower pH. The diagrams imply that Ad5 at pH 4 in MRK2 is more stable by 10 °C compared to the virus in low salt at pH 8. Further comparisons argue that the structural integrity of Ad5 is maintained at pH 4 and 5 in MRK2, but significant perturbation is observed at low salt under the same pH conditions.

## DISCUSSION

It is well established that low concentrations of salt (<0.2 M) stabilize proteins through a reduction of the net positive charge on the macromolecule by either anion binding and/or Debye-Huckel charge screening. At higher salt concentrations, stabilization is thought to be primarily achieved by preferential hydration of the protein and exclusion of the cosolute from the protein's surface. These preferential interactions result in a thermodynamic state that disfavors the unfolding or perturbation of the protein from its native state. Since it is observed that Ad5 is physically more stable in the presence of 1M NaCl, these mechanisms are presumably active on intact viral particles. Since an enhancement in the thermal stability of the secondary and tertiary structure of Ad5 was previously observed in the presence of 10% sucrose,<sup>4</sup> stabilization of Ad5 by preferential

hydration of its capsid by a variety of cosolutes may be an effective general method of preserving its conformation and activity.

There is increasing evidence that stabilization of protein's conformation is not only important for preventing deleterious processes such as aggregation, but it can also inhibit chemical degradation processes such as oxidation and deamidation.<sup>22</sup> In the case of Ad5, this may be especially important since recent work found that major inactivation pathways of Ad5 during storage include oxidation and surface adsorption/aggregation.<sup>10</sup> The inclusion of antioxidants and excipients that hinder the perturbation of a protein's native state should significantly enhance its storage life. Further modification of such formulations to include high concentrations of appropriate cosolutes should provide additional stability. Although an Ad5 formulation containing 1M NaCl at pH 4 is not pharmaceutically plausible, the production of high titers (e.g., T10<sup>12</sup> vp/mL) of Ad5 are now common. Stock formulations containing high concentrations of Ad5 could therefore be stored under optimized storage conditions and diluted to yield working formulations of acceptable properties.

Dynamic light scattering, second derivative UV absorbance, and extrinsic fluorescence spectroscopies reveal that two distinct transitions occur during thermal stress of Ad5. The first of these occurs near 50 °C and is followed by an additional event near 65 °C. Dynamic light scattering measurements suggest that the Ad5 capsid undergoes an initial loosening of the capsid that results in an increase in the hydrodynamic radius. Extrinsic fluorescence spectroscopy measurements manifest a two-part increase in fluorescence intensity reflecting enhanced accessibility of the DNA further supporting this claim.

Second derivative UV spectroscopy also shows major transitions near these temperatures that are consistent with structural alterations. Previous observations from transmission electron microscopy (TEM) revealed that the majority of viral particles remained intact after heating to 50 °C with the exception of ruptured vertices. TEM images of Ad5 heated to 70 °C revealed significantly fewer icosahedral virions while no viral particles with characteristic morphology were observed at 90 °C.<sup>4</sup> It can therefore be hypothesized that the initial loosening event observed here is accompanied or immediately followed by the loss of penton capsomeres which results in the initial increase in DNA accessibility to the extrinsic probe. A similar process has also been observed in the bacteriophage P22 in which heat-treated virus undergoes an expanded capsid as a result of the release of the pentons from its vertices.<sup>23</sup> It was concluded from the latter studies that this release of pentons may be a common process among double-stranded DNA viruses. Heating to higher temperatures results in more extensive capsid disruption and virtually complete accessibility of the nucleic acid to the dye. Recent work by Martin-Fernandez et al. also indicates that Ad5 undergoes two phases of capsid disassembly.<sup>24</sup> In these studies, it was demonstrated that disassembly can be attributed to the dissociation of fibers, followed by the combined dissociation of penton, hexon, and protein IX. Although performed in cell culture, the capsid disassembly process described by Martin-Fernandez et al. correlates well with our observations. It is therefore proposed that the two transitions observed here are indicators of these capsid dismantling events.

One of the steps that occur during Ad5 infection prior to capsid disassembly and transport of the packaged genome to the nucleus is the acidification of maturing endosomes.<sup>25</sup> It has previously been suggested that exposure to acidic environments (~pH 6.0) is

sufficient to trigger penton release at low ionic strength.<sup>26,27</sup> Additionally, recent work by Wiethoff et al. suggests that the Ad5 vertex is dissociated at pH < 5.5 at 37 °C.<sup>28</sup> Here, we describe an increase in capsid stability with decreasing pH in both Ad5 formulations. Although a decrease in pH to as low as 3 is not enough to trigger capsid disassembly in Ad5 at low temperatures, a significant decrease in the stability of the viruses quaternary structure as well as an increase in the aggregation state of the virus is observed with decreasing pH in MRK1. Thus, the decrease in pH during endosome acidification may perturb the capsid proteins enough to assist in capsid dismantling.

The changes in physical stability that result from the changes in solution conditions and temperature are conveniently manifested as color changes in empirical phase diagrams. The images generated not only provide a more intuitive description of the average physical stability of Ad5 over a broad range of conditions, but these diagrams can also be employed to determine the boundary conditions where physical changes in Ad5 occur. By going to those boundary conditions, degradation pathways will be accelerated and their inhibition can be used to identify potential stabilizers. The employment of high-throughput screening methods such as turbidity assays or extrinsic fluorescence spectroscopy at elevated temperatures would be a practical way to screen large libraries for potentially stabilizing compounds.

Previous work investigating the effect of heat on adenovirus established that adenovirus loses significant activity upon heating above 50 °C.<sup>5,6,29,30</sup> Furthermore, physical inactivation of Ad5 is routinely performed by heating the virus to 56 °C<sup>31</sup> although a more robust method was recently developed that exposes Ad5 to 70 °C for at least 20

minutes.<sup>5</sup> The success of these methods in conjunction with our present and previous studies suggests that the transitions detected near 50 °C may be the key event(s) in the inactivation of Ad5, although this hypothesis has not been rigorously tested.

1. (GeMCRIS) NFGMCRIS. 2004. NIH Genetic Modification Clinical Research Information System (GeMCRIS). ed.: NIH/FDA Genetic Modification Clinical Research Information System (GeMCRIS).
2. Stewart PL, Fuller SD, Burnett RM 1993. Difference imaging of adenovirus: bridging the resolution gap between X-ray crystallography and electron microscopy. *Embo J* 12(7):2589-2599.
3. Stewart PL, Burnett RM 1990. The structure of adenovirus. *Seminars in Virology* 1:477-487.
4. Rexroad J, Wiethoff CM, Green AP, Kierstead TD, Scott MO, Middaugh CR 2003. Structural stability of adenovirus type 5. *J Pharm Sci* 92(3):665-678.
5. Maheshwari G, Jannat R, McCormick L, Hsu D 2004. Thermal inactivation of adenovirus type 5. *J Virol Methods* 1 18(2):141-146.
6. Russell WC, Valentine RC, Pereira HG 1967. The effect of heat on the anatomy of the adenovirus. *J Gen Virol* 1(4):509-522.
7. Galdiero F 1979. Adenovirus aggregation and preservation in extracellular environment. *Arch Virol* 59(1-2):99-105.
8. Blumenthal R, Seth P, Willingham MC, Pastan I 1986. pH-dependent lysis of liposomes by adenovirus. *Biochemistry* 25(8):223 1-2237.
9. Greber UF, Willetts M, Webster P, Helenius A 1993. Stepwise dismantling of adenovirus 2 during entry into cells. *Cell* 75(3):477-486.
10. Evans RK, Nawrocki DK, Isopi LA, Williams DM, Casimiro DR, Chin S, Chen M, Zhu DM, Shiver JW, Volkin DB 2004. Development of stable liquid formulations for adenovirus-based vaccines. *J Pharm Sci* 93(10) :2458-2475.
11. Blanche F, Cameron B, Somarriba S, Maton L, Barbot A, Guillemin T 2001. Stabilization of recombinant adenovirus: site-directed mutagenesis of key asparagine residues in the hexon protein. *Anal Biochem* 297(1):1-9.
12. Croyle MA, Cheng X, Wilson JM 2001. Development of formulations that enhance physical stability of viral vectors for gene therapy. *Gene Ther* 8(17):1281-1290.
13. Croyle MA, Roessler BJ, Davidson BL, Hilfinger JM, Amidon GL 1998. Factors that influence stability of recombinant adenoviral preparations for human gene therapy. *Pharm Dev Technol* 3(3):373-383.
14. Cheng X, Ming X, Croyle MA 2003. PEGylated adenoviruses for gene delivery to the intestinal epithelium by the oral route. *Pharm Res* 20(9):1444-1451.

15. Gloss LM, Simler BR, Matthews CR 2001. Rough energy landscapes in protein folding: dimeric *E. coli* Trp repressor folds through three parallel channels. *J Mol Biol* 312(5):1 121-1134.
16. Hu CQ, Sturtevant JM, Thomson JA, Erickson RE, Pace CN 1992. Thermodynamics of ribonuclease T1 denaturation. *Biochemistry* 31(20) :4876-4882.
17. Nishimura C, Uversky VN, Fink AL 2001. Effect of salts on the stability and folding of staphylococcal nuclease. *Biochemistry* 40(7):2 113-2128.
18. Pace CN, Grimsley GR 1988. Ribonuclease T1 is stabilized by cation and anion binding. *Biochemistry* 27(9):3242-3246.
19. Kueltzo LA, Ersoy B, Ralston JP, Middaugh CR 2003. Derivative absorbance spectroscopy and protein phase diagrams as tools for comprehensive protein characterization: a bGCSF case study. *J Pharm Sci* 92(9): 1805-1820.
20. Sweeney JA, Hennessey JP, Jr. 2002. Evaluation of accuracy and precision of adenovirus absorptivity at 260 nm under conditions of complete DNA disruption. *Virology* 295(2):284-288.
21. Oliver CJ, Shortridge KF, Belyavin G 1976. Diffusion coefficient and molecular weight of type 5 adenovirus by photon-correlation spectroscopy. *Biochim Biophys Acta* 437(2):589-598.
22. Meyer JD, Ho B, Manning MC 2002. Effects of conformation on the chemical stability of pharmaceutically relevant polypeptides. *Pharm Biotechnol* 13:85-107.
23. Teschke CM, McGough A, Thuman-Commike PA 2003. Penton release from P22 heat-expanded capsids suggests importance of stabilizing penton-hexon interactions during capsid maturation. *Biophys J* 84(4):2585-2592.
24. Martin-Fernandez M, Longshaw SV, Kirby I, Santis G, Tobin MJ, Clarke DT, Jones GR 2004. Adenovirus type-5 entry and disassembly followed in living cells by FRET, fluorescence anisotropy, and FLIM. *Biophys J* 87(2): 1316-1327.
25. Van Dyke RW 1996. Acidification of lysosomes and endosomes. *Subcell Biochem* 27:331-360.
26. Laver WG, Wrigley NG, Pereira HG 1969. Removal of pentons from particles of adenovirus type 2. *Virology* 39(3):599-604.
27. van Oostrum J, Burnett RM 1985. Molecular composition of the adenovirus type 2 virion. *J Virol* 56(2):439-448.

28. Wiethoff CM, Wodrich H, Gerace L, Nemerow GR 2005. Adenovirus protein VI mediates membrane disruption following capsid disassembly. *Journal of Virology* 79(4): 1992-2000.
29. Wallis C, Yang CS, Melnick JL 1962. Effect of cations on thermal inactivation of vaccinia, herpes simplex, and adenoviruses. *Journal of Immunology* 89:41-46.
30. Yang CS, Tai FH, Wallis C, Melnick JL 1963. Adenovirus Vaccine Prepared By Thermal Inactivation Of The Infective Moiety Of The Virus In Magnesium Ions. *J Immunol* 91:283-286.
31. Canada PHAo. 2001. Adenovirus types 1, 2, 3, 4, 5 and 7 - Material Safety Data Sheet. ed.: Public Health Agency of Canada.

**Figure 1.** Representative UV absorption spectrum of Ad5 at pH 7 in MRK1 (open circles) and its second derivative (solid line).

**Figure 2.** High-resolution second derivative UV spectroscopy negative peak positions as a function of temperature for Ad5 at pH 7 in MRK2. Peaks below 270 nm cannot be definitively assigned due to the overlapping absorbances of Phe and DNA, however, peaks near 278, 284, and 292 nm are attributed to the absorbance of Tyr, a combination of Tyr/Trp, and Trp, respectively.

**Figure 3.** Second derivative UV spectroscopy  $T_m$  values versus pH from the peak trace near 284 nm for Ad5 in MRK1 (open circles) and MRK2 (solid squares). The peak near 284 nm is attributed to the overlapping absorbance of Tyr and Trp and should therefore be a good indicator of the overall tertiary structural stability of the Ad5 proteins.

**Figure 4.** Intrinsic fluorescence spectroscopy  $T_m$  values versus pH for Ad5 in MRK1 (open circles) and MRK2 (solid squares). The  $T_m$  values were calculated from a plot of the wavelength of maximum fluorescence intensity (max) versus temperature.

**Figure 5.** Optical density at 350 nm versus temperature for Ad5 in MRK2. Symbols represent data for Ad5 as follows: pH 4 (solid squares), pH 5 (open squares), pH 6 (open circles), pH 7 (open triangles), and pH 8 (crosshairs).

**Figure 6.** Extrinsic fluorescence spectroscopy melting temperature for Ad5 in MRK1 (solid squares) and MRK2 (open circles). Melting temperatures were calculated from the plot of fluorescence intensity at 607 nm versus temperature.

**Figure 7.** Propidium iodide fluorescence intensity at 607 nm versus temperature for Ad5 in MRK2 at pH 5 (solid squares) and pH 6 (open circles). T1 designates the first significant increase in fluorescence intensity that is attributed to the loss of the penton capsomeres at the vertices. T2 designated a second transition that occurs at higher temperatures relative to T1. T2 is attributed to the further disassembly of the capsid which results in complete DNA accessibility to the extrinsic fluorescent probe.

**Figure 8.** Dynamic light scattering melting temperatures versus temperature for Ad5 in MRK1 (open circles) and MRK2 (solid squares).  $T_m$ s were not obtainable due to extensive Ad5 aggregation below pH 6 in MRK1.

**Figure 9A.** Empirical phase diagram of Ad5 in MRK1. Data employed to generate this image were taken at 2.5 °C intervals over the temperature range 10-85 °C. Data included in the empirical phase diagram are: second derivative UV peaks near 279, 284, and 291 nm, optical density at 350 nm, intrinsic fluorescence wavelength of maximum fluorescence intensity (max), fluorescence intensity at max, propidium iodide fluorescence intensity at 607 nm, and hydrodynamic diameter obtained from dynamic light scattering measurement. The blue region in this figure represents conditions under which the Ad5 particles

are in their native, intact form; green regions represent conditions under which the viral particles are at least partially structurally perturbed (*e.g.*, penton

bases and fibers are detached from the Ad5 capsid); colors at higher temperatures beyond the green region represent conditions under which the Ad5 capsid is completely dismantled; the orange-brown region at low temperatures at pH 5 as well as the multicolored region at low temperatures at pH 4 represent conditions under which the Ad5 particles have undergone extensive aggregation.

**Figure 9B.** Empirical phase diagram of Ad5 in MRK2. Data employed to generate this image were from the same techniques, temperature intervals, and temperature range employed in the generation of the empirical phase diagram for Ad5 in MRK1. Similar to Figure 9A, magenta regions represent conditions under which the Ad5 particles are in their active, intact form; yellow colors represent conditions under which the viral particles have undergone penton base and fiber dissociation; colors at temperatures higher than the aqua regions represent conditions under which the Ad5 virion capsids are completely structurally disrupted.

Figure 1.

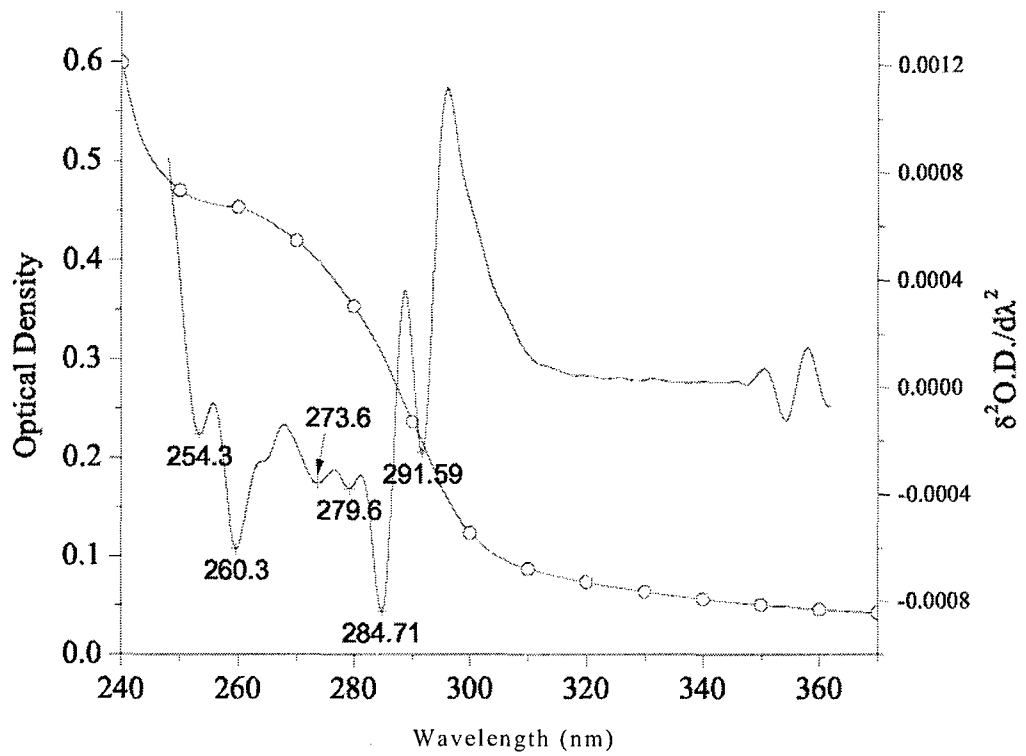
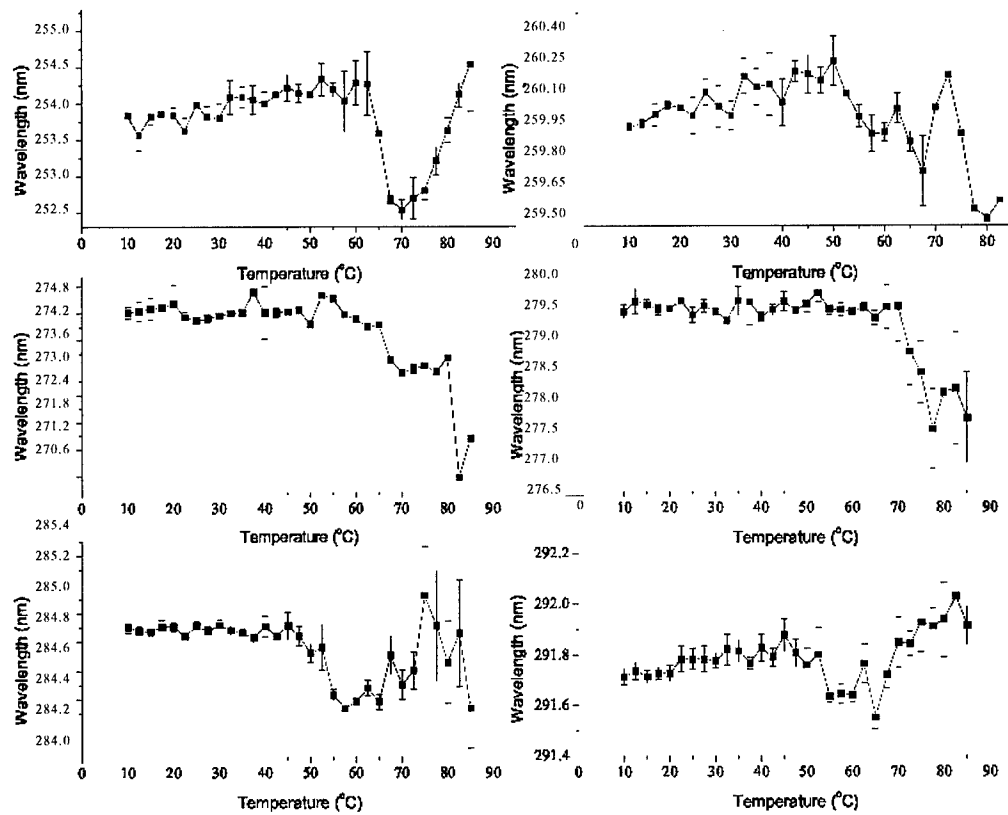


Figure 2.

Ad5, pH 7, MRK2 (1M NaCl)



Average 2nd Derivative UV Peak Position vs Temperature

Figure 3.

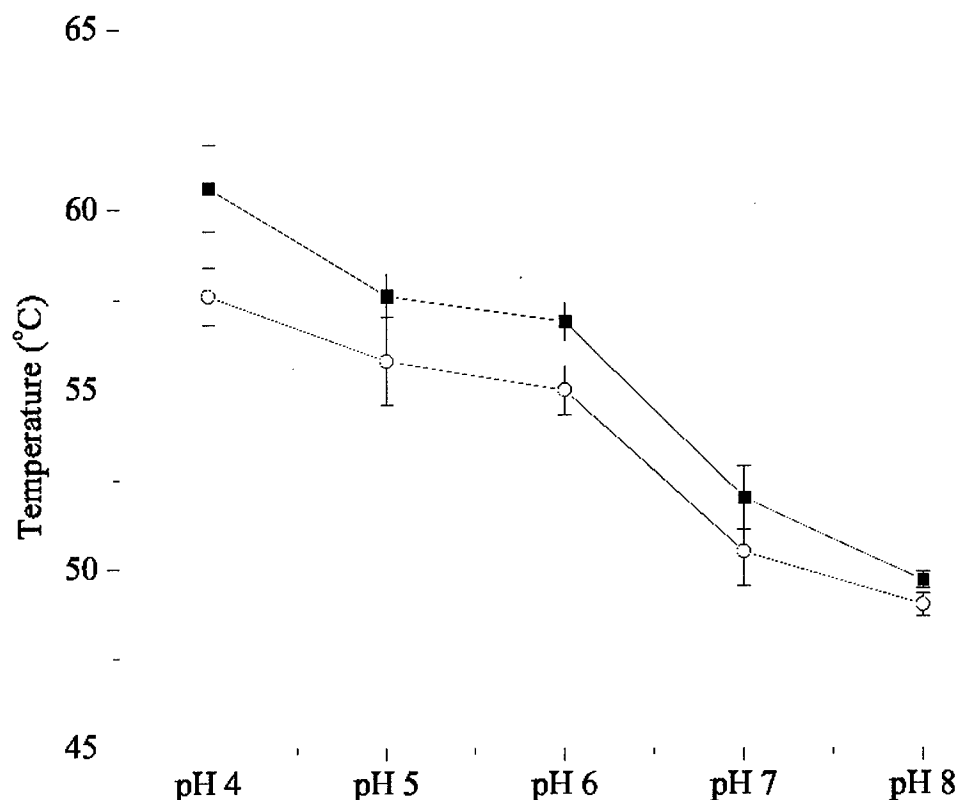


Figure 4.

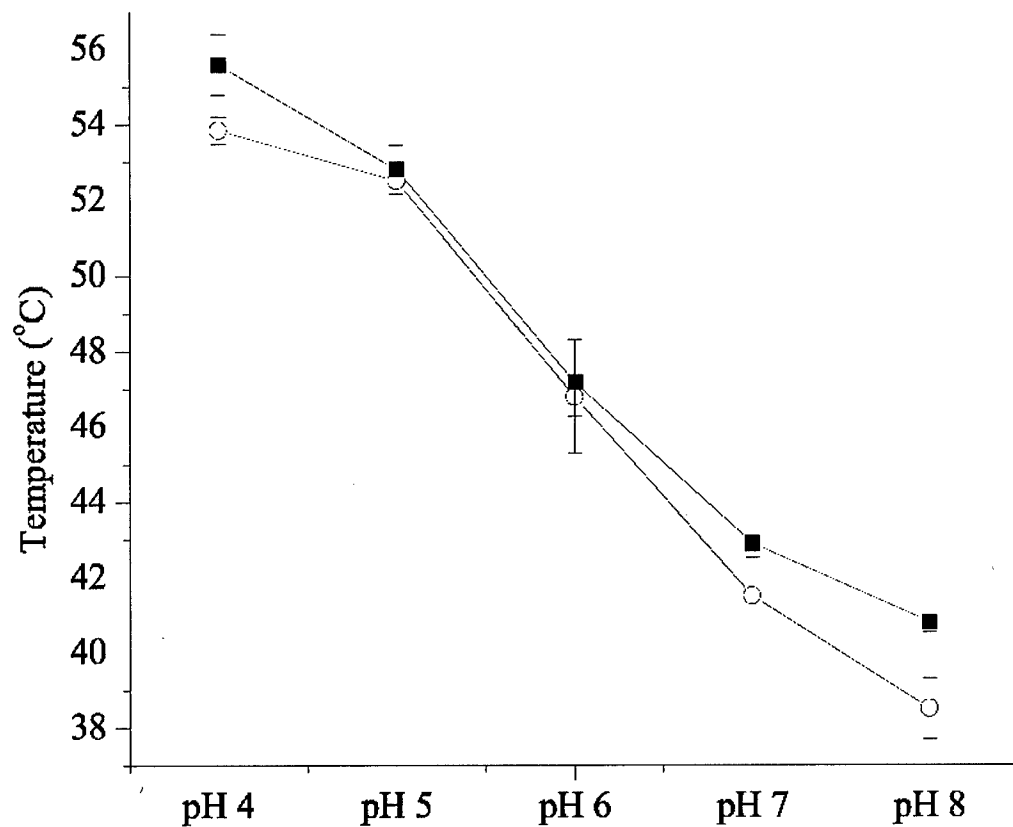


Figure 5.

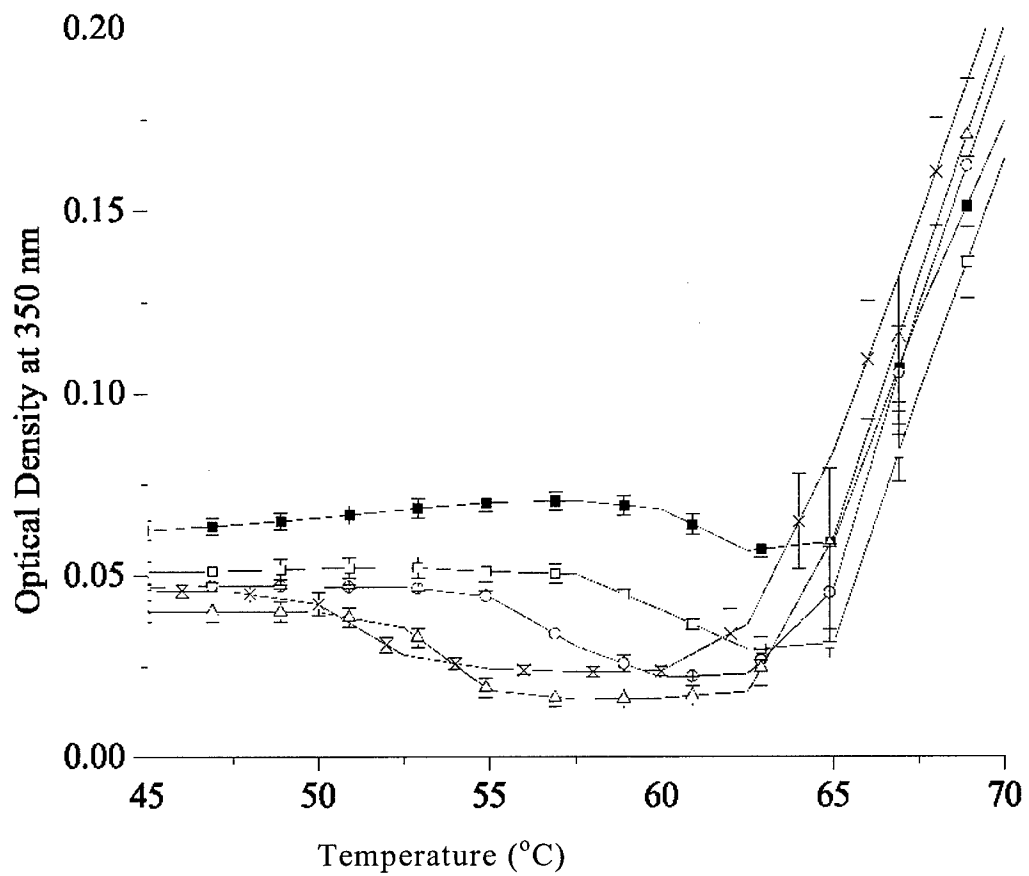


Figure 6.

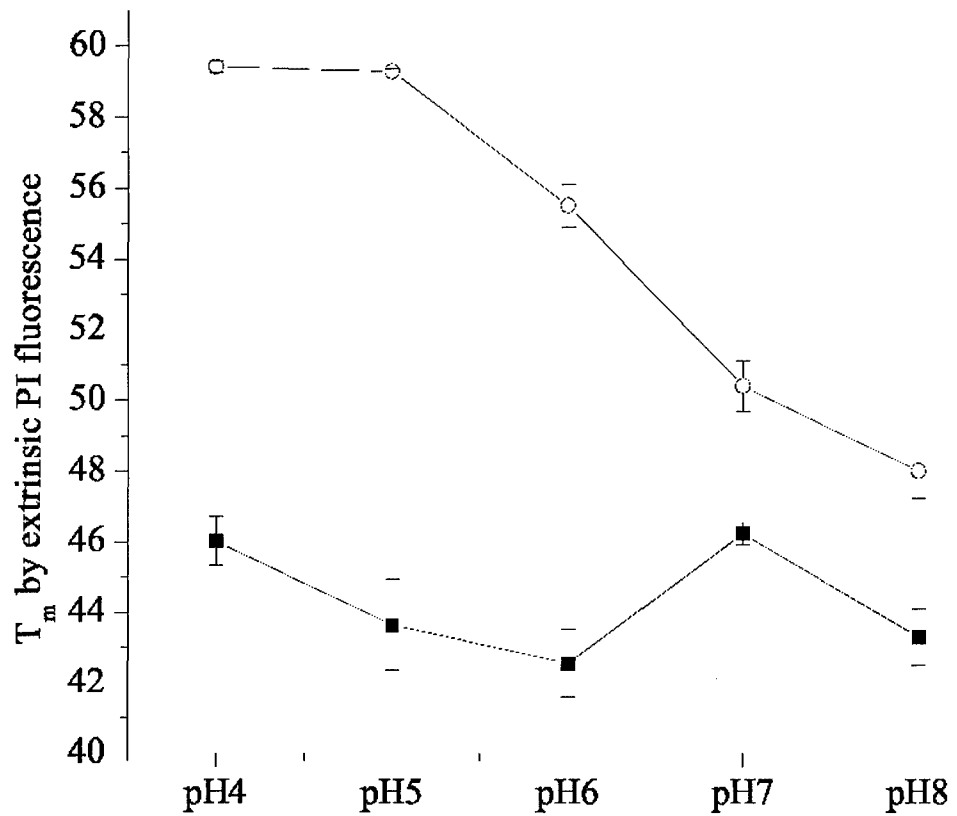


Figure 7.

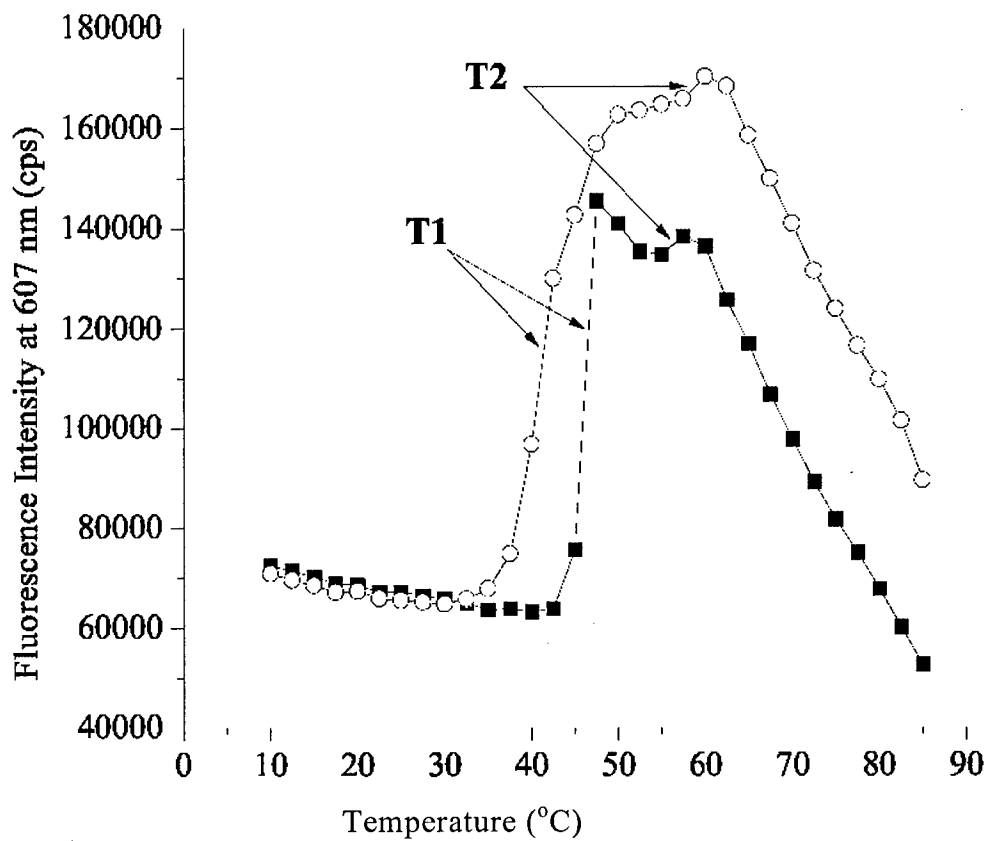


Figure 8.

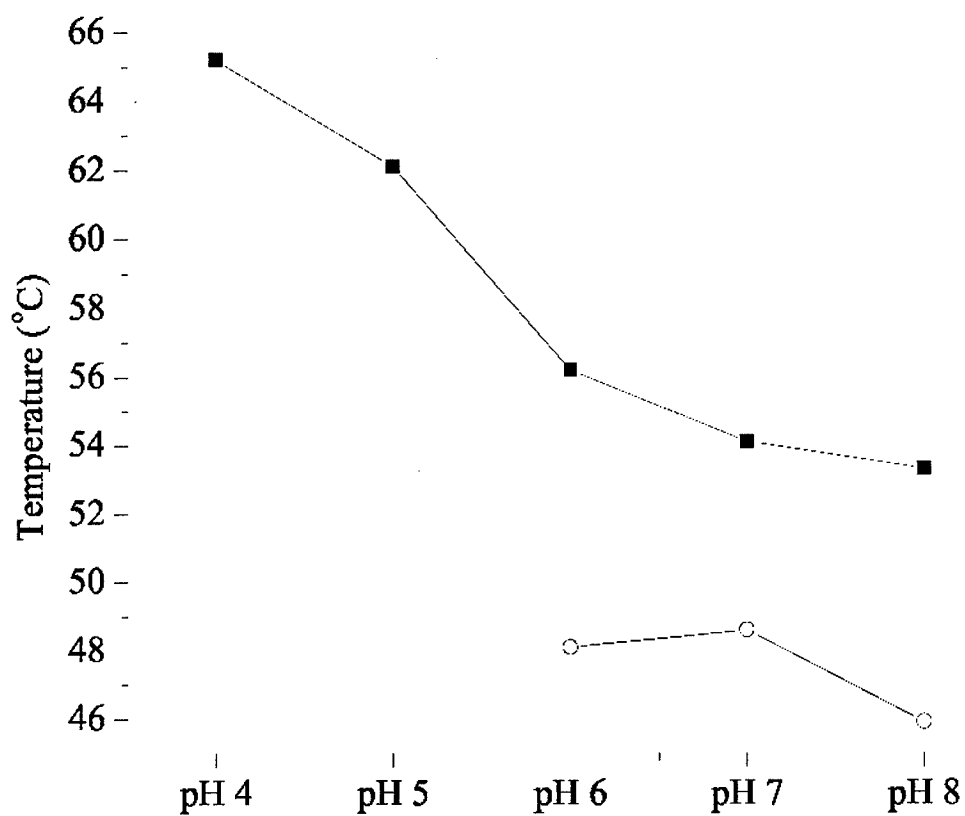
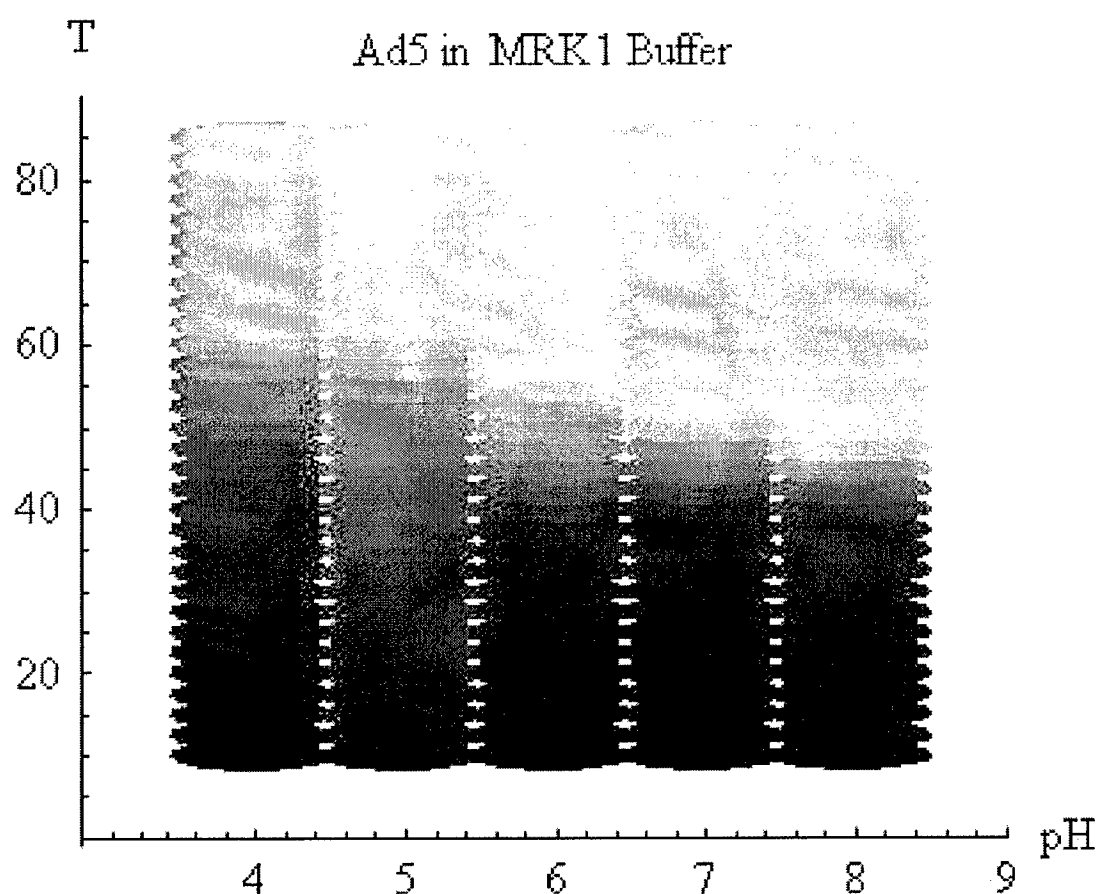
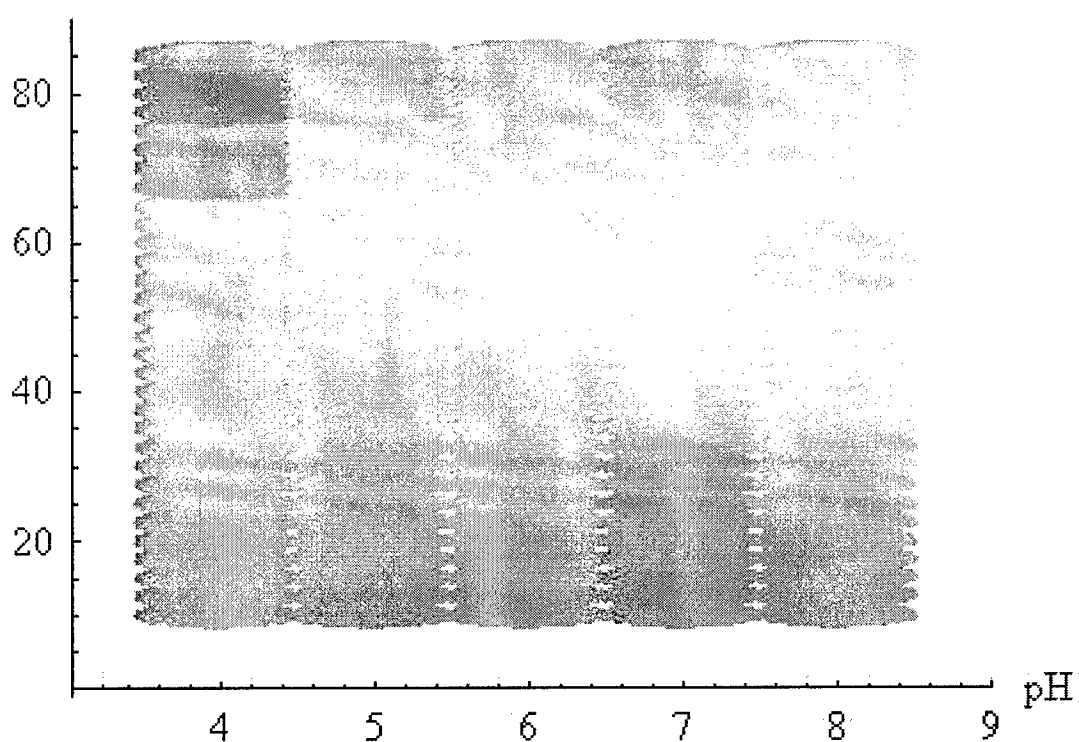


Figure 9B.



T

Ad5 in MRK2 Buffer (1M NaCl)



**Appendix III: Adenovirus 2 manuscript**

**Thermal Stability of Adenovirus Type 2 as a Function of pH**

***Jason Rexroad<sup>1</sup>, Talia Martin<sup>1</sup>, David McNeilly<sup>2</sup>, Simon Godwin<sup>2</sup>, and C. Russell Middaugh<sup>1\*</sup>***

***<sup>1</sup>Department of Pharmaceutical Chemistry, University of Kansas,  
Lawrence, KS 66047***

***<sup>2</sup>Genzyme Corporation, 500 Kendall Street, Cambridge, MA 02142***

\*To whom correspondence should be addressed

Department of Pharmaceutical Chemistry  
University of Kansas  
2095 Constant Ave  
Lawrence, KS 66047  
Tel: (785) 864-5813  
Fax: (785) 864-5814  
[middaugh@ku.edu](mailto:middaugh@ku.edu)

## INTRODUCTION

Recombinant adenoviral vectors, especially types 2 and 5 (Ad2 and Ad5) are used widely in both human gene therapy and genetic vaccination.<sup>1</sup> Although several recent studies have focused on the characterization and formulation of Ad5,<sup>2-4</sup> comparable efforts concerning Ad2 have been lacking. Similar to the development of any drug, however, formulation development will be a critical step in the production of a successful Ad2 pharmaceutical product.

Ad2 possesses icosahedral symmetry and a molecular weight of 150 MDa. The virus contains a protein coat that is composed of multiple copies of approximately seven different proteins and a linear double-stranded DNA core of approximately 35 kb which is associated with multiple copies of 4 different proteins.<sup>5,6</sup> Although it has been shown that deleterious physical and chemical changes can lead to losses in activity of adenoviral vectors,<sup>3,7</sup> the actual mechanisms of inactivation have proven elusive.

In addition to the challenge of characterizing a complex entity such as a virus, the aggressive product timelines put forth by today's pharmaceutical industry requires that formulations be developed as rapidly as possible. To accomplish this in an adequate timeframe, it is necessary to understand the degradation pathways of potential pharmaceuticals and utilize that knowledge to rationally develop a formulation that prevents or inhibits those events that lead to losses in activity. These requirements argue for the employment of high throughput methods when available.

To this end, we have employed multiple biophysical techniques (*i.e.*, dynamic light scattering, circular dichroism, derivative UV absorption, and fluorescence spectroscopies) to assess the thermal stability of the secondary, tertiary, and quaternary structure of Ad2 as a function of pH. We have been able to detect thermally induced conformational changes that appear to lead

to losses in Ad2 activity, as well as identify conditions under which Ad2 is most physically stable. Since perturbations in the physical state of a protein can also lead to chemical degradation (*e.g.*, oxidation, deamidation, disulfide scrambling, and/or hydrolysis),<sup>8</sup> formulating Ad2 under conditions to minimize physical changes should also enhance its chemical stability. Furthermore, because retention of the physicochemical structure of biological macromolecules is critical to maintaining activity, this approach should also yield a formulation that retains the activity of Ad2 during storage for longer periods.

Extensive biophysical characterization typically generates large amounts of data which can be difficult to analyze in a comprehensive manner. To address this issue, we have employed a multi-dimensional Eigenvector approach to generate an empirical phase diagram (EPD) of Ad2.<sup>9</sup> The EPD offers an intuitive representation of the data. It not only identifies conditions, or “phase boundaries,” where structural integrity is altered, but also provides a tool that can be used to identify conditions under which forced degradation studies can be performed to screen for potentially stabilizing excipients. In this study we use temperature and pH to accelerate changes in Ad2 structure for this purpose.

## MATERIALS AND METHODS

### **Preparation of Ad2.**

The second generation, replication-incompetent adenovirus type 2 (Ad2) vector employed in these studies was propagated in human embryonic kidney (HEK) cells under serum-free conditions. Upon completion of the infection period, virus was released from the cells using a non-ionic surfactant. The milieu was subsequently clarified by centrifugation and purified over a

series of chromatography columns. The purified virus was formulated in PBS containing 10% sucrose and stored at -70 °C prior to use in experiments. Ad2 concentration ( $2.0 \times 10^{12}$  viral particles/mL [vp/mL]) was determined by anion exchange HPLC as previously described.<sup>19</sup> Test material preparations were loaded over an anion exchange resin and virus was eluted over a salt gradient. Adenoviral particle peak elution profiles were detected by UV absorbance at a wavelength of 280nm. The assay detection lower limit for this method is approximately  $1.0 \times 10^9$  vp/mL. Prior to measurements, Ad2 stocks were diluted to a concentration of  $5 \times 10^{11}$  vp/mL and subsequently dialyzed overnight at 4 °C against 20 mM citrate-phosphate buffer containing 110 mM sodium chloride at the appropriate pH (pH 3-8) at one unit intervals.

**UV Absorption Spectroscopy.** To assess tertiary structure changes in Ad2, second derivative UV absorption spectroscopy was employed at a concentration of  $5 \times 10^{11}$  viral particles/mL (vp/mL). Absorption spectra were obtained employing an Agilent 8453 diode-array spectrophotometer. A baseline was obtained with the appropriate buffer and baseline-corrected spectra were obtained every 2.5° C from 10-85° C. A 5-minute hold time was used at each desired temperature for sample equilibration. Calculated second derivative spectra were fit to a spline function with 99 points of interpolation using software supplied with the instrument. Negative peak positions were determined and plotted versus temperature. Additionally, the optical density at 350 nm (OD) was monitored as a function of temperature. Data was plotted using Microcal Origin® version 7. Second derivative UV and optical density data are presented as mean values with standard errors (N=3).

**Fluorescence Spectroscopy.** To further assess the thermal stability of the tertiary structure of the Ad2 proteins, intrinsic fluorescence emission spectra were obtained in 2.5° C increments from 10-85° C employing a QuantaMaster™ spectrofluorometer (Photon Technology International, Inc.) equipped with a 4-position cell holder and Peltier temperature control device. A 5-minute equilibration time was used at each temperature before data acquisition. The intrinsic fluorescence spectra were collected at a viral concentration of  $5 \times 10^{11}$  viral particles/mL (vp/mL) by exciting samples at 280 nm while the emission was monitored between 305 and 450 nm using excitation and emission slit widths of 4 nm. Spectra were smoothed using the software included with the instrument and the wavelength of emission maximum ( $\lambda_{\text{max}}$ ) for each spectrum was determined in Microsoft Excel®. The  $T_m$  at each pH was determined by calculating the point where the second derivatives of the  $\lambda_{\text{max}}$  versus temperature plots crossed the x-axis using Microcal Origin®. Values are presented as the mean with accompanying standard errors (N=3)

Extrinsic fluorescence spectroscopy was conducted to determine the accessibility of Ad2 DNA as the temperature was varied using 7.5  $\mu\text{M}$  propidium iodide (PI, Molecular Probes, #P1304MP) as an extrinsic fluorescent probe. Sample volumes of 1 mL were examined in sealed quartz cuvettes and excited at 535 nm. Emission was monitored from 550 to 650 nm using excitation and emission slit widths of 6 nm. The fluorescence intensity near the wavelength of maximum fluorescence intensity for each spectrum (613 nm) was plotted as a function of temperature in Microsoft Excel®. PI intensities as a function of temperature are presented as mean intensities with standard errors (N=3)

**Circular Dichroism Spectroscopy (CD).** CD data were obtained to assess the secondary structural stability of the Ad2 proteins employing a Jasco 810 spectropolarimeter equipped with a

Peltier temperature control device and a 6-position sample holder. CD spectra were acquired at 10° C and single wavelength CD measurements at 208 nm were taken over the temperature range 10-85° C. Ad2 samples were contained in sealed 0.1 cm path length cells at a concentration of  $\sim 5 \times 10^{11}$  vp/mL. A resolution of 0.2 nm and a scanning speed of 20 nm/min with a 2-s response time were employed. The CD at 208 nm was measured at 0.2° C intervals using a 15° C/h temperature ramp rate and a 2-s response time. Data was smoothed with Jasco software and subsequently plotted in Microcal Origin®. CD traces at 208 nm are presented as mean data with standard errors (N=3).

**Dynamic Light Scattering.** The hydrodynamic diameter of Ad2 as a function of temperature was measured by dynamic light scattering using a viral concentration of  $5 \times 10^{11}$  vp/mL. Measurements were obtained every 2.5 °C using a light scattering instrument (Brookhaven Instruments Corp, Holtszille, NY) equipped with a 50 mW diode-pumped laser ( $\lambda=532$  nm) incident upon a sample cell immersed in a bath of decalin. Temperature was controlled by a circulating water bath. The scattered light was monitored by a PMT (EMI 9863) at 90° to the incident beam and the autocorrelation function was generated by a digital correlator (BI-9000AT). Data was collected continuously for five 30-s intervals for each sample and averaged. The autocorrelation function was fit by the method of cumulants to yield the average diffusion coefficient of the complexes. The effective hydrodynamic diameter (Z-average particle size) was obtained from the diffusion coefficient by the Stokes-Einstein equation. In the cases of pH-induced aggregation, the data was fit to a non-negatively constrained least squares algorithm to yield multi-modal distributions on a number average basis.

**Empirical Phase Diagram (EPD) Generation.** The EPD was generated using data points at 2.5° intervals from 10-85° C. The data used to construct the EPD are: the second derivative UV peak near 285 nm, CD at 208 nm, optical density at 350 nm, intrinsic fluorescence peak position, intrinsic fluorescence intensity at  $\lambda_{\text{max}}$ , hydrodynamic diameter, and the propidium iodide fluorescence intensity at 613 nm. Data from these techniques were formatted in Microsoft Word® and copied into Mathematica® version 4.2 (Wolfram Research, Inc.) for phase diagram generation. The EPD represents the physical state of Ad2 as a multi-component vector with the individual components defined by indicated measurements. The three components which contributed the greatest are represented as colors in a RGB-based scheme. A more detailed explanation of this method is described elsewhere.<sup>9</sup>

## RESULTS

**UV Absorption Spectroscopy (UV).** High resolution second derivative UV absorption spectroscopy was employed to investigate the tertiary structural stability of Ad2 as a function of temperature over the pH range 3-8. Changes in the polarity of the environment of the aromatic amino acids within the Ad2 virion should be manifested as shifts in the negative peak positions. Figure 1 illustrates the UV absorption spectrum of Ad2 at pH 7, 10 °C and its second derivative. The “tailing” in the spectrum above 300 nm indicates a significant degree of light scattering due to the relatively large size of the Ad2 particles. By concomitantly following the optical density at 350 nm (O.D.) with increasing temperature, the aggregation state of the Ad2 particles can be assessed under the various conditions examined. Although the peaks below 270 nm cannot be definitively assigned due to the spectral overlap of protein phenylalanine residues and viral DNA

bases, peaks near 274, 279, 285, and 292 nm can be assigned to signals arising from the absorption of tyrosine, tryptophan, a combination of tyrosine/tryptophan, and tryptophan, respectively.<sup>10-12</sup>

Analysis of the second derivative UV data reveals that major structural transitions within the Ad2 virion take place near 40 and 65 °C at pH 7 (Figure 2). Shifts in the negative peak positions of the Tyr, Tyr/Trp, and Trp bands to lower wavelengths near these temperatures suggest that the average solvent environment of these aromatic side chains is becoming more polar, presumably as a result of thermally induced structural perturbations that increase the side chains' exposure to water. Peaks below 260 nm of Ad2 at pH 7 manifest transitions near the same temperatures although the transition near 40 °C is less pronounced. Shifts in these peak positions, however, are to higher wavelengths suggesting that either the Phe residues and/or the nucleic acids may be adopting a less solvent exposed conformation.

Comparison of the structural stability of Ad2 at pH 7 with that at other pH values suggests that the stability increases with decreasing pH from pH 8 to 5. Calculation of the transition temperature midpoints near 40 and 65 °C suggest that the tertiary thermal stability is at a maximum near pH 5 (Figure 3). Measurements by other techniques, however, reveal that Ad2 undergoes significant aggregation below pH 5 (discussed below).

Extensive aggregation was observed following dialysis of Ad2 at pH 3 and 4. The pH-induced self-association was manifested as larger O.D. values at 10 °C (Figure 4) when compared to the O.D. of Ad2 at higher pH. The O.D. at pH 5-8, however, is below 0.09 A.U. reflecting the absence of significant aggregation. The O.D. values at pH 5 remain relatively constant with increasing temperature up to approximately 42 °C at which point a dramatic increase in the amount of scattered light is observed. This increase in O.D. near 42 °C suggests that Ad2

undergoes thermally induced structural perturbations at or below this temperature which culminate in aggregation. At pH 6-8, OD<sub>350</sub> measurements remain relatively constant at low temperatures. Prior to abrupt increases in the O.D., however, a sharp decrease in the amount of scattered light is observed (Figure 4). Although this has not been rigorously explored, dynamic light scattering (DLS) measurements suggest that the initial decrease in scattered light may be a result of swelling of the Ad2 particles. Data from extrinsic fluorescence spectroscopy (described below) and transmission electron microscopy<sup>4</sup> suggest that the swelling of Ad2 particles follows release of penton bases and their fibers at the vertices of the capsid. These particles are less dense and therefore have a lower refractive index which produces a decrease in scattering intensity and an increase in size (as measured by DLS). This phenomenon is also discussed in more detail below.

The onset temperatures at which increases in O.D. are observed are not significantly different over the pH range 5-7 (onset is near 45 °C); however, increases in O.D. at pH 8 occur near 30 °C. Together, the O.D. data suggest that Ad2 is particularly sensitive to aggregation outside the pH range 5-7 and a structural change occurs prior to aggregation that results in a decrease in the amount of scattered light. This structural change is attributed to the loss of penton bases and fibers at the capsid vertices (see below).

**Intrinsic Fluorescence Spectroscopy.** As a complementary approach to the UV absorbance method, intrinsic fluorescence spectroscopy was employed to further investigate the tertiary structural stability of the Ad2 proteins. Fluorescence spectra of Ad2 at 10 °C, pH 7 manifest an emission maximum ( $\lambda_{\text{max}}$ ) near 329 nm suggesting that the majority of the Trp residues are in a relatively apolar environment. Upon heating at pH 7, however, the  $\lambda_{\text{max}}$  shifts to higher

wavelengths near 43 °C suggesting that the average environment of the Trp residues becomes more polar as a result of thermal perturbation and consequent increased exposure to the aqueous solution. Similar to the results obtained by UV absorption spectroscopy, intrinsic fluorescence measurements detect two major thermally induced structural transitions. The transitions at higher temperatures (near 65 °C) were not, however, as well-defined by this technique. Conversion of plots of the wavelength of emission maximum to Tm's (Figure 5) as well as following the fluorescence intensity at  $\lambda_{\text{max}}$  with increasing temperature reveal that with the exception of pH 3, the thermal stability of Ad2 increases with decreasing pH. These results are in general agreement with those obtained by UV absorption.

**Extrinsic Fluorescence Spectroscopy.** Propidium iodide (PI) was employed to probe the integrity of the Ad2 capsid. The fluorescence signal of PI is quenched when free in solution. Upon DNA intercalation, however, its fluorescence intensity is enhanced up to 30-fold thereby permitting detection of the temperature at which the structure of the capsid is compromised. When PI is incubated in the presence of Ad2 at pH 7, an initial increase is observed in fluorescence intensity near 40 °C followed by a second marked increase near 62 °C (Figure 6). With the exception of pH 3, two distinct transitions are also detected at the other pH values. Extrinsic fluorescence of PI also suggests that the stability increases with decreasing pH from pH 8-4 in agreement with data obtained from the other techniques. The increase in fluorescence intensity of PI at pH 3 is not as dramatic as the initial increases at the other pH values, but a slight increase in the PI fluorescence signal is observed near 50 °C. These data at pH 3 prompted the investigation of PI fluorescence in the presence of free DNA at pH 3 with increasing temperature. Although an increase in fluorescence intensity was observed upon the addition of PI to free DNA at 20° C, the intensity

was decreased by ~15% compared to pH 4-8 (data not shown). At temperatures above 55 °C, however, an increase in the fluorescence intensity of PI was not observed upon the addition of PI to free DNA. This suggests that intercalation of the dye is inhibited at elevated temperatures at pH 3. Thus, these data suggest that the viral particles are still intact at 10° C since the fluorescence intensity of PI is not significantly different from PI alone at low temperatures. The conformational changes that lead to an increase in the accessibility of PI to the DNA core, however, are not as easily detected by this technique at high temperatures at pH 3.

***Far UV Circular Dichroism Spectroscopy (CD).*** CD was employed to assess the thermal stability of the secondary structure of Ad2 proteins. The CD spectrum of Ad2 at pH 7 possesses a minimum near 208 nm with a shoulder near 222 nm suggesting the presence of a mixture of  $\alpha$ -helix and  $\beta$ -sheet secondary structure. When the CD signal at 208 nm is followed with increasing temperature, losses in secondary structure are detected near 45 and 68 °C (Figure 7). These CD data also suggest that the thermal stability of the secondary structure of Ad2 increases with decreasing pH from pH 8-4. At pH 3, however, the magnitude of the CD signal at 208 nm increases above 60 °C. By collecting CD spectra at 5 °C intervals, it can be seen that the negative peak at 208 nm shifts to lower wavelengths suggesting an increase in the content of disordered structure within the viral proteins (data not illustrated). This shift also results in an increase in the magnitude of the CD signal at 208 nm further consistent with increased disordered structure.

Similar to the changes in tertiary structure that were detected by UV absorbance and intrinsic fluorescence spectroscopies, CD also suggests that Ad2 undergoes two major structural changes with increasing temperature. Furthermore, the temperatures at which these changes in

secondary structure occur correlate with those of the tertiary structural changes suggesting that these transitions are highly cooperative.

**Dynamic Light Scattering (DLS).** To further investigate the stability of the quaternary structure of Ad2, we employed DLS as a function of temperature. The hydrodynamic diameter of Ad2 at pH 7 and 10 °C was approximately 131 nm which is in good agreement with previous measurements.<sup>4,13</sup> In addition, the polydispersity index of Ad2 remained below 0.2 from 10-45 °C suggesting the presence of a relatively homogeneous particle size distribution. An abrupt increase in the size and polydispersity index was observed near 45 °C (Figure 8). These changes were accompanied by a concomitant decrease in the intensity of scattered light (Figure 8). As described above, these results are thought to be due to swelling of the viral particles which causes a decrease in the refractive index of the viral particles. Since scattering intensity is proportional to the square of the refractive index increment, decreases in scattering are consistent with particle swelling. Although a related phenomenon has been observed with another serotype of adenovirus, this hypothesis has yet to be rigorously tested. Previous EM studies, however, have shown that the thermally induced transition near 45 °C is due to the loss of penton bases and their fibers at the icosahedral vertices.<sup>4</sup>

Again like the results obtained by the other methods, the stability of Ad2 as examined by DLS demonstrates an increase in thermal stability with decreasing pH from pH 8-5. At pH 3 and 4, however, Ad2 undergoes extensive aggregation resulting in polydispersity indices above 0.2. When the autocorrelation data is fit by a non-negatively constrained least squares method, the largest population of particles is approximately 950 nm in diameter while particles smaller than 900 nm are not observed. Despite the presence of significant aggregation, data from the other

techniques suggest that the Ad2 capsid remains intact under these conditions. The relatively large size and heterogeneity of the aggregated particles results in a lack of DLS detectable thermally induced structural transitions at pH 3 and 4.

***A Temperature/pH Empirical Phase Diagram (EPD) of Ad2 Behavior.*** When the above data is combined in the form of an EPD, the increase in thermal stability with decreasing pH from pH 8 to 5 is apparent (Figure 9). The two marked conformational changes that take place near 45 and 65 °C are manifested as regions of color change near those temperatures. The areas of color change can be considered forms of “phase boundaries.” Based on color changes in the EPD, which reflect a combination of effects on secondary, tertiary, and quaternary structure, Ad2 remains in a conformationally similar state at low temperatures from pH 5-8 (the light pink color in Figure 9). Upon heating, however, Ad2 undergoes highly cooperative transitions which involve changes in the secondary, tertiary and quaternary structure of the proteins. These perturbations lead to capsid disruption. In addition, aggregation at pH 3 and 4 results in dispersed colors relative to pH 5-8 over the entire range of temperature. Conformational changes that take place at pH 4, however, are similar to those that occur at higher pH values despite the presence of aggregated viral particles.

## DISCUSSION

By employing comprehensive biophysical characterization of Ad2 as a function of temperature and pH, we have detected changes in the secondary, tertiary, and quaternary structure of the virus. Data from each technique manifested at least two distinct thermally-induced transitions. The first transition occurs near 42 °C at neutral pH. Previously, we showed that a

similar transition in Ad5 was due to the loss of penton bases and their fibers at the icosahedral vertices.<sup>4</sup> Since earlier studies have shown that the penton fibers and base are ultimately required for the maintenance of biological activity,<sup>14,15</sup> this transition can be considered to contribute significantly to a loss of activity.

Although the loss of penton bases and fibers is detected by extrinsic fluorescence spectroscopy, a maximum in emission intensity is not observed until a second transition occurs near 65 °C at neutral pH. This suggests that additional capsid disruption occurs at higher temperatures, allowing complete access of the extrinsic fluorophore to the nucleic acid core. Transmission electron microscopy (TEM) images of adenovirus following incubation at 70 °C (data not shown here since the images are essentially identical to those seen previously for Ad5 under the same conditions) reveal that 100% of the viral particles are structurally disrupted as a result of this thermal stress and that the majority have lost their triangular faces which give rise to the icosahedral symmetry of adenovirus. It is proposed, therefore, that the second transition is a result of the dissociation of the triangular faces of the capsid and the resultant exposure of the nucleic acid core.

The transitions identified during these studies suggest that Ad2 is thermally more stable under mildly acidic conditions since the temperature at which these transitions occur increase with decreasing pH from pH 8 to 4. In contrast, Ad2 at pH 3 and 4 undergoes significant aggregation at low temperatures. Despite the problem of aggregation at pH 4, EM images and the detection of two discrete structural transitions suggest that the overall icosahedral symmetry remains intact. Thus, if the aggregation of Ad2 is minimized by the addition of stabilizing excipients, preparing the virus for distribution at pH 4 versus pH 7 should yield a more thermally stable formulation. Whether these increases in thermal stability correlate with increases in storage stability and the

retention of activity remains to be demonstrated. Since recent studies of Ad5 suggest that its activity during storage is best maintained near pH 6, but its activity is lost at an increased rate at pH 5,<sup>3</sup> formulating adenovirus below pH 6 may lead to inactivation by an alternative, previously undescribed pathway. Additional studies to correlate increases in thermal stability under mildly acidic conditions with maintenance of activity during storage are therefore warranted.

Since these studies have identified these two capsid disruption events as common pathways of thermally-induced physical degradation, inhibition of these events by formulation modification should yield a more thermally stable adenovirus formulation. The EPD generated using data described herein identifies solution conditions (*i.e.*, temperature and pH) where Ad2 is not only physically stable, but conditions where the virus is structurally perturbed. For example, Ad2 is in a similar conformation with respect to its secondary, tertiary, and quaternary structure at low temperatures over the pH range 5-8 (the light pink region in Figure 8). As the temperature is increased, however, the color changes from light pink to purple and an empirical phase boundary is encountered (*i.e.*, a region of color change is observed). Although the phase boundaries at higher temperatures are not as distinct as those near 45 °C (suggesting less cooperative changes), the capsid disruption events that occur at higher temperatures are also reflected in EPD. Structurally, the phase boundaries near 45 °C represent the loss of the penton bases and their fibers at the icosahedral vertices. This capsid disruption event is associated with an increase in the hydrodynamic diameter of Ad2. A thermally-induced loss of pentons and subsequent increase in size has also been described for the bacteriophage P22.<sup>16</sup> Since the nucleic acid core within the capsid is under pressure and tightly packed often to the density of a liquid crystal,<sup>17,18</sup> penton release and resultant heat-expanded capsids may be a common route of thermal degradation among double-stranded DNA viruses with icosahedral symmetry.

Since the phase boundaries represent conditions where structural disruption of Ad2 occurs, these conditions can be used to perform forced degradation studies. For example, preliminary experiments performed in our laboratory were conducted employing phase boundary conditions of pH 6 at 55 °C. By incubating Ad2 in the presence of GRAS excipients under these conditions and monitoring the extrinsic fluorescence of PI in a 96-well plate, we were able to screen excipients in a high-throughput format to identify solutes that enhance the thermal stability of Ad2 formulations. Although this approach has permitted the identification of several excipients that enhance the tertiary and quaternary structural stability of Ad2, additional work is required to optimize excipient concentrations and correlate increases in thermal stability with biological activity.

1. Liu M, Acres B, Balloul JM, Bizouarne N, Paul S, Slos P, Squiban P 2004. Gene-based vaccines and immunotherapeutics. *Proc Natl Acad Sci U S A* 101 Suppl 2:14567-14571.
2. Croyle MA, Cheng X, Wilson JM 2001. Development of formulations that enhance physical stability of viral vectors for gene therapy. *Gene Ther* 8(17):1281-1290.
3. Evans RK, Nawrocki DK, Isopi LA, Williams DM, Casimiro DR, Chin S, Chen M, Zhu DM, Shiver JW, Volkin DB 2004. Development of stable liquid formulations for adenovirus-based vaccines. *J Pharm Sci* 93(10):2458-2475.
4. Rexroad J, Wiethoff CM, Green AP, Kierstead TD, Scott MO, Middaugh CR 2003. Structural stability of adenovirus type 5. *J Pharm Sci* 92(3):665-678.
5. Stewart PL, Burnett RM 1990. The structure of adenovirus. *Seminars in Virology* 1:477-487.
6. Stewart PL, Burnett RM, Cyrklaff M, Fuller SD 1991. Image reconstruction reveals the complex molecular organization of adenovirus. *Cell* 67(1):145-154.
7. Croyle MA, Roessler BJ, Davidson BL, Hilfinger JM, Amidon GL 1998. Factors that influence stability of recombinant adenoviral preparations for human gene therapy. *Pharm Dev Technol* 3(3):373-383.
8. Meyer JD, Ho B, Manning MC. 2002. Effects of Conformation on the Chemical Stability of Pharmaceutically Relevant Polypeptides. In Carpenter JF, Manning MC, editors. *Rational Design of Stable Protein Formulations*, ed., New York: Klewer Academic/Plenum Publishers. p 85-107.
9. Kueltzo LA, Ersoy B, Ralston JP, Middaugh CR 2003. Derivative absorbance spectroscopy and protein phase diagrams as tools for comprehensive protein characterization: a bGCSF case study. *J Pharm Sci* 92(9):1805-1820.
10. Mach H, Middaugh CR 1994. Simultaneous monitoring of the environment of tryptophan, tyrosine, and phenylalanine residues in proteins by near-ultraviolet second-derivative spectroscopy. *Anal Biochem* 222(2):323-331.
11. Mach H, Volkin DB, Burke CJ, Middaugh CR 1995. Ultraviolet absorption spectroscopy. *Methods Mol Biol* 40:91-114.
12. Ragone R, Colonna G, Balestrieri C, Servillo L, Irace G 1984. Determination of tyrosine exposure in proteins by second-derivative spectroscopy. *Biochemistry* 23(8):1871-1875.
13. Oliver CJ, Shortridge KF, Belyavin G 1976. Diffusion coefficient and molecular weight of type 5 adenovirus by photon-correlation spectroscopy. *Biochim Biophys Acta* 437(2):589-598.

14. Wickham TJ, Mathias P, Cheresh DA, Nemerow GR 1993. Integrins alpha v beta 3 and alpha v beta 5 promote adenovirus internalization but not virus attachment. *Cell* 73(2):309-319.
15. Louis N, Fender P, Barge A, Kitts P, Chroboczek J 1994. Cell-binding domain of adenovirus serotype 2 fiber. *J Virol* 68(6):4104-4106.
16. Teschke CM, McGough A, Thuman-Commike PA 2003. Penton release from P22 heat-expanded capsids suggests importance of stabilizing penton-hexon interactions during capsid maturation. *Biophys J* 84(4):2585-2592.
17. Cerritelli ME, Cheng N, Rosenberg AH, McPherson CE, Booy FP, Steven AC 1997. Encapsidated conformation of bacteriophage T7 DNA. *Cell* 91(2):271-280.
18. Lepault J, Dubochet J, Baschong W, Kellenberger E 1987. Organization of double-stranded DNA in bacteriophages: a study by cryo-electron microscopy of vitrified samples. *Embo J* 6(5):1507-1512.
19. Huyghe BG, Liu X, Sutjipto S, Sugarman BJ, Horn MT, Shepard HM, Scandella CJ, Shabram P 1995. Purification of a type 5 recombinant adenovirus encoding human p53 by column chromatography. *Hum Gene Ther* 6(11):1403-16.

**Figure 1.** Representative UV absorption spectrum of Ad2 at 10 °C, pH 7 (open circles) and its second derivative (solid line).

**Figure 2.** High-resolution second derivative UV spectroscopy negative peak positions as a function of temperature for Ad2 at pH 7. Peaks below 270 nm cannot be definitively assigned due to the overlapping absorbance of Phe and the DNA. Peaks near 275, 279, 284, and 292 nm, however, are attributed to the absorbance of Tyr, Trp, and a combination of Tyr/Trp, and Trp, respectively.

**Figure 3.** Second derivative UV absorption spectroscopy transition temperature midpoints for the peak near 285 nm of Ad2 versus pH. The peak near 285 nm is assigned to the overlapping absorbance of Tyr and Trp and should therefore be a good overall indicator of the tertiary structural stability of the viral proteins.

**Figure 4.** Optical density at 350 nm (O.D.) versus temperature for Ad2 at pH 3 through 8. Plots are ordered A through F by increasing pH from 3-8 at one unit intervals.

**Figure 5.** Intrinsic fluorescence  $T_m$  values versus pH for Ad2. The  $T_m$  values were calculated from a plot of the wavelength of maximum fluorescence intensity ( $\lambda_{max}$ ) versus temperature. Data reported are mean values with standard error (N=3). These data suggest an increase in the tertiary structural stability of Ad2 proteins with decreasing pH from pH 8 to 4.

**Figure 6.** Fluorescence intensity of propidium iodide (PI) at 613 nm versus temperature in the presence of Ad2 over the pH range 3-8. Symbols represent data obtained as follows: solid squares, pH3; empty squares, pH 4; triangles, pH 5; circles, pH 6; crosshairs, pH 7; solid line, pH 8. T1 designates the first significant increase in fluorescence intensity that is attributed to the loss of the penton capsomeres at the vertices. T2 is attributed to further capsid disassembly resulting in complete DNA accessibility to the extrinsic fluorescent probe. Although these transitions are also observed at other pH values, arrows indicate the transitions at pH 8. An increase in the stability of the virus' quaternary structure is observed with decreasing pH.

**Figure 7.** CD signal at 208 nm of Ad2 versus temperature. Plots are ordered A through F by increasing pH from 3-8. Two significant losses in secondary structure are observed. These transitions occur at higher temperatures with decreasing pH suggesting an increase in secondary structural stability with decreasing pH over the pH range 8-4.

**Figure 8.** Hydrodynamic radius (top panel) and normalized scattering intensity (bottom panel) of Ad2 obtained by dynamic light scattering measurements. Plots are assigned as follows: solid squares, pH 5; open squares, pH 6; open circles, pH 7; crosshairs, pH 8. Data were excessively noisy due to extensive aggregation of Ad2 below pH 5, however, the data collected suggests that the quaternary structural stability of Ad2 increases with decreasing pH from 8 to 5. Note that the DLS does not provide accurate measurements of size above 1  $\mu\text{m}$ .

**Figure 9.** Empirical phase diagram (EPD) of Ad2. The light pink region represents conditions under which the Ad2 particles are in their native, intact form. Structural changes are manifested as

color changes (*e.g.*, from light pink to purple near 45 °C at pH 7). The yellow and aquamarine colors at pH 3 and 4, low temperatures are a result of aggregation that occurs upon exposure to acidic conditions. Note that the nature of the colors themselves has no meaning.

Figure 1.

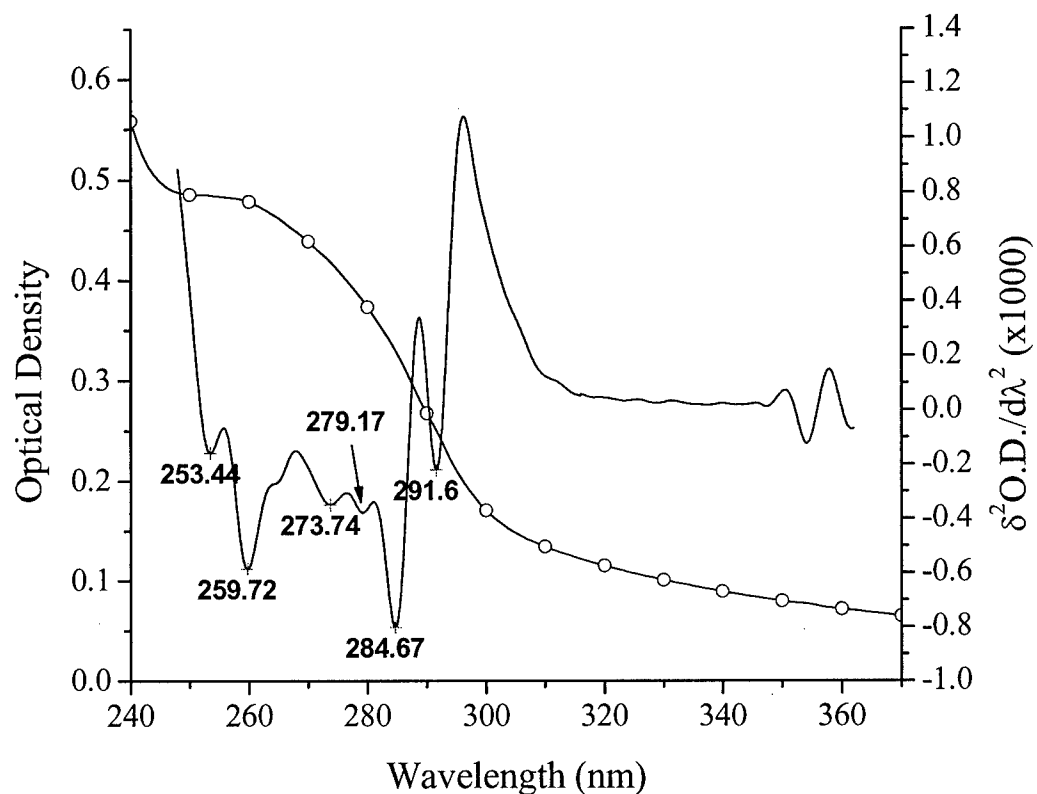


Figure 2.

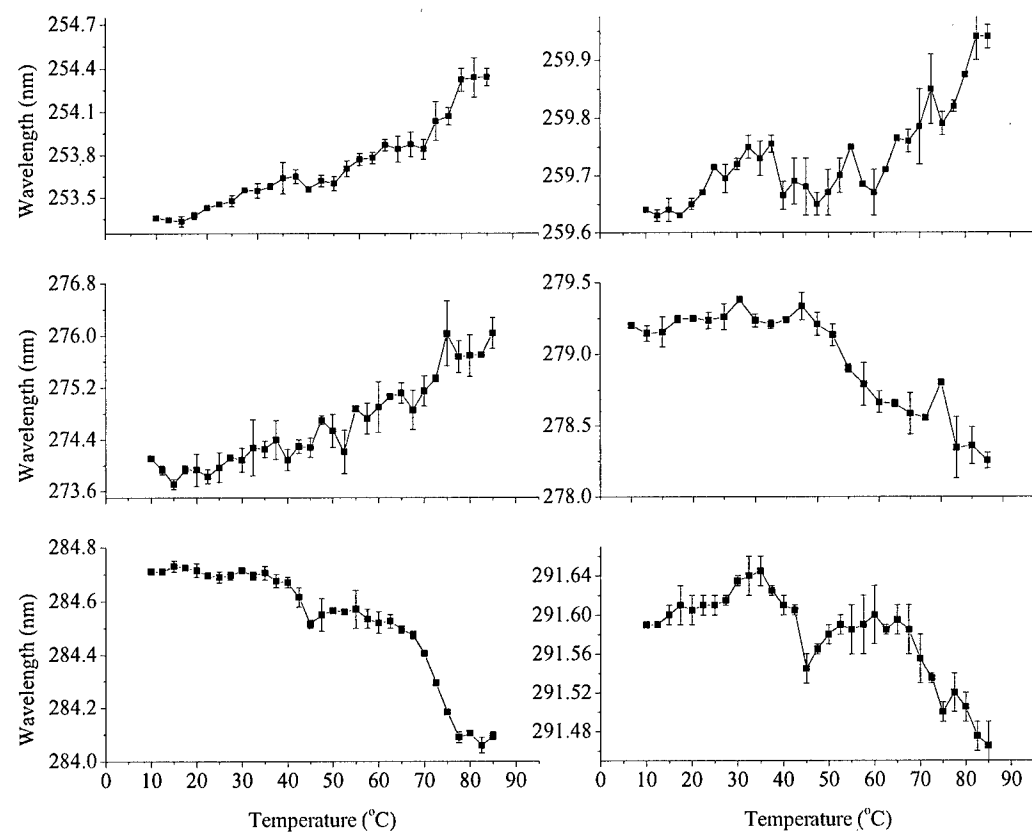


Figure 3.

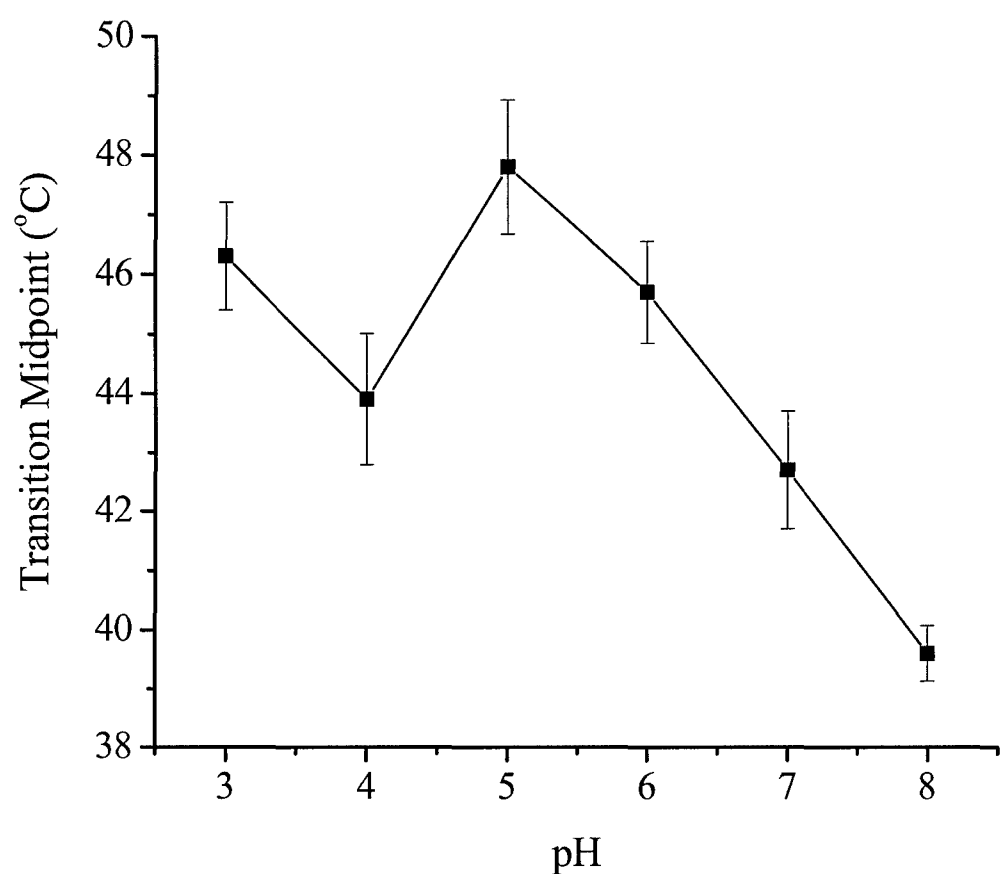


Figure 4.

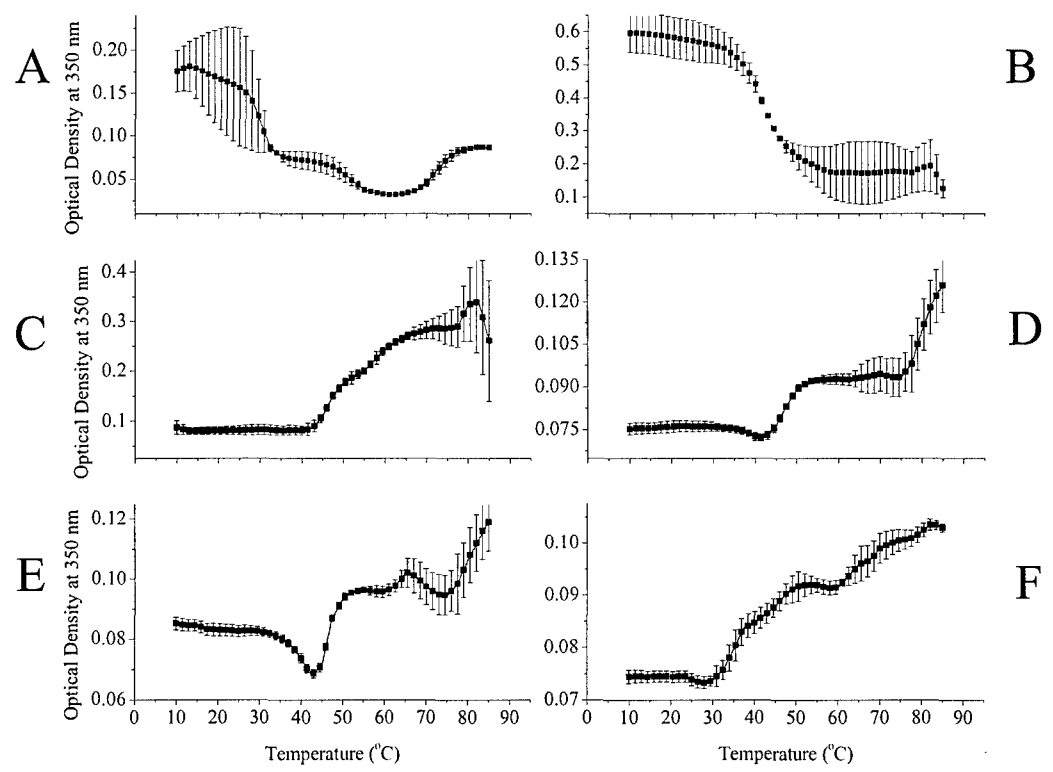


Figure 5.

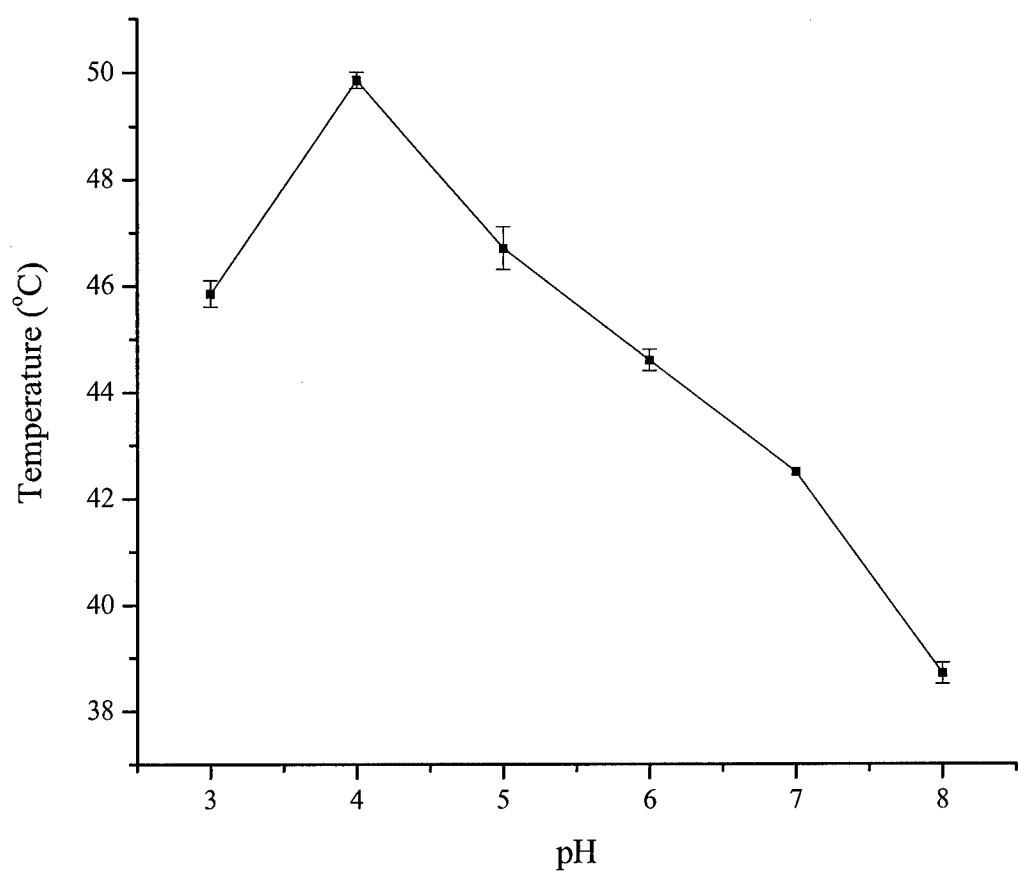


Figure 6.

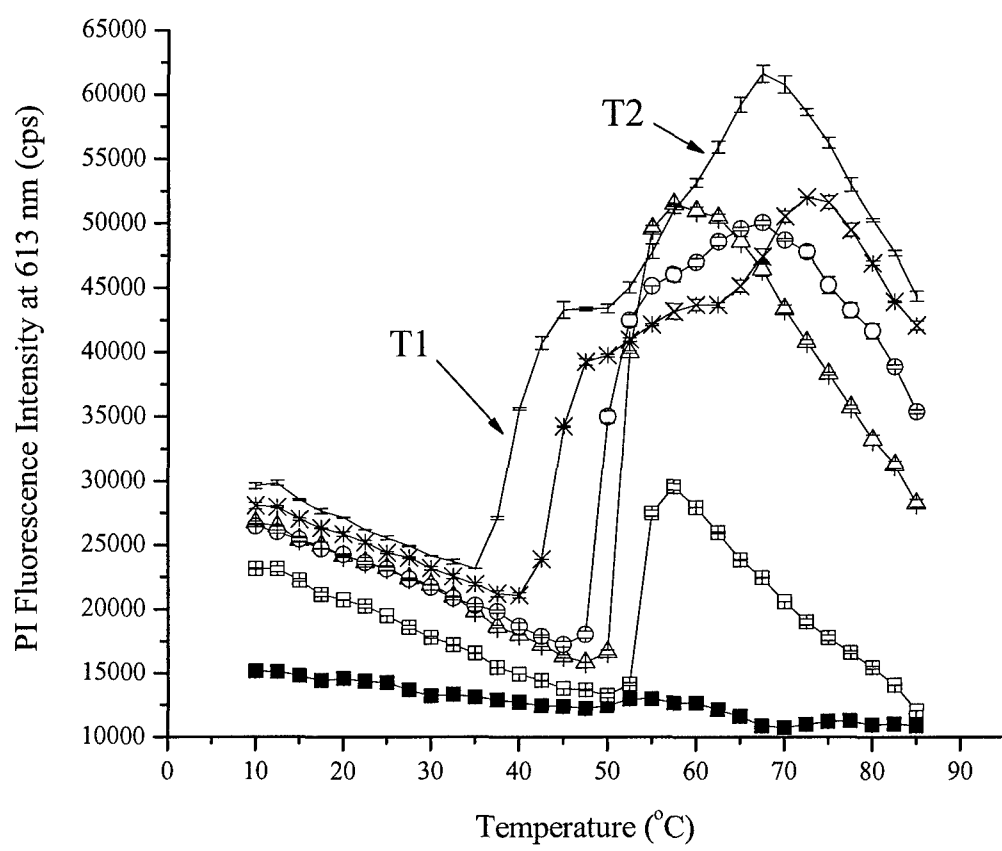


Figure 7.

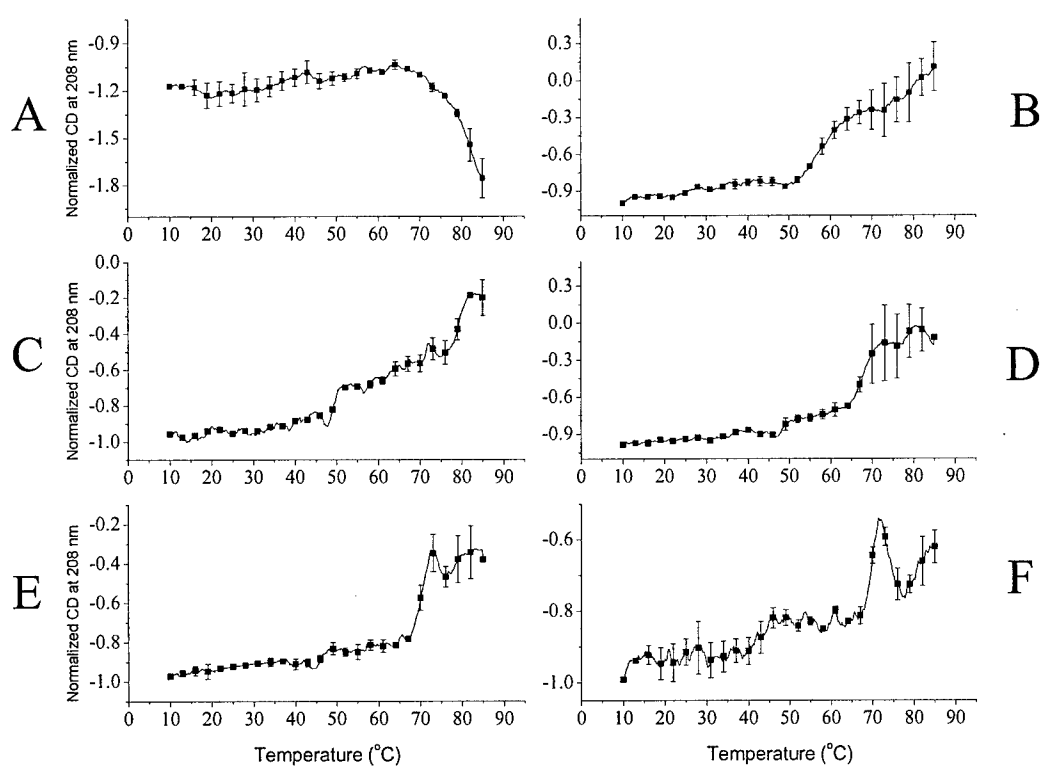


Figure 8.

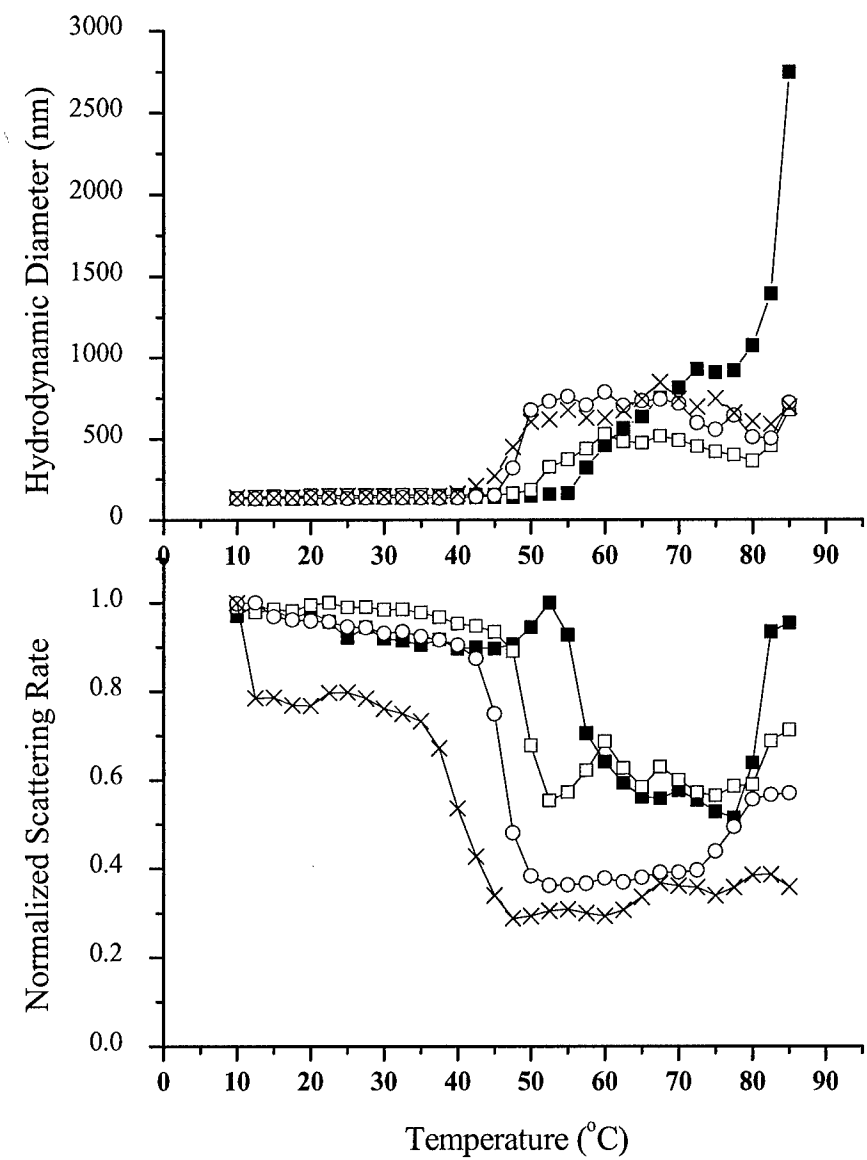


Figure 9.

